THE UNIVERSITY OF MICHIGAN

INDUSTRY PROGRAM OF THE COLLEGE OF ENGINEERING

INFLUENCE OF ACCELERATION ON SUBCOOLED NUCLEATE BOILING

Ross L Judd

A dissertation submitted in partial fulfillment
of the requirements for the degree of
Doctor of Philosophy in
The University of Michigan
1968

December, 1968

IP-826

To Joyce

ACKNOWLEDGEMENTS

The author gratefully acknowledges the assistance of Professor Herman Merte, Jr., who provided guidance and advice in planning and performing the research investigation and the assistance of Professor Poul S. Larsen, who reviewed the manuscript and provided many worthwhile suggestions.

The author also expresses his appreciation to Professors Vedat S. Arpaci, James O. Wilkes and Wen-Jei Yang for their interest and co-operation in serving as members of the Doctoral Thesis Advisory Committee.

Special thanks are due to Mr. Erol Ulucakli who assisted in obtaining the data and to Mr. Frank Kartje who provided guidance and assistance in the design and construction of the apparatus.

The financial support of the National Science Foundation under Grants G-15014 and GK-1296 is gratefully acknowledged.

TABLE OF CONTENTS

TABLE OF CONTENTS (CONT'D)

LIST OF TABLES

LIST OF FIGURES

LIST OF FIGURES (CONT'D)

LIST OF FIGURES (CONT'D)

LIST OF FIGURES (CONT'D)

LIST OF APPENDICES

NOMENCLATURE

Roman Symbols

a	Acceleration
a/g	Dimensionless Acceleration
A	Length, Area
B	Length
C	Length, Specific Heat
d	Depth
D	Length, Diameter
E	Voltage
f	Frequency
g	Gravitational Acceleration
g/g_c	Mass Force Conversion Constant
h	Heat Transfer Coefficient
h_{fg}	Heat Of Vapourization
I	Current
k	Thermal Conductivity
K	Constant
l	Length
L	Length
M	Molecular Weight
n/A	Average Population Density
N/A	Active Site Density
N*	Avogadro's Number
N_o	Constant
P	Pressure

Q	Heat
Q/A	Heat Flux
R	Radius, Result
T	Temperature
ΔT	Temperature Difference
V	Variable, Volume
W	Uncertainty
X	Coordinate Dimension
Y	Coordinate Dimension
Z	Coordinate Dimension

Greek Symbols

α	Thermal Diffusivity
δ	Thickness
θ	Angle
μ	Viscosity
ρ	Density
σ	Surface Tension, Standard Deviation
τ	Period
ϕ	Angle, Constant
ω	Angular Velocity

Dimensionless Parameters

Gr	Grashof Number
Nu	Nusselt Number
Pr	Prandtl Number

Subscripts

d	Departure
f	Fluid
ℓ	Liquid
g	Gas
h	Hydrostatic
i	Influence, Inactive
t	Total
v	Vapour
B	Bulk
MAX	Maximum
SAT	Saturated
SUP	Superheated
SUB	Subcooled
W	Wall
NB	Nucleate Boiling
NC	Natural Convection
T	Total

CHAPTER I

INTRODUCTION

A. Purpose

In spite of the extensive application of nucleate boiling as a means of transferring heat, the physical phenomenon is inadequately understood. Firstly, heat transfer rates in nucleate boiling are generally very high so that the thermal resistance attributed to nucleate boiling is not a limiting factor in the design of many heat exchanging devices. Consequently, there has been little incentive to investigate the mechanism of nucleate boiling heat transfer until comparatively recently when the advent of high power density systems created a need for more comprehensive knowledge of the phenomenon. Secondly, the nucleate boiling process is extremely complicated so that it is difficult to postulate a model which adequately describes the complete phenomenon. None of the many models in existence can consistently predict heat transfer rates in agreement with those measured for various combinations of fluid and heat transfer surface.

A number of experiments performed to determine the influence of acceleration level upon the saturated nucleate boiling phenomenon have demonstrated that although the mechanics of vapour removal depends upon the acceleration level, the corresponding rate of heat removal is not greatly affected. Photographic studies have shown that the departure diameter, the frequency of vapour bubble emission and the number of active sites per unit area are affected by the acceleration level. Apparently, these bubble characteristics interact in such a way that little change occurs in the rate of heat removal.

The few experiments performed to determine the influence of acceleration level upon the subcooled nucleate boiling phenomenon have shown effects similar to those described above. The research investigation which forms the subject of this dissertation was undertaken to determine the influence of acceleration and subcooling upon the rate of heat removal in general and to investigate the influence of these parameters upon the boundary layer thickness, the number of active nucleation sites per unit area, the frequency of vapour bubble emission and the maximum bubble size in particular.

B. Literature Survey

In order to be able to predict heat transfer rates from a surface to a liquid by nucleate boiling, the knowledge of three separate items is required. These are respectively the number of active nucleation sites, the frequency with which bubbles are emitted at these sites and the heat transfer associated with the emission of a bubble. At the present time, it is not possible to determine these items a priori, and consequently a nucleate boiling model which will adequately predict heat transfer rates irrespective of surface-liquid combination is lacking. Zuber[1] reports that over thirty models exist although none of these is capable of explaining the entire phenomenon. Rohsenow[2] and Westwater[3] in their reviews of the existing literature suggest that a generalized correlation cannot be formulated which does not take account of the nucleating characteristics of the boiling surface as well as the characteristics of bubble growth and departure or collapse. Some of the more important models attempting to explain the nucleate boiling phenomenon are presented below.

The bubble agitor model was postulated by Jakob[4] and was advanced by Rohsenow and Clark[5] and Gunther and Kreith[6]. These investigators suggested that the marked improvement in heat transfer associated with this phenomenon was the result of agitation of the thermal boundary layer adjacent to the heat transfer surface. Rohsenow[7] formulated an equation based upon this model of the form

$$Q/A \sim \frac{\mu_\ell \, h_{fg}}{[(g_c/g)\sigma/(a/g)(\rho_\ell-\rho_v)]^{1/2}} \left[\left(\frac{k}{\mu C}\right)_\ell^{1.7} \frac{C_\ell(T_W-T_{SAT})}{h_{fg}}\right]^3 \quad (1)$$

which satisfactorily correlated considerable of the existing nucleate boiling heat transfer data. However, a different coefficient was required for each fluid-surface combination. Levy[8] formulated another equation based upon this model of the form

$$Q/A \sim \frac{k_\ell C_\ell \rho_\ell^2}{\sigma T_{SAT}(\rho_\ell-\rho_v)} \, (T_W-T_{SAT})^3 \quad (2)$$

which satisfactorily correlated the nucleate boiling data for numerous liquids. The coefficient was found to depend upon the product $\rho_v h_{fg}$ in this case. Neither of these correlations directly accounts for the influence of surface nucleation characteristics, and this deficiency accounts for the need of a correlating coefficient. Mixon, Chon and Beatty[9], who performed heat transfer experiments from a heated surface at which hydrogen bubbles were generated electrolytically, found that although heat transfer was increased, bubble agitation could not account for the much higher heat fluxes experienced in boiling.

Forster and Grief[10] postulated a vapour-liquid exchange model to explain the observed heat transfer rate. It was suggested that the role of the bubbles was to displace a volume of liquid from the superheated layer adjacent to the heat transfer surface, allowing cooler liquid to move into the immediate vicinity of the heat transfer surface. The high rate of heat transfer was thought to be due to the exchange of vapour and liquid at the heat transfer surface. The following correlation based upon this model was advanced

$$Q/A \sim \rho_\ell C_\ell \, R_{MAX}^3 \, f(T_W - T_B)(N/A) \qquad (3)$$

which was claimed to satisfactorily correlate nucleate boiling heat transfer data for fluids as diverse in behaviour as water and mercury. In common with the previous correlations, this correlation does not account for the characteristics of the boiling surface. The correlation predicts that the heat transfer rate is sensitive to bulk liquid temperature and although this effect has been shown to exist by Bergles and Rohsenow[11] and by Rallis, Kok and Greenland[12], the magnitude of the effect is not nearly as great as the correlation indicates. Forster and Grief suggested that the influence of the bulk liquid temperature upon the maximum bubble radius and frequency acted to counter the influence of the bulk liquid temperature itself upon the heat transfer rate.

Hara[13] postulated a model in which the heat flow from the heat transfer surface to the thermal boundary layer was equated to the heat flow within the thermal boundary layer to the nucleation sites where liquid was evaporated to form bubbles. This model resulted in a correlation of the form

$$Q/A \sim (T_W - T_{SAT})^{3/2} (N/A)^{3/8} \qquad (4)$$

which compares favourably with that derived experimentally by Nishikawa and Yamagata[14]. The correlation advanced accounts for the influence of surface condition through the inclusion of the site density parameter.

Han and Griffith[15] proposed a model combining the effect of bulk convection due to bubble action in the vicinity of the nucleation sites with the effect of natural convection in the regions of the heating surface remote from the nucleation sites. The bulk convection contribution was derived from the premise that portions of the thermal boundary layer in the vicinity of the nucleation sites were displaced into the bulk liquid each time that a bubble departed from the heating surface and that the bulk liquid flowed in behind the departing bubble, locally creating a large temperature difference from surface to liquid which was responsible for the transfer of heat. After a finite time lapse, the development of a new thermal layer was postulated, subsequently followed by the initiation and development of another bubble. The natural convection contribution was derived from the premise that heat was transferred from the heating surface into the bulk liquid by the usual convection processes for those portions of the heating surface unaffected by bubble action. This model resulted in a very complicated correlating equation of the form

$$Q/A \sim \left[(1-\pi \sum^{N} R_i^2) Nu\, \alpha/D + 2 \sum^{N} \left\{ f\,[R_i^2\, \delta_d - (R_d^2/3)(\delta_d - \delta)] \right\}\right] \rho_\ell C_\ell (T_W - T_B) \qquad (5)$$

which correlated the authors' data satisfactorily but required a detailed knowledge of the bubble frequency, the number and size distribution of the active sites, the wall temperature and the bulk temperature as well as various boundary layer thicknesses. The equation presented by Han and Griffith is similar in form to that presented by Forster and Grief but the underlying physical models are different. The rate of heat exchange in the Han and Griffith model is proportional to the product of bubble area and boundary layer thickness whereas the rate of heat exchange in the Forster and Grief model is proportional to the bubble volume at departure. Han and Griffith conceded that the relationship derived was too complicated to be used as a working formula but claimed that it served as a guide to further useful research.

A markedly different approach was taken by Mesler and Moore[16] who interpreted rapid surface temperature fluctuations which they had measured as indication of evaporation of a thin layer of liquid at the base of the bubble. This interpretation was further substantiated by Hendricks and Sharp[17] who furnished proof that the surface temperature fluctuations observed corresponded to the period during which the bubble developed and not the period subsequent to the departure of the bubble. These observations tend to contradict the models advocating vapour-liquid exchange and at the present time, the paradox has not been resolved.

Only the first of the correlations presented above incorporates the acceleration level as an independent variable. This does not imply that the remaining correlations are independent of acceleration level in as much as the variables of which they are comprised, such as the bubble frequency, the bubble departure size, the site density and the superheat may themselves be dependent on acceleration level.

Usiskin and Siegel[18,19] studied the influence of reduced acceleration level upon saturated nucleate boiling water. Various levels of acceleration $0 \leq a/g \leq 1$ were investigated. The phenomenon investigated was essentially transient in nature since the duration of the test, corresponding to the fall of the platform upon which the test assembly was mounted, was short. However, the authors claim to have observed conditions which they believed to be representative of steady state nucleate boiling.

Usiskin and Siegel obtained high speed photographs of the boiling phenomenon during the fall. Analysis of their photographs indicated that reducing the acceleration level caused the velocity of vapour bubbles leaving the heat transfer surface to decrease and caused the diameter of the vapour bubbles at departure to increase in proportion to a/g to the $-1/3.5$ power. These two effects resulted in the accumulation of vapour near the heat transfer surface. Although it was thought that this vapour accumulation would reduce the heat removal, this effect was not observed. At constant heat dissipation, measurements of the temperature beneath the heat transfer surface remained unaffected during the fall, suggesting that the heat transfer rate did not change. The authors were careful to point out that the duration of their experiments was short and that the temperature beneath the heat transfer surface might not have been able to adjust to changes in the temperature of the heat transfer surface.

Merte and Clark[20] studied the influence of increased acceleration level $1 \leq a/g \leq 21$ upon nucleate boiling heat transfer in saturated and slightly subcooled water. Centrifugal motion was used to create the increased acceleration level. A test package containing the boiling

phenomenon was pivoted on an arm and rotated so that at steady conditions, the test package assumed a position such that the acceleration was applied normal to the heat transfer surface. Steady state boiling heat transfer conditions were observed.

For saturated boiling conditions, Merte and Clark detected an acceleration effect which depended upon the heat flux level. For constant values of heat flux less than 50,000 BTU/hr ft ^{2}, increased acceleration decreased the superheat; for constant values of heat flux greater than 50,000 BTU/hr ft ^{2}, the superheat increased slightly with increased acceleration. This behaviour undoubtedly indicates the existence of two different modes of heat transfer. It was postulated that the relative contributions of boiling and convection at the heat transfer surface caused this effect. At low levels of heat flux, boiling heat transfer occupied a relatively small portion of the heat transfer surface and consequently convection heat transfer, which is affected by acceleration in the manner described above, governed the heat removal. At high levels of heat flux, boiling heat transfer occupied a much greater portion of the heat transfer surface and in this case, boiling heat transfer governed the heat removal.

Merte and Clark also observed the effect of a limited variation in the level of subcooling. Subcooling the water at constant heat flux up to approximately 5°F caused the superheat to increase whereas further subcooling the water caused the superheat to decrease. This effect was quite dependent upon the levels of heat flux and acceleration; generally, increasing the acceleration at constant heat flux and subcooling or increasing the heat flux at constant acceleration and subcooling caused

the superheat to increase. The eventual decrease in superheat with increasing subcooling is the result of the enhancement of convection heat transfer; the reason for the initial increase in superheat with increasing subcooling is not known.

Costello and Tuthill[21] presented the results of a study of the influence of increased acceleration level $1 \leq a/g \leq 45$ upon nucleate boiling heat transfer in saturated water at the surface of a vertical heater strip. The increased acceleration level was created by centrifugal action since the heater strip was rotated in a boiling capsule at constant angular speed. Photographs of the boiling phenomenon could be taken when the heater strip rotated into view. Steady state boiling heat transfer was observed.

The results of this experiment indicated a systematic dependence upon acceleration, somewhat greater than that observed by Merte and Clark. At constant heat flux, an increase in acceleration level resulted in an increase in superheat, which was entirely consistent with the results of Merte and Clark since these experiments were performed for heat flux levels greater than 100,000 BTU/hr ft^2. Costello and Tuthill determined that the superheat varied as a/g to a power which varied from 0.143 to 0.073 as the heat flux varied from 100,000 BTU/hr ft^2 to 200,000 BTU/hr ft^2 respectively.

Costello and Tuthill observed the boiling process at the heated surface by high speed photography. Analysis of the photographs obtained indicated that the radius of the bubbles leaving the heated surface varied as a/g to the -0.5 power and that the velocity of the vapour bubbles leaving the heated surface increased with increased acceleration level. These observations complement those of Usiskin and Siegel.

Slember[22] presented the results of an investigation to determine the influence of increased acceleration $1 \leq a/g \leq 20$ upon nucleate boiling heat transfer and bubble departure mechanics in saturated water. An open container with either a fine platinum wire or a small stainless steel tube mounted horizontally was rotated about a vertical axis thereby creating a centrifugal acceleration oriented perpendicular to the length of the heater element. The resultant acceleration was therefore comprised of a centrifugal component and a gravitational component and consequently its orientation in space varied with the centrifugal component. However, since the heater surface was cylindrical rather than plane, it is questionable whether or not the results obtained can be directly compared with those of other investigators.

Slember detected a significant dependence upon acceleration very similar to that observed by Merte and Clark. Slember also obtained still photographs taken with a light source synchronized to the rotation of the container and was able to determine the variation in bubble departure diameter. Assuming that the bubbles could be represented by ellipsoids and that the bubble departure diameter could be represented by the mean value of the major and minor diameters, Slember was able to determine that the bubble departure diameter varied as a/g to the $-1/2.165$ power. This dependence was substantiated by a large number of excellent photographs of bubbles growing in the artificially created acceleration field.

Adelberg[23] reviewed the existing literature pertinent to the influence of acceleration on nucleate boiling and interpreted the results by dimensional analysis. Three dimensionless numbers, the Froude number representing the ratio of inertia forces to buoyancy forces, the Weber number representing the ratio of surface tension forces to

inertia forces and the Bond number representing the ratio of buoyancy forces to surface tension forces were derived for nucleate pool boiling and were evaluated from the existing data to explain the observed behaviour. Adelberg postulated that the saturated boiling data presented by Merte and Clark, which showed that heat flux level determined the affect which acceleration had upon the phenomenon, actually indicated the existence of a critical Froude number. It was postulated that at low heat flux levels, a Froude number smaller than the critical value existed, resulting in a condition governed by buoyancy forces whereas at high heat flux levels, a Froude number greater than the critical value existed, resulting in a condition governed by inertia forces. The reason given to explain why the phenomenon appeared nearly acceleration insensitive when governed by inertia forces, was that within the range of acceleration studied $1 \leq a/g \leq 21$ surface tension forces dominated since the value of the Bond number was small and the value of the Weber number was large. For the particular range of acceleration studied by Costello and Tuthill $1 \leq a/g \leq 45$, the value of the Bond number increased, so that although the nucleate boiling was predominantly governed by inertia forces, buoyancy forces once again began to influence the phenomenon. Hence the results presented by Costello and Tuthill showing acceleration dependence were explained.

Graham and Hendricks[24] investigated the influence of acceleration upon the mechanism of heat transfer to water in saturated and subcooled boiling. High speed motion pictures and heat transfer data were obtained over a range of accelerations $1 \leq a/g \leq 10$ for saturated conditions and two levels of subcooling $\Delta T_{SUB} = 12°F$ and $\Delta T_{SUB} = 32°F$. The heat transfer surface was a narrow ribbon mounted in a camera equipped test package supported on trunnions at the end

of an arm such that the acceleration vector resulting from the rotation of the arm was oriented perpendicular to the heat transfer surface. All tests were performed at relatively low heat flux conditions and because there were no more than fifteen active boiling sites, natural convection heat transfer was predominant over much of the surface.

Graham and Hendricks commented on the marked influence which subcooling had upon nucleate boiling heat transfer. At standard gravity $a/g = 1$, an increase of 2.5°F in the subcooling was reputed to have produced an increase of 8.0°F in the superheat at constant heat flux. Hence, the increase in superheat corresponding to small increases in subcooling which Merte and Clark had detected was confirmed although the magnitude of the effect was considerably greater. The effect reported by Graham and Hendricks may partly be explained by the fact that the results presented were obtained by allowing the heat flux to increase progressively and might have been confounded by the "hysterisis effect" which often accompanies results obtained in this fashion.

Graham and Hendricks demonstrated that increasing acceleration in the range $1 \leq a/g \leq 10$ tended to shift the boiling characteristic curve in proportion to (T_W-T_B) to the 1/4 power, which suggests the influence of natural convection. Acceleration effects were shown to be negligible in comparison with subcooling effects, but as explained above, natural convection most likely masked the effects of nucleate boiling.

Graham and Hendricks also reported that bubble growth rate and maximum bubble size were diminished by increasing acceleration. Furthermore, the ratio of the time elapsed between cycles of bubble formation

to the time elapsed during the period of bubble growth was observed to increase. These effects were determined for only one level of subcooling and it is not possible to speculate on the influence of subcooling on the formation and collapse of vapour bubbles in subcooled nucleate boiling in general.

Although this investigation explores many of the areas which concern the present research, the geometry of the heat transfer surface was such that the numerical values reported are not typical of nucleate boiling heat transfer in general.

Merte and Clark[25] reported the results of an investigation in which the influence of decreased acceleration $0.01 \leq a/g \leq 1$ upon saturated liquid nitrogen boiling at the surface of a small copper sphere was investigated. Similar to the earlier experiments of Usiskin and Siegel, the decrease in acceleration level was accomplished by a controlled fall which was of the order of one second duration. The boiling heat transfer capsule was counterbalanced with an appropriate counterweight and the actual acceleration level existing during the fall was measured with an accelerometer.

The heat transfer relationships for nucleate boiling, transition boiling and film boiling were deduced from a transient analysis of conduction heat transfer within the copper sphere. The temperature measured near the surface of the copper sphere was recorded as a function of time during the fall and this measurement alone was sufficient to calculate the heat flow rate per unit area and the difference between the temperature of the sphere and the saturation temperature of

the liquid nitrogen. The nucleate boiling heat transfer results are of particular interest since the experiment indicated that nucleate boiling heat transfer to saturated liquid nitrogen was independent of the acceleration level to which the heat transfer surface was subjected within the sensitivity of the measurements.

Siegel and Keshock[26] studied the influence of a reduced acceleration level $0.01 \leq a/g \leq 1$ upon nucleate boiling heat transfer to water from a smooth horizontal nickel surface on which there were only a few nucleating sites. The test apparatus used to accelerate the heat transfer surface and to obtain high speed photographs of the resulting phenomenon was essentially that used in the earlier investigation of Usiskin and Siegel. Measurements were made of bubble departure diameters and frequencies, growth rates, contact angles and rise velocities in order to evaluate the gravity dependence predicted by a number of existing correlations.

One notable observation was that the large vapour bubbles which accumulated near the heat transfer surface at reduced acceleration levels acted as local vapour sinks, attracting small bubbles from the surface beneath at frequencies much higher than those with which vapour bubbles formed and departed at isolated sites. In this regard, the large vapour bubbles served to increase the local turbulence level. This observation undoubtedly explains the fact that Usiskin and Siegel detected no reduction in heat removal despite the fact that the heat transfer surface appeared to be covered by vapour bubbles.

Rehm[27] derived expressions for each of the forces acting upon a vapour bubble and then evaluated these forces from data obtained

from a photographic study of saturated and subcooled boiling heat transfer to water. The purpose of this analysis was to determine the relative magnitude of each of the forces at various levels of heat flux and subcooling and to predict the influence of those forces which were acceleration dependent on the mechanics of vapour removal. Rehm concluded that although acceleration dependent forces constituted the entire removal force in saturated boiling, acceleration dependent forces represented only a small portion of the removal force in subcooled boiling.

Beckman, Merte and Clark[28] presented information concerning the influence of acceleration upon several aspects of bubble dynamics in subcooled nucleate boiling. High speed photographs of the boiling phenomenon were obtained over a considerable range of acceleration $1 \leq a/g \leq 100$ for two levels of subcooling $\Delta T_{SUB} = 2°F$ and $\Delta T_{SUB} = 10°F$. The test apparatus was similar to that used by Graham and Hendricks in that the narrow chromel ribbon which comprised the heat transfer surface was mounted in a test package which pivoted at the end of an arm. An artificial acceleration field was generated perpendicular to the heat transfer surface when the arm was rotated. An ingeneous optical system which rotated with the test package permitted the formation and departure of the vapour bubbles at the heat transfer surface to be continuously photographed by a high speed motion picture camera mounted outside the test facility.

From an analysis of the photographic results, Beckman, Merte and Clark were able to investigate the dynamics of bubble growth and departure. It was demonstrated that the radius of the vapour bubbles

at departure from the heat transfer surface decreased by a factor of two as acceleration increased from $a/g = 1$ to $a/g = 10$ and that a further increase in acceleration did not appear to affect the radius of the vapour bubbles at departure from the heat transfer surface. This affect was observed for both $\Delta T_{SUB} = 2°F$ and $\Delta T_{SUB} = 10°F$. The radius of the vapour bubbles at departure for $\Delta T_{SUB} = 2°F$ was approximately twice as great as the corresponding radius for $\Delta T_{SUB} = 10°F$.

It was not possible to comment on the maximum bubble size for $\Delta T_{SUB} = 2°F$ in as much as the bubbles achieved maximum size outside of the field of view of the optical system. For the experiments conducted at $\Delta T_{SUB} = 10°F$, the maximum radius was found to decrease from 4.5×10^{-2} inches to 2.0×10^{-2} inches as acceleration increased from $a/g = 1$ to $a/g = 10$. For values of acceleration greater than $a/g = 10$, the maximum size attained by the bubbles appeared to remain constant.

It was also demonstrated that the average time for isolated bubbles to grow to their maximum size decreased with increased acceleration in proportion to a/g to the -0.27 power and the average time from initiation to departure decreased with increased acceleration in proportion to a/g to the -0.5 power. The frequency of departure varied with acceleration in proportion to a/g to the 0.5 power. The product of bubble departure frequency and departure radius was found to be independent of acceleration for acceleration levels up to $a/g = 10$; for values of acceleration greater than $a/g = 10$, this product increased with increasing acceleration. Bubble radius was found to vary with time to the 0.44 power and this result appeared to be independent of acceleration and subcooling.

Schwartz[29] reported the results of an experiment to investigate nucleate boiling heat transfer to water in which an aircraft flying a Keplerian trajectory was used to generate a reduced acceleration environment. The test assembly was a magnesium box containing an instrumented nickel alloy resistance ribbon which could be tested in either a standard or zero acceleration environment. The nature of the experiment was such that the duration of each test was of the order of ten seconds. This test duration was sufficiently long enough to permit steady state boiling conditions to be achieved since precise temperature measurements indicated that steady temperature distributions were attained early in the test period. High speed photographs of the mechanics of vapour bubble formation were obtained at standard and reduced acceleration in order to evaluate the influence of this parameter on size and growth of vapour bubbles.

The results of this experiment generally confirmed those of Usiskin and Siegel with regard to the influence of acceleration on the rate of heat removal. Temperature measurements indicated only a slight decrease in superheat at constant heat flux as the acceleration level was reduced from $a/g = 1$ to $a/g = 0.01$. Vapour bubbles were observed to grow in proportion to time to the 0.32 power and similar to the result presented by Beckman, Merte and Clark, this result appeared to be independent of acceleration level. The departure diameter of isolated bubbles was observed to vary with a/g to the -0.5 power. The general observations of Siegel and Keshock concerning the nature of vapour removal at reduced acceleration levels were confirmed since Schwartz also observed large vapour bubbles near the heat transfer

surface interfering with and absorbing smaller vapour bubbles growing on the heat transfer surface.

Adelberg and Schwartz[30] reviewed the literature pertinent to acceleration effects on nucleate boiling. In addition, the authors performed an experimental investigation of the influence of acceleration on nucleate boiling heat transfer to water at increased acceleration levels $1 \leq a/g \leq 134$ using the test assembly of the low acceleration level investigation mounted on the arm of a large centrifuge. The heat transfer surface was mounted vertically such that the centrifugal component of the gravity vector was perpendicular to it. High speed photographs were taken with a camera mounted at the center of rotation.

Of the twenty four references reviewed which reported on the experimental determination of the effect of acceleration on nucleate boiling heat transfer, only four observed any consistent effect and these four were in the high acceleration level range. Adelberg and Schwartz concluded that acceleration effects are manifest only at higher acceleration levels, despite the fact that acceleration has been shown to influence the mechanics of vapour removal at all acceleration levels. Adelberg and Schwartz were able to correlate all of the data indicating an acceleration effect as well as their own data in two different ways. Depending on the interpretation of the data, it was possible to show either that (i) acceleration affected nucleate boiling heat transfer in proportion to a/g raised to an exponent which increased with increasing a/g or (ii) acceleration affected nucleate boiling heat transfer only indirectly through variation of the hydrostatic head. No detailed

analysis was performed on the photographs obtained but the results of the investigation were in qualitative agreement with those of the investigation by Beckman, Merte and Clark.

CHAPTER II

EXPERIMENTAL APPARATUS

A. Introduction

In order to create levels of acceleration different from standard gravitational acceleration for prolonged periods of time, an existing centrifuge located in the Heat Transfer Laboratory of the Mechanical Engineering Department was utilized for this experimental investigation. Specific details of this test facility are presented in Reference 28. Modifications to the test facility, which consisted mostly of changes in the internal geometry of the test package and the addition of a temperature scanning system and a pressurization system, are described in the following section. The test facility is a versatile apparatus capable of:

1. Accelerating a 100 pound test package from $a/g = 1$ to $a/g = 100$ and maintaining any acceleration level selected for extended periods of time.

2. Permitting continuous photography of events occurring within the test package by means of a mirror system rotating with the centrifuge.

3. Transmitting instrument signals originating at the test package to externally located measuring and recording equipment by means of twenty three thermocouple trays.

4. Transmitting A.C. power to each of three guard heaters located in the test package from three independently controlled auto transformers by means of a four channel slip ring assembly.

5. Transmitting D.C. power to the test specimen located within the test package from an externally located battery supply by means of a dual channel mercury commutator.

6. Providing cooling water to the heat exchangers within the test package by means of a fluid coupling assembly.

A sectional view of the centrifuge is shown in Figure 1, which depicts the various components of which it is comprised.

A glass plate coated with an electrically conducting oxide coating served as the heat transfer surface. The fluid tested, trichlorotriflouroethane $CCl_2F\text{-}CClF_2$ which is commercially known as "Freon 113", was pressurized with a helium atmosphere, whose pressure was varied with the level of acceleration. Further details of the design and operation of the experimental apparatus are presented in the sections which follow.

B. Test Specimens

In as much as the research investigation required observation of the nucleate boiling phenomenon normal to the surface at which boiling occurred in order to determine the influence of acceleration and subcooling upon the frequency of vapour bubble formation and the number of active sites per unit area, a transparent 1/8 inch thick oxide coated borosilicate glass plate similar to that used by Westwater and Kirby[31] and Hsu[32] was chosen as the heat transfer surface in order that the phenomenon might be viewed from below. This "test specimen" was arranged within the test package perpendicular to the axis of symmetry along which the acceleration vector was directed, with the oxide coated surface in contact with the Freon. A single test specimen of this type was used for the duration of the study, after which a geometrically similar test specimen, consisting of a thin stainless steel foil resistance element bonded to an uncoated glass surface was tested briefly in order to compare the boiling characteristics of the two types of surface. Figure 2 shows representative samples of the two types of test specimen.

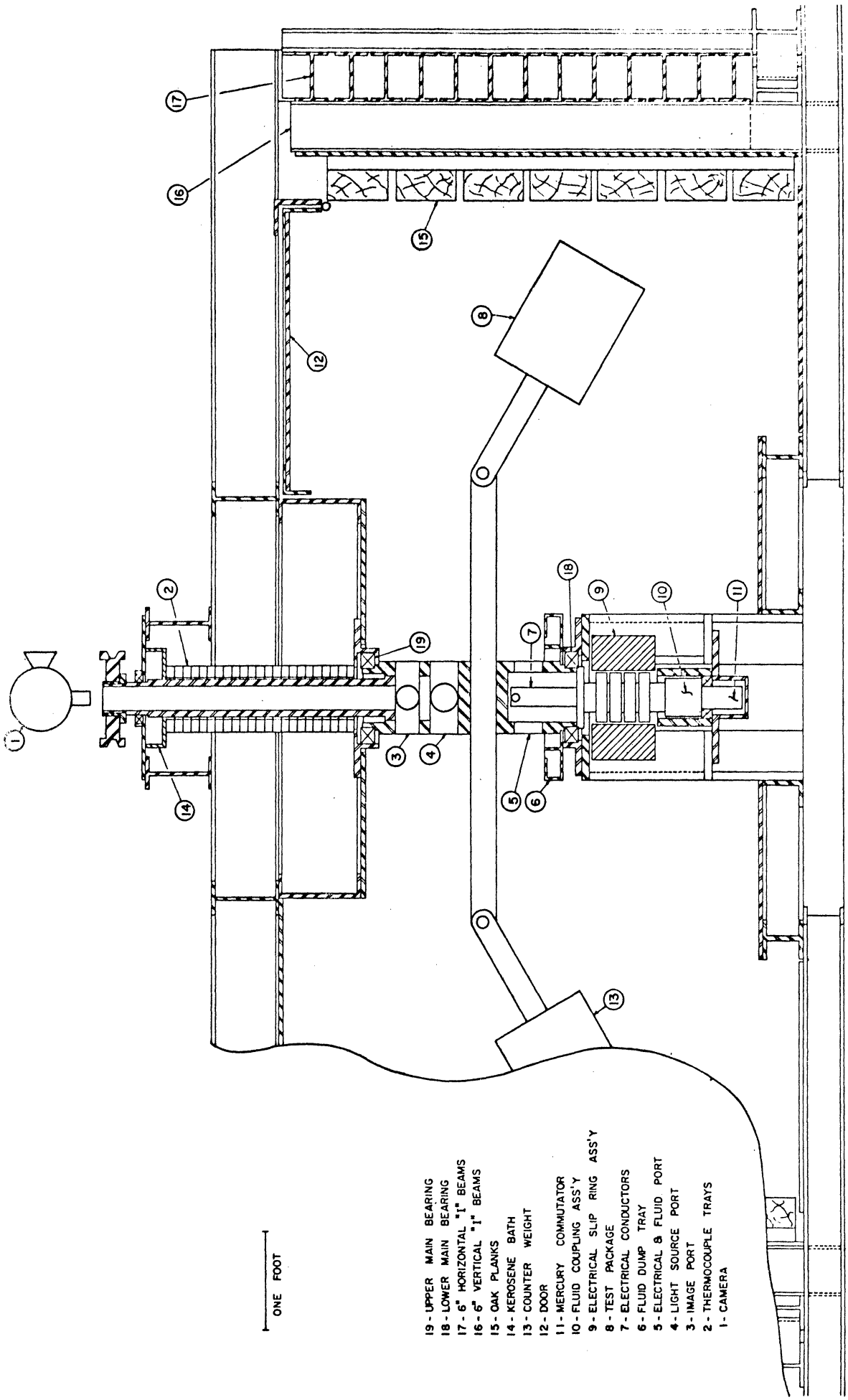

Figure 1. Sectional View Of Centrifuge.

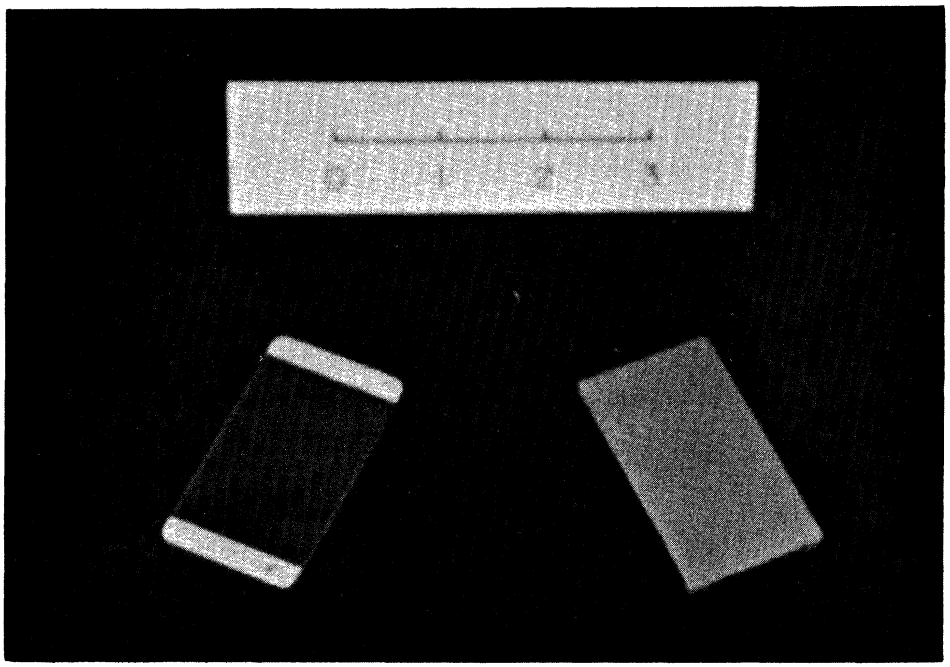

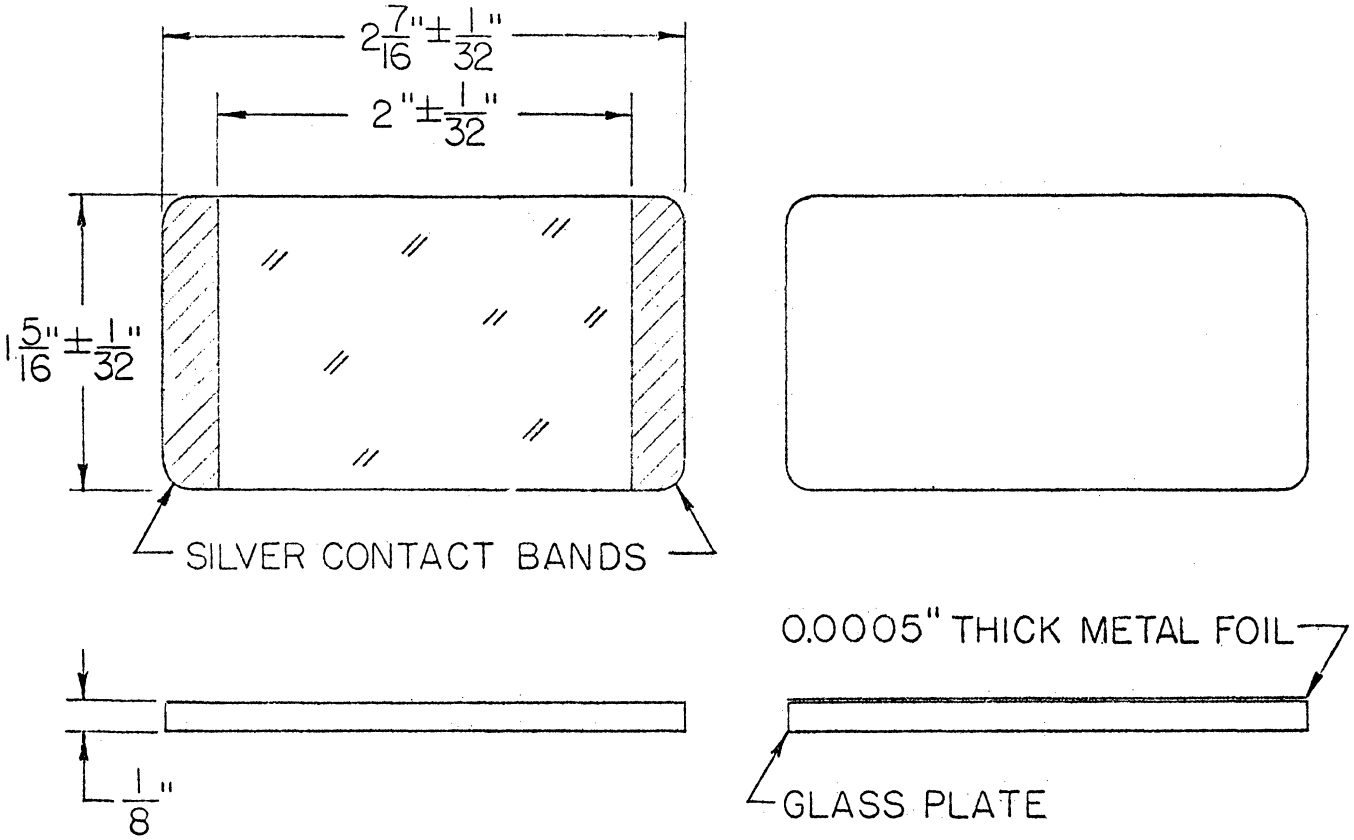

Figure 2. Test Specimens.

Ten test specimens were prepared according to specification by Corning Glass Works. Each test specimen was cut to size 2 7/16 ± 1/32 inch long by 1 5/16 ± 1/32 inch wide from sheets of 1/8 inch thick oxide coated borosilicate glass and after the corners were rounded to 1/8 inch radius, a layer of metallic silver was deposted on each end, leaving an effective heat transfer surface 2 ± 1/32 inch long by 1 5/16 ± 1/32 inch wide. The silver bands facilitated electrical contact with the oxide coating.

The variation in the electrical resistance of the ten test specimens received was no greater than 1 ohm. A periodic check on the resistance of the particular test specimen used in the study was performed during the course of the investigation in order to detect any change which might indicate deterioration of the test surface. No significant change was detected. The test specimen was subjected to over 200 hours of service at various levels of heat flux during which the resistance decreased from 29.19 ohms to 29.13 ohms in a monotonic fashion when measured at room temperature conditions.

Since it was not possible to evaluate local heat flux values, it had to be assumed that the oxide coating had been deposited uniformly and that the heat was generated uniformly over the heat transfer surface. This assumption was tested by a simple experiment to determine the distribution of equipotential lines over the heat transfer surface and it was found to be quite reasonable. Results of this experiment are presented in Appendix A.

An oxide coated glass surface differs considerably from the usual boiling heat transfer surfaces encountered in industrial applications.

As explained above, the selection of this surface was dictated by optical considerations, but since the same test specimen was used throughout the study, surface condition was eliminated as a test variable. However, the unknown relationship of the nucleate boiling characteristics of the oxide coated glass surface to the corresponding characteristics of a metallic surface prompted an additional set of tests conducted under identical conditions using such a metallic surface. A piece of hard rolled stainless steel foil 0.0005 inches thick was trimmed to the contour of one of the ten oxide coated glass test specimens and was bonded to the nonconducting side of the glass with Schramm Fiberglass Products "Minit-Grip" epoxy. Another glass piece was placed on top of the metal foil and weights were heaped upon this assembly to smooth the surface and to ensure satisfactory adhesion, after which the epoxy was allowed to set for approximately 8 hours. The resulting bond was quite adequate since subsequent tests showed that the foil did not separate from the glass during boiling and that the bond strength actually increased.

Although it is acknowledged that surface roughness measurements alone are insufficient to characterize a boiling surface, these measurements are related to the number and size of the pits and scratches in the surface. For this reason, the following average roughness results obtained with a Brush Electronics Model BL110 surface roughness indicator are presented for comparison of the two types of test specimen in Table I below.

TABLE I

SURFACE ROUGHNESS MEASUREMENTS

Unused Oxide Film Heater Surface	Used Oxide Film Heater Surface	Metal Foil Heater Surface
5 μ inch	12 μ inch	12 μ inch

The apparent agreement of the average roughness results for the used oxide film heater surface and the metal foil heater surface does not imply identical surface roughness characteristics; real differences in the type and depth of pits and scratches might exist which could influence the initiation and growth of vapour bubbles differently for the two surfaces. Nevertheless, the similarity of the average roughness results is worthy of mention.

Figure 3 is an isometric drawing of the test specimen mounting fixture which was designed and constructed to insulate the unheated surface of the test specimen with an encapsulated volume of air. This rather complicated design was decided upon in order to reduce the heat transfer at the unheated surface of the test specimen without restricting observation of the phenomenon occurring at the heated surface. Because the natural convection heat transfer behaviour of air is reasonably well understood, the flow of heat across the unheated surface could be estimated. However, such an estimation is dependent upon the temperature difference between the unheated surface and the air. For this purpose two thermocouple junctions were located within the mounting fixture; one was bonded to the

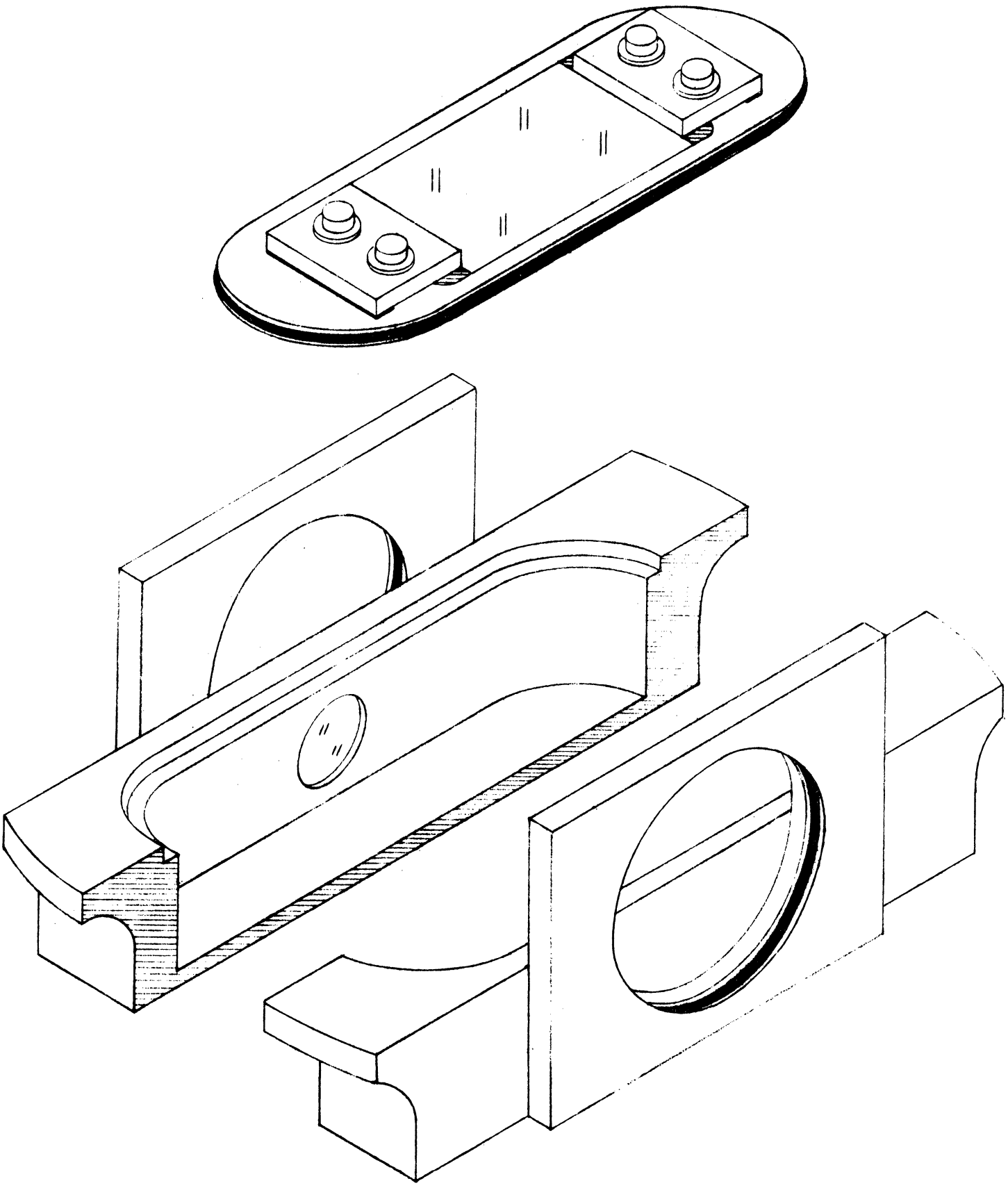

Figure 3. Test Specimen Mounting Fixture.

unheated surface of the test specimen with "Minit-Grip" epoxy and the other was supported in the air. The thermocouple wires leading to the junctions were led out of the mounting fixture through a 1/8 inch diameter capillary tube which was extended right through the cover of the test package. A complete discussion of the installation of these thermocouple junctions, the method used in calculating temperatures and the errors involved is presented in a later section.

C. Test Package And Counterweight

An existing test package was modified in accordance with the special requirements of the present research investigation. Although the complete details of the design and construction of this test package are found in Reference 28, some of the pertinent information will be reproduced in this section in order to provide continuity and to assist in understanding the consideration which governed the design of the equipment for the present research investigation. The test package provided a test platform on which the various components could be assembled and a controlled environment in which nucleate boiling tests could be performed. Figure 4 is a detail drawing of the test package and Figure 5 is a photograph of the assembled test package.

The basic component of the test package was the test vessel which was constructed of welded pieces of 6 inch diameter type 304 stainless steel pipe, the upper portion of schedule number 10 and the lower portion of schedule number 40. Two stainless steel sight tube supports were tack welded to opposite ends of one of two mutually perpendicular diagonal braces to keep them collinear and then were

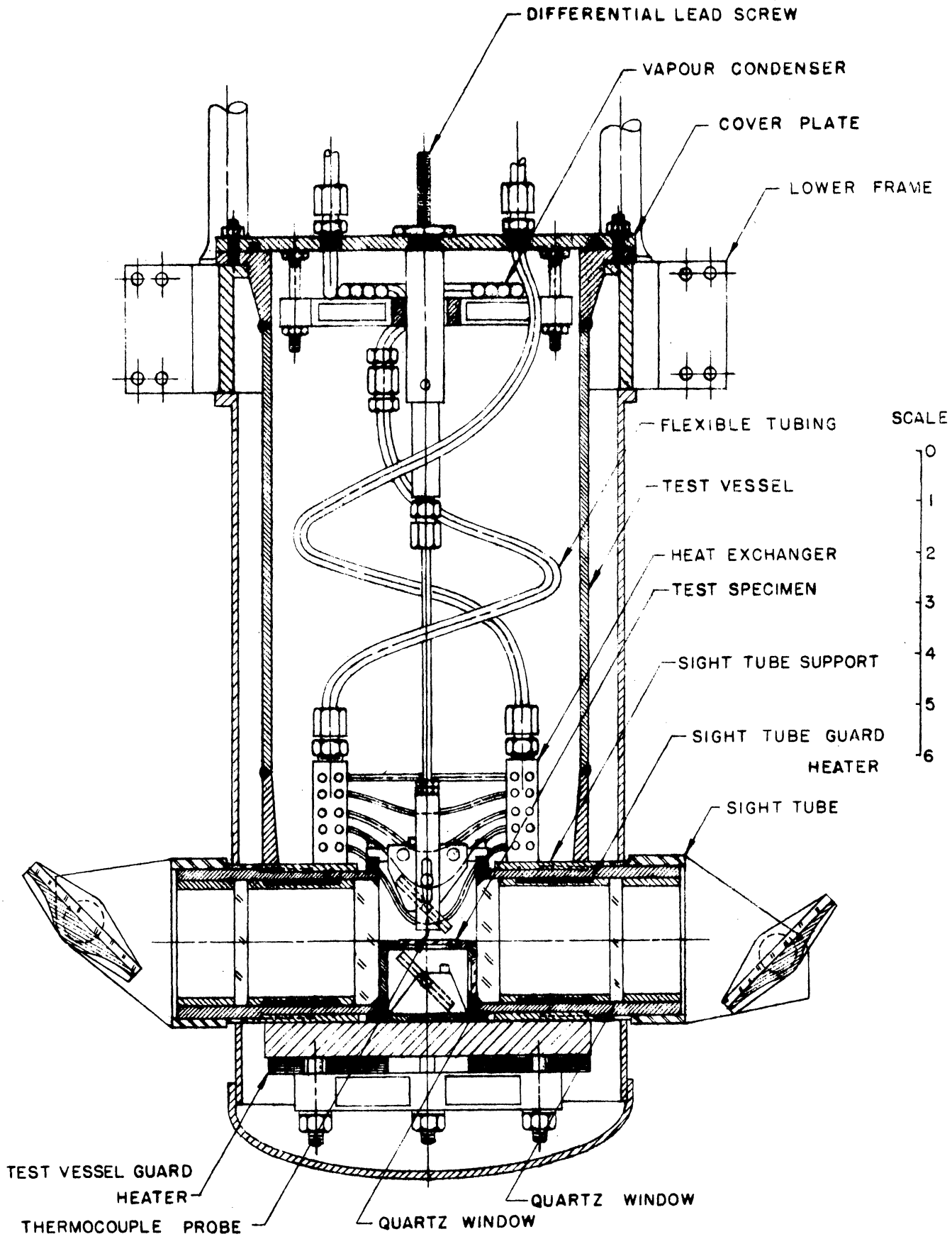

Figure 4. Detail Drawing Of Test Package.

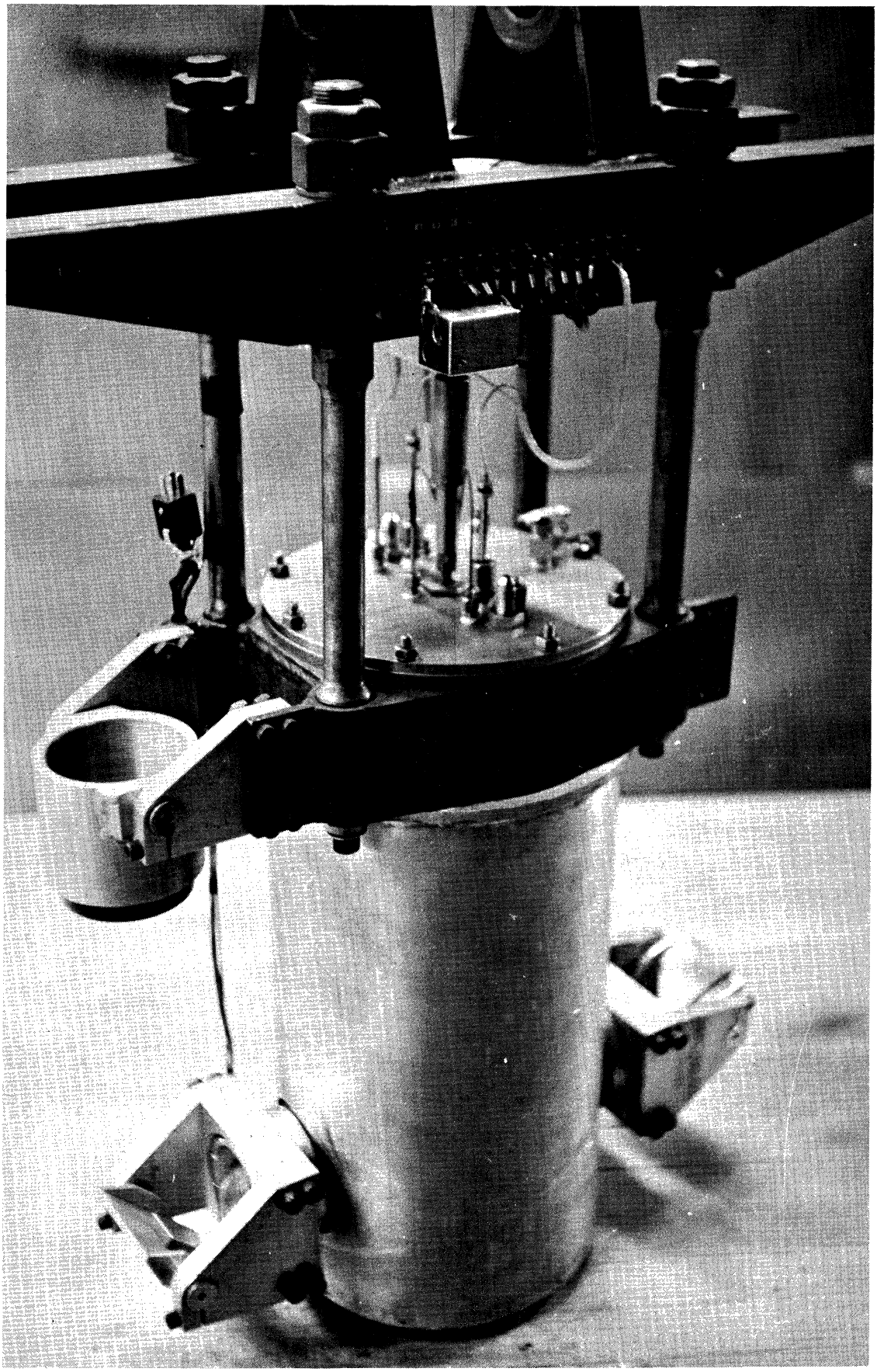

Figure 5. Test Package.

welded into opposing holes prepared in the schedule number 40 portion with the diagonal braces oriented toward the bottom of the test vessel. The bottom of the test vessel was closed with four stainless steel circular segments which were welded to the diagonal braces and to bottom edges of the schedule 40 portion of the test vessel. Internal threads were machined into the sight tube supports after the completion of the welding. A machined flange which rested on the lower frame of the test package assembly was welded to the schedule 10 portion of the test vessel. Four high alloy steel rods connected the lower frame to the upper frame which served as the pivot point of the test package assembly. The fact that the test package assembly could pivot during operation enabled the heat transfer surface to assume a position approximately perpendicular to the acceleration vector. The entire test vessel was covered with a one inch thick layer of fibre glass insulation which was then surrounded with a thin walled aluminum jacket for protection.

The mounting fixture described in the proceeding section, which with the exception of the cover was machined from a solid brass block, was installed between the sight tube supports. The mounting fixture was anchored in place by the sight tubes which were threaded through the sight tube supports approximately 1/8 inch to enter the recesses machined in the opposing surfaces of the mounting fixture. Rubber "O" rings set in grooves machined inside the recesses were compressed as the sight tubes entered thereby ensuring a solid connection. The cover was designed to be installed and removed independent of the mounting fixture since it carried the test specimen which had to be

removed from time to time. For this reason, it was provided with an "O" ring around the edge which provided a continuous seal when the cover was pressed into place. Figure 6 shows the test specimen mounted in the cover. Details of the mounting fixture and cover can be determined from examination of the detail drawing of the test package.

The optical sight tubes were constructed from 2 1/2 inch diameter number 160 stainless steel pipe. External threads were machined on the outside surface of the tubes for one half of the length which permitted the tubes to be threaded into the sight tube supports. A rubber "O" ring set in an internal groove in each of the sight tubes was compressed by the unthreaded portion of the sight tubes thereby effecting a seal. Two circular optically flat quartz windows separated by a cylindrical spacer were inserted within each sight tube and were clamped in place by a locknut. The front quartz window was bevelled to conform with an internal bevel of the sight tube. The leading edge of the cylindrical spacer was also bevelled in order to hold and compress a rubber "O" ring against the back edge of the front quartz window. The rear quartz window served to encapsulate a quantity of air within the sight tube.

The requirements of the research investigation necessitated the ability to vary subcooling. At a constant pressure level, this variation could only be accomplished by changing the temperature of the test fluid and this was accomplished with a heat exchanger. A single pass heat exchanger was constructed to conform with the internal geometry of the test package. Twenty 1/8 inch diameter stainless steel

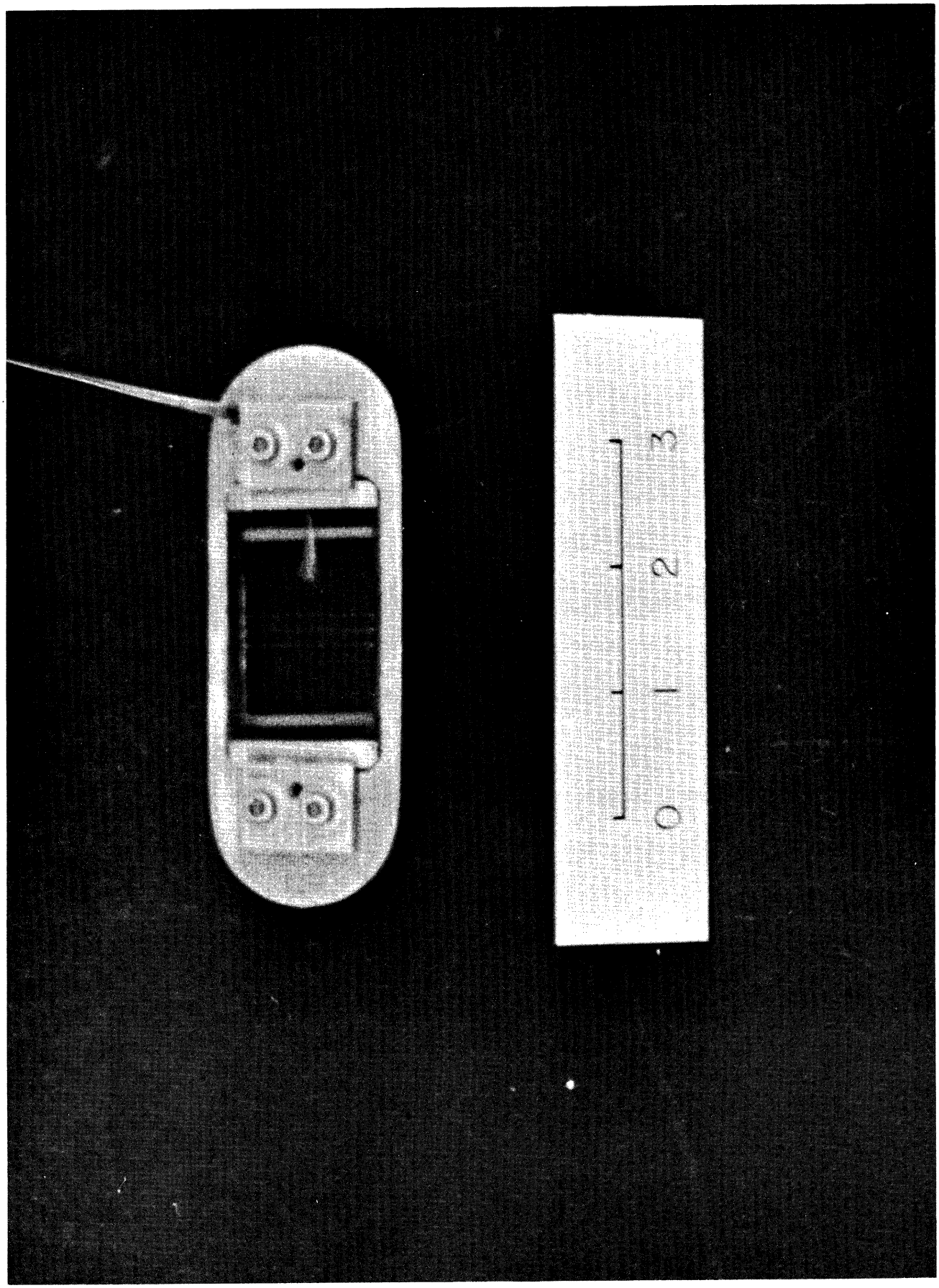

Figure 6. Mounted Test Specimen.

tubes approximately 10 inches long were arranged into two rows five deep on each side of 7/8 inch square stainless steel bar stock headers which rested upon the upper surfaces of the sight tube supports. The tubes were bent into a hollow form which followed the circular contour of the inside of the test package and dipped down into the test fluid between the headers. The effective heat transfer area of the heat exchanger was approximately 72 square inches when completely submerged.

A vapour condenser was mounted at a fixed position 1 inch beneath the test package cover plate in order to condense the vapour formed during a test. The vapour condenser was constructed of 1/4 inch diameter stainless steel tubing wound in a spiral fashion and was supported on a cross frame connected to the underside of the cover by four 1/4 inch diameter threaded stainless steel rods. The vapour condenser and the heat exchanger were connected in series; connections were made by lengths of commercially available teflon tubing with stainless steel braid outer jacket. Figure 7 shows the cover plate, vapour condenser and heat exchanger.

Mirrors were positioned above and below the heat transfer surface by mirror mounts attached to the mounting fixture. Details of these mirror mounts are shown in the detail drawing of the test section. These mirrors could be adjusted independently. Fine alignment of the upper mirror was performed by replacing the test specimen in the cover of the mounting fixture by an auxiliary mirror which was viewed along the axis of one of the sight tubes through the upper mirror from a distance of approximately three feet with an optical cathemoter. The upper mirror was then carefully adjusted until the reflection of the

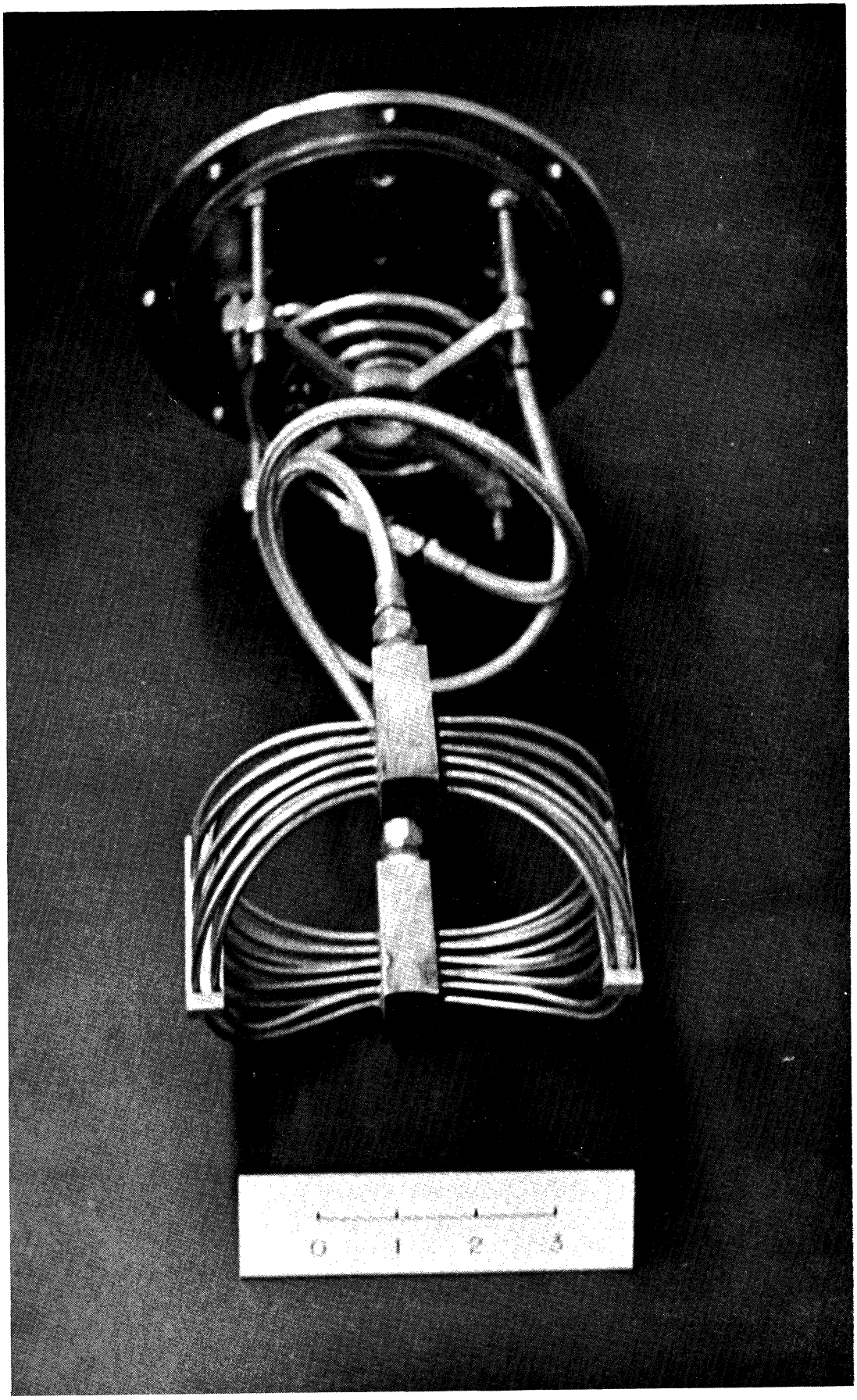

Figure 7. Cover Plate, Vapour Condenser And Heat Exchanger.

end of the cathetometer appeared symmetrically within the eyepiece of the cathetometer itself. In this way the upper mirror was adjusted to direct a beam of light perpendicular to the heat transfer surface. The test package was then revolved 180° about its axis of symmetry and the process was repeated by viewing the inverted auxiliary mirror through the lower mirror along the axis of the other sight tube with the same optical cathetometer.

Two ring shaped guard heaters of 700 watt total capacity were fastened to the bottom of test vessel and held in place by a four arm cross frame. Thermal contact between these heaters and the test vessel was accomplished by embedding the heaters in Thermon cement. These guard heaters were used during a test to control the temperature of the test fluid. Two more guard heaters were arranged one in each of the sight tubes between the quartz windows. A groove was machined on the outer surface of the spacer separating the two quartz windows large enough to accept a winding comprised of 16 feet of insulated resistance wire. These guard heaters were used during the test to minimize heat loss along the sight tubes. The heat generation within each sight tube was adjusted independently to maintain the temperature of the air in the vicinity of the front sight glass at the same temperature as the test fluid within the test package.

Discussion of the thermocouple probe, the differential lead screw which positioned the probe and the associated instrumentation which indicated the probe position are reserved for a later section.

A counterweight was utilized to eliminate dynamic unbalance in the rotating system. The outer configuration of the counterweight

was made to resemble the outer configuration of the test package such that air resistance would be the same during rotation. The inner vessel of the counterweight was constructed of 6 inch diameter schedule number 10 stainless steel pipe closed at one end by an elliptical end cap and joined at the other to a machined flange which was closed by a cover plate. The lower frame upon which the inner vessel rested was supported on the upper frame by threaded rods which permitted variation of the center of gravity. Lead shot was added to the counterweight to equalize the weights of the counterweight and test package and mis-adjustment of the centers of gravity was eliminated by adjusting the threaded rods to eliminate unbalance during rotation. Figure 8 shows the test package and counterweight mounted on the cross arm.

D. Thermocouples

Seven chromel-constantan thermocouples were used in the present research investigation. Chromel-constantan thermocouples were selected because the EMF characteristic for this combination of materials is approximately 36 μ Volts/°F, the maximum attainable in the temperature range under consideration. Table II identifies these thermocouples and indicates the location of each of the thermocouple junctions.

The boundary layer traversing thermocouple is considered separately in the next section. The other thermocouples were formed from 30 gauge fiberglass insulated and jacketed duplex thermocouple wire. The output of each thermocouple was individually compared with a thermocouple conversion table prepared by Beckman from data published by the National Bureau of Standards[33], using a precision platinum resistance

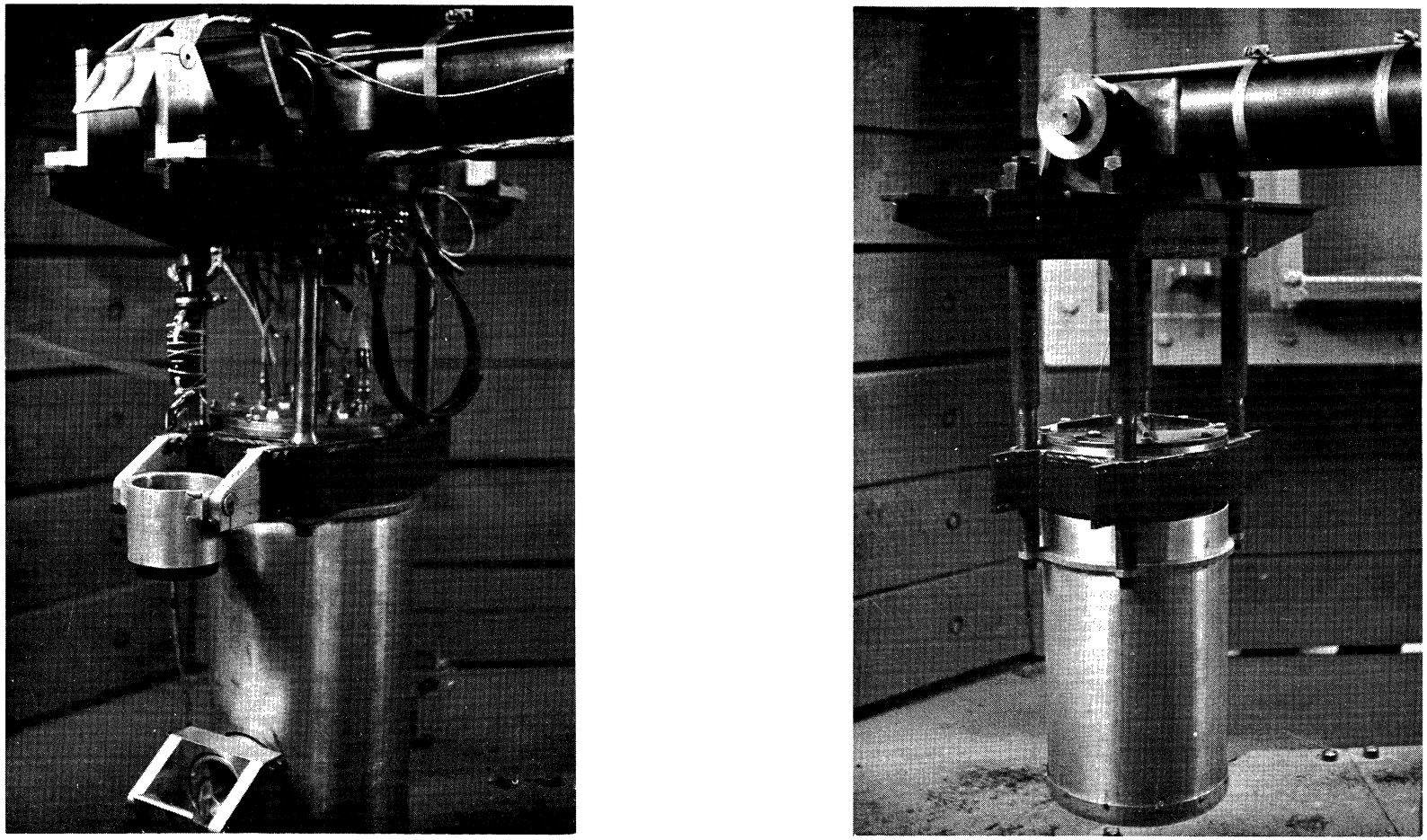

Figure 8. Mounted Test Package And Counterweight.

TABLE II

THERMOCOUPLE DESIGNATION

Thermocouple	Location
B.L.* Traversing T.C.	Thermocouple probe sensing junction
Stationary Fluid T.C.	One inch above heat transfer surface
Reference Fluid T.C.	Thermocouple probe cross bar
Test Specimen T.C.	Unheated surface of test specimen
#1 Sight Guard T.C.	Inside #1 optical sight tube
#2 Sight Guard T.C.	Inside #2 optical sight tube
Air temperature T.C.	Air space inside mounting fixture

*Boundary Layer

thermometer which had been calibrated by the National Bureau of Standards to measure the reference temperature. The six thermocouples and the platinum resistance thermometer were tested in a constant temperature block capable of being maintained within $\pm 0.01°F$. The resistance thermometer and the six thermocouples were read at four temperature levels spanning the anticipated range of operating temperature. Deviations of the output of each thermocouple from that predicted by the thermocouple conversion table at the temperature level measured by the resistance thermometer were computed. The spread of these deviations about the average value was less than ± 2 μ Volts and consequently a single curve obtained by plotting the average deviation from the thermocouple conversion table as a function of thermocouple EMF sufficed to correct all six thermocouples. The maximum correction was of the order of 20 μ Volts.

The thermocouple circuit used in the centrifuge is shown schematically in Figure 9. The circuit requires the use of two intermediate metals, molybdenum and mercury in order to create a rotating connection. Molybdenum was chosen as one of the intermediate metals since chromel and constantan could not survive in the mercury whereas molybdenum exhibits good wetability and chemical stability in mercury. Since it was essential to avoid errors resulting from the creation of transition junctions, the transition junctions between chromel and molybdenum and constantan and molybdenum for both the stationary and rotating portions of the circuit were made in a constant temperature kerozene bath.

E. Thermocouple Probe

A boundary layer traversing thermocouple was required to measure the variation of temperature within the thermal boundary layer immediately adjacent to the heat transfer surface. However, the conditions under which the traversing thermocouple probe had to operate were quite severe. In the immediate vicinity of the heat transfer surface the temperature gradient is extremely steep; Marcus and Dropkin[34] reported that the temperature in nucleate boiling water varied at approximately 1,6000°F/in in the vicinity of the heat transfer surface. Consequently it was essential that the thermocouple probe be capable of measuring extremely localized temperatures and that the position of the thermocouple probe be known within one thousandth of an inch. The design and construction of the thermocouple probe is presented in this section; the design and construction of the probe positioning system is presented in the next section. The thermocouple probe can be seen in Figure 10 which shows both a photograph and a detail drawing of the assembled thermocouple probe and probe positioning mechanism.

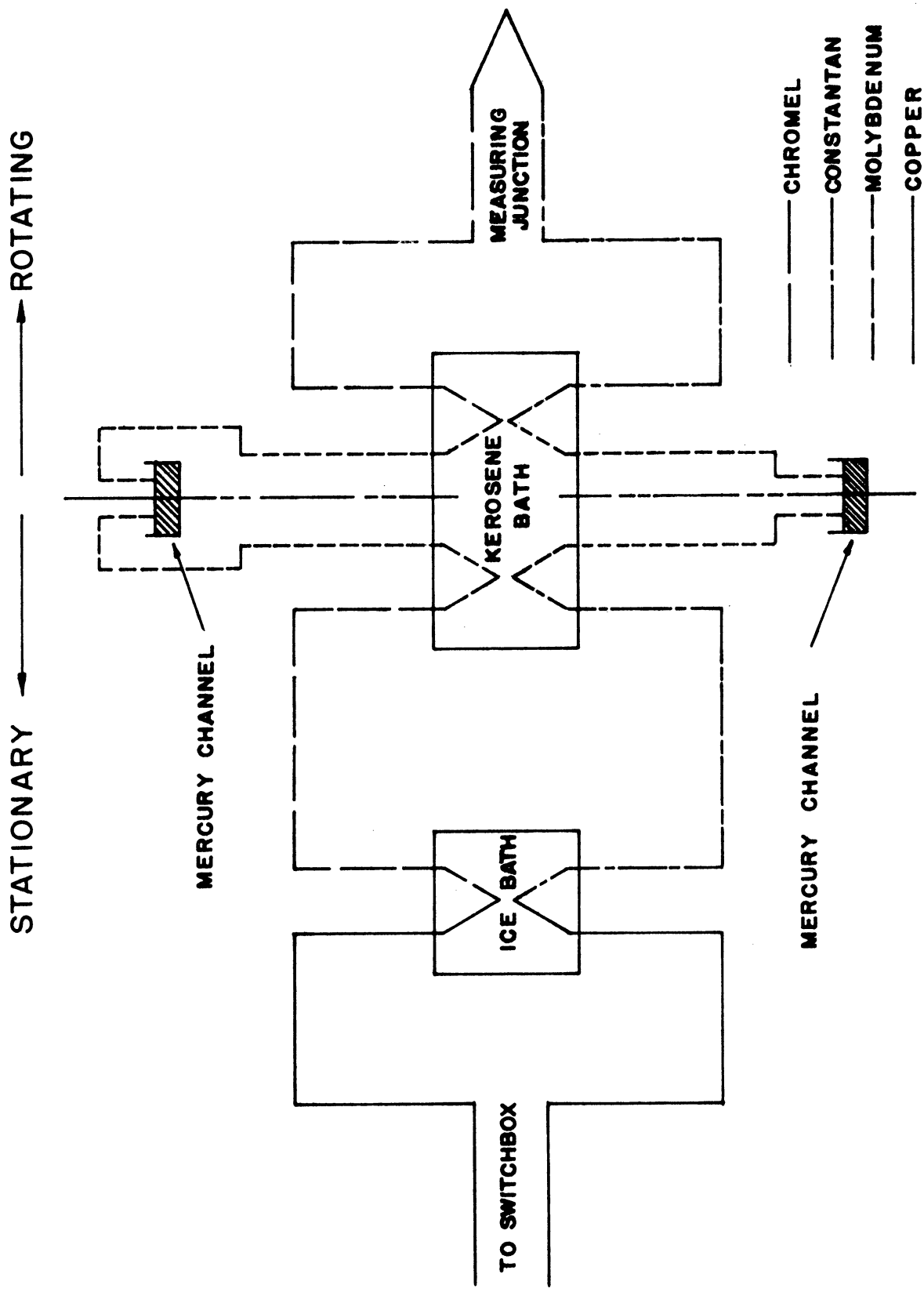

Figure 9. Thermocouple Circuit.

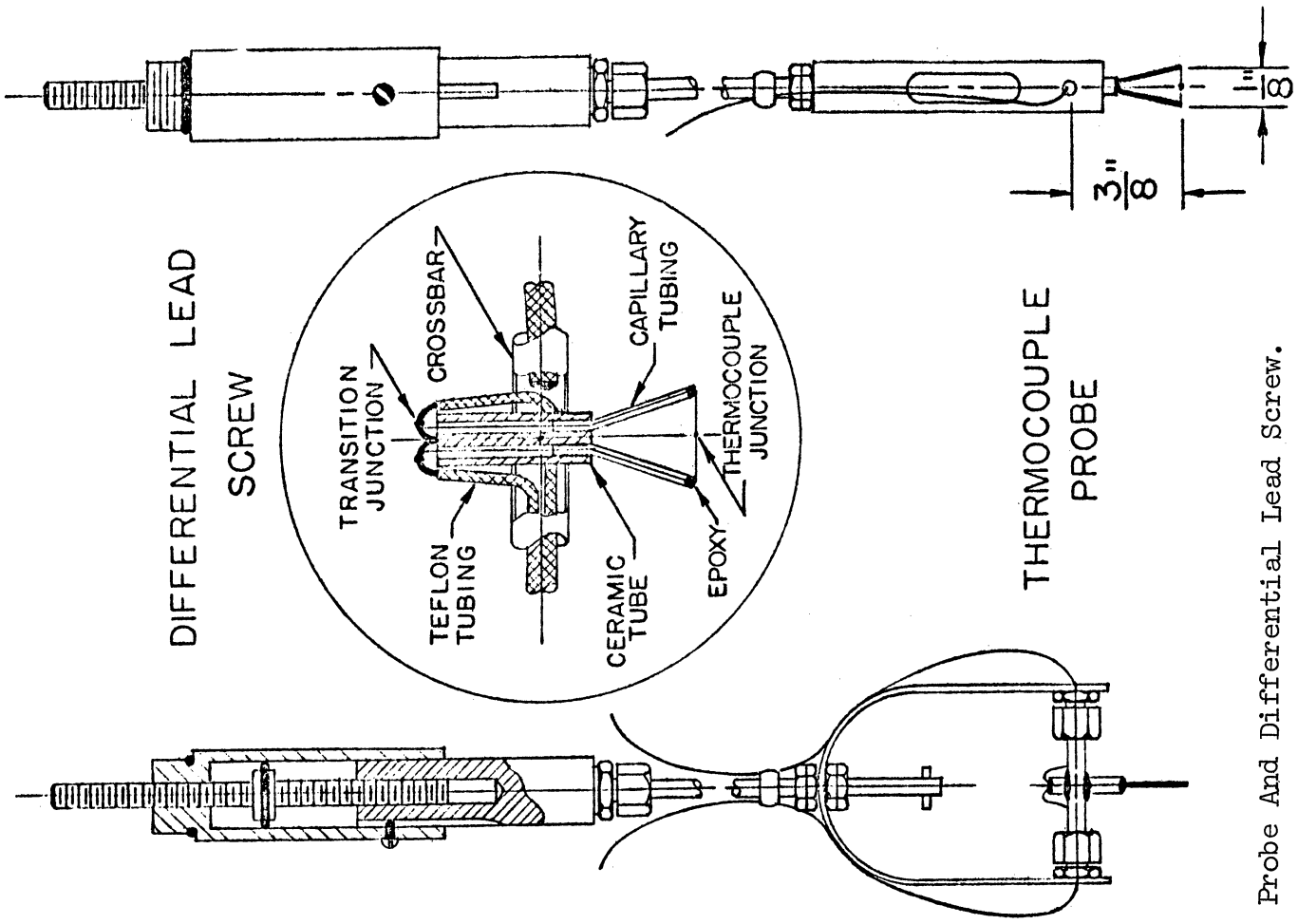

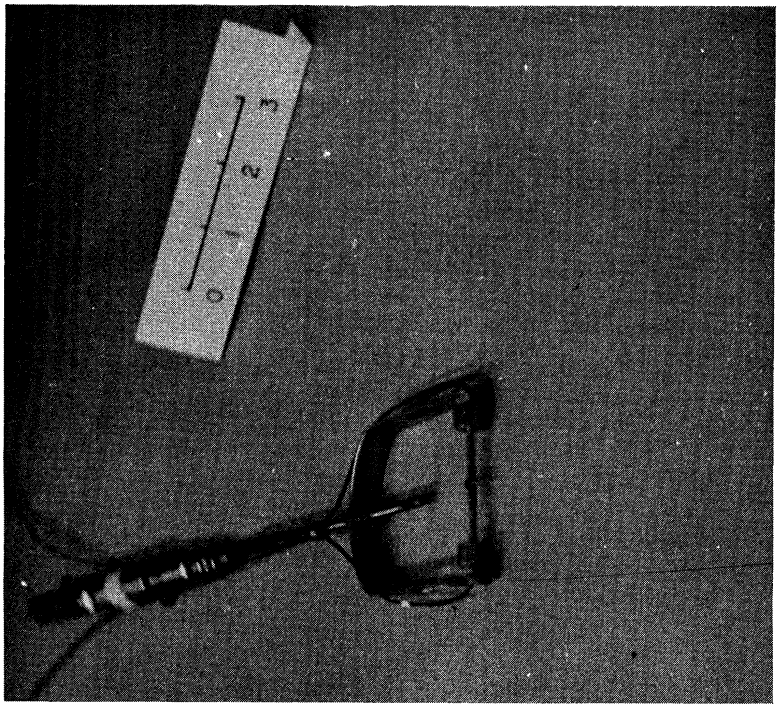

Figure 10. Thermocouple Probe And Differential Lead Screw.

The techniques of Gelb, Marcus and Dropkin[35] were applied to the design and construction of the thermocouple probe. Bare chromel and constantan wires 0.001 inch in diameter were joined by discharge welding. Two lengths of chromel and constantan wire were placed side by side and were temporarily cemented together with fingernail polish. The cemented pair of wires was clipped at one end and then was clamped in a small welding fixture with the clipped end protruding approximately 1/2 inch. A carbon electrode was brought into contact with the clipped end, discharging a capacitor at this point. The fingernail polish was then dissolved and the wires were separated. A satisfactory weld was obtained approximately every second or third attempt, yielding a junction having approximately 2/3 of the strength of the basic wire. The resulting weld bead was examined under a microscope and it was generally found that the diameter of the bead varied between 0.0025 inch and 0.0035 inch.

The probe itself was constructed of four hole ceramic tube and 0.016 inch diameter stainless steel capillary tubing. Two 3/8 inch lengths of capillary tubing which served as supports for the fine wire thermocouple, were inserted 1/8 inch into two opposing holes in a 3/8 inch length of four hole ceramic tube. The entire assembly was inserted in a hole prepared in a 0.095 inch diameter stainless steel tube such that the tips of the supports were located exactly 3/8 inch from the centerline of the "crossbar". "Minit-Grip" epoxy was used to join the components. The supports were spread 1/8 inch apart and a fine wire thermocouple was threaded into the supports such that the junction was located precisely between them. The assembly at this point was inverted and was supported in space by the crossbar; weights amounting

to approximately 20 grams were attached to each fine thermocouple wire in order to load the thermocouple junction in tension. A single drop of relatively slow setting Woodhill Chemical Corporation "Duro" epoxy was placed on the tip of each support. Since this epoxy remained fluid sufficiently long that it flowed inside the supports, essentially no epoxy was left on the tips of the supports to prevent the probe from touching down on the heat transfer surface.

Short lengths of 1/32 inch diameter teflon tubing were inserted in holes prepared in the upper surface of the crossbar one on each side of the ceramic tube. These lengths of teflon tubing served to electrically insulate the bare 30 gauge chromel and constantan thermocouple wires passing from the inside of the crossbar to the end of the ceramic tube where transition junctions were made. The two lengths of teflon tubing were slipped along the bare wires until they butted against the fiberglass wrap on the duplex thermocouple wire. The bare wires were then cut to length and inserted in the holes in the ceramic tube opposite to those occupied by the supports. Then the 0.001 inch thermocouple wires coming from the holes occupied by the supports were wrapped twice around the corresponding 30 gauge thermocouple wires and a drop of solder was placed on each junction. The end of the ceramic tube was then covered with "Minit-Grip" epoxy.

The thermocouple probe presented difficulties with regard to calibration since calibration of a probe in the constant temperature block revealed nothing about the thermoelectric potential of the fine wire thermocouple junction. According to the laws of thermoelectric behaviour, the inclusion of foreign metals between two lengths of

thermoelectric material does not in any way influence the thermoelectric potential so long as the assembly is maintained in an isothermal environment. Thus the thermoelectric potential of the junction in the fine thermocouple wires was completely undetectable. Another scheme had to be devised to evaluate these characteristics.

A dummy thermocouple was constructed by threading a fine wire thermocouple in two opposite holes of a four hole ceramic tube about 3 inches long. The junction in the fine thermocouple wires was placed at the very end of the ceramic tube and transition junctions were formed between the 0.001 inch thermocouple wires and the 30 gauge thermocouple wires at the other end of the ceramic tube. Both ends of the ceramic tube were covered with "Minit-Grip" epoxy. The sensing junction of the dummy thermocouple and the junction of another 30 gauge chromel constantan thermocouple were cemented side by side in a small copper block which was immersed in a variable temperature bath. A chromel alumel thermocouple was cemented to the transition junction which was located in the vapour space above the temperature bath. The lead wires from the dummy thermocouple and the 30 gauge thermocouple were connected together to measure the difference in thermoelectric potential of the two junctions. Now assuming that a real difference existed between the thermoelectric potential of the two types of junction, this difference could be measured directly as a function of the temperature of the sensing junction and the temperature of the transition junction. Effectively, the fine wire thermocouple could be calibrated against a 30 gauge thermocouple which had already been calibrated as described above. A simple experiment was conducted which demonstrated that such an effect existed; the

difference in thermoelectric potential was plotted as a function of the difference in temperature between the sensing junction and the transition junction. The magnitude of the effect was of the order of 10 μ Volts. Thus the thermocouple probe required an additional correction to relate the measurements to the thermocouple conversion table.

F. Probe Positioning System

The thermocouple probe had to be moved and located remotely since it was required that the temperature variation in the thermal boundary layer be measured while the centrifuge was rotating. The thermocouple probe was advanced and retracted by a "differential lead screw" which was driven by a small reversible motor mounted inside the upper frame which nominally turned at 10 revolutions per minute. The position of the differential lead screw was indicated by a wire wound potentiometer connected between the output shaft of the motor and the input shaft of the differential lead screw. This method for indicating the position of the differential screw is feasible because the displacement of the lead screw is directly proportional to the number of rotations of the input shaft. The differential lead screw can be seen in Figure 10 which shows both a photograph and a detail drawing of the assembled thermocouple probe and probe positioning mechanism.

The operation of the differential lead screw is dependent upon the relative motion of two components in response to rotation of a single threaded shaft with different threads on each end. The input end of the differential lead screw shaft was threaded by means of a 1/4-28UNF thread into the fixed portion of the differential lead screw

which in turn was fixed to the cover plate of the test package; one rotation moved the shaft 1/28 inch relative to the cover plate. The output end of the differential lead screw was threaded by means of a 1/4-32UNEF thread into the moving portion of the differential lead screw which was attached to the thermocouple probe; one rotation moved the probe 1/32 inch relative to the shaft, since the rotation of the moving portion with regard to the fixed portion was prevented by a small set screw. Consequently the differential motion was simply the difference between 1/28 inch and 1/32 which is equivalent to 1/224 inch per rotation of the shaft.

It was essential that the threads run smoothly in order for the differential lead screw to operate satisfactorily. This was especially important since it was shown to be impossible to lubricate the threads because the Freon vapour very quickly dissolved the lubricant. For these reasons the shaft was constructed of brass while the other components were made of stainless steel. A small "O" ring set into a groove in a collar which formed an integral part of the shaft and separated the two threads, served as a pressure seal as it moved on the inside surface of the fixed portion of the differential lead screw.

The wire wound potentiometer was energized by an externally located battery connected through one of the instrument channels. The potential sensed by the rotating wiper of the potentiometer was transmitted through another instrument channel and this signal was used to indicate the position of the differential lead screw through the relationship that one rotation of the shaft moved the thermocouple probe

1/224 inch. Before making a traverse of the thermal boundary layer, the thermocouple probe was always driven in toward the heat transfer surface until the fine wire thermocouple contacted the surface as indicated by a sudden increase in the voltage level of the boundary layer traversing thermocouple. The motion of the thermocouple probe was then reversed and the number of rotations of the motor was counted from the instant that the fine wire thermocouple broke contact with the surface as indicated by a sudden decrease in the voltage level of the boundary layer traversing thermocouple. In this way the position of the thermocouple probe with respect to the heat transfer surface could be determined precisely.

G. Pressure Transducer

Throughout the research investigation, the pressure at the heat transfer surface was maintained constant in order to maintain the saturation temperature constant at the heat transfer surface. In as much as acceleration changed the hydrostatic pressure at the heat transfer surface, this change had to be compensated by a change in the pressure of a helium atmosphere maintained above the Freon for this purpose. A pressure transducer was used to measure the pressure of the helium atmosphere in order that corrective action could be taken to maintain the pressure at the heat transfer surface at a specified level. An independent measurement of the pressure of the helium atmosphere was obtained from a mercury manometer connected to the test package through a rapid disconnect coupling on the end of a flexible tube.

A Norwood Controls pressure transducer was selected for this purpose. This instrument employed bonded strain gauges to sense the

deflection of a small stainless steel diaphragm which was subjected to the unknown pressure. The strain gauges formed two arms of a Wheatstone bridge; the other two arms were provided by wire wound resistors. The Wheatstone bridge was energized by an externally located power supply through two instrument channels; the output from the Wheatstone bridge was transmitted through another two instrument channels to the readout equipment. The power supply and balancing resistors were located external to the centrifuge so that the energization voltage and bridge balance could be measured and/or corrected during rotation of the centrifuge if necessary. The transducer was mounted on the arm of the centrifuge near the shaft so that the device would be unaffected by acceleration. The unknown pressure was transmitted from the test package to the pressure transducer by a small capillary tube which was wound once around the pivot upon which the test package pivoted. The pressure transducer can be seen in Figure 11 which shows both the pressure transducer and the pressurization system.

The pressure transducer was calibrated in situ at $a/g = 1$ against a precision Heise gauge and a calibration curve was obtained by plotting the pressure measured by the Heise gauge as a function of the output/excitation characteristic. The balance of the Wheatstone bridge could be varied at will by adjusting the balancing resistors and hence before every set of tests, the balance of the Wheatstone bridge was readjusted so that zero output corresponded to atmospheric pressure, in agreement with the measurement of the mercury manometer. Experience at $a/g = 1$ indicated that the balance of the Wheatstone bridge tended to drift with time in a predictable linear fashion at approximately

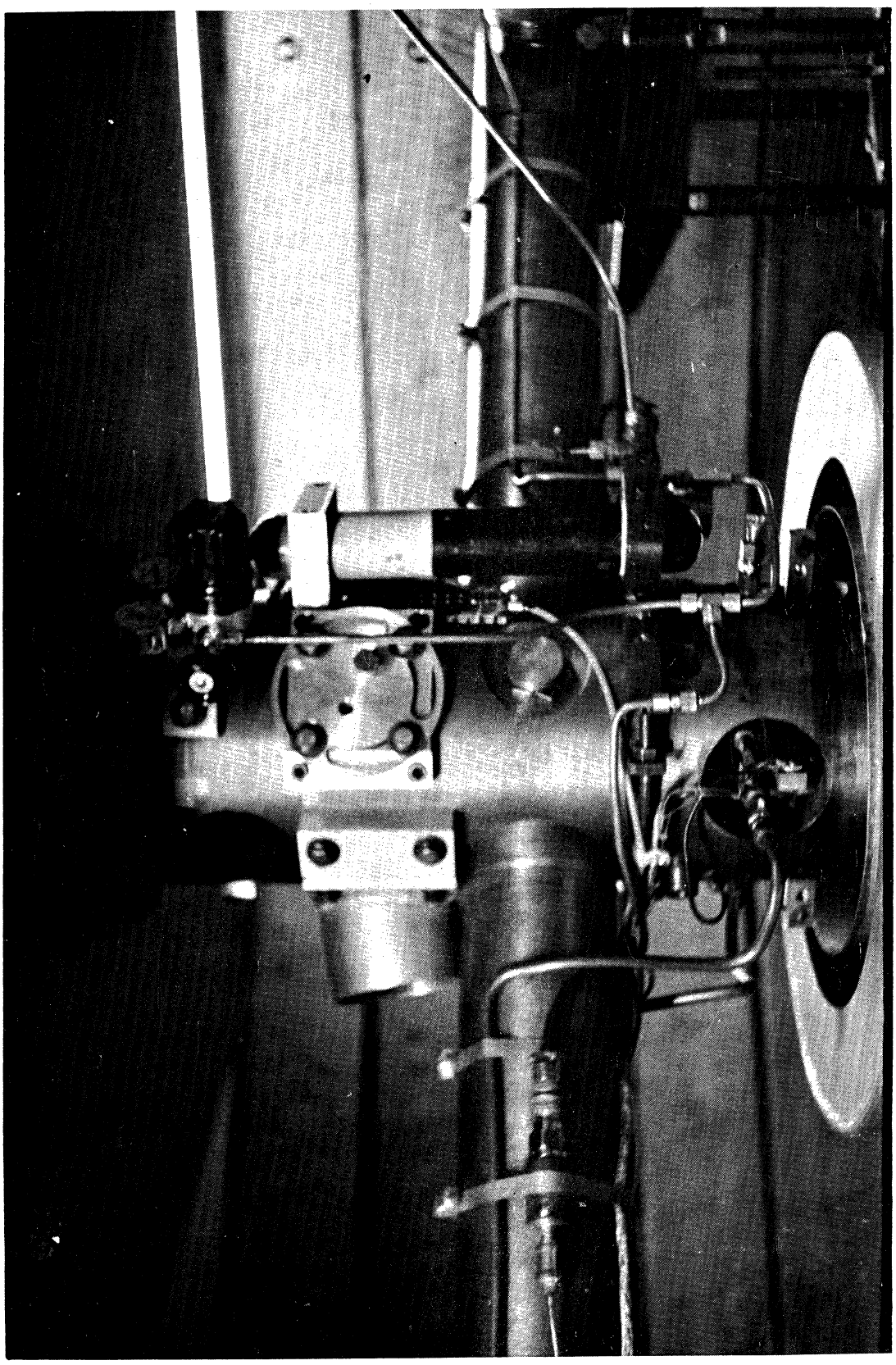

Figure 11. Pressure Transducer And Pressurization System.

1/4 pound/in^2 per hour. Consequently, when the centrifuge was rotated and the pressure transducer could no longer be checked against the mercury manometer, the output corresponding to zero pressure was determined by prorating the difference in the measurements of the pressure transducer and mercury manometer taken at atmospheric pressure before and after the set of tests against the time elapsed since the Wheatstone bridge had been adjusted. A knowledge of the output corresponding to zero pressure was required to correct the measurements of the pressure transducer.

The pressure transducer could be used at acceleration levels up to and including $a/g = 30$ although excessive noise in the instrument channels prevented its use at higher acceleration levels. A calibration performed at $a/g = 10$, $a/g = 20$ and $a/g = 30$ and various levels of pressure under isothermal conditions revealed a small consistent effect which was due to the acceleration effect upon the transducer and/or the rotational effect upon the instrument channels. This effect was taken into consideration when pressure was measured under rotating conditions.

H. Pressurization System

The need for a helium pressurization system was explained in the previous section. The nominal pressure maintained at the heat transfer surface was 8.00 ± 0.80 pounds/in^2 gauge which was determined in the following way. Since hydrostatic pressure at the heat transfer surface varies in direct proportion to acceleration level, the vapour space pressure must be varied in inverse proportion to acceleration level in order to maintain the pressure at the heat transfer surface constant. The independent variables in this simple analysis are the maximum acceleration level ($a/g = 100$), the height of the fluid above the heat transfer

surface (d = 1.50 inches) and the minimum vapour space pressure (P_v = 0 pounds/in^2 gauge). Proceeding from these considerations, it is easily seen that the governing condition occurs at a/g = 100 when the hydrostatic pressure is maximum* and the vapour space pressure is minimum. Table III below summarizes the results of this analysis.

TABLE III

SYSTEM PRESSURE ANALYSIS

Acceleration Level a/g	Hydrostatic Pressure P_h	Vapour Space Pressure P_v
	pounds/in^2 gauge	pounds/in^2 gauge
1	0.08	7.92
10	0.80	7.20
100	8.00	0

The pressurization system which was comprised of a small helium cylinder, regulator and relief valve connected together by copper tubing and tubing fittings can be seen in Figure 11 which shows both the pressure transducer and pressurization system. A small 2 cubic foot capacity helium cylinder fitted with a Matheson model 3300 two stage pressure regulator was attached to the shaft of the centrifuge. Copper tubing from the regulator was attached to the arm of the centrifuge where a transition was made to a small capillary tube which was wound once around the pivot pin upon which the test package pivotted and then terminated at the test package. A solenoid

*$P_h = (a/g)(g/g_c)\rho d$ = 100x92.33x1.50/12x144 = 8.00 pounds/in^2 gauge

operated pressure relief valve which could be operated remotely from outside the centrifuge was connected into the copper tubing. A large 220 cubic foot capacity helium cylinder fitted with a Matheson model 8 two stage pressure regulator was located outside the centrifuge; whenever the centrifuge was stationary, a copper tubing from the regulator was connected into the pressurization system at a valved connection.

The pressurization system was not entirely leak tight in as much as helium continually flowed around the seal in the differential lead screw. The leak rate was tolerable though and the volume of helium in the cylinder attached to the shaft was sufficient to maintain the pressure level in the test package for approximately four hours. The cylinder located outside the centrifuge was used exclusively for controlling the pressure in the test package whenever the centrifuge was stationary. Whenever the centrifuge had to be rotated and the pressure in the test package was being controlled by the large cylinder, the transfer of control to the small cylinder was done in such a way that the pressure level was virtually unaffected. The mercury manometer was disconnected at the rapid disconnect coupling; in the act of disconnecting this coupling helium was trapped on both sides of the coupling so that when the coupling was later reconnected there was little disturbance to the pressure level in the test package.

I. Optical System

A complete description of the high speed camera and optical system used in photographing phenomena occurring in the test package is presented in Reference 28. The only modification made for the purposes

of this research investigation was the addition of two mirrors within the test package to deflect the light beam. However, certain of the details are reproduced below for purposes of continuity.

The camera used to photograph the nucleate boiling phenomenon was a Beckman and Whitley Company "Dynafax" model 326 which was capable of filming events occurring at any rate from 200 frames/second to 26,000 frames/second. A magnetic pickup built into the camera enabled the framing rate to be determined within $\pm 0.02\%$. Three shuttering speeds 1.0 μ second, 2.5 μ second and 5.0 μ second were obtainable at maximum framing rate, depending upon the choice of "stops" used within the camera. This camera employed both a rotating film drum and a rotating octagonal mirror to expose a maximum of 224 frames on a 33 7/8 inch long 35 mm film strip at a uniform framing rate. Two different shutting systems were used in the camera; the octagonal mirror operating in conjunction with the stops controlled the shuttering of the individual frames whereas the capping shutter mounted at the entrance to the camera controlled the maximum exposure time. This particular camera features a light tight cassette which enabled the camera to be loaded and unloaded in daylight since the cassette could be loaded or unloaded in the darkroom.

The camera could not withstand acceleration forces other than normal gravity and for this reason the image of the nucleate boiling phenomenon was transmitted to the camera which was mounted on a frame supported from the ceiling of the laboratory. Figure 12 shows the camera mounted above the centrifuge.

Triple perforated Tri-X film was exposed exclusively in this research investigation. Each film strip was developed immediately after it was exposed in order that the quality of the pictures could be assessed

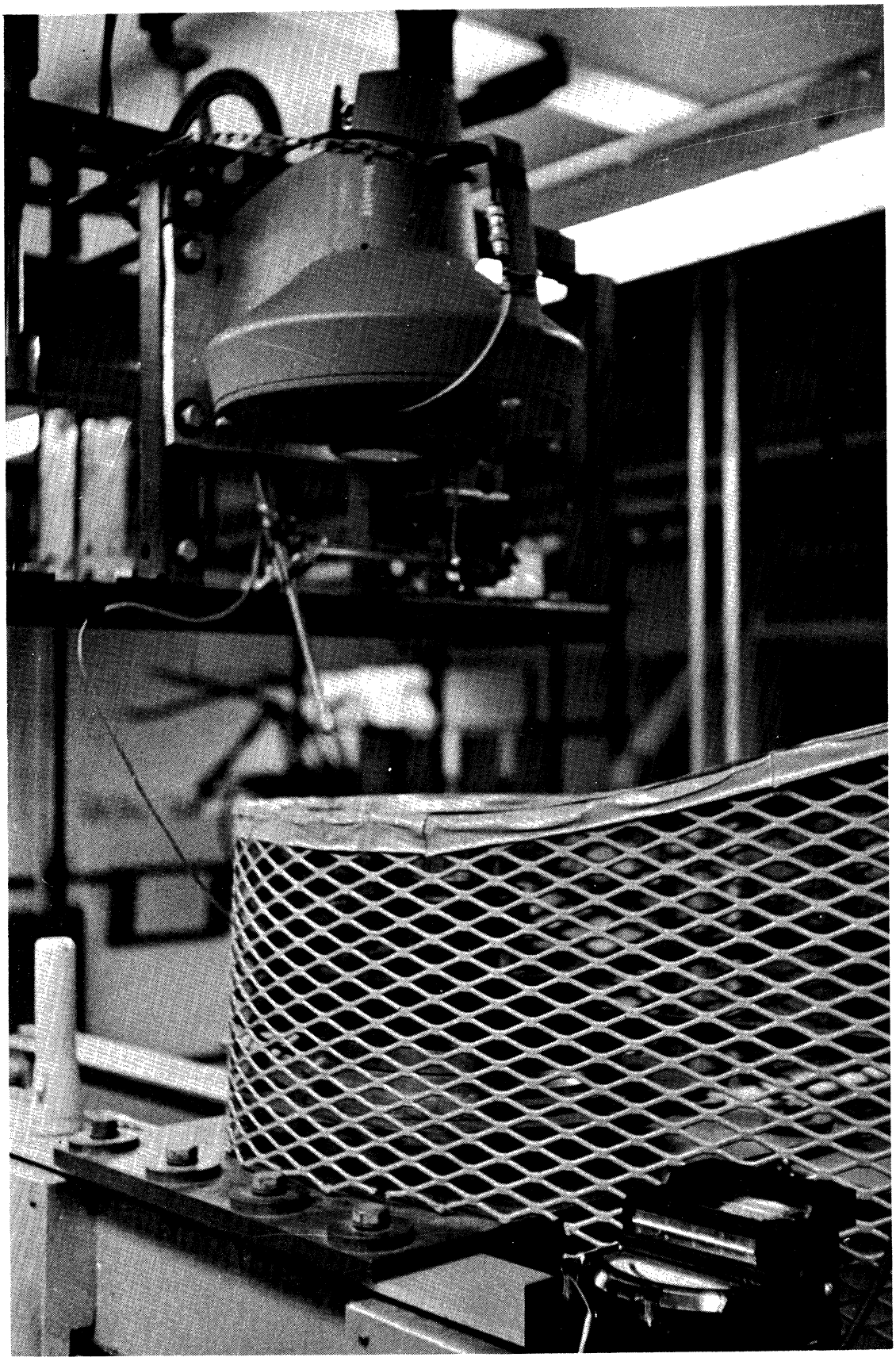

Figure 12. Camera Mounted Above Centrifuge.

in time to permit another film strip to be exposed under identical conditions if necessary. Since the camera laid down successive images in two alternate rows on the 35 mm film strip, this film strip could be split into two 16 mm film strips and a 3 mm wide piece of scrap. Whenever the images on a single 16 mm film strip were projected or otherwise examined for interpretation, the effective framing rate at which the event had been photographed was determined by multiplying the actual framing rate by 1/2 since each successive image was separated in time by two units of the basic time increment.

Figure 13 shows a schematic drawing of the optical system used to transmit the image of the boiling phenomenon to the camera. The high intensity light source which was used to back light the nucleate boiling phenomenon was located on the axis of rotation; further details of the light source are presented in the next section. A condensing lens with a 134 mm focal length was placed 149 mm from the light source producing a slightly converging beam of light focused on the test surface approximately 48 inches away. This beam of light was transmitted by reflection off mirrors, 1, 2, 3 and 4 respectively. The image of the phenomenon occurring at the test surface was transmitted by reflection off mirrors 5 and 6 to the first lens located approximately 17 inches from the test surface. The first lens which had a focal length of 18.25 inches transmitted the image by reflection off mirrors 7, 8 and 9 to the second lens. The second lens which also had a focal length of 18.25 inches, focused the image at the focal plane of the camera located approximately 17 inches away.

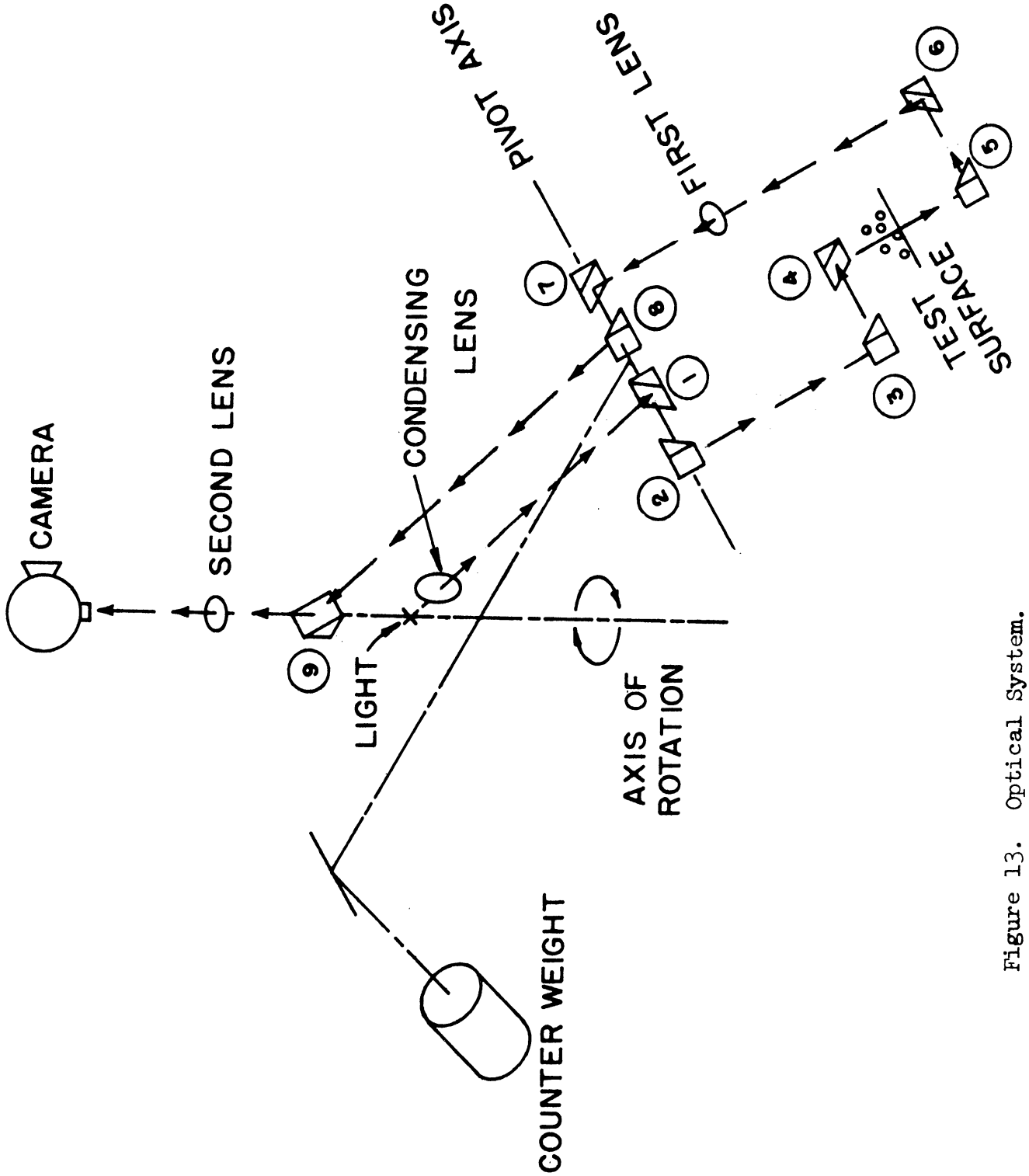

Figure 13. Optical System.

Mirrors 1 and 8 were fastened to the pivot pin upon which the test package pivotted; mirrors 2 and 7 were located on the axis of the pivot pin but were fastened to the test package. These four mirrors permitted the light beam and optical image to be transmitted for all angular positions assumed by the test package relative to the cross arm. Mirrors 3 and 6 were located on the sight tubes and served to deflect the light beam into the test package and the optical image out of the test package respectively. Mirror 4 located above the test surface deflected the light beam entering the test package and mirror 5 located below the test surface deflected the optical image leaving the test surface. Mirror 9 located on the axis of rotation above the light source served to deflect the optical image up the hollow shaft.

As a result of the particular arrangement of the lenses in the optical system, the image of the boiling phenomenon was transmitted approximately 120 inches at unity magnification. The optical system was focused by a procedure in which the image of a 0.001 inch diameter wire located on the test surface was brought into sharp focus in the focusing eyepiece of the camera by adjusting the location of the second lens within the shaft.

J. Light Sources

Adequate exposure of the film for all combinations of heat flux, subcooling and acceleration was difficult to achieve because of the nature of the phenomenon being photographed. The formation and subsequent release and/or collapse of vapour bubbles at the heat transfer surface served to disperse the light beam incident upon the heat transfer surface. For certain combinations of the three parameters mentioned above photography

was impossible because no image was transmitted even for the most intense back lighting. The combination of high heat flux, low subcooling and standard gravitational acceleration was particularly bad in this regard.

Actually, three different high intensity lamps and power supplies were used in the present research investigation to backlight the phenomenon occurring at the heat transfer surface. Table IV below lists these lamps and power supplies and tabulates the specified operating characteristics of each.

TABLE IV

LAMP AND POWER SUPPLY SPECIFICATIONS

Lamp	Power Supply	Source Intensity	Source Brightness	Luminous Flux
#	#	Candles	Candles/mm^2	Lumens
Engelhard Hanovia 976C-1	Engelhard Hanovia 27801	1575*	350*	32,000*
Osram HBO-200W/2	Gates P110D	435	330	10,000
Sylvania K100P	Electron Arc 823	100	39	157

*Maximum Values

The Engelhard Hanovia lamp was used exclusively at $a/g = 1$. The lamp consumed 1,000 watts DC at 43.5 amperes and 23 volts; a 30,000 volt starting potential was required. The high pressure xenon atmosphere contained within the quartz glass envelope served to constrict the arc between the electrodes thereby producing an extremely intense point

source of light. By varying the setting of a control on the power supply, the light intensity could be varied. The lamp was always started at the maximum intensity setting after which the intensity setting could be reduced to the point at which the lamp was extinguished. This feature provided an approximate five fold variation in the light intensity.

The current level at which this lamp operated excluded the possibility of making electrical connections with the external power supply through the instrument channels. Although the slip rings could transmit the current at operating conditions, experience showed that the slip rings could not transmit the starting potential. Consequently, this lamp could only be operated under stationary conditions. Fortunately, the very conditions which required the use of this lamp occurred at $a/g = 1$. Photographs were taken under all combinations of heat flux and subcooling for which it was possible to obtain adequate exposure of the film. The light intensity was adjusted from test to test to accomodate the phenomenon being photographed. Unfortunately, photographs could not be obtained for the combination of high heat flux and low subcooling.

The Osram lamp was used exclusively at $a/g = 10$. This lamp consumed 200 watts DC at 3.6 amperes and 57 volts; a 5,000 volt starting potential was required. The starting intensity of the lamp was quite low, but as the temperature of the lamp increased, the mercury vapour pressure contained within the quartz glass envelope increased rapidly, restricting the arc between the electrodes until an intense light was produced.

The conditions under which this lamp operated and the potential required to start the lamp were such that electrical connections with the

external power supply could be made through the instrument channels. Thus operation under rotating conditions was possible. The light intensity was sufficient to obtain adequate exposure of the film for all combinations of heat flux and subcooling at $a/g = 10$ except those corresponding to the very highest level of heat flux.

The Sylvania lamp was used exclusively at $a/g = 100$. This lamp consumed 100 watts DC at 6.2 amperes and 16 volts; a 2,000 volt starting potential was required. An argon atmosphere was contained within the quartz glass envelope. A moderately intense light was produced immediately upon starting.

Electrical connections with the external power supply were made through the instrument channels. The light intensity was sufficient to obtain adequate exposure of the film for all combinations of heat flux and subcooling at $a/g = 100$.

K. Associated Equipment And Instrumentation

The power supply which furnished power to the oxide coated test specimen is shown in Figure 14. Ten 12 volt automobile batteries which could be connected in series of parallel by the manipulation of knife switches provided a ripple free source of power. Fine control over the voltage level was achieved through the use of a large series connected rheostat. The approximate levels of test voltage and test current were indicated by instruments mounted on the power supply. A rectifier set furnished power to the metal foil heater surface.

Various of the control devices used in the present research investigation are shown in Figure 15. The three variacs which controlled the guard heaters are seen in the foreground, the thermocouple probe

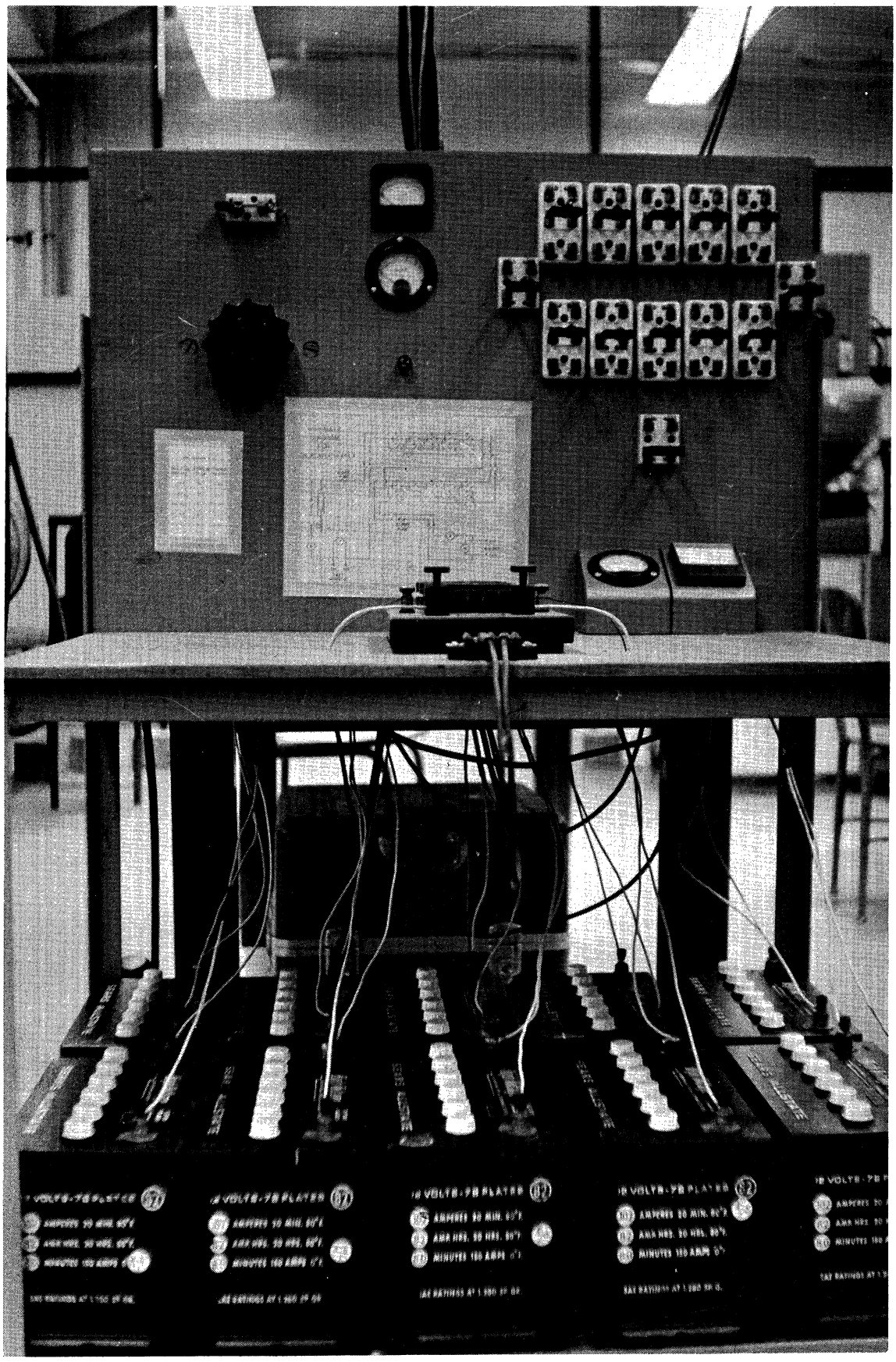

Figure 14. Direct Current Power Supply.

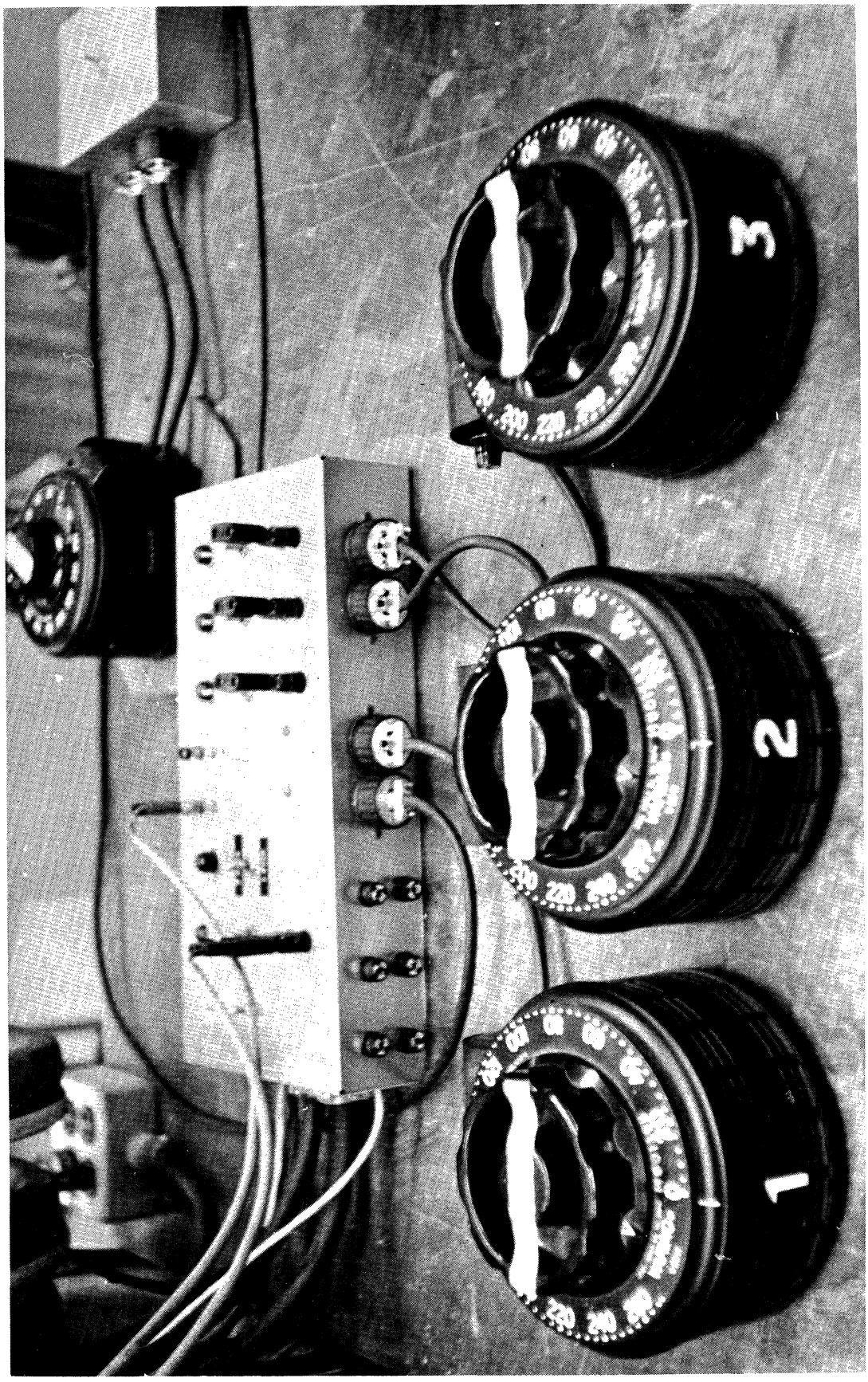

Figure 15. Control Devices.

positioning controls are seen in the middle ground and the camera framing rate control variac is seen in the background.

The flow of cooling water through the test package was controlled by a needle valve equipped with a vernier handwheel which was located downstream of the test package. In this way, the vapour condenser and heat exchanger were kept under pressure. A sand filter was provided upstream of the test package to remove particulate matter which might have lodged in the "O" ring seals of the fluid coupling.

Figure 16 shows a number of instruments used for measuring the output signals of various sensing devices. The Leeds and Northrup K3 precision potentiometer is seen on the left; the Sanborn Electronics Series 150 four channel recorder is seen on the right. The switch box situated to the right of the potentiometer selected the instrument signal to be measured. This Ellis bridge amplifier and Dumont oscilloscope situated to the left of the recorder monitored the unbalance of the centrifuge. The Hewlett Packard electronic counter which indicated the rotational speed of the centrifuge is seen in the center of the photograph supported on a frame above the Engelhard Hanovia power supply.

The output signals of all of the thermocouples plus the output signals of a number of other instruments were fed into the switchbox from which each output signal could be directed to the potentiometer or the recorder, depending upon the channel selected by the rotary switch and knife switches seen in the photograph. In addition, the switchbox contained the power supply and balancing resistors for the pressure transducer bridge and a precision 100:1 voltage divider which was used to reduce either the voltage drop measured across the test specimen at the

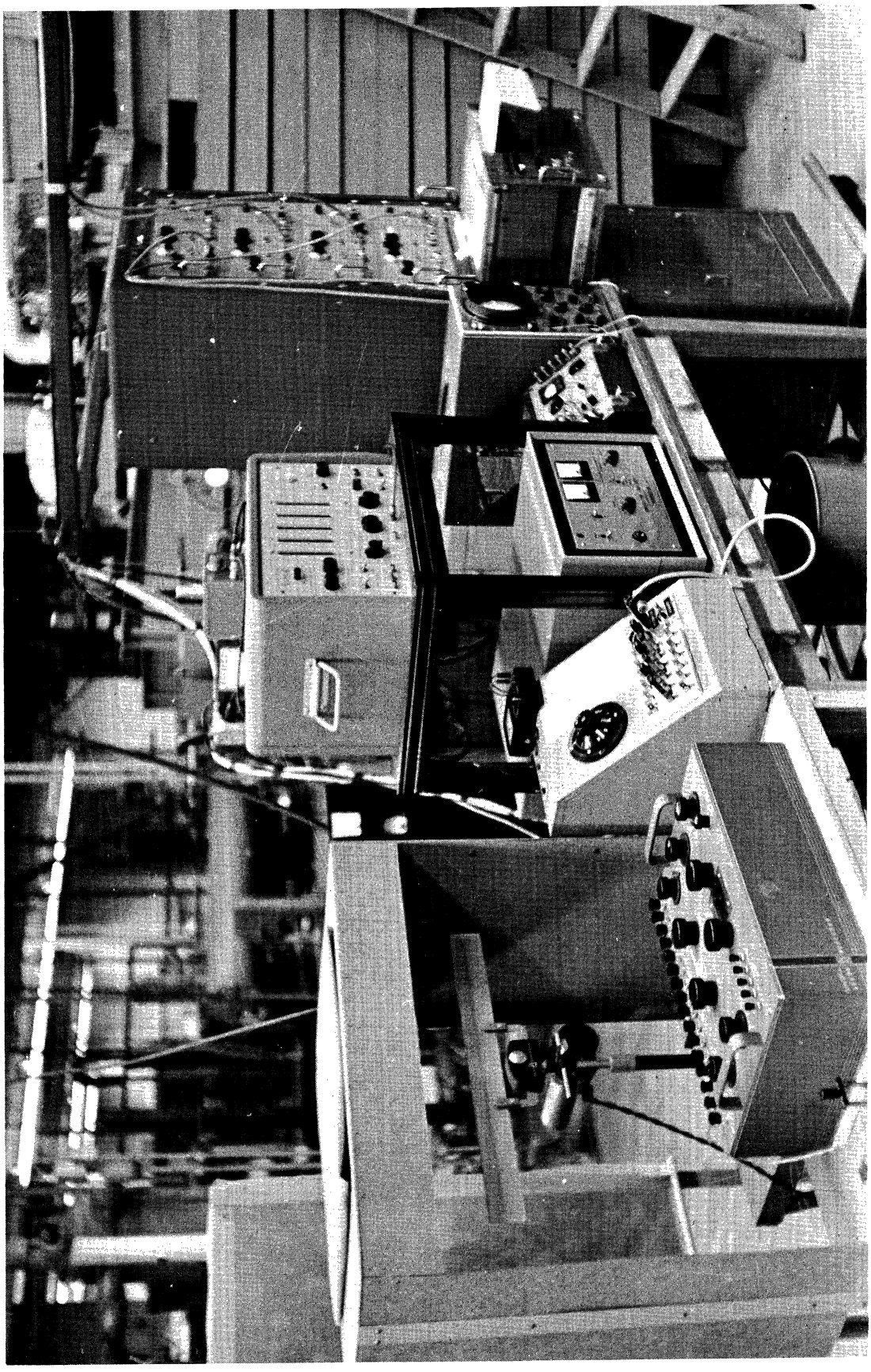

Figure 16. Instrumentation.

test package or the voltage drop measured across a precision resistor connected in series with the test specimen to a level which could be measured by the precision potentiometer. Table V below tabulates the output signals which could be selected at the switchbox.

TABLE V

OUTPUT SIGNALS SELECTED THROUGH SWITCHBOX

Switch Position	Knife Switch		Output Signal
	Number	Position	
0			B. L. Traversing Thermocouple
1			Stationary Fluid Thermocouple
2			Reference Fluid Thermocouple
3			Test Specimen Thermocouple
4			#1 Sight Guard Thermocouple
5			#2 Sight Guard Thermocouple
6			Air Temperature Thermocouple
7	1	Up	#1 Sight Guard Differential
7	1	Down	#2 Sight Guard Differential
8	2	Up	Pressure Transducer Output
8	2	Down	Pressure Transducer Excitation
9	3	Up	Test Voltage
9	3	Down	Test Current
10			Millivolt Calibration Signal

The Leeds and Northrup potentiometer was capable of reading instrument signals as large as 1.6110 volts with a reading accuracy of $\pm$ 0.5 μ Volt and a maximum uncertainty of $\pm$ 2 μ Volts in the millivolt range. When steady state operating conditions had been established, this instrument was used for precision measurement of all the instruments with the exception of the boundary layer traversing thermocouple. The inertia of this instrument was such that fluctuations in the instrument signals induced by rotation of the centrifuge were not detected.

The Sanborn recorder was capable of simultaneously recording four instrument signals. Each recording galvanometer was capable of 5 millisecond response. Channel A recorded thermocouple signals exclusively. The span was set 0 - 2 millivolts and the zero suppression was varied from 0 - 4 millivolts in one millivolt increments depending upon the output being recorded. Channel B recorded the output of the wire wound potentiometer which indicated the position of the thermocouple probe. Channel C recorded the voltage level of the boundary layer traversing thermocouple. Channel D was used to record the output of the pressure transducer bridge. The chart speed was stepwise variable; all of data was recorded at 0.25 mm/sec with the exception of the boundary layer traverse data which was recorded at 10 mm/sec.

The Ellis bridge amplifier completed a four arm strain gauge bridge attached to the upper bearing of the centrifuge in such a way that dynamic unbalance in the centrifuge could be detected. Reference 28 presents complete details of the balancing equipment. The output of the bridge amplifier was displayed on a Dumont oscilloscope so that the dynamic balance could be assessed at a glance and corrective action could be taken if necessary. As it turned out, it never was necessary to make use of this equipment.

The Hewlett Packard electronic counter indicated the number of revolutions of a forty eight tooth gear turning with the shaft of the centrifuge in a standard one second counting period, since the action of each tooth passing a magnetic counting head created an electronic pulse which was sensed by the electronic counter. Forty eight pulses

per second corresponded to one revolution per second or sixty revolutions per minute. The rotational speed of the centrifuge upon which the calculation of acceleration depended could be determined quite accurately in this way.

CHAPTER III

TEST CONDITIONS

Freon 113 was chosen as the test fluid since experimentation with water boiling on the oxide coated glass indicated that the oxide coating was incompatible with the boiling water. The water boiling on the oxide coated surface subjected the coating to electrolytic attack which limited the useful lifetime of the coating to the order of minutes. Westwater and Kirby[31] reported the same results, and solved the problem by selecting methanol and carbon tetrachloride as the test fluids. Freon 113 was chosen as the test fluid for the present research investigation since this fluid is considerably less hazardous than methanol and carbon tetrachloride. The properties of the fluid are well established and can be obtained from the manufacturer's publications[36,37,38]. In addition, Freon 113 is one of the purest organic chemicals commercially available, it exhibits excellent thermal stability characteristics and it has an exceedingly low helium solubility. These characteristics made Freon 113 an excellent choice as the test fluid in this heat transfer investigation.

The experimental results reported by Jakob[4] for water boiling on a horizontal surface showed the existence of a thin boundary layer adjacent to the heat transfer surface. These results indicated that the major portion of the temperature drop in the bulk liquid between the heat transfer surface and the free surface occurred in the boundary layer and that the temperature of the bulk liquid decreased little outside of the boundary layer until the free surface was approached where

a further decrease in the bulk liquid occurred. It can reasonably be assumed that the bulk liquid temperature for Freon varies similarly. Furthermore it can be deduced that the saturation temperature in the bulk fluid varies linearly between the heat transfer surface and the free surface since the hydrostatic pressure varies linearly and saturation temperature is directly proportional to hydrostatic pressure to a first order approximation. In as much as both profiles attain the temperature of the liquid at the free surface for saturated boiling conditions, it is actually possible for these profiles to intersect twice, depending upon the depth of liquid and the acceleration level. Figure 17 shows typical temperature profiles for nucleate boiling under saturated conditions for the three levels of acceleration $a/g = 1$, 10 and 100.

Since the bulk liquid temperature profile and the saturation temperature profile intersect for certain conditions, it can be seen in the foregoing diagram that the liquid can actually be subcooled throughout the bulk with the exception of the regions adjacent to the heat transfer surface and the free surface. Beckman, Merte and Clark[28] refer to this phenomenon as "natural subcooling". Unfortunately natural subcooling cannot be predetermined and can only be computed by comparing data from a complete temperature traverse with the corresponding saturation temperature data. Consequently, for the purposes of this research investigation, subcooling had to be defined in such a way as to be independent of the level of natural subcooling but related to the actual bulk liquid temperature profile in a realistic manner. The method used was to define subcooling as the difference between the saturation temperature at the heat transfer surface and the temperature level at an arbitrarily chosen position in the bulk liquid.

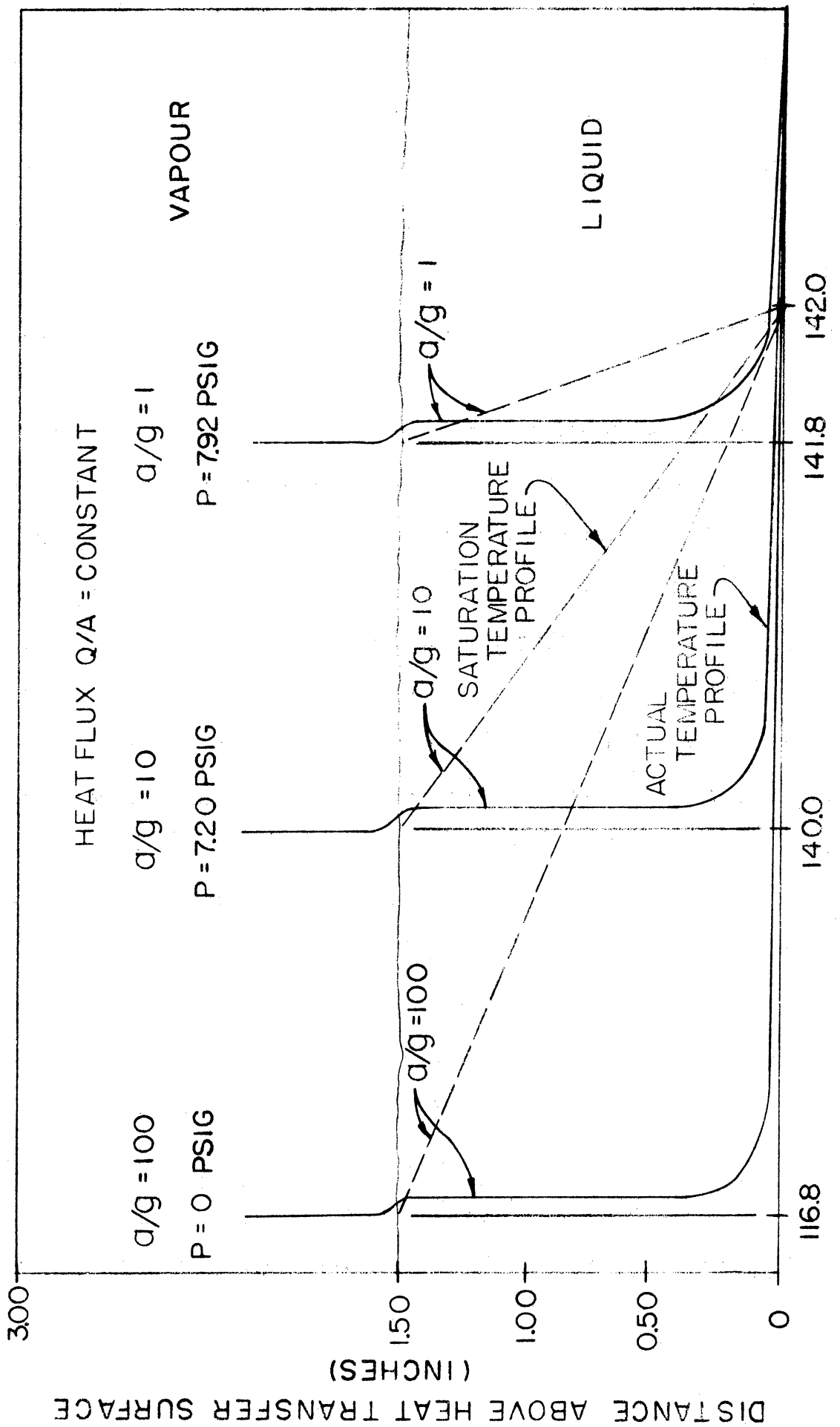

Figure 17. Temperature Profile In A Typical Boiling System.

As previously explained, the saturation temperature at the heat transfer surface was maintained constant for all levels of acceleration since the pressure at the heat transfer surface was maintained constant within specified limits. This temperature was determined for each test by measuring the pressure in the vapour space above the test fluid, correcting this measurement for the hydrostatic pressure corresponding to the particular depth of fluid and acceleration level and then computing the temperature corresponding to this pressure from published vapour pressure-temperature data. The location chosen for measuring the bulk liquid temperature was the crossbar of the thermocouple probe. Whenever measurements of the bulk liquid temperature were made, the crossbar of the thermocouple probe was located precisely 0.400 inches from the heat transfer surface. Subcooling was then computed by subtracting the measured bulk liquid temperature from the computed saturation temperature at the heat transfer surface.

Another interesting phenomenon can be seen in the foregoing diagram. Notice that if the bulk liquid temperature profiles actually vary in the manner suggested, then it is physically impossible for the bulk liquid temperature to exceed 141.8°F, and 140.0°F and 116.8°F at $a/g = 1$, 10 and 100 respectively by any appreciable amount. This observation leads to the conclusion that minimum levels of subcooling exist equivalent to 0.2°F, and 2.0°F and 25.2°F at $a/g = 1$, 10 and 100 respectively when the saturation temperature at the heat transfer surface is 142.0°F, corresponding to a pressure of 8.00 pounds/in^2 gauge. This conclusion proved to be valid although the magnitude of the minimum subcooling effect was somewhat less than that predicted.

Three levels of acceleration were used in the test program a/g = 1, 10 and 100 respectively. Although Beckman, Merte and Clark[28] used five levels of acceleration, the results obtained indicated that the variation in nucleate boiling characteristics which were investigated were such that three levels of acceleration would have been sufficient. A similar variation in the site density and frequency was suspected and consequently three levels of acceleration were selected. Five levels of heat flux were investigated, $Q/A \cong 4{,}000$ BTH/hr ft^2, 7,000 BTU/hr ft^2, 13,000 BTU/hr ft^2, 25,000 BTU/hr ft^2 and 40,000 BTU/hr ft^2 respectively, chosen on the basis of equal increments on a logarithmic scale. For every combination of acceleration and heat flux investigated, subcooling was varied from the minimum value obtainable to the maximum value obtainable in six increments on the average. This test program was performed twice, once to obtain temperature data including temperature traverses of the thermal boundary layer and again to obtain photographic data from which the number of active sites per unit area and the frequency of vapour bubble emission could be determined. Table VI presents a complete summary of all the test conditions.

A total of two hundred and sixty five individual tests were performed for various combinations of acceleration, heat flux and subcooling. These tests have been grouped in Table VI into forty six test series in which two of the parameters have been held constant and the third one has been varied over the range of values indicated in the tabulation. The numerical values presented have been arrange in order of increasing acceleration and heat flux which is not the chronological sequence in which the tests were performed.

TABLE VI

SUMMARY OF TEST CONDITIONS

Test Series	a/g	Q/A	ΔT_{SUB}	Boundary Layer Traverse	Photographs	Surface
#	-	BTU/hr ft^2 $x10^{-3}$	°F	-	-	-
0	1	4 - 40	+0.1			Oxide Coated Glass
1	1	40 - 4	+0.2	*		"
2	1	4 - 40	-0.1			"
3	1	40 - 4	-0.2			"
4	1	4 - 40	+0.1			"
5	1	40 - 4	-0.1			"
6	1	4	+0.2 - 34.3	*		"
7	1	7	-0.5 - 21.9	*		"
8	1	13	-0.1 - 15.1	*		"
9	1	25	+0.2 - 3.5	*		"
10	1	40	+0.2 - 1.4	*		"
11	10	4	3.0 - 39.8	*		"
12	10	7	1.2 - 39.8	*		"
13	10	13	1.1 - 22.7	*		"
14	10	13	0.6 - 22.2	*		"
15	10	25	1.3 - 23.8	*		"
16	10	25	0.8 - 19.0	*		"
17	10	40	0.8 - 5.7	*		"
18	100	4	15.5 - 61.7			"
19	100	7	15.4 - 58.4			"
20	100	13	14.0 - 49.6			"
21	100	25	19.3 - 38.0			"
22	100	40	15.3 - 23.6			"
23	1	4	+ 0.2 - 32.8		*	"
24	1	7	+ 0.4 - 33.4		*	"
25	1	13	+ 0.1 - 22.9		*	"
26	1	13	+ 0.5 - 28.6		*	"
27	1	25	+ 0.4 - 3.9		*	"
28	10	7	2.8 - 48.4		*	"
29	10	13	1.8 - 36.8		*	"
30	10	25	1.7 - 23.6		*	"
31	10	40	2.5 - 6.4		*	"
32	100	13	14.6 - 48.6		*	"
33	100	25	16.2 - 42.2		*	"
34	100	40	14.9 - 31.7		*	"
35	1	4 - 40	+0.1			"
36	1	40 - 4	+0.1			"
37	1	4 - 25	0.5			Metal Foil
38	1	25 - 4	0.5			"
39	1	25	0.3 - 6.2			"
40	10	25	2.8 - 17.2			"
41	100	25	13.2 - 44.6			Oxide Coated Glass
42	100	4	9.6			"
43	100	7	9.9			"
44	100	13	9.5			"
45	100	25	10.3			"
46	100	40	10.5			"

The first six test series (0 - 5 in Table VI) were performed to establish a nucleate boiling characteristic curve at $a/g = 1$ for Freon boiling on an oxide coated glass surface. Saturated boiling conditions were established and the heat flux was varied over the range indicated in the tabulations. Test series 0, 2 and 4 investigated the influence of increasing heat flux; test series 1, 3 and 5 investigated the influence of decreasing heat flux.

The next seventeen test series (6 - 22 in Table VI) were performed to determine the influence of heat flux and subcooling upon the temperature of the heat transfer surface and temperature distribution in the thermal boundary layer for nucleate boiling at $a/g = 1$, 10 and 100. Test series 6 - 10 investigated the effect of these parameters at $a/g = 1$, test series 11 - 17 investigated the effect of these parameters at $a/g = 10$ and test series 18 - 22 investigated the effect of these parameters at $a/g = 100$. Temperature traverses of the thermal boundary layer were obtained for all combinations of acceleration and heat flux at $a/g = 1$ and $a/g = 10$ but it proved impossible to obtain temperature traverses of the thermal boundary layer at $a/g = 100$ since the forces on the components of the differential lead screw were too great for the drive motor to overcome.

The next twelve test series (23 - 34 in Table VI) were performed to enable photographic data to be obtained for the various combinations of acceleration, heat flux and subcooling investigated previously. Test series 23 - 27 obtained photographic data for all the combinations of heat flux and subcooling investigated previously at $a/g = 1$ with the exception of these corresponding to $Q/A = 40{,}000$ BTU/hr ft^2 which proved

impossible to photograph. Test series 28 - 31 obtained photographic data for all the combinations of heat flux and subcooling investigated previously at $a/g = 10$ with the exception of those corresponding to $Q/A = 4{,}000$ BTU/hr ft^2 for which there was little boiling. Test series 32 - 34 obtained photographic data for all the combinations of heat flux and subcooling investigated previously at $a/g = 100$ for which significant boiling occurred.

Two test series (35 - 36 in Table VI) were performed to verify the nucleate boiling characteristic curve previously established. Test series 35 investigated the influence of increasing heat flux; test series 36 investigated the influence of decreasing heat flux.

The next five test series (37 - 41 in Table VI) were performed to study nucleate boiling heat transfer on a metal foil heater surface. Test series 37 and 38 investigated the influence of increasing and decreasing heat flux at saturated boiling conditions. Test series 39, 40 and 41 investigated the influence of subcooling on nucleate boiling heat transfer at $Q/A = 25{,}000$ BTU/hr ft^2 at 1, 10 and 100 respectively.

The last five test series (42 - 46 in Table VI) were performed to obtain heat transfer data at $a/g = 100$ for as low a value of subcooling as could be attained. In order to achieve this result, the standard 1 1/2 inch fluid depth was reduced to 1/2 inch and the pressurization system was used to adjust the pressure at the heat transfer surface to the level maintained throughout the investigation.

CHAPTER IV

TEST PROCEDURE

Preliminary tests were conducted prior to the commencement of the research investigation during which maximum attainable acceleration level was determined and the dynamic balance of the centrifuge was established.

The depth of Freon in the test package was checked from time to time, particularly before each test series at $a/g = 100$. An exact knowledge of this parameter was especially important in as much as the calculation of the hydrostatic pressure depended upon it. Although the test package was disassembled and reassembled approximately half a dozen times during the course of the research investigation only two charges of Freon were used. One charge of Freon was used during the tests which obtained temperature data and another charge of Freon was used during the tests which obtained phtographic data. However, the process of checking the depth of Freon in the test package necessitated the addition of small quantities of Freon as explained below.

The end of a small capillary tube supported from the cover of the test package was positioned accurately above the heat transfer surface at a distance equivalent to the prescribed depth of Freon. Approximately 20 cubic centimeters of Freon were added to the test package and the space above the Freon was pressurized with helium. Unless Freon flowed from the capillary tube, an additional 20 cubic centimeters of Freon were added to the test package. This procedure was continued until Freon issued from the capillary tube. When the flow ceased, the

depth of Freon precisely equalled the prescribed depth. Generally, it was unnecessary to replenish the Freon at all; the exception to this rule occurred for the tests at $a/g = 100$ for which the test package was vented to the atmosphere. The depth of Freon in the test package was checked before each test series; the addition of approximately 50 cubic centimeters of Freon corresponding to a maximum variation in the depth of approximately 1/16 inch was required to maintain the depth of Freon constant.

Except for the very earliest tests, the usual procedure was to maintain a helium atmosphere above the Freon at all times. Even when the pressurization system was shut off, a helium atmosphere remained in the test package although the pressure decreased to atmospheric pressure over a period of many hours. This procedure served to exclude air from the vapour space above the Freon and in as much as the maximum solubility of helium in Freon did not exceed 10^{-5} moles of helium/mole of Freon per pound/in^2 of helium partial pressure, a relatively simple system resulted comprised of a single component liquid in equilibrium with a two component gas-vapour mixture. No effort was made to degas the Freon prior to obtaining test data since the amount of helium which could be dissolved in the Freon was small.

The first pretest procedure was the adjustment of the pressure transducer bridge to make zero output correspond to atmospheric pressure. Following this, the pressurization system was activated and the pressure level was set to the standard helium pressure level at $a/g = 1$. When the pressure transducer output recorded on the Sanborn recorder indicated that the specified pressure level had been attained, the guard heaters

at the bottom of the test package and in each of the sight tubes were energized. The direct current power supply was switched on and set to the appropriate operating level and the cooling water flowrate was adjusted to a level just sufficient to condense the vapour in the vapour space. The temperature level of the Freon within the test package was permitted to increase until saturated boiling conditions were attained at $a/g = 1$. The purpose in this procedure was to establish a reference test condition which could be used to determine the effects of subsequent changes in acceleration and subcooling. A similar reference test condition was established at the conclusion of many of the test series to confirm the reproducibility of the reference test condition established at the beginning of the test series.

During the period of time in which steady state boiling conditions were being established, the outputs of each of the thermocouples with the exception of the output of the boundary layer traversing thermocouple were recorded one after the other in a continuous fashion on the Sanborn recorder. The variacs which controlled the guard heaters in each of the sight tubes were varied in order to adjust the temperature of the air within the sight tubes to the same level as that of the reference fluid thermocouple.

Steady state test conditions were considered to have been reached when the output of the reference fluid thermocouple remained constant within $\pm$ 20 μ Volts for a period of five minutes or longer and the differences in the output of the reference fluid thermocouple and the sight guard thermocouples did not exceed $\pm$ 40 μ Volts. When these conditions were fulfilled, steady state values of each of the

thermocouple outputs and the outputs of the other instrument systems were measured with the Leeds and Northrup potentiometer. This information was later analyzed to determine the influence of heat flux, subcooling and acceleration upon the temperature of the heat transfer surface.

Once the data for the reference test had been obtained, the acceleration level and/or the subcooling level were changed in accordance with a consistent pattern. The sequence in which the individual tests comprising the test series were performed is illustrated schematically in Table VII below for all three levels of acceleration investigated.

TABLE VII

SCHEMATIC REPRESENTATION OF TEST SEQUENCE

Test	Acceleration													
	a/g = 1						a/g = 10				a/g = 100			
	Subcooling						Subcooling				Subcooling			
	Min					Max	Min			Max	Min			Max
First	*													
						*	*				*			
					*					*				*
				*					*				*	
			*					*				*		
		*					*				*			
Last	*													

For those tests involving the measurement of the temperature distribution in the thermal boundary layer, a boundary layer traverse was performed immediately following the potentiometer measurements. The thermocouple probe was driven downward during which operation the Sanborn recorder was switched off to prevent damage to the amplifiers resulting from the sudden increase in the voltage level which occurred when the probe made contact with the heat transfer surface. The thermocouple probe was then driven upward and at the precise instant that the probe broke contact with the heat transfer surface, the Sanborn recorder was switched on. The angular position of the drive motor at the instant that the probe broke contact as indicated by the Sanborn recorder was carefully noted. Thereafter, the boundary layer traverse was interrupted for several seconds at intervals corresponding to one revolution of the drive motor. This procedure was continued for a total of ten revolutions after which the outputs of each of the other thermocouples, the outputs of the other instrument systems and a millivolt calibration signal were recorded in turn. Each chart paper recording obtained was later analysed to determine the variation in liquid temperature with distance from the heat transfer surface for the particular combination of heat flux, sub-cooling and acceleration investigated.

For those tests involving photography of the phenomenon ocurring on the heat transfer surface, two high speed motion pictures were obtained immediately following the potentiometer measurements. The first film strip was exposed at 2,000 frames/second; the second film strip was exposed at 1,000 frames/second. The film strips were processed immediately in a nearby darkroom while an assistant maintained the test conditions constant.

At the end of the 15 minute processing period, both film strips were examined for suitable image density and contrast in order to decide whether to repeat the photographic process or to change the test conditions. The framing rates chosen enabled a complete cycle of vapour bubble emission including active and inactive periods to be photographed on one or both of the film strips. Although it was not possible to determine whether or not this condition had been satisfied at the time that the film strips were processed, subsequent experience indicated that the two standard framing rates did satisfy this condition. Each of the film strips obtained was later analysed to determine the frequency of vapour bubble emission and the density of active nucleation sites for the particular combination of heat flux, subcooling and acceleration investigated.

CHAPTER V

DATA REDUCTION

The following sections describe the methods used in calculating the acceleration level, saturation temperature, heat flux, surface temperature, bubble frequency, site density and maximum bubble size relationships. In each of these sections, the uncertainty in the quantity calculated is computed from the uncertainty associated with each of the independent variables comprising it, using the procedure of Kline and McClintock.[39] The percentage uncertainty in R, a result obtained by combining a number of independent variables $V_1, V_2, V_3, \ldots V_n$ is given by

$$\frac{W_R}{R} = \left[\left(\frac{\partial R}{\partial V_1} \frac{W_1}{R} \right)^2 + \left(\frac{\partial R}{\partial V_2} \frac{W_2}{R} \right)^2 + \left(\frac{\partial R}{\partial V_3} \frac{W_3}{R} \right)^2 \cdots \left(\frac{\partial R}{\partial V_n} \frac{W_n}{R} \right)^2 \right]^{1/2} \quad (6)$$

where W_R is the uncertainty in the result R and $W_1, W_2, W_3, \ldots W_n$ is the uncertainty in each of the independent variables.

A. Acceleration At The Test Surface

The total acceleration level at the heat transfer surface was computed through the use of the relationships derived in Reference 28. In terms of the significant parameters which are illustrated schematically in Figure 18, the angle Θ was given by the transcendental equation

$$\Theta = \tan^{-1} \left[\omega^2 \left(\frac{B + C \sin \Theta}{g} \right) \right] \quad (7)$$

and the non dimensional acceleration a/g was given by the relationship

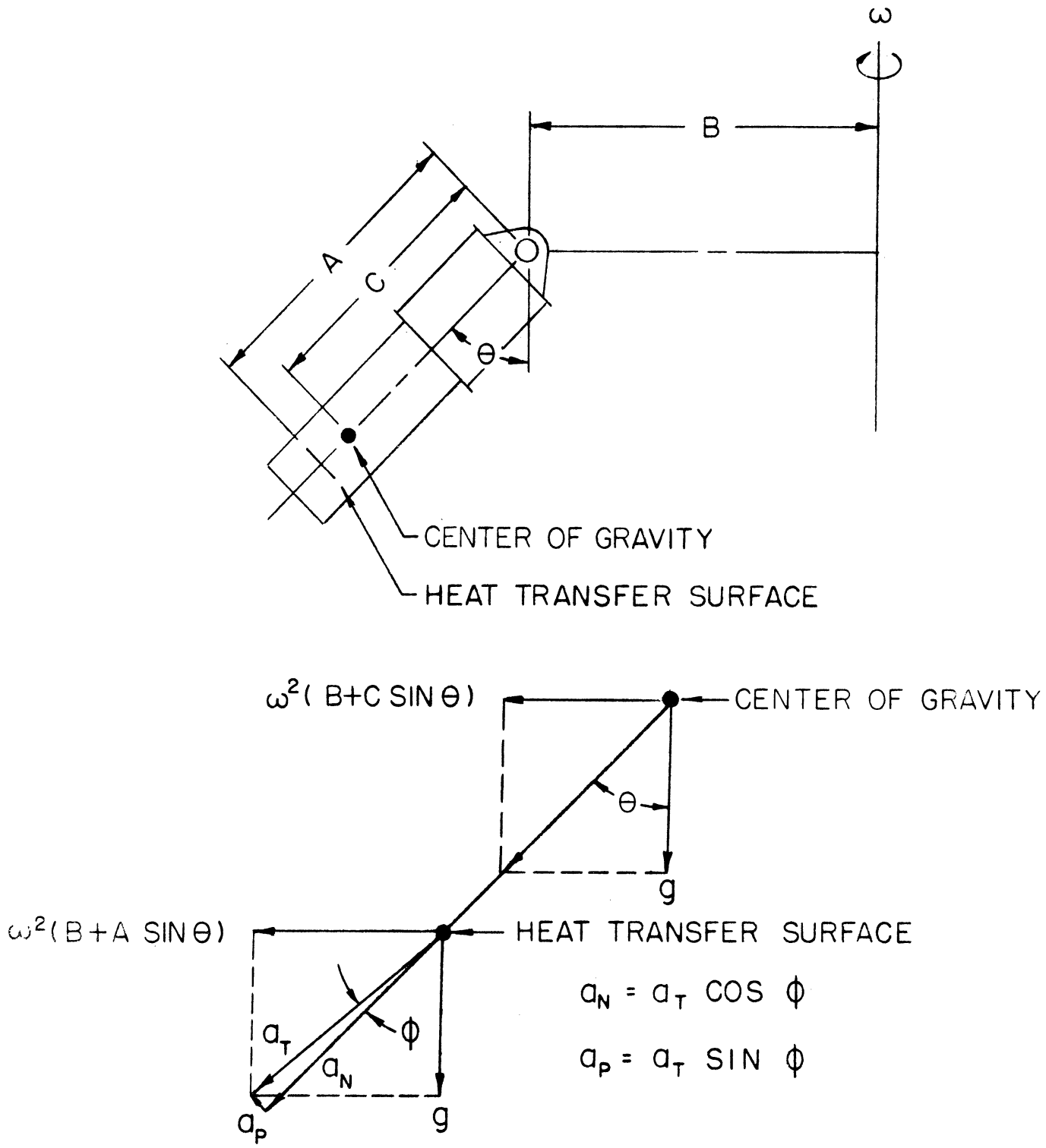

Figure 18. Schematic Representation Of Centrifuge For Acceleration Analysis.

$$a/g = \left[\frac{\omega^4}{g^2} (B + A \sin \Theta)^2 + 1 \right]^{1/2} \qquad (8)$$

In the present investigation, three different levels of angular velocity $\omega = 0$, 8.47 and 27.01 radians/second respectively were employed. Substituting the latter two values of angular velocity into Equations (7) and (8) in conjunction with the information tabulated below

$$A = 2.165 \pm 0.010 \text{ feet}$$

$$B = 2.250 \pm 0.005 \text{ feet}$$

$$C = 1.216 \pm 0.050 \text{ feet}$$

yields $\Theta = 1.452$ radians corresponding to $a/g = 10$ and $\Theta = 1.582$ radians correspoinding to $a/g = 100$. Equation (6) predicts the uncertainty in a/g to be $\pm 3.05\%$ and $\pm 1.00\%$ at $a/g = 10$ and 100 respectively.

The value of the angle ϕ corresponding to the most extreme combination of conditions was 0.019 radians. Consequently, the component of acceleration parallel to the heat transfer surface a_P was negligible and the component of acceleration normal to the heat transfer surface a_N represented the entire acceleration acting at the heat transfer surface for all purposes.

B. Saturation Temperature At The Test Surface

In as much as the saturation temperature of the liquid at the heat transfer surface could not be measured, it had to be deduced from the pressure existing at the heat transfer surface. This pressure was

determined by summing the hydrostatic pressure and the vapour space pressure in the package for the particular level of acceleration according to the relationship

$$P_T = (a/g)(g/g_c)\ \rho d + P_V \qquad (9)$$

The liquid in the test package under rotating conditions assumes the shape of a portion of a parabola of revolution. Consequently, the liquid depth varies across the heat transfer surface and this variation affects the calculation of P_T slightly since the effective depth under rotating conditions is not precisely that measured under non rotating conditions. However, a simple computation based upon the analysis of Reference 28 indicates that this variation is small at both $a/g = 10$ and $a/g = 100$, of the same order of magnitude as the uncertainty in measuring the liquid depth under non rotating conditions.

The uncertainty in the saturation temperature at the heat transfer surface as determined from the total pressure at the heat transfer surface will now be evaluated. The uncertainty in P_T is computed from the corresponding uncertainties in a/g, d and P_V. The uncertainty in a/g was analysed in Section A, Chapter V. The uncertainty in d varies with acceleration level, depending upon the uncertainty in the measurement of this parameter and the extent to which the vapour-liquid interface deviates from a plane surface under rotational conditions. The magnitude of this uncertainty was estimated to be 0.0016 feet, 0.0160 feet and 0.0046 feet at $a/g = 1$, 10 and 100 respectively. The vapour space pressure is the pressure measured by the pressure transducer,

corrected for the hydrostatic pressure of the gas-vapour mixture between the point at which the pressure was measured and the liquid-vapour interface and therefore the uncertainty in P_V is dependent upon the uncertainty in the pressure measurement and the uncertainty in the hydrostatic pressure correction. As outlined in Section G, Chapter II, the pressure transducer was standarized with a mercury manometer at least twice during each test series. Consequently, it was possible to correct for a small drift in the pressure transducer balance and the uncertainty in the pressure measurement is simply that associated with measuring the output of the pressure transducer, correcting the output for drift in the pressure transducer balance and converting the corrected output to pressure by means of the calibration curve. The magnitude of this uncertainty is approximately $\pm$ 0.10 pounds/in^2. An evaluation of the hydrostatic pressure correction by means of an analysis presented in Reference 28, indicates that the hydrostatic pressure correction is of the order of $0.003 \times (a/g)$ pounds/in^2. The maximum uncertainty in this correction is estimated to be no greater than 50% of the correction itself and the uncertainty in the vapour space pressure P_V is then approximately $\pm$ 0.10 pounds/in^2, $\pm$ 0.12 pounds/in^2 and $\pm$ 0.15 pounds/in^2 at $a/g = 1$, 10 and 100 respectively. The uncertainty at $a/g = 100$ is simply the uncertainty in the hydrostatic pressure correction itself, since the vapour space pressure was not measured at this acceleration level (the vapour space was vented to atmospheric pressure).

Applying Equation (6) to the analysis of the uncertainty in P_T as computed by Equation (9) yields

$$\frac{W_{P_T}}{P_T} = \left[\left(\frac{(g/g_c)\rho d}{P_T} W_{a/g} \right)^2 + \left(\frac{(a/g)(g/g_c)\rho}{P_T} W_d \right)^2 + \left(\frac{1}{P_T} W_{P_v} \right)^2 \right]^{1/2} \quad (10)$$

Table VIII below summarizes the analysis performed to determine the uncertainty in P_T .

TABLE VIII

ANALYSIS OF UNCERTAINTY IN PRESSURE MEASUREMENT

a/g	d	W_d	P_v	W_{P_v}	P_T	W_{P_T}
	feet	feet	$\frac{\text{pounds}}{\text{in}^2}$	$\frac{\text{pounds}}{\text{in}^2}$	$\frac{\text{pounds}}{\text{in}^2}$	$\frac{\text{pounds}}{\text{in}^2}$
1	0.125	$\pm$ 0.0016	7.92	$\pm$ 0.10	8.00	$\pm$ 0.10
10	0.125	$\pm$ 0.0160	7.20	$\pm$ 0.12	8.00	$\pm$ 0.14
100	0.125	$\pm$ 0.0046	0	$\pm$ 0.15	8.00	$\pm$ 0.20

From the calculations presented above, it can be seen that the maximum uncertainty in the total pressure at the heat transfer surface is of the order of $\pm$ 0.20 pounds/in^2. The corresponding uncertainty in the saturation temperature T_{SAT} as determined from the vapour pressure relationship presented in Figure 19 is approximately $\pm$ 0.50°F. The curve plotted from the data of Reference 36 was used in preference to the curve plotted from the data of Reference 40 since this curve was verified experimentally at atmospheric pressure.

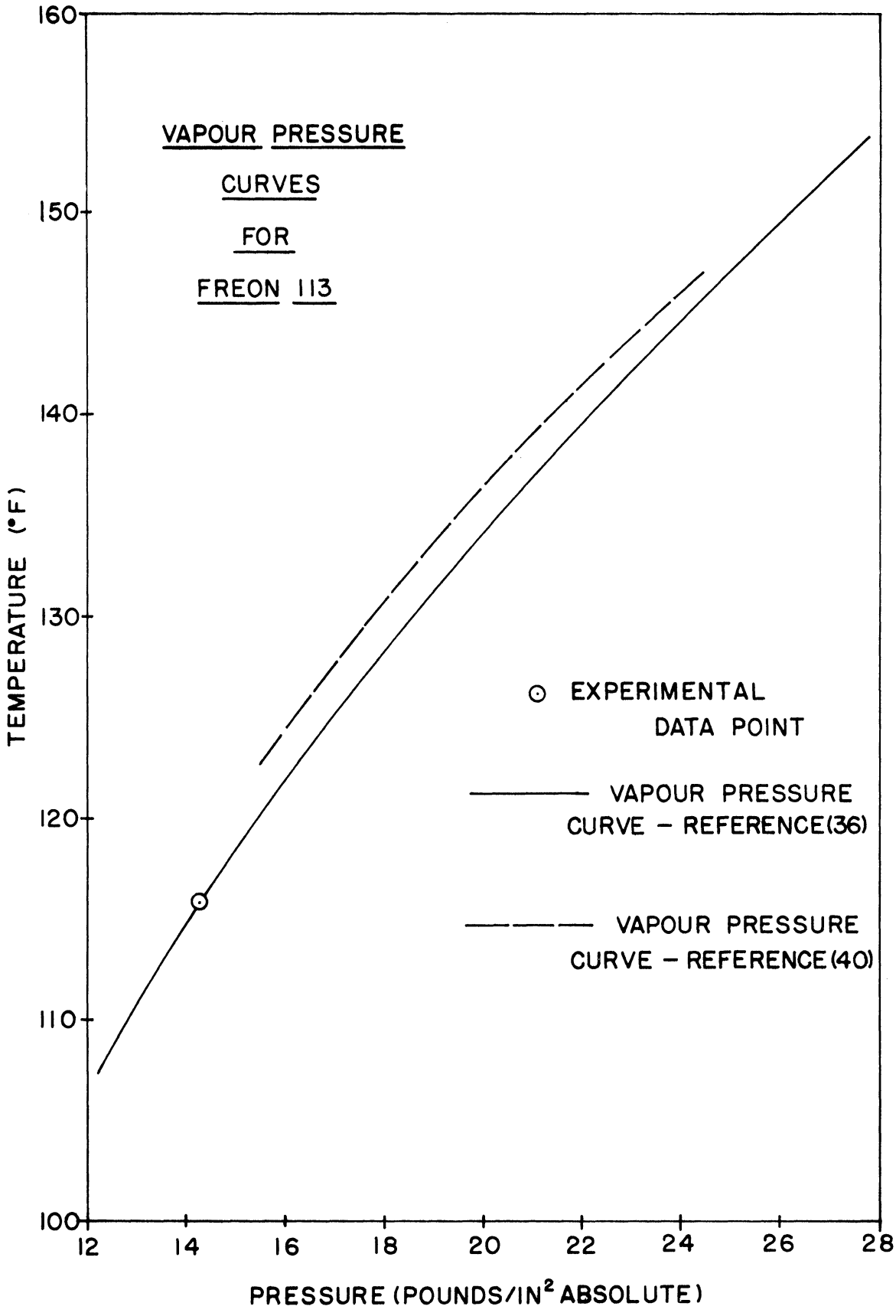

Figure 19. Vapour Pressure-Temperature Characteristics.

C. Heat Flux

The heat dissipated at the heat transfer surface was calculated from the total power dissipation in the oxide coating or metal foil, corrected for heat losses to the air space beneath the test specimen and the edges of the test specimen. The heat loss to the air space was computed by means of the correlation

$$Nu = 0.27(PrGr)^{1/4} \tag{11}$$

advanced by Fishenden and Saunders[41] for natural convection from a heated surface facing downward. A heat loss correction $Q_{Underside}$ resulted which was dependent upon the acceleration level and the difference in the temperature of the underside of the test specimen and the temperature of the air beneath the test specimen. The magnitude of this difference in temperature was observed to be of the order 45°F, for which the corresponding heat loss $Q_{Underside}$ was computed to be 0.4 BTU/hr, 0.8 BTU/hr and 1.4 BTU/hr at $a/g = 1$, 10 and 100 respectively.

The heat loss to the edges of the test specimen was computed by an analysis of the heat conducted through the rubber gasket separating the test specimen and cover plate which can be seen in Figure 20. An approximate analysis of the heat conduction phenomenon was necessitated by the fact that the temperature difference across the rubber gasket was unknown. One dimensional conduction was postulated and the boundary conditions were assumed to be T_W on the test specimen side and T_B on the cover plate side. The implications of this assumption are that the test specimen is isothermal and that the cover plate assumes the temperature

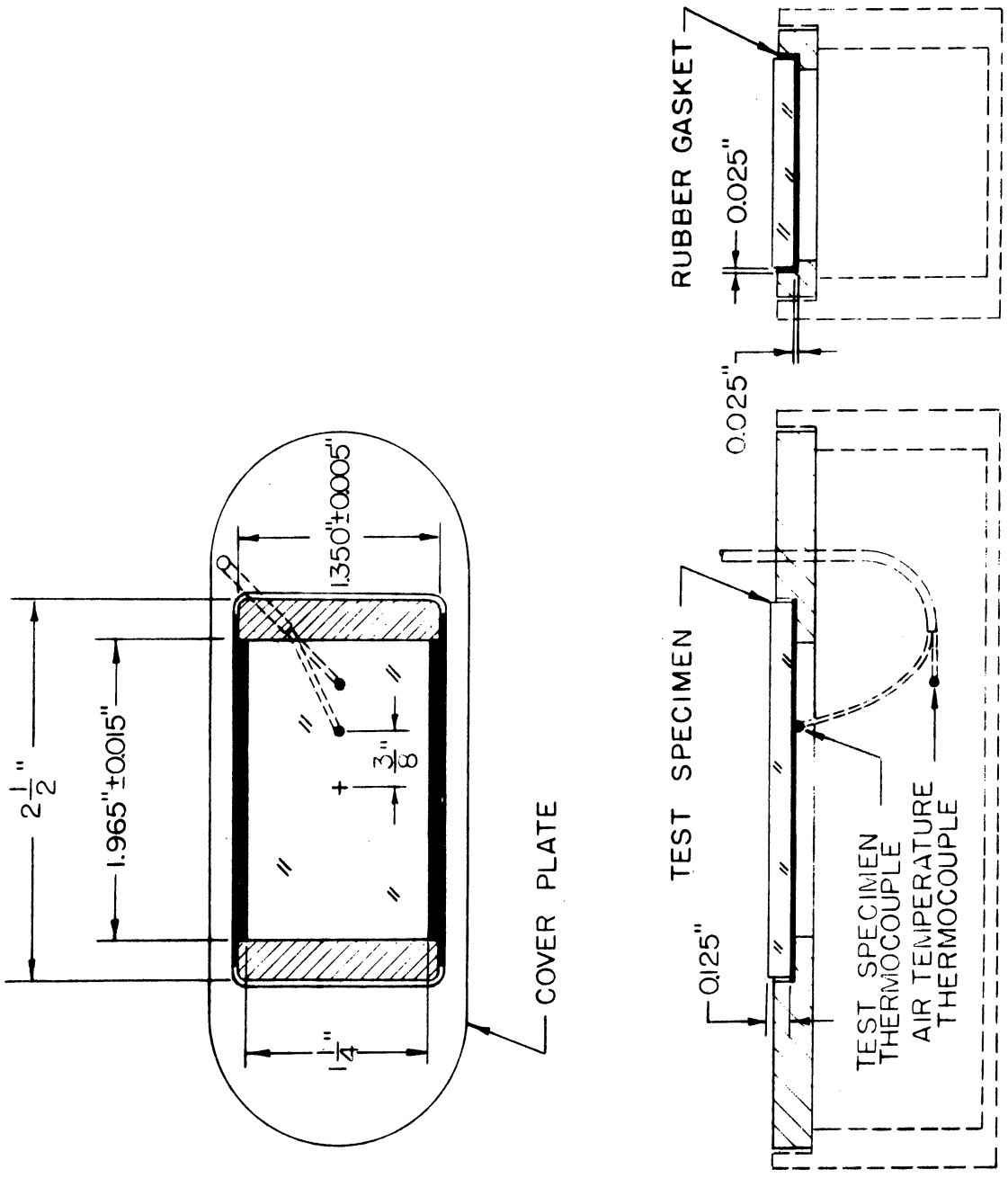

Figure 20. Scale Drawing Of Heat Transfer Surface.

of the fluid which contacts it. This assumption leads to a heat loss estimate somewhat greater than the actual heat loss.

The average temperature difference $T_W - T_B$ was observed to be of the order of 35°F. Using k_{Rubber} equivalent to 0.070 BTU/hr ft °F as the thermal conductivity of the rubber gasket, the heat loss to the ends of the test specimen was calculated to be 4.4 BTU/hr and the heat loss to the sides of the test specimen was calculated to be 4.2 BTU/hr, the former being greater than the latter as a result of the greater contact with the rubber gasket beneath the ends than along the sides as indicated in Figure 20. Accordingly, the heat loss to the edges of the test specimen Q_{Edges} was computed to be 8.6 BTU/hr.

Considering the heat loss from the test specimen Q_{Loss} to be comprised of the sum of $Q_{Underside}$ and Q_{Edges}, then the maximum correction amounted to 9.0 BTU/hr, 9.4 BTU/hr and 10.0 BTU/hr at a/g = 1, 10 and 100 respectively. The heat flux was calculated by dividing the heat dissipated at the heat transfer surface corrected for heat losses by the area of the heat transfer surface according to

$$Q/A = 3.414\ EI/A - Q_{Loss}/A \qquad (12)$$

The application of Equation (6) to the analysis of the uncertainty in Q/A as computed by Equation (12) indicates that the maximum uncertainty associated with low levels of heat flux and high levels of acceleration is of the order of $\pm$ 7.00%, assuming a $\pm$ 50% uncertainty in the heat loss correction. Under the most severe conditions, the heat loss correction Q_{Loss} approaches 13% of 3.414 EI of which the heat loss to the

underside $Q_{Underside}$ accounts for approximately 14% and the heat loss to the edges Q_{Edges} accounts for approximately 86%.

D. Surface And Bulk Liquid Temperature

The temperature of the heat transfer surface was calculated from the temperature at the underside of the test specimen, corrected for the temperature drop through the test specimen resulting from the conduction of heat from the heat transfer surface to the air space beneath the test specimen. The junction of the test specimen thermocouple was offset approximately 3/8 inch from the geometric center of the test specimen as indicated in Figure 20. Assuming the flow of heat to be one dimensional in the vicinity of the geometric center of the test specimen, in accordance with the results of the derivation in Appendix B, the correction

$$\Delta T' = 3.75 \times 10^{-3} (\Delta T)^{5/4} (a/g)^{1/4} \qquad (13)$$

was derived by combining the expression for the heat loss to the air space beneath the test specimen $Q_{Underside}$ with the Fourier conduction equation in which k_{Glass} equivalent to 0.56 BTU/hr ft°F was used as the thermal conductivity of the test specimen. The temperature difference ΔT used in this expression is the difference between the temperature measured at the underside of the test specimen and the temperature measured in the air space beneath the test specimen. The values of the temperature correction ranged from 0.40°F to 0.69°F at $a/g = 1$, 0.77°F to 1.34°F at $a/g = 10$ and 1.50°F to 2.19°F at $a/g = 100$.

The surface temperature was then computed by the relationship

$$T_W = T_{Test\ Specimen} + \Delta T' \qquad (14)$$

for which Equation (6) indicates the maximum uncertainty in T_W as computed by Equation (14) to be approximately $\pm$ 0.30°F. Consequently, the maximum uncertainty in the heater surface superheat computed by subtracting T_{SAT} from T_W is $\pm$ 0.80°F.

The bulk liquid temperature T_B was measured by the reference fluid thermocouple located within the crossbar to the thermocouple probe placed 0.400 inches from the heat transfer surface. The metal crossbar served to average the temperature variations in the fluid so that the temperature measurement was relatively free of fluctuation. The uncertainty in T_B is approximately $\pm$ 0.20°F corresponding to the uncertainty in measuring the thermocouple output and correcting the output by means of the correction curve discussed in Section D, Chapter II. Consequently, the maximum uncertainty in the subcooling, computed by subtracting T_B from T_{SAT} is $\pm$ 0.70°F.

In accordance with the discussion of Chapter III, the subcooling computed by subtracting the bulk liquid temperature from the saturation temperature at the heat transfer surface is independent of acceleration level since the saturation temperature at the heat transfer surface was maintained constant at all levels of acceleration as explained in Section H, Chapter II. The position at which the bulk liquid temperature was measured was chosen arbitrarily. However, temperature profiles obtained during the present investigation, such as those presented in Section C, Chapter VI, indicate that bulk liquid temperature is relatively insensitive to displacement from the heat transfer surface outside of the thermal boundary layer. Consequently, this particular method for computing subcooling is a reasonable means of relating bulk liquid temperature and saturation temperature.

E. Temperature Scan

The temperature distribution in the liquid in the vicinity of the heat transfer surface was measured by means of a remotely controlled traversing thermocouple and recorded as described earlier. Figure 21 presents a sample of the recording obtained. The average of the thermocouple output recorded during the interval in which the thermocouple was held stationary was obtained by inspection of the temperature recording. Rapid temperature fluctuations were observed which were believed to be the result of the somewhat random "pumping action" of the boiling process. Therefore, the measurements of liquid temperature in the vicinity of the heat transfer surface presented in Chapter VI correspond to the mean temperature level observed at each location.

In order for the traversing thermocouple to be able to measure temperature variation in the presence of a severe temperature gradient, it was essential that the thermocouple junction be capable of measuring extremely localized temperatures. This requirement was satisfied by the use of a microthermocouple with an extremely small thermocouple junction nearly spherical in shape which has already been described in Section E, Chapter II. Because of the small size and mass associated with the thermocouple junction, the microthermocouple was capable of responding to rapid fluctuations in temperature as illustrated in Figure 21.

The flow of heat along the wires connecting the thermocouple junction to the supports affected the temperature measured to a certain extent. Although the wires were small and were placed parallel to the heat transfer surface in a supposedly isothermal field, the supports

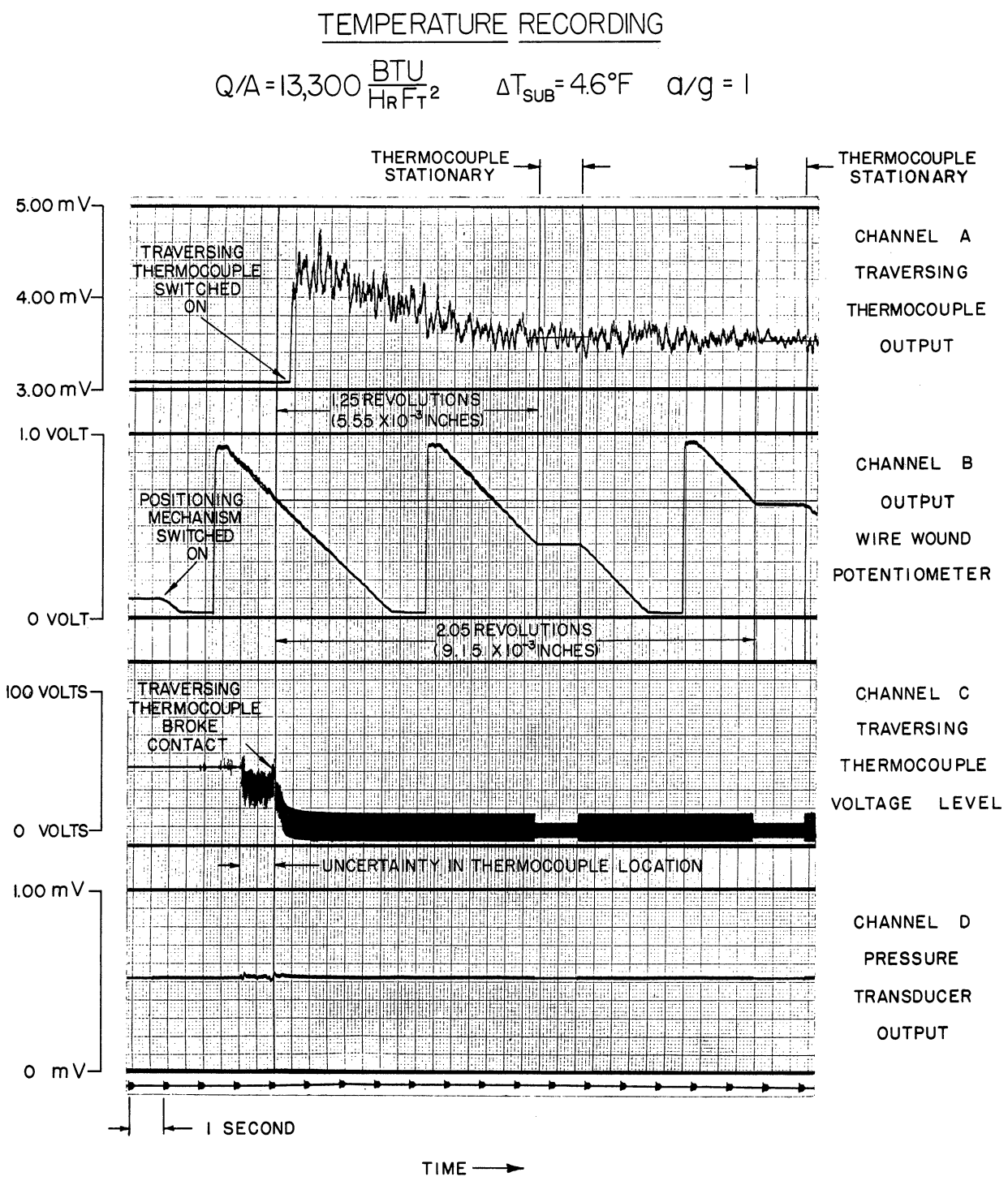

Figure 21. Representative Temperature Recording.

at either end acted as a finite sink and therefore facilitated the flow of heat away from the thermocouple junction. An estimation of the steady error in temperature measurement was made by means of a fin analysis. The results of this analysis indicated that the support wires were sufficiently long and slender (L/D = 60) that the temperature of the thermocouple junction was essentially unaffected by the presence of the supports. The maximum error was estimated to be of the order of 10^{-4}°F.

The response of the traversing thermocouple was assessed by analysing the response characteristics of a small sphere representing the thermocouple junction. Jakob[4] indicates that the average heat transfer coefficient at a boiling surface is of the order of 1,000 BTU/hr ft^2°F. Assuming the heat transfer coefficient at the surface of the thermocouple junction to be one tenth of this magnitude, the value of the time constant $\rho CV/hA$ was computed to be 80 milliseconds. In as much as the Sanborn recorder had a 5 milliseconds response time, the recorder was capable of following the thermocouple output. Figure 21 indicates that the period of the individual temperature fluctuations is of the order of 200 milliseconds, so that the thermocouple junction apparently responded to fluctuations in fluid temperature up to 5 cycles/second. On the basis of this analysis, it can be concluded that the fluctuations in the recorded thermocouple output represent the temperature fluctuations at the thermocouple junction in a relative manner at least.

The greatest uncertainty in the temperature measurement was the uncertainty associated with reading the temperature recording; all other uncertainties connected with this measurement were insignificant in comparison. In as much as it was common for the thermocouple output

to vary as much as 1.5 millivolts during a boundary layer traverse, it was necessary to set the recording span at 2.0 millivolts. The chart paper was 5 centimeters in width subdivided into 50 increments and therefore 1 millimeter, the smallest chart division, corresponded to 40 microvolts. Thus the uncertainty in reading the temperature recording was of the order of $\pm$ 40 microvolts which corresponds to $\pm$ 1.0°F approximately.

Figure 21 illustrates the procedure by which the position of the traversing thermocouple relative to the heat transfer surface was determined, as described in Section F, Chapter II. The greatest uncertainty in determining the position of the traversing thermocouple was that associated with determining the position of the wire wound potentiometer at the instant when the traversing thermocouple broke contact with the heat transfer surface, although the uncertainty in reading the output of the wire wound potentiometer was also significant. As can be seen in Figure 21, the voltage level of the traversing thermocouple did not change abruptly, but tended to fluctuate. This effect was believed to be the result of the extreme agitation in the fluid adjacent to the heat transfer surface tending to force the traversing thermocouple to break contact prematurely. The position of the fine wire thermocouple was estimated to be uncertain by approximately one fifth revolution of the wire wound potentiometer, corresponding to $\pm$ 1.0 x 10^{-3} inches approximately.

F. Site Density

The active site density and average population density were determined from photographic enlargements of select frames on the film strips of the nucleate boiling phenomenon. Every sixth frame from

a portion of each film strip chosen arbitrarily was printed for a total of five prints spanning twenty five consecutive frames. In this way, only a fraction of the available data was examined, raising the question of the representativeness of the sample selected. Several film strips were analysed in detail to examine this question and the results of this analysis, which are presented in Appendix C, indicated that the active site density and average population density could be determined accurately from a sample selected in the manner indicated.

Since the depth of view of the optical system was of the order of 0.030 inches, according to a simple experiment performed to investigate this parameter, only bubbles in proximity to the heat transfer surface were visible and only those bubbles attached to the heat transfer were seen in sharp focus. It was therefore possible to distinguish bubbles attached to the heat transfer surface from those detached. The possibility of mistaking a detached bubble for an attached one, and thereby mistakenly identifying a nucleation site was small.

In the determination of active site density, each point at which bubbles were seen to be attached to the heat transfer surface was identified as a nucleation site. The possibility of a bubble moving sidewise while remaining attached to the heat transfer surface and therefore being counted twice was ignored. However, observation of a number of film strips projected in slow motion failed to identify a bubble which behaved in this fashion.

At least two of the three wires seen in Figure 6 spaced 1/8 inches apart were always visible in the field of view. The boundaries

of the area between the wires, seen in the photographs in Appendix E, represented between 1/2 and 2/3 of the field of view. The active nucleation sites within the specified area on each of the prints were identified and then transferred to the first print, using reference points established by the intersection of the image of the wires with the image of the shadow of the thermocouple probe crossbar as locators. In many instances, previously observed sites were duplicated. However, a diminishing number of additional sites, corresponding to nucleation sites which had been inactive in the first print were added by each successive print. The active site density was based upon a count of the total sites superimposed on the first print.

The average population density, determined by averaging the count of the bubbles attached to the heat transfer surface in each of the five prints, corresponds to the average number of sites which were active at any particular instant of time.

G. Bubble Frequency

The period of time between cycles of vapour bubble emission was determined by a detailed examination of the film strips projected on a screen. The events occurring at ten different nucleation sites chosen at random on the heat transfer surface were observed. The limitation in the sample was dictated by necessity since in many of the film strips it was impossible to distinguish more than ten sites which passed through a complete cycle of bubble emission without becoming obscured. Once again, this procedure raised the question of representativeness of the sample selected. The results of an analysis performed

to answer this question which are presented in Appendix C, indicate that the period of bubble emission based upon the events occurring at ten different nucleation sites reasonably represents the period of bubble emission, at least for those test conditions where sufficient unobscured sites were available to perform the analysis.

The growth of a single vapour bubble at each site was followed frame by frame in order to determine the interval of time which elapsed from the frame at which the bubble was initiated to the frame at which the bubble departed or collapsed. This interval of time has been designated as the "active period" and corresponds to the interval of time during which a vapour bubble was present at the nucleation site, irregardless of whether the vapour bubble eventually departed or collapsed. Frame by frame observation of the nucleation site was then continued in order to determine the interval of time which elapsed from the frame at which the vapour bubble departed or collapsed to the frame at which another vapour bubble was initiated at the same nucleation site. This interval of time has been designated as the "inactive period" and corresponds to the interval of time during which the nucleation site was devoid of a vapour bubble. In the great majority of cases, only one complete cycle of vapour bubble emission could be seen at a particular site within the total number of frames on the film strip and consequently it was not possible to determine the variation in bubble period at a particular site. The active period and inactive period were summed to obtain the period of time between cycles of bubble emission. The frequency of vapour bubble emission was obtained from the reciprocal of this quantity.

The fate of a vapour bubble could always be discerned from the photographic data. Those vapour bubbles which departed from the heat transfer surface could be seen to detach themselves and move across the heat transfer surface before eventually disappearing from view. Those vapour bubbles which collapsed in proximity to the heat transfer surface could be seen to disappear without moving from the nucleation site. The vapour bubbles which grew and collapsed were generally considerably smaller than the vapour bubbles which grew and departed. Both types of vapour bubble were seen in varying proportions under the same conditions of heat flux, subcooling and acceleration. The proportion of collapsing bubbles in the ten bubble sample is presented in Table XIV, Appendix D for the various parameters.

Figure 22 illustrates the random nature of the nucleate boiling phenomenon by presenting the distribution of vapour bubble period for three test conditions at $a/g = 1$, 10 and 100 having the same nominal value of heat flux and subcooling. The relatively small scatter in the measured values within a test is typical of all the combinations of heat flux, subcooling and acceleration investigated. The numerical values presented in Chapter VI represent the mean values of these distributions.

H. Maximum Bubble Size

The maximum diameter attained by the vapour bubbles while attached to the heat transfer surface was determined from the same photographic enlargements used to determine active site density and average population density. In these enlargements the field of view was magnified eight times. The diameter of the images of the vapour bubbles attached to the heat transfer surface which appeared

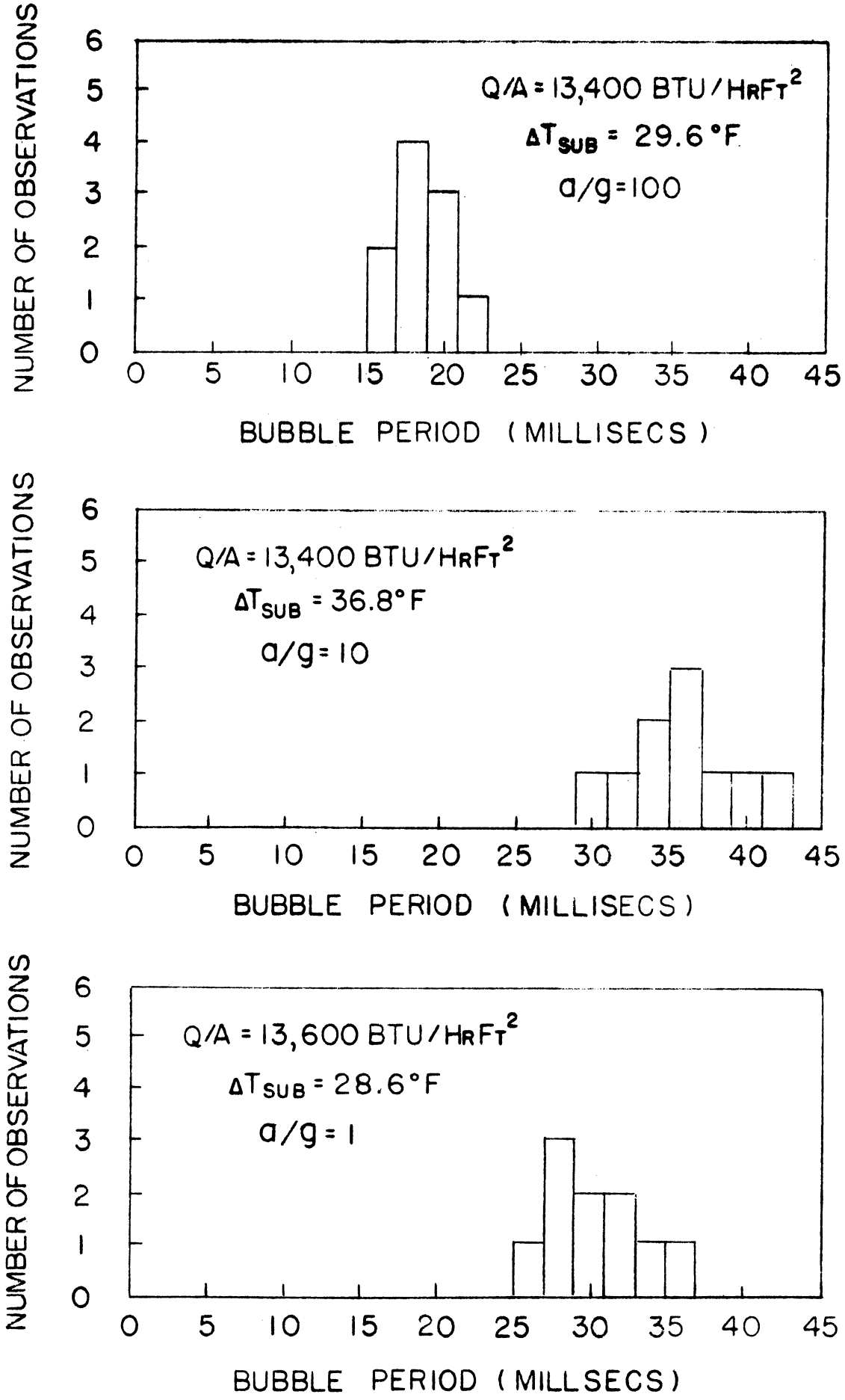

Figure 22. Statistical Distribution Of Photographic Results.

to have reached maximum size was measured in two mutually perpendicular directions by means of a scale graduated in hundredths of inches used in conjunction with a magnifying glass. The average value of these two measurements was taken to be the maximum bubble size.

Many uncertainties are associated with this particular measurement. Without being able to view the bubbles across the heat transfer surface, it was impossible to say with certainty whether or not a bubble had attained its maximum size. As employed here, the maximum bubble size is the diameter of the image projected in the plane of the heat transfer surface. Furthermore it was impossible to know whether or not the maximum size had been attained in the interval of time separating two consecutive frames and had therefore not been detected. Bubble size ranged between 0.005 inches and 0.020 inches and even with the enlargements, large uncertainty was introduced by the insensitivity of the measuring technique. Despite these uncertainties, it is believed that the measurements of maximum bubble size provided relative indications of the influence of the parameters concerned. Information concerning the influence of subcooling is almost totally lacking in the literature.

CHAPTER VI

RESULTS

In this section, the results obtained are presented with little or no comment. Discussion and interpretation of the results will be given in the following section. The experimental results are categorized under the headings General, Heat Transfer Results, Temperature Scan Results, Site Density Results and Bubble Frequency Results. The data is presented in a series of graphs showing the influence of heat flux, subcooling and acceleration upon each of the quantities measured. The numerical values plotted are tabulated in Appendix D. A sample of the photographic data obtained is presented in Appendix E.

A. General

The results of a series of tests performed at the beginning of the research investigation to determine a characteristic boiling curve for Freon boiling on the oxide coated glass heater surface are presented in Figure 23. These results, which were obtained for various levels of heat flux under saturated boiling conditions at $a/g = 1$ are presented as a plot of heat flux versus superheat, the classical manner in which saturated boiling heat transfer results are plotted.

During the series of tests represented by Figure 23, the heat flux was alternately increased and decreased as indicated by the arrowheads on the curves in the plot. A trend for the curves to shift toward higher values of superheat was detected and this trend was initially attributed to surface aging. The final curve obtained was

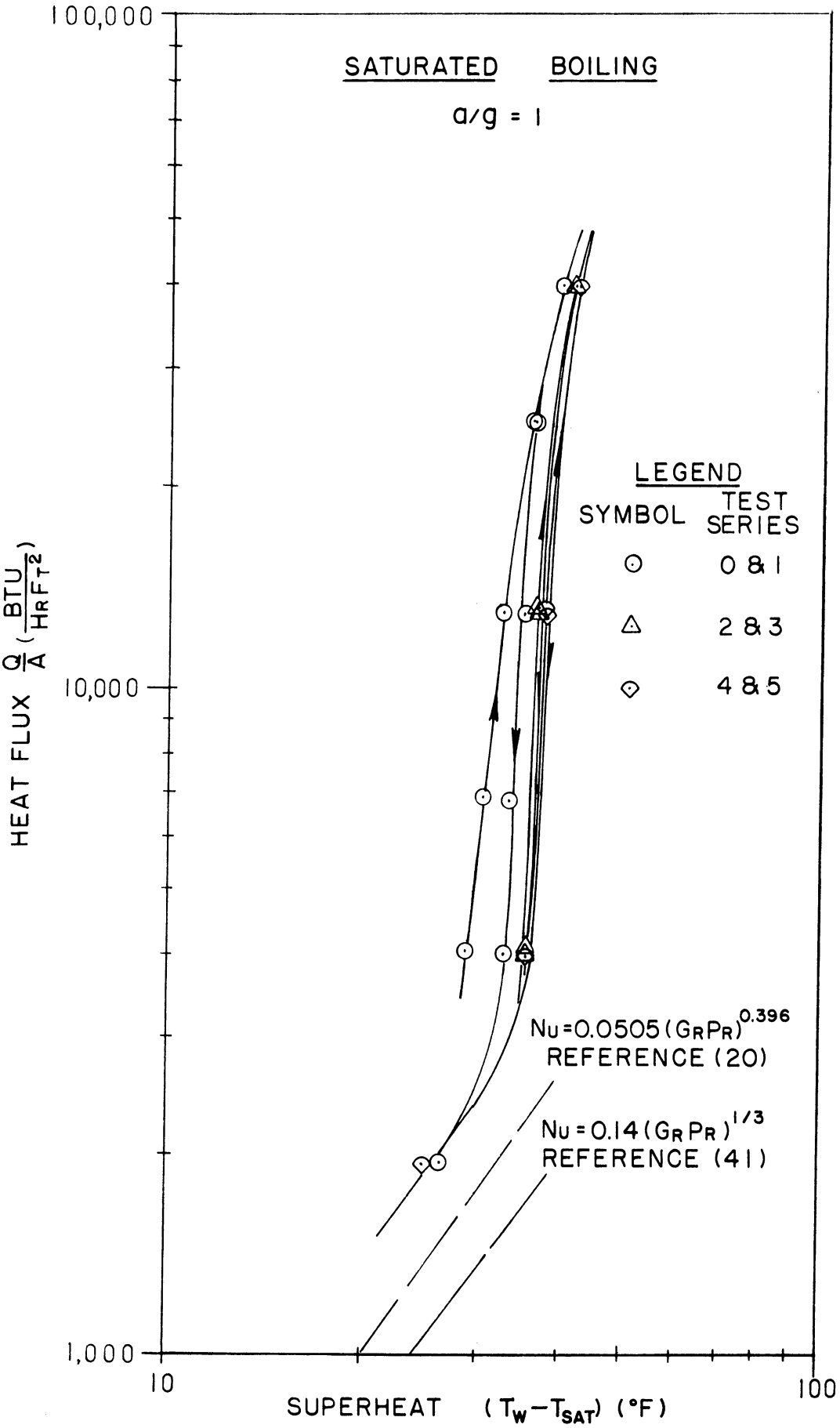

Figure 23. Saturated Boiling Heat Transfer Results.

assumed to be the characteristic boiling curve corresponding to the fully aged condition in as much as the data was reproducible at this time. Figure 23 also shows the transition from natural convection to nucleate boiling as well as to two correlations predicting natural convection heat transfer from the upper surface of a horizontal plate advanced by Merte[20] and Fishenden and Saunders[41] respectively. The data points representing the natural convection heat transfer results lie approximately 25% above the former and approximately 70% above the latter.

Figure 24 presents a plot of the reference test results obtained during the temperature study as described in Chapter IV. For the first four test series, it is apparent that the reference test results correlate well with Characteristic Curve #1 which was supposed to have been the characteristic boiling curve corresponding to the fully aged condition. For the remainder of the test series represented on this diagram, the reference test results shifted to lower values of superheat, clustering about Characteristic Curve #2. This behaviour was completely unexpected and could not be correlated with any intentional change in the test conditions.

Figure 25 presents a plot of the reference test results obtained during the photographic study as described in Chapter IV. All of the test series represented correlate reasonably well with Characteristic Curve #2. The fact that the reference test results reproduced within 1°F between the first and last test of each test series gave some assurance that the apparatus was performing in a reproducible fashion, even though individual reference test results deviated from Characteristic Curve #2 by as much as 6.5°F.

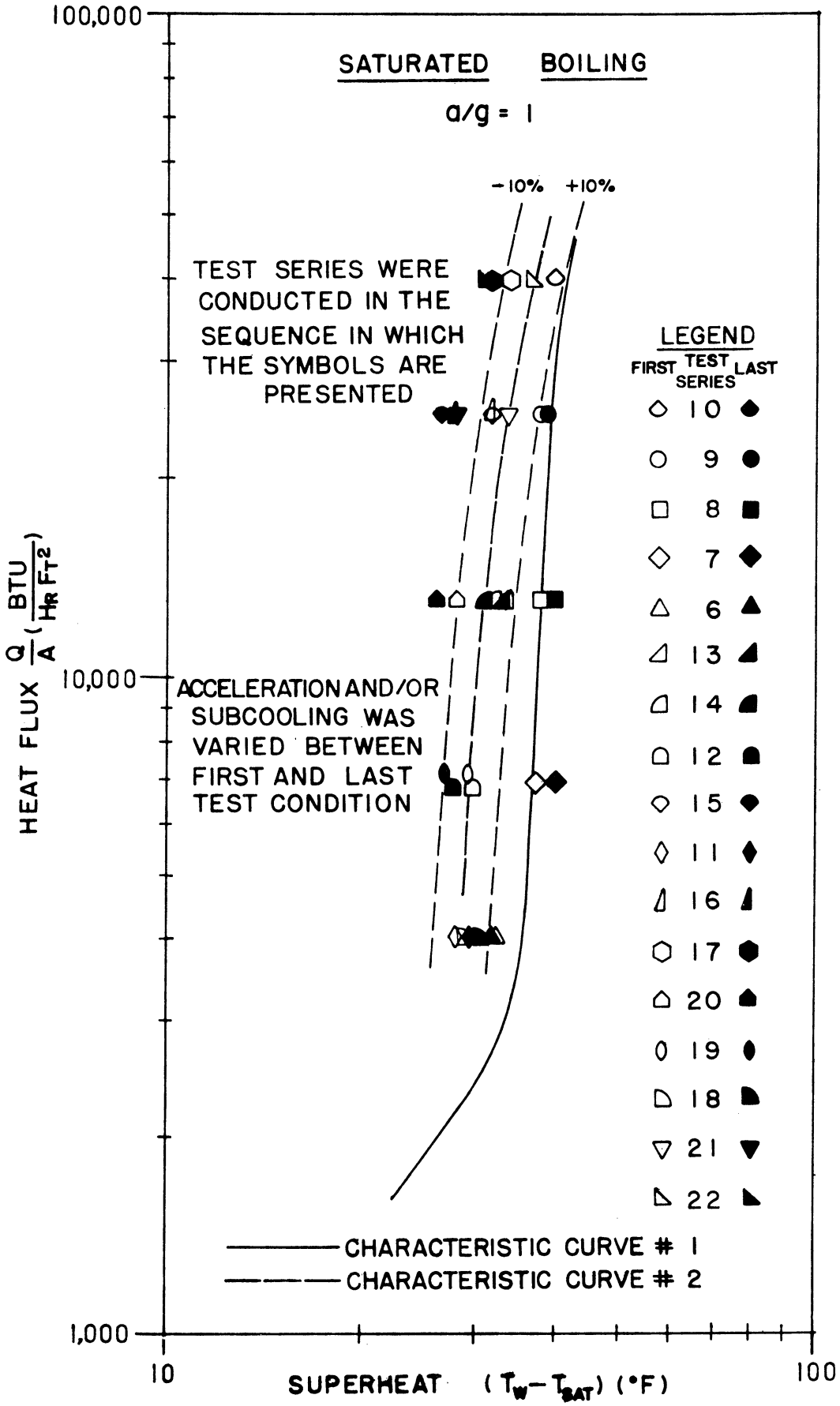

Figure 24. Reference Test Results For Temperature Study.

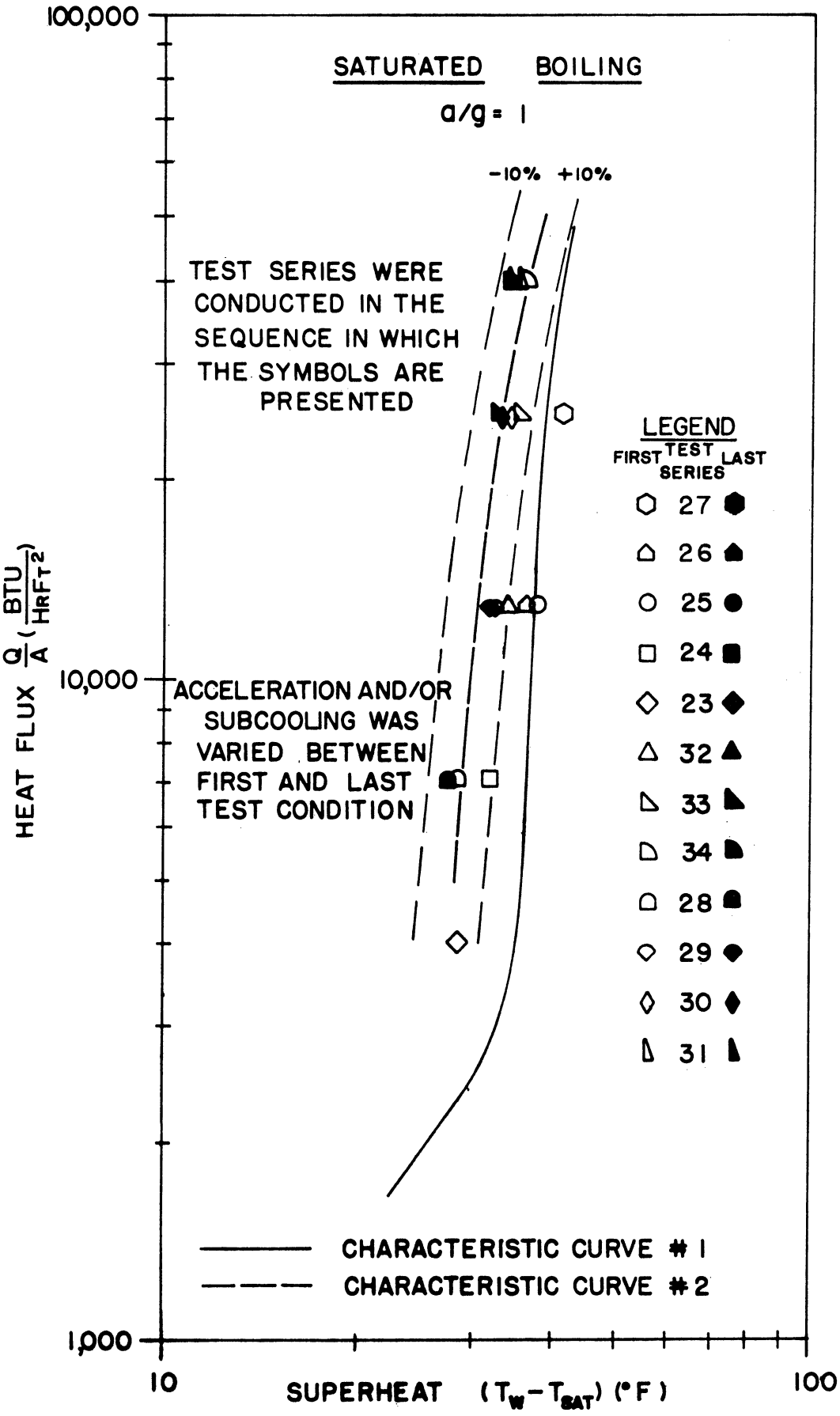

Figure 25. Reference Test Results For Photographic Study.

Figure 26 presents a comparison of the results of a series of tests performed at the conclusion of the research investigation to compare the characteristic boiling curves for Freon boiling on an oxide coated glass heater surface and on a metal foil heater surface. In both cases, the heat flux was first increased and then decreased. The results from the oxide coated glass heater surface reproduced perfectly and correlated exceedingly well with Characteristic Curve #2. The results from the metal foil heater surface varied in the manner indicated by the arrowheads on the curves, showing a hysterisis effect frequently observed. Such an effect is also indicated by the results of References 42 and 43. The lack of hysterisis with the oxide coated glass suggests that this heater surface differs from the metal foil heater surface with respect to the number and size of the cavities and/or the ability of the cavities to retain vapour and to remain active.

B. Heat Transfer Results

The heat transfer results are presented in the form of plots of superheat versus subcooling with levels of heat flux and acceleration as parameters, since this parametric form clearly shows the effect of heat flux, subcooling and acceleration upon the superheat. Figures 27 to 29 depict all of the heat transfer results obtained at $a/g = 1$, 10 and 100 with the oxide coated glass heater surface. The variation in superheat with heat flux, subcooling and acceleration is indicative of the manner in which these parameters influence the heat transfer phenomenon.

Figures 27 to 29 include the reference test results obtained under saturated boiling conditions at $a/g = 1$. These results have been

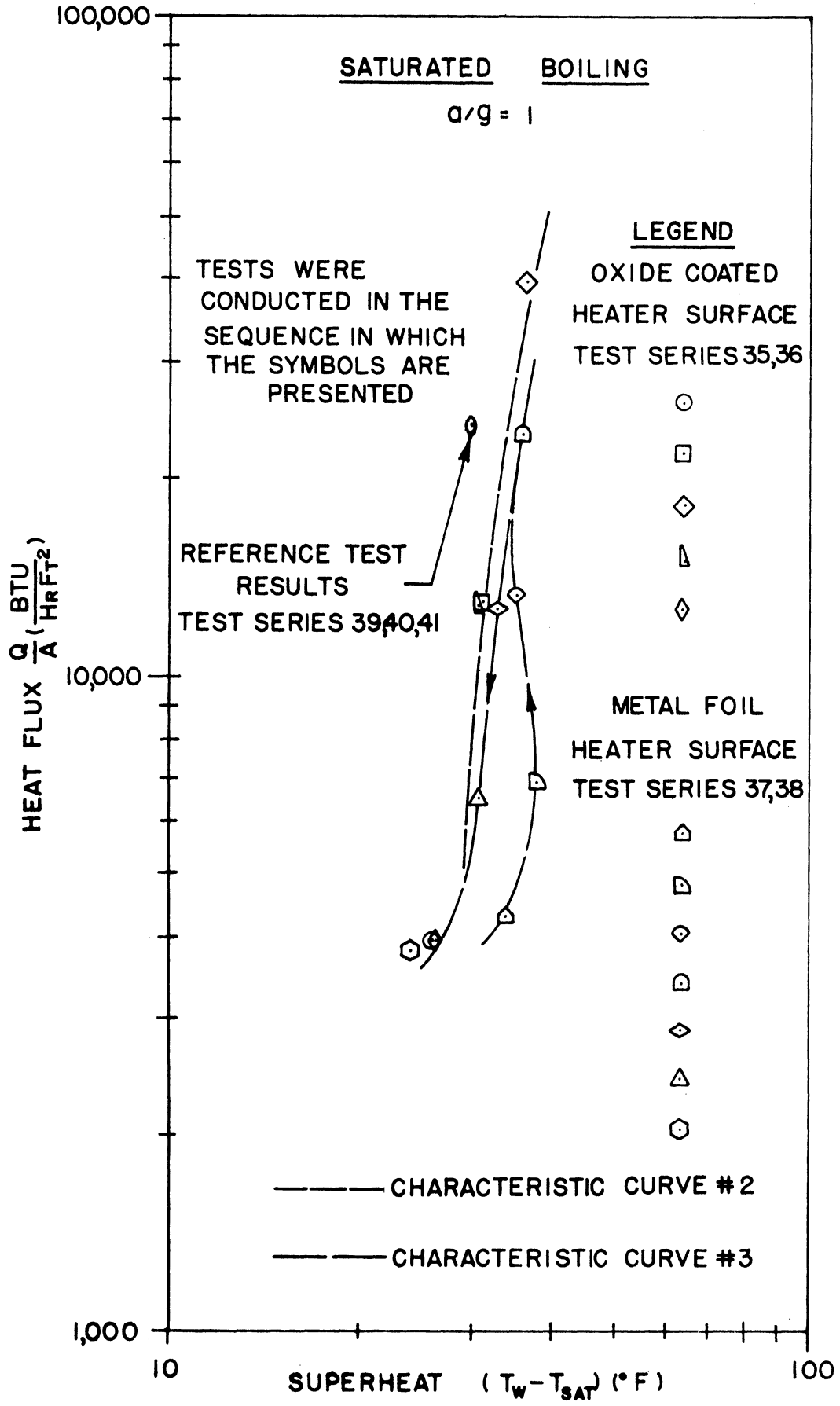

Figure 26. Comparison Of Saturated Boiling Heat Transfer Results.

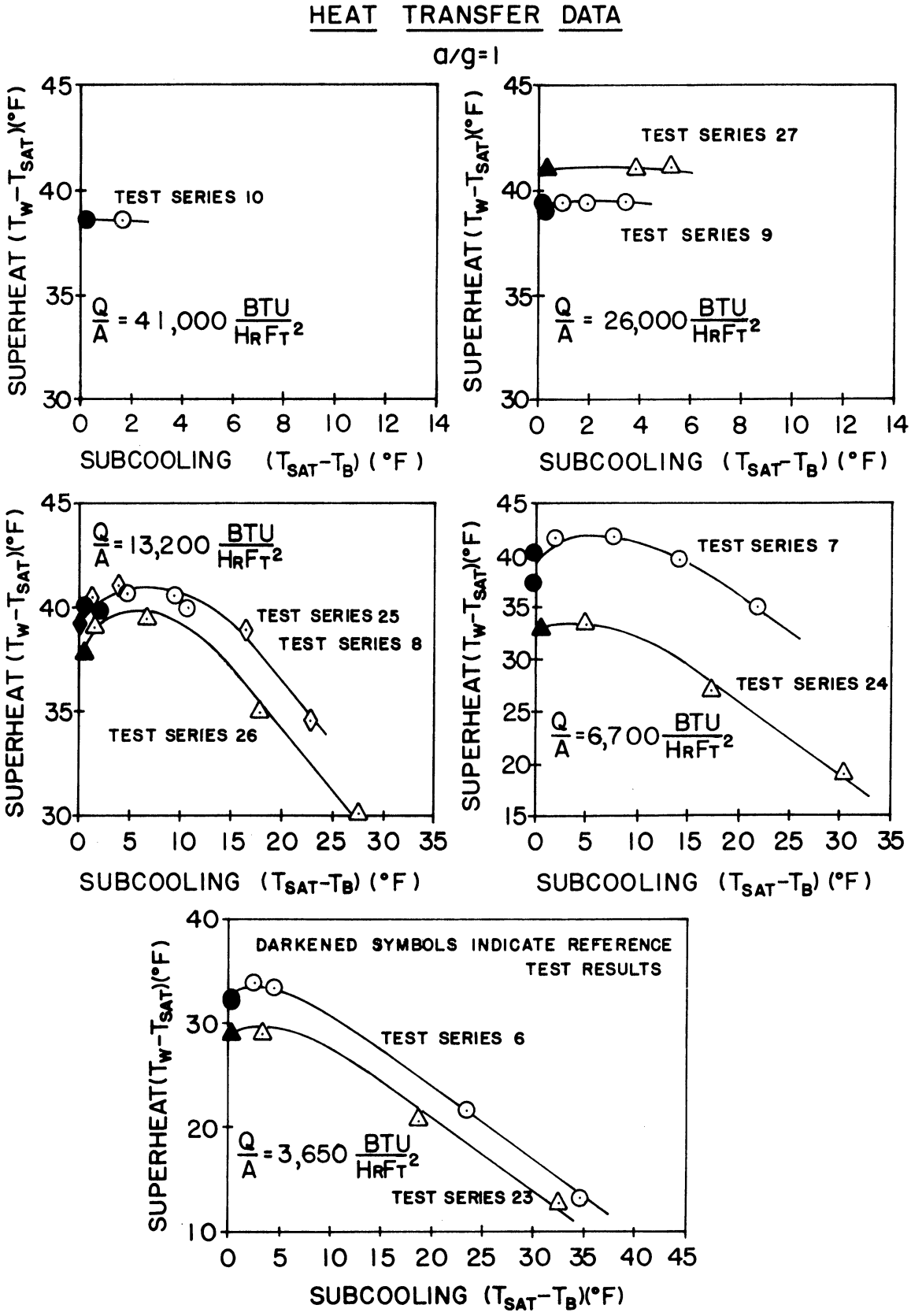

Figure 27. Heat Transfer Results At a/g = 1.

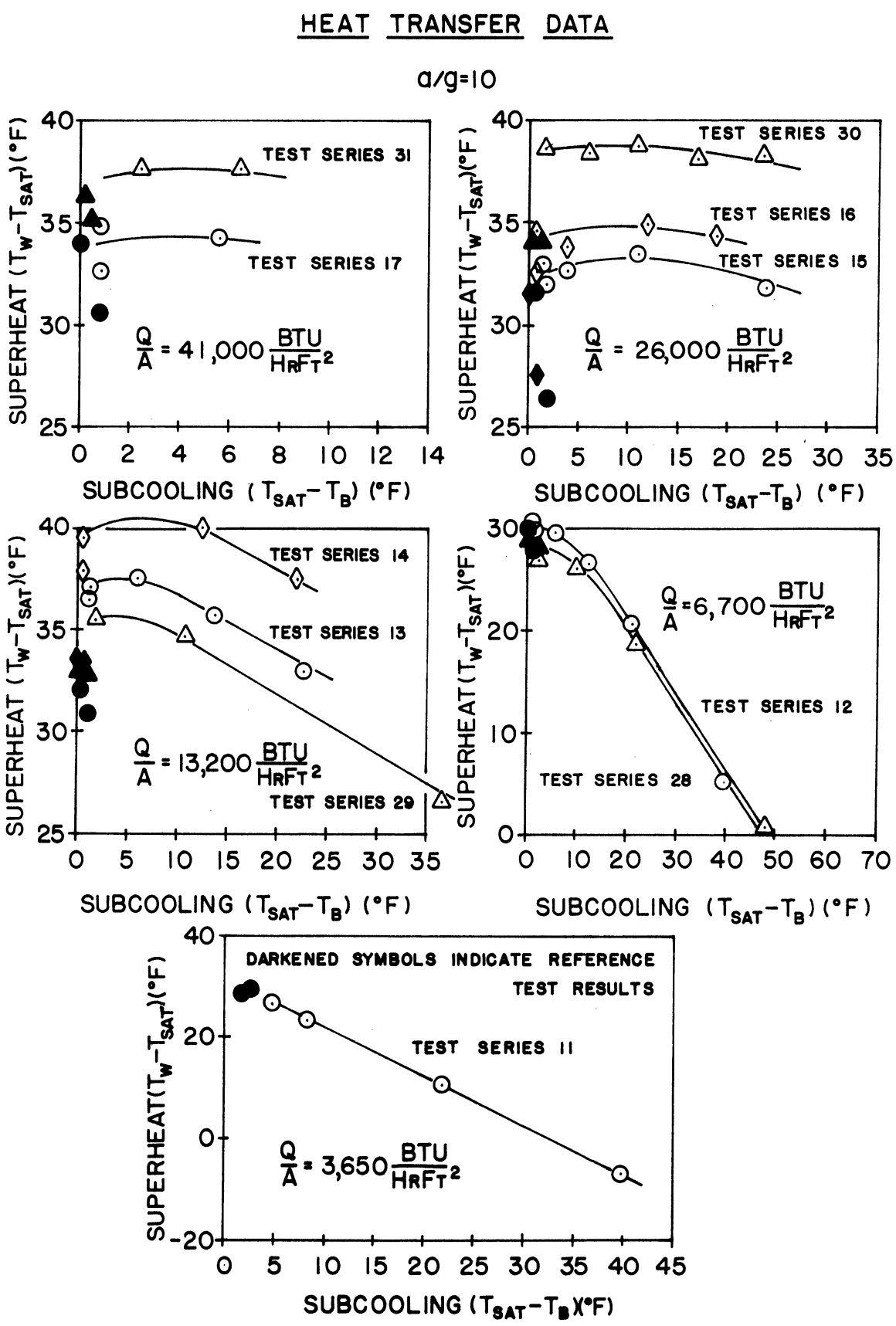

Figure 28. Heat Transfer Results At a/g = 10.

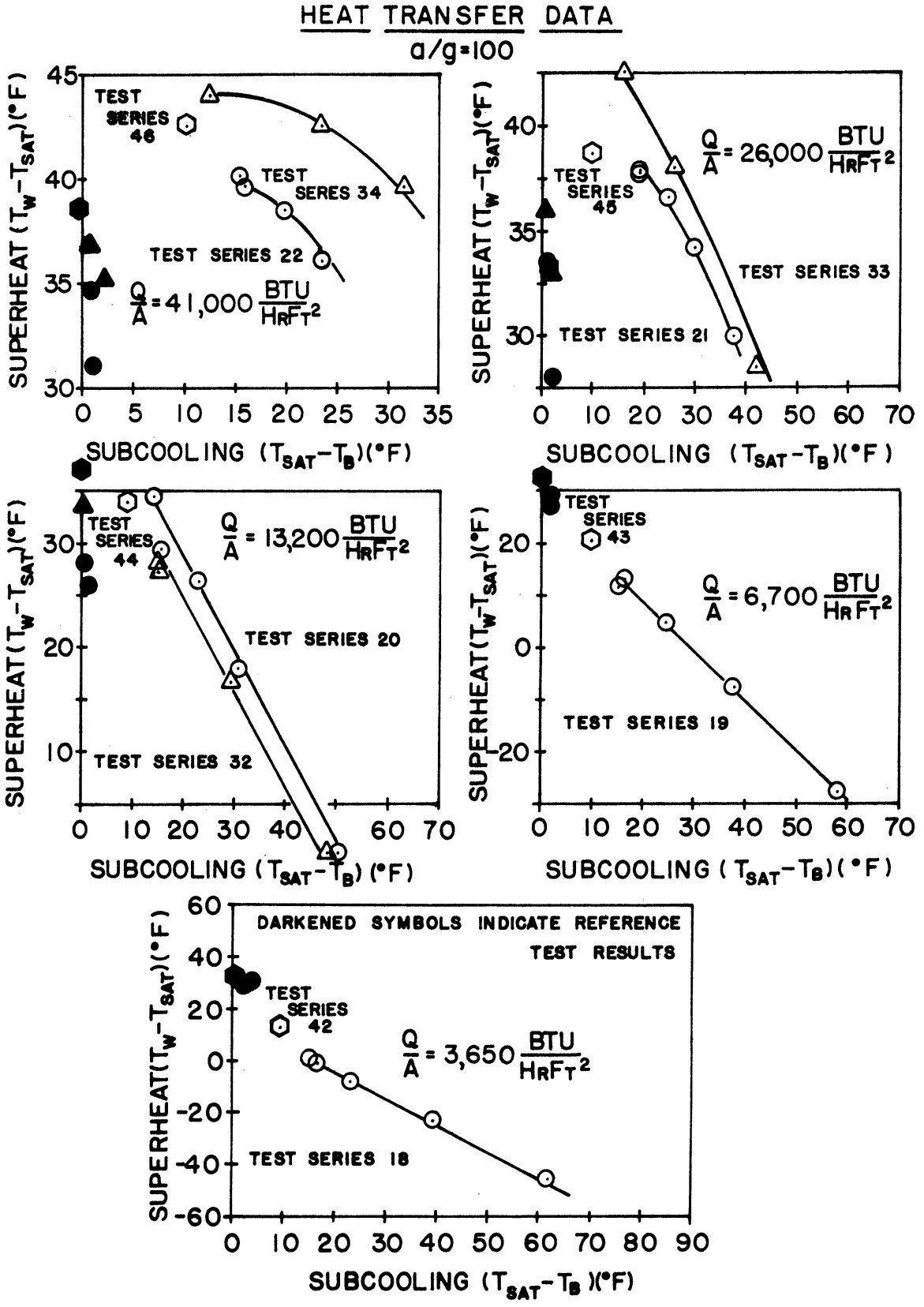

Figure 29. Heat Transfer Results At a/g = 100.

represented by darkened symbols. The discrepancy between the heat transfer results obtained under test conditions which were ostensibly identical is apparent in these graphs. In general, the curves presented appear to have been shifted in the ordinate direction in as much as the difference between any two curves remains constant, independent of subcooling. The maximum discrepancy is of the order of 20%. Also, it is significant that for the results obtained at $a/g = 10$ and $a/g = 100$, the shift in the curves correlates roughly with the shift in the corresponding reference test results. This observation suggests that the phenomenon responsible for the variable behaviour is independent of acceleration level as well. The manner in which these results were treated in order to determine the influence of heat flux, subcooling and acceleration upon the heat transfer results is discussed in Chapter VI.

Figure 30 depicts the more limited heat transfer results obtained at $a/g = 1$, 10 and 100 with the metal foil heater surface. In a similar manner, the results are represented in the form of a plot of superheat versus subcooling for a single heat flux level $Q/A = 26{,}000$ BTU/hr ft^2 . The plot includes the reference test results obtained under saturated boiling conditions at $a/g = 1$ represented by darkened symbols as indicated above.

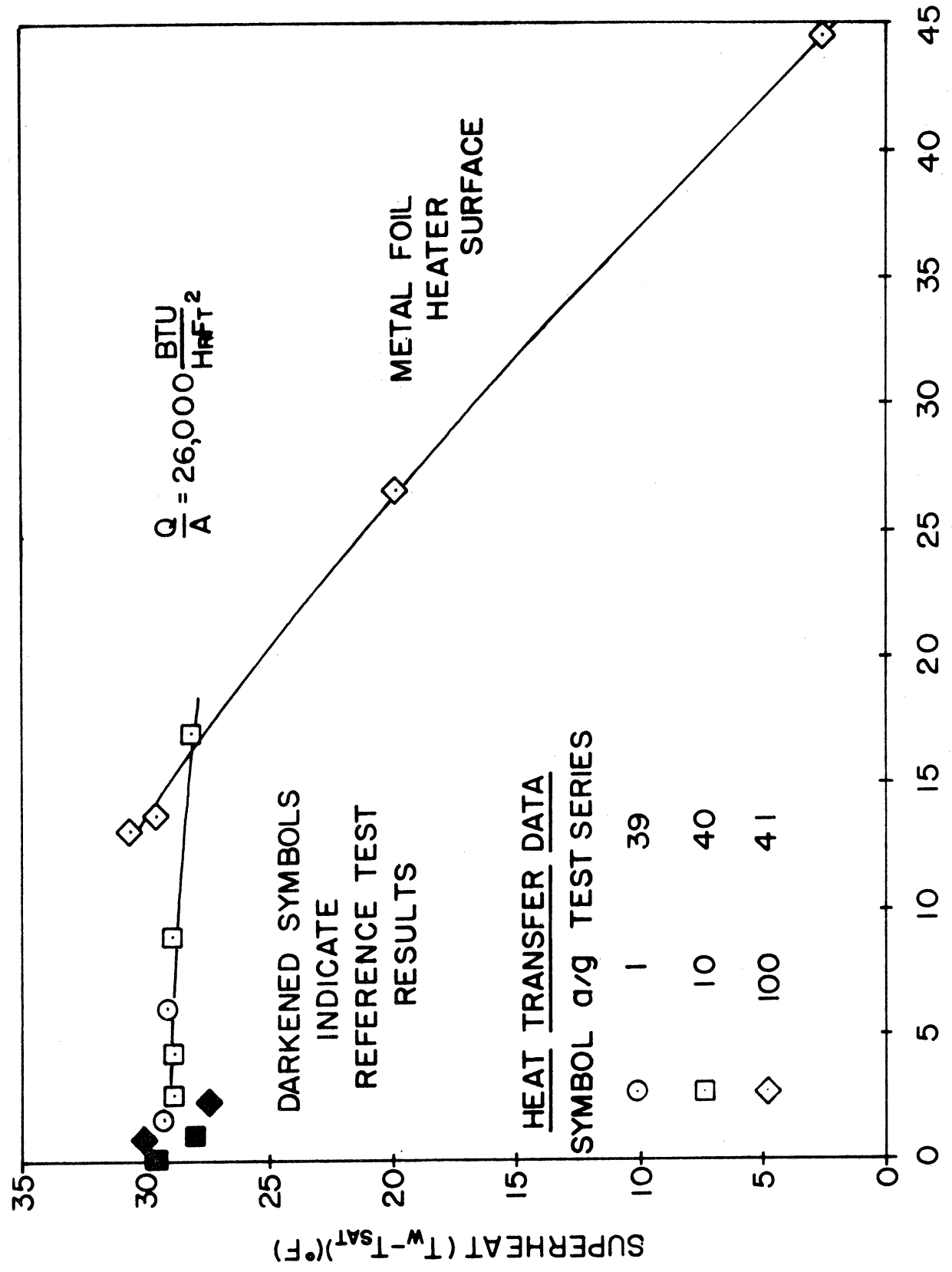

Figure 3. Heat Transfer Results For Metal Foil Heater Surface.

C. Temperature Scan Results

Figure 31 presents the results of three temperature scans performed for $Q/A = 4{,}000$ BTU/hr ft^2, 13,000 BTU/hr ft^2 and 40,000 BTU/hr ft^2 respectively under saturated boiling conditions at $a/g = 1$. The results are presented in the form of curves of temperature versus displacement measured from the heat transfer surface for each of the levels of heat flux under investigation. Each of the data points represents the numerical average of the output of the thermocouple probe over the short interval during which the probe was held stationary. The value of displacement at which each of these data points is plotted corresponds to the mid point of the thermocouple bead. Consequently, because of the limitation imposed by the physical size of the thermocouple bead, the data points corresponding to the condition at which the thermocouple probe had just broken physical contact with the surface are plotted at a displacement of 1.50×10^{-3} inches, the radius of the thermocouple bead, and represent the liquid temperature closest to the surface. The surface temperature itself, plotted at zero displacement corresponds to the heater surface temperature measured immediately prior to the temperature scan. These data points have been designated by T_W. Each of the curves through the data points has been drawn tangent to a line drawn from the appropriate value of the heater surface temperature having the slope $dT/dZ = -(Q/A)/k$. This approximation, suggesting a conduction sublayer adjacent to the surface, is seen to be in reasonable agreement with the data and was necessitated by the inability to measure liquid temperature in the vicinity of the displacement origin.

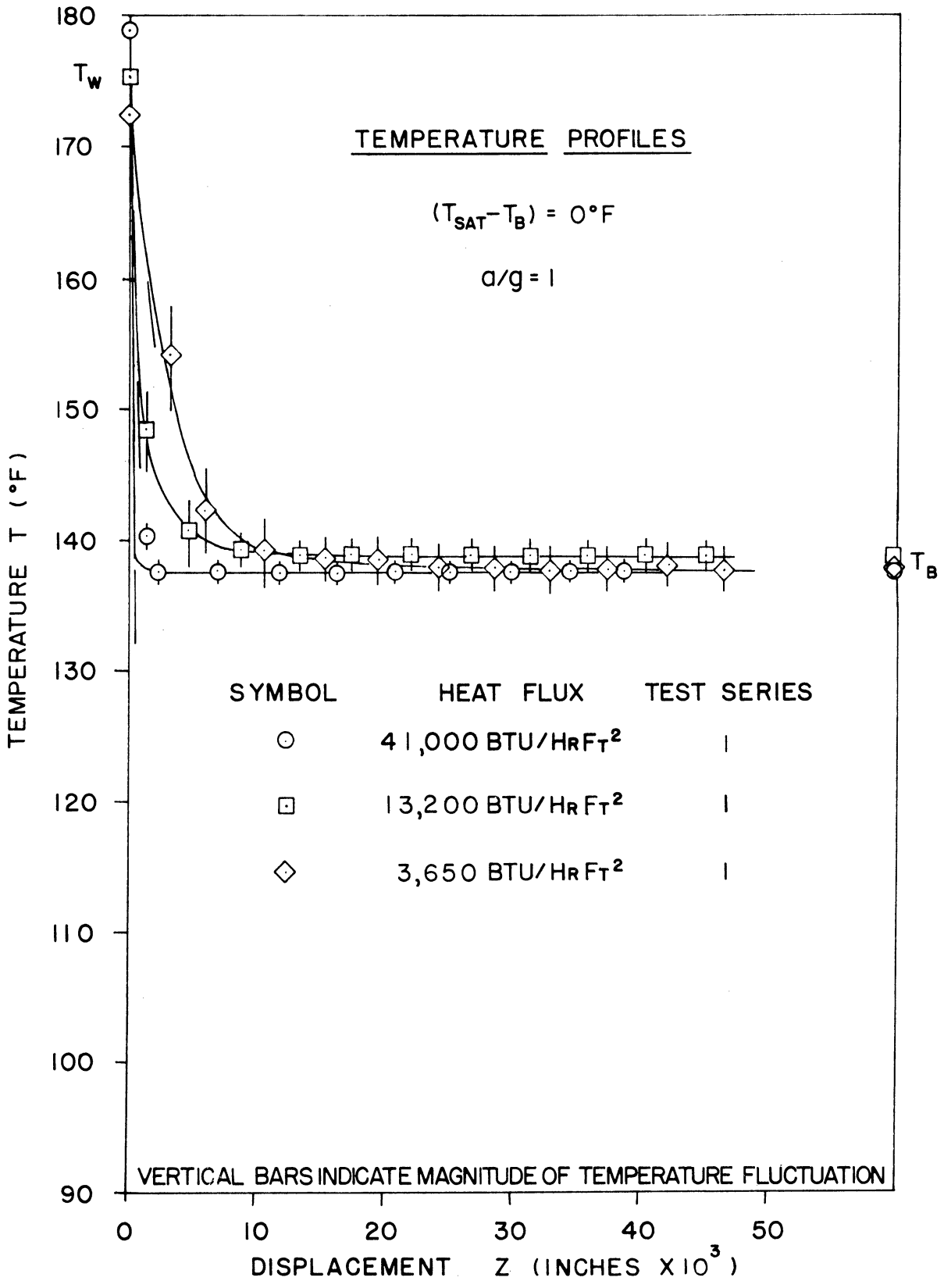

Figure 31. Temperature Profiles For Saturated Boiling.

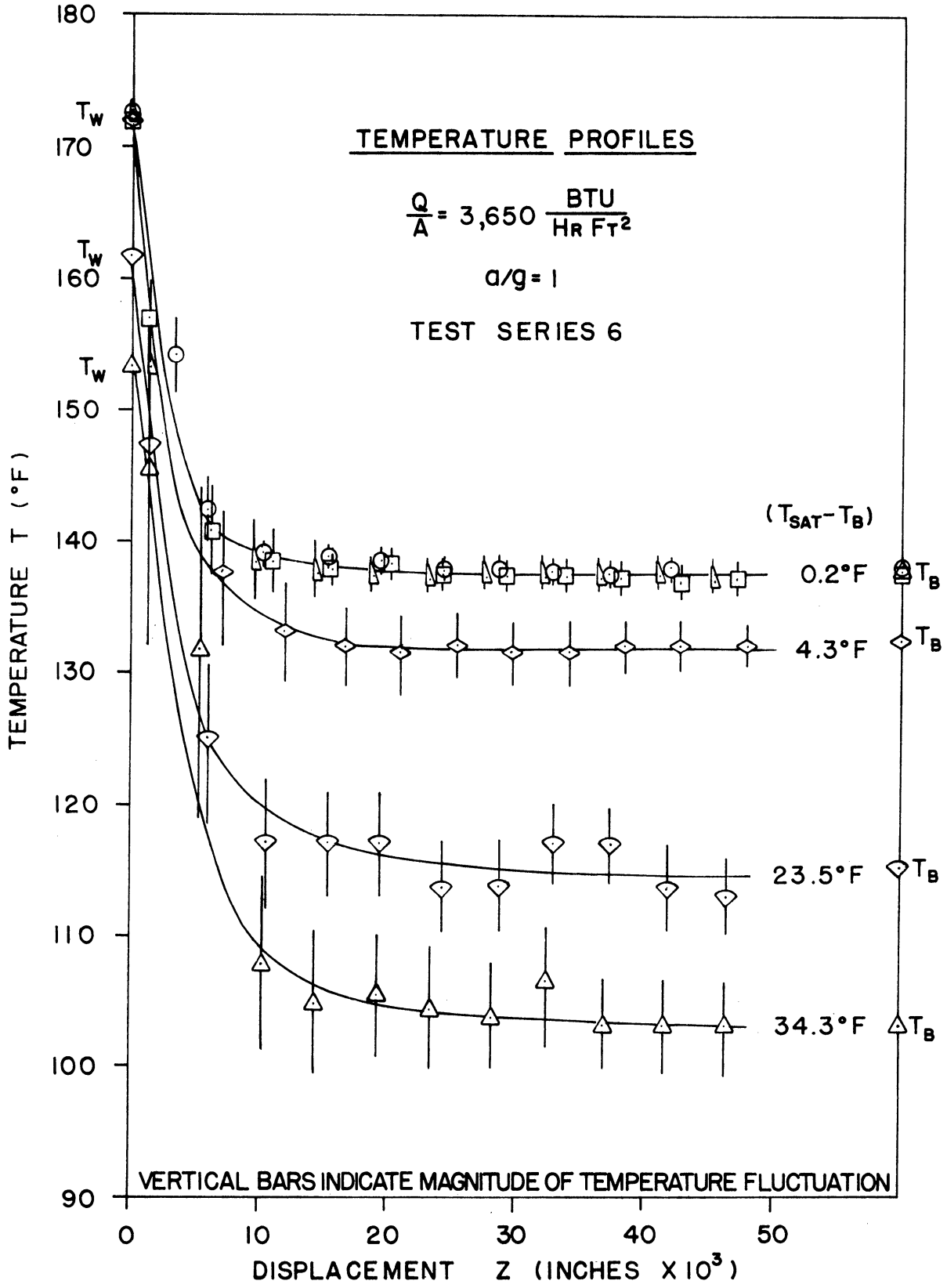

Figure 32. Temperature Profiles At a/g = 1 And Q/A = 3,650 BTU/HrFt^2.

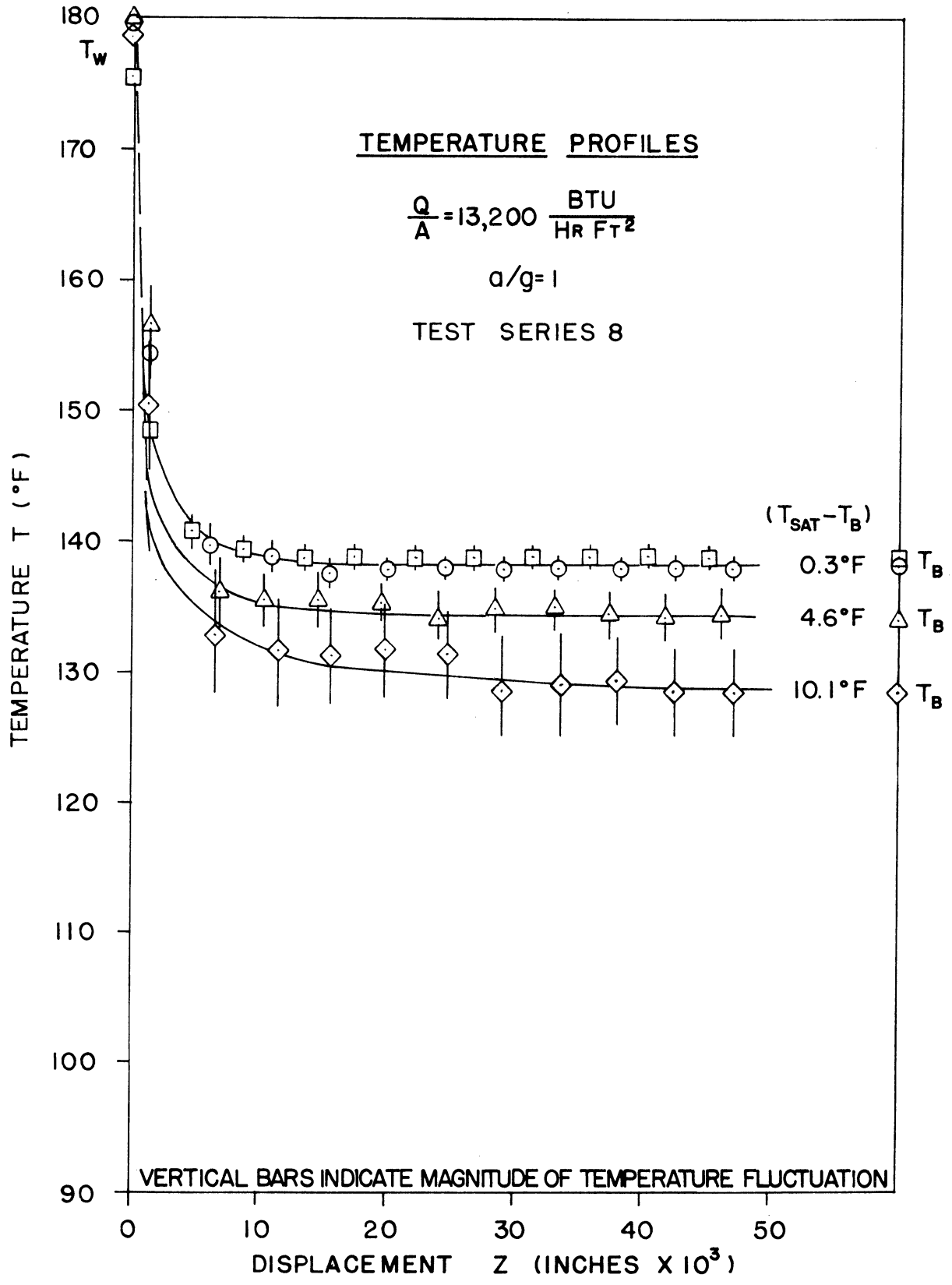

Figure 33. Temperature Profiles At a/g = 1 And Q/A = 13,200 BTU/HrFt^2.

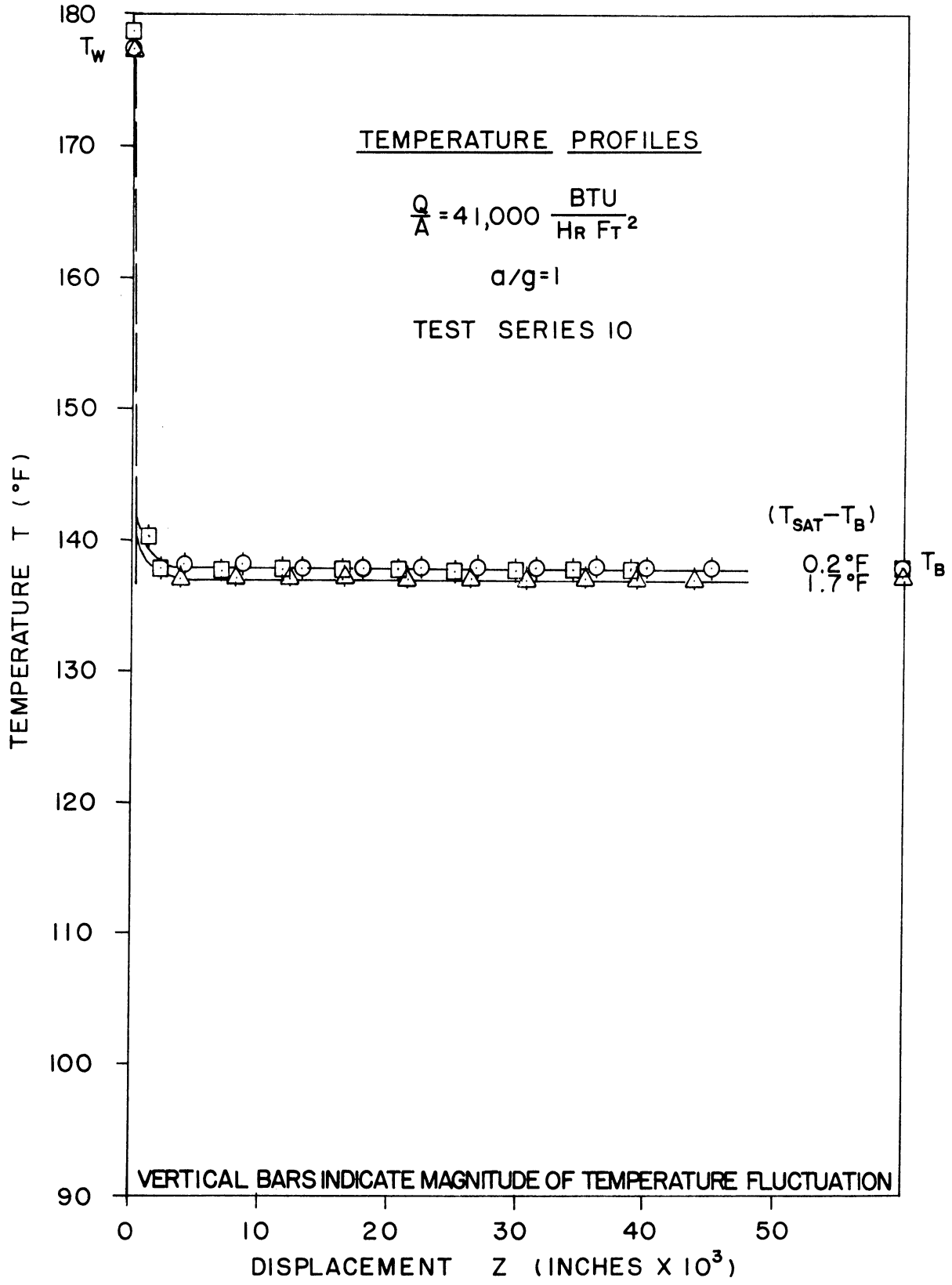

Figure 34. Temperature Profiles At a/g = 1 And Q/A = 41,000 BTU/HrFt^2.

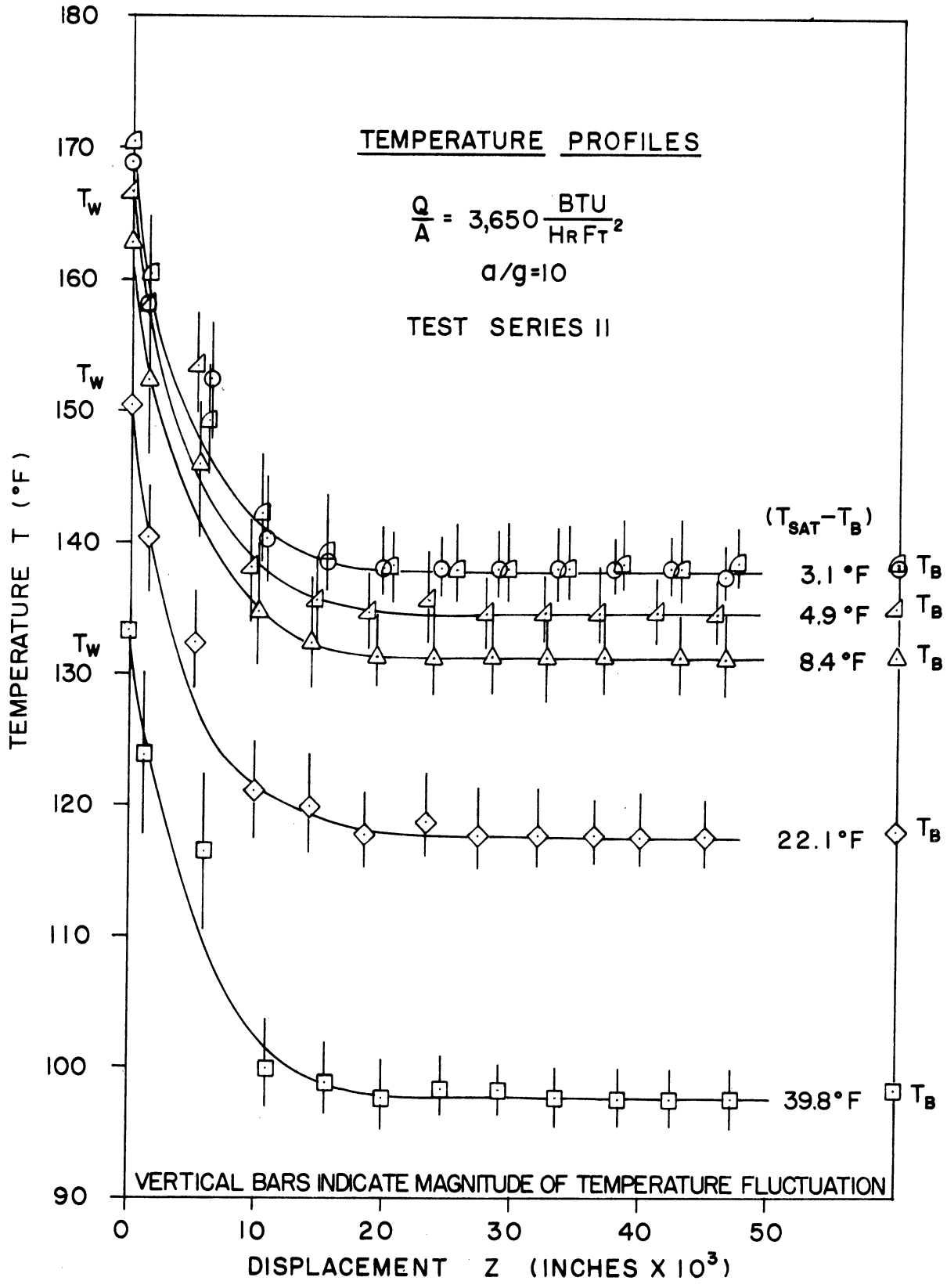

Figure 35. Temperature Profiles At a/g = 10 And Q/A = 3,650 BTU/HrFt^2.

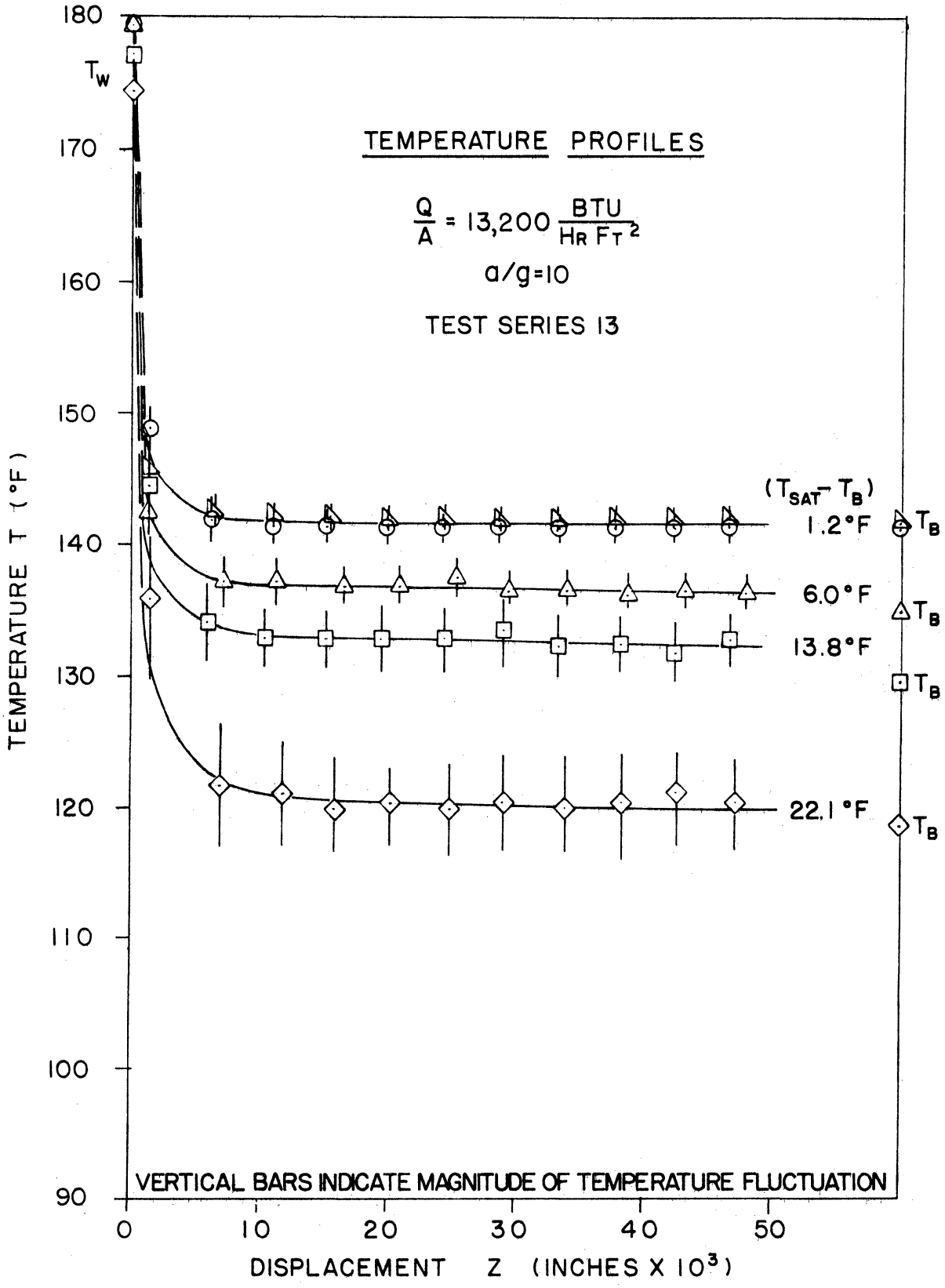

Figure 36. Temperature Profiles At a/g = 10 And Q/A = 13,200 BTU/HrFt^2.

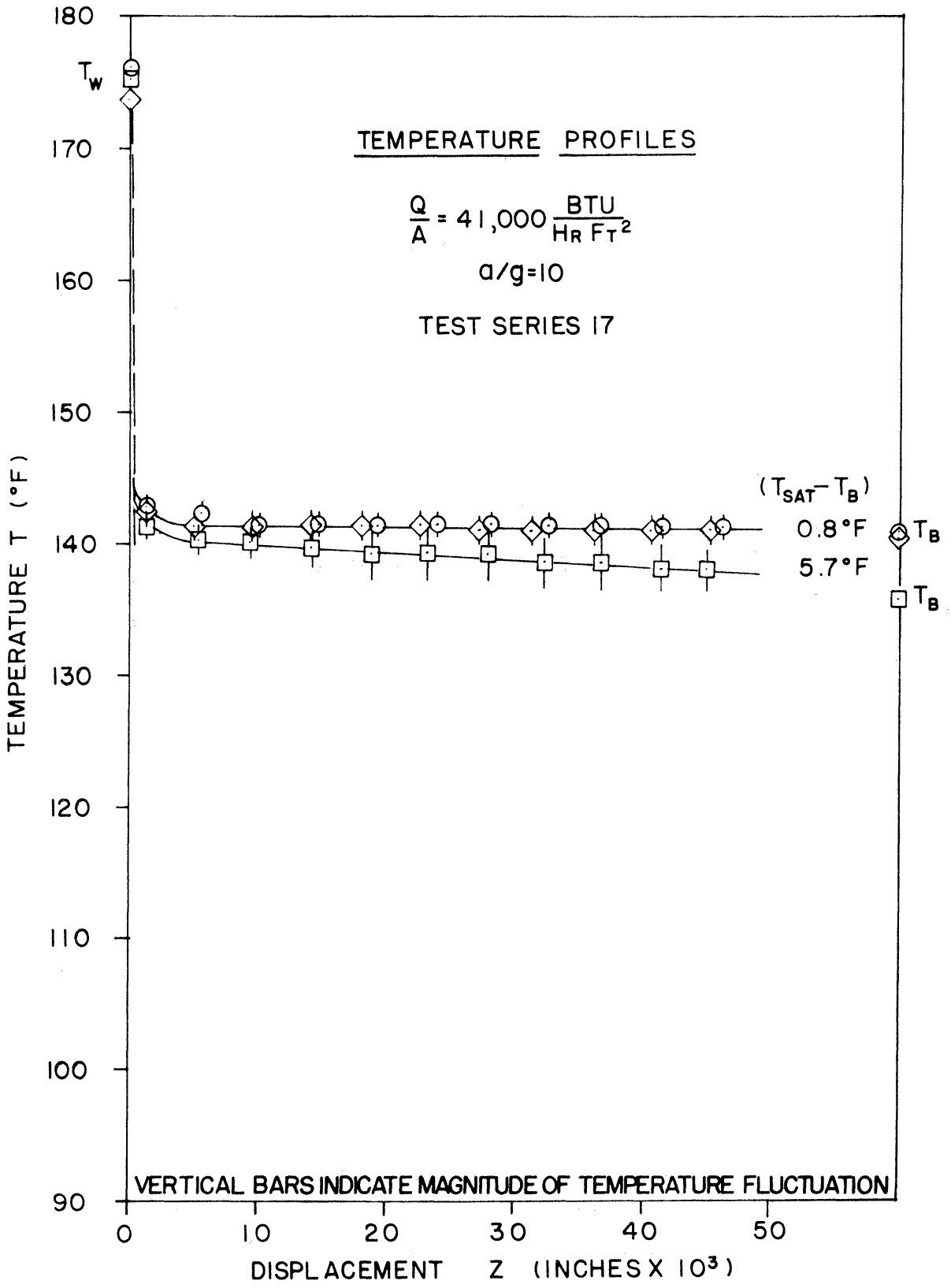

Figure 37. Temperature Profiles At a/g = 10 And Q/A = 41,000 BTU/HrFt^2.

The data points denoted T_B and plotted at the right hand border of the graph correspond to the bulk liquid temperature measured above the heat transfer surface at the same time that the surface temperature was measured.

Figures 32 to 34 present the results of temperature scans performed for $Q/A = 4{,}000$ BTU/hr ft^2, 13,000 BTU/hr ft^2 and 40,000 BTU/hr ft^2 at various levels of subcooling and $a/g = 1$ respectively. Figures 35 to 37 present the results of temperature scans performed for $Q/A = 4{,}000$ BTU/hr ft^2, 13,000 BTU/hr ft^2 and 40,000 BTU/hr ft^2 at various levels of subcooling and $a/g = 10$ respectively. These results are presented in the same manner as the results of the temperature scans of Figure 31. A family of curves may be seen showing the influence of subcooling upon the temperature profile for each level of heat flux and acceleration investigated. All of the individual temperature profiles have attained the bulk liquid temperature within the displacement range of the temperature scan.

D. Site Density Results

Figures 38 to 40 present the results of the photographic study which determined the active site density and the average population density at $a/g = 1$, 10 and 100 respectively. The results are presented in the form of plots of active site density and average population density versus subcooling for constant values of heat flux and acceleration. The values presented in the plot of active site density versus subcooling represent the number of nucleation sites per unit area which were observed to be active during the standard counting period. The values presented in the plot of average population density versus subcooling represent the bubble population on the surface at a given instant of time.

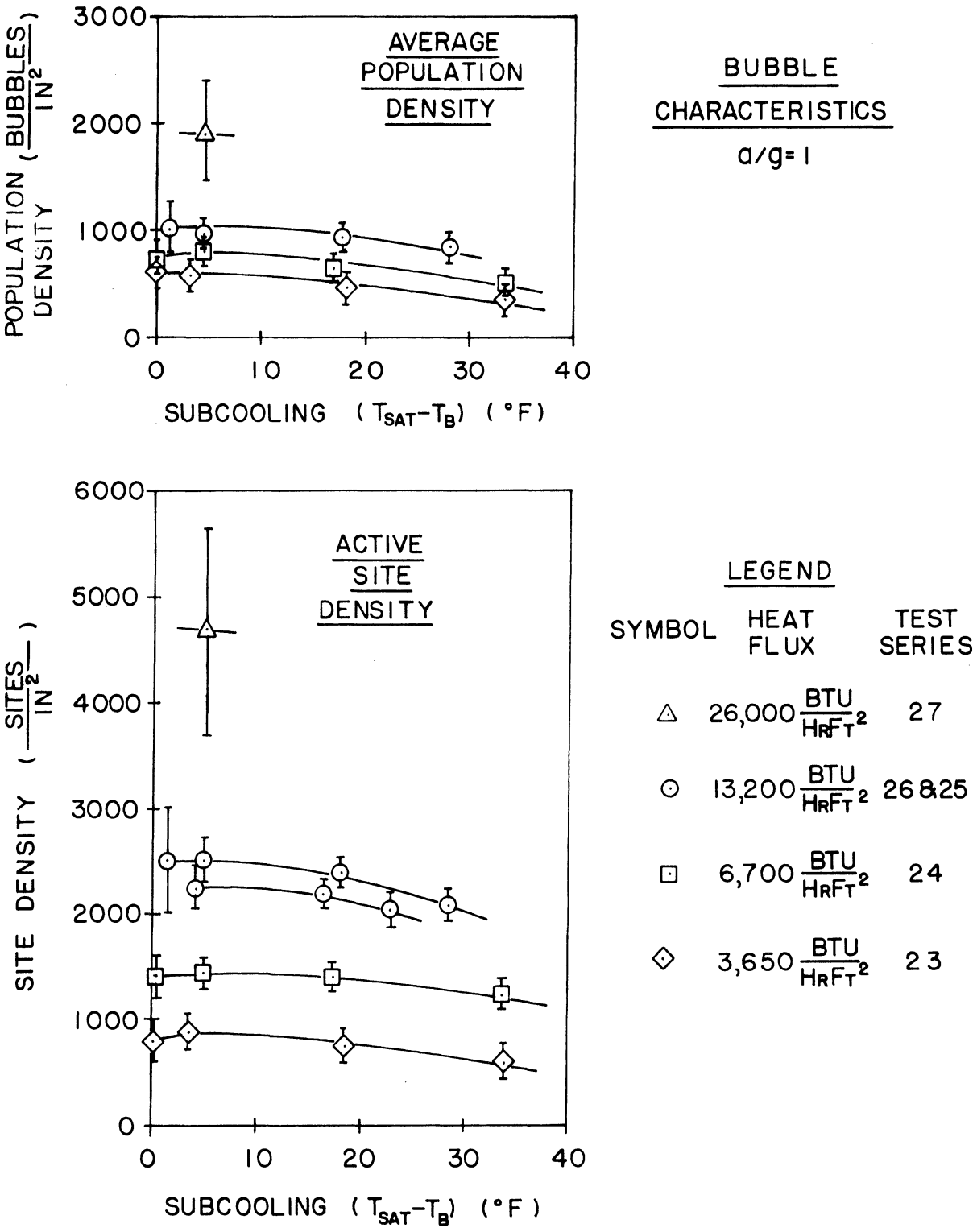

Figure 38. Average Population Density And Active Site Density At a/g = 1.

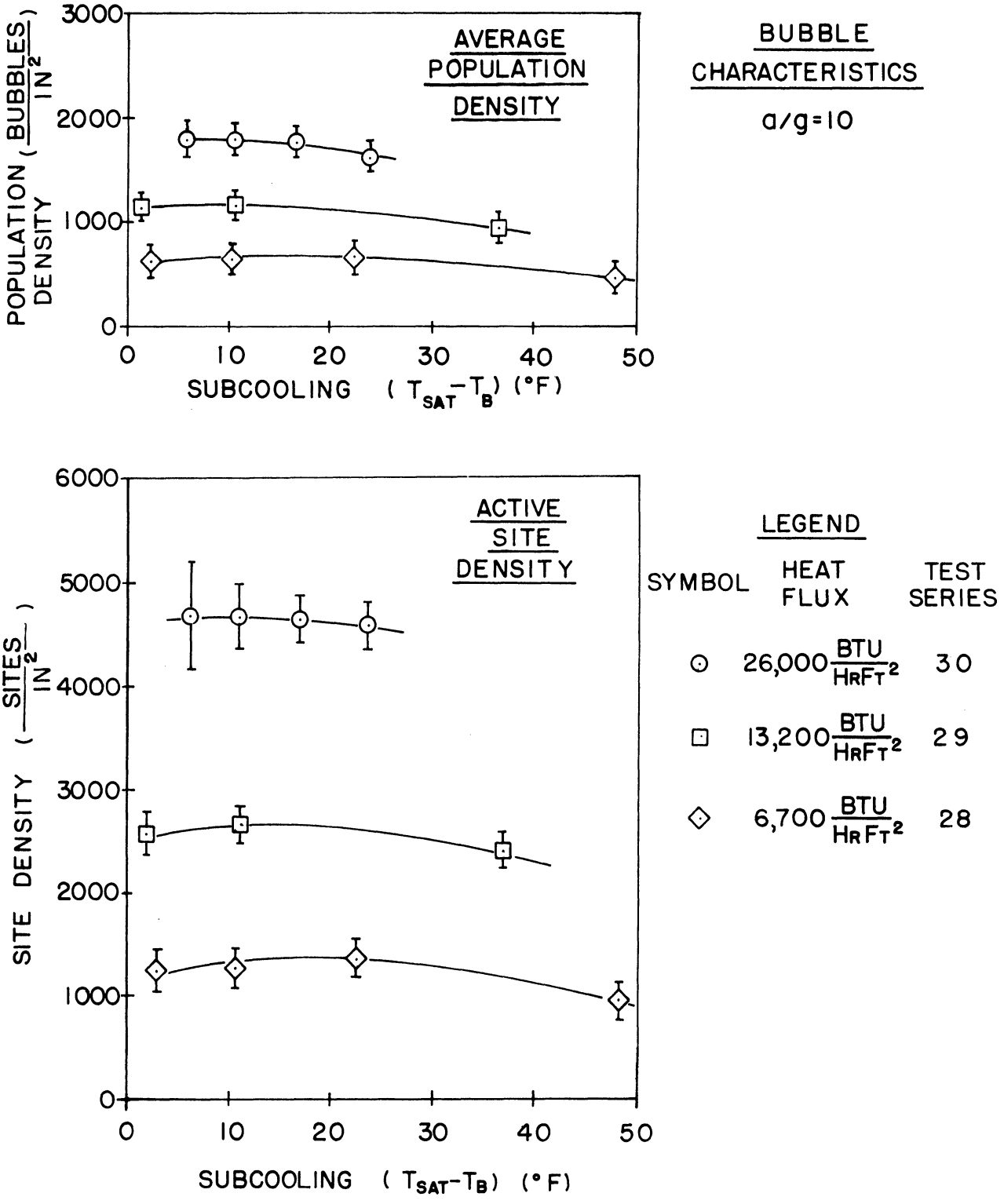

Figure 39. Average Population Density And Active Site Density At a/g = 10.

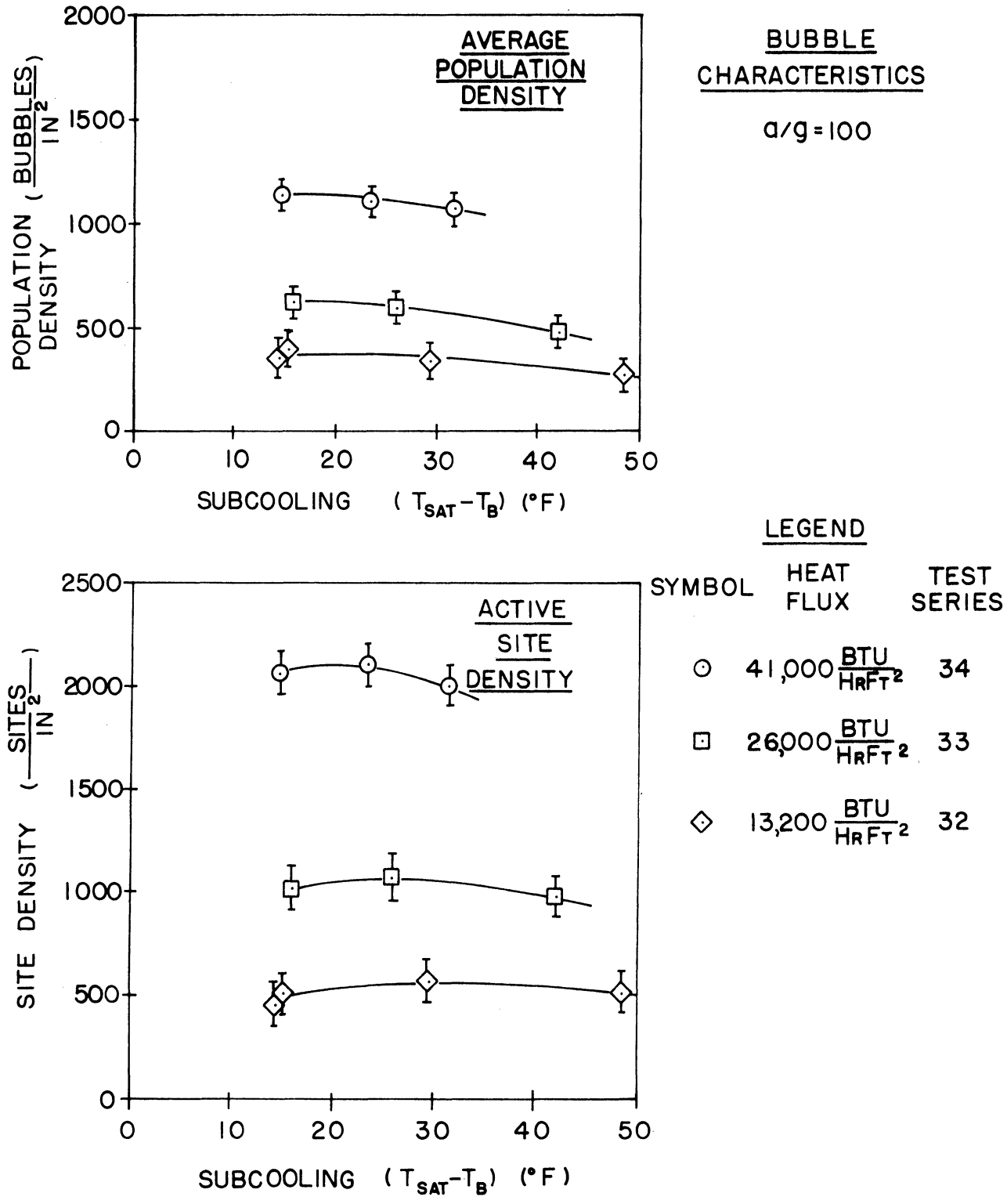

Figure 40. Average Population Density And Active Site Density At a/g = 100.

The vertical bars on each of the data points indicate the level of uncertainty associated with the particular measurement. These levels of uncertainty were established during the analysis of the photographs based upon the uncertainty encountered in obtaining an accurate count of the number of active sites. The magnitude of this uncertainty was arbitrarily equated to the number of so called doubtful sites, defined as those sites which were seen to issue only a single vapour bubble either because the site failed to nucleate another bubble within the sample of the data examined or because the site was subsequently obscured by the passage of a vapour bubble. The level of uncertainty can be seen to increase with increasing heat flux, particularly as the saturated boiling condition is approached.

The conditions corresponding to $Q/A = 13{,}000$ BTU/hr ft^2 at $a/g = 1$ were repeated in order to assess the reproducibility of the site density analysis. The two sets of data reproduced within 10% as indicated in Figure 38.

E. Bubble Frequency Results

Figures 41 to 43 present the results of the photographic study which determined the time which elapsed between cycles of vapour bubble emission at $a/g = 1$, 10 and 100 respectively. The results are presented in the form of plots of bubble period versus subcooling for constant values of heat flux and acceleration. Each of the plots in Figures 41 to 43 present additional information concerning the portion of the bubble period during which the nucleation site was active in comparison to the portion of the bubble period during which the nucleation site was inactive.

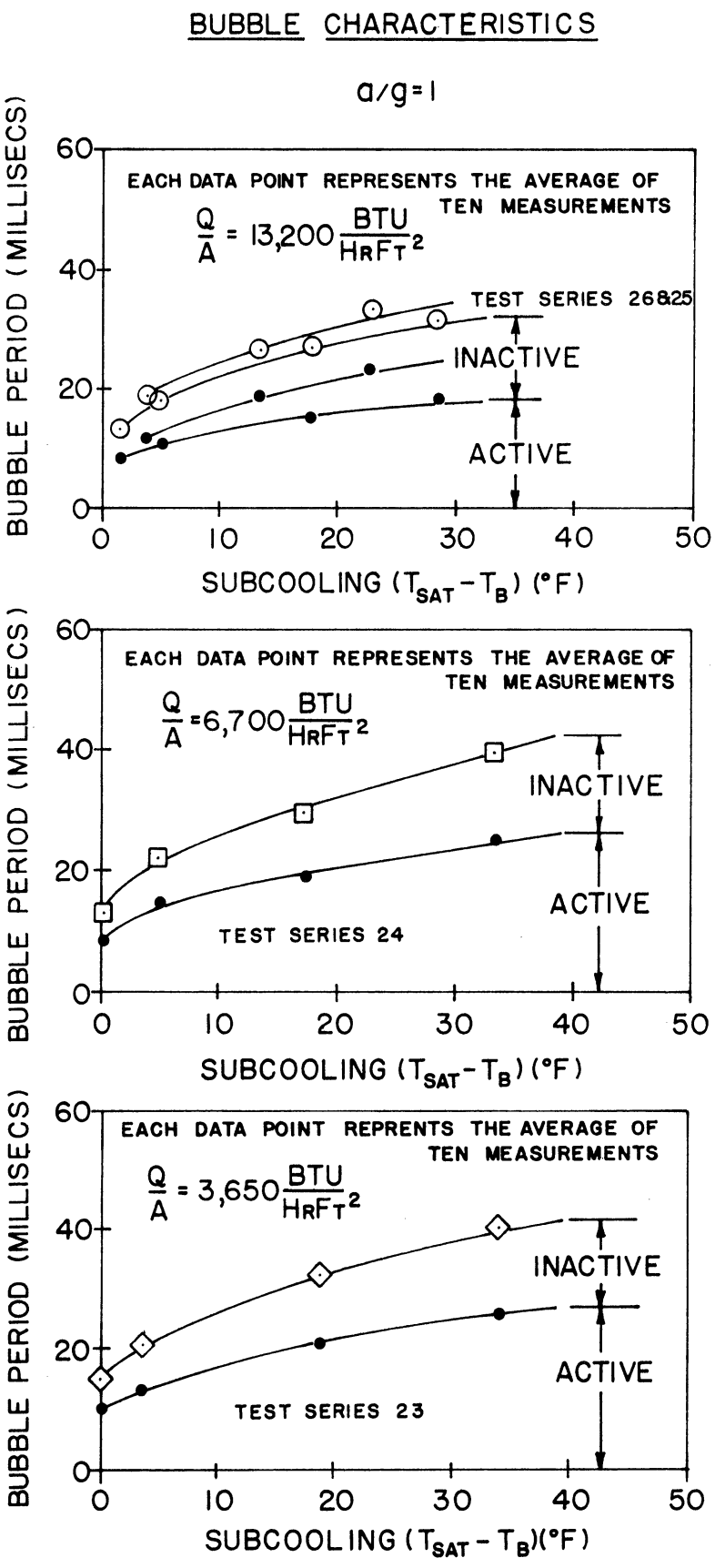

Figure 41. Bubble Period Results At a/g = 1.

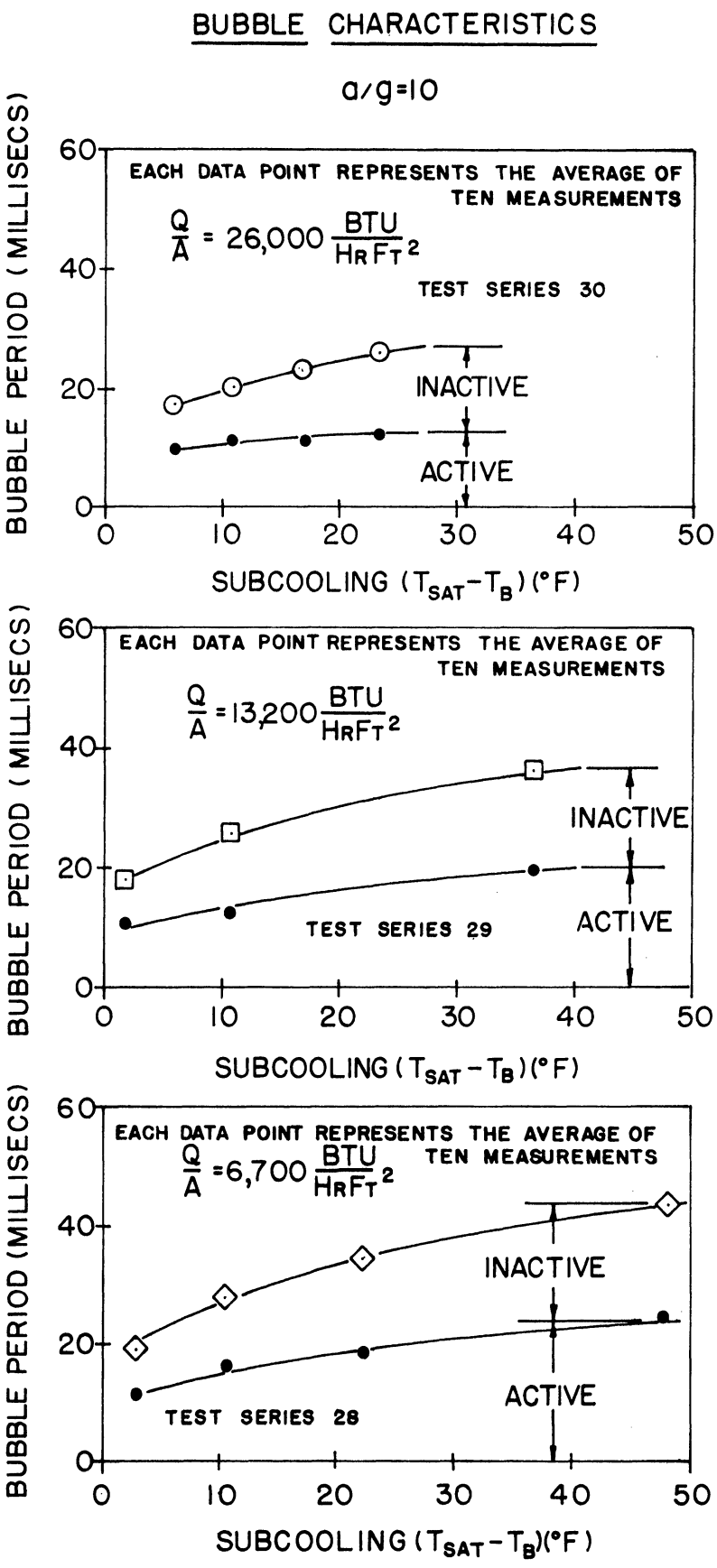

Figure 42. Bubble Period Results At a/g = 10.

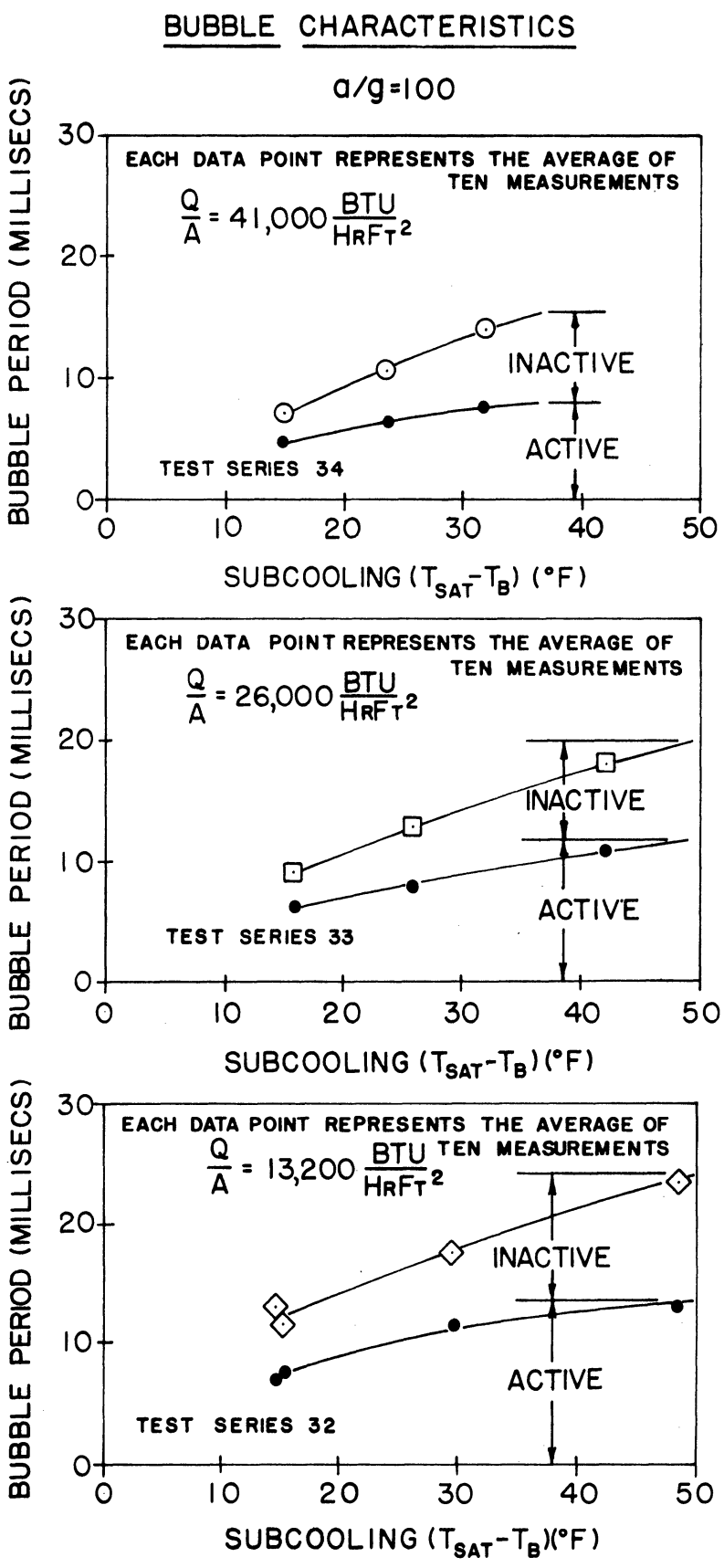

Figure 43. Bubble Period Results At a/g = 100.

Each of the data points presented represents the numerical average of the bubble period observed at ten different nucleation sites chosen at random on the heat transfer surface.

The total bubble periods presented in Figures 41 to 43 have been combined in Figure 44 to 46 for a/g = 1, 10 and 100 respectively to emphasize the influence of heat flux. The vertical bars on each of the data points in the composite plot indicate the uncertainty associated with the particular measurement. These levels of uncertainty were based upon the extreme variations in the measurement of bubble period. The level of uncertainty can be seen to be relatively independent of the conditions investigated. Figures 44 to 46 also include the bubble frequency, obtained from the reciprocal of the bubble period.

The conditions corresponding to $Q/A = 13{,}000$ BTU/hr ft^2 at $a/g = 1$ were repeated in order to assess the reproducibility of the bubble frequency analysis. The two sets of data reproduced within 10% as indicated in Figure 41 and Figure 44.

F. Maximum Bubble Size Results

Figure 47 presents the results of the analysis of the maximum bubble size, the maximum diameter attained by the vapour bubbles while attached to the heat transfer surface. No attempt is made in this plot to distinguish vapour bubbles which departed from the heat transfer surface from those which collapsed on the heat transfer surface. The maximum bubble size results are presented as a function of subcooling and acceleration but no attempt is made to indicate the influence of heat flux, since this effect is totally obscured by the large uncertainty

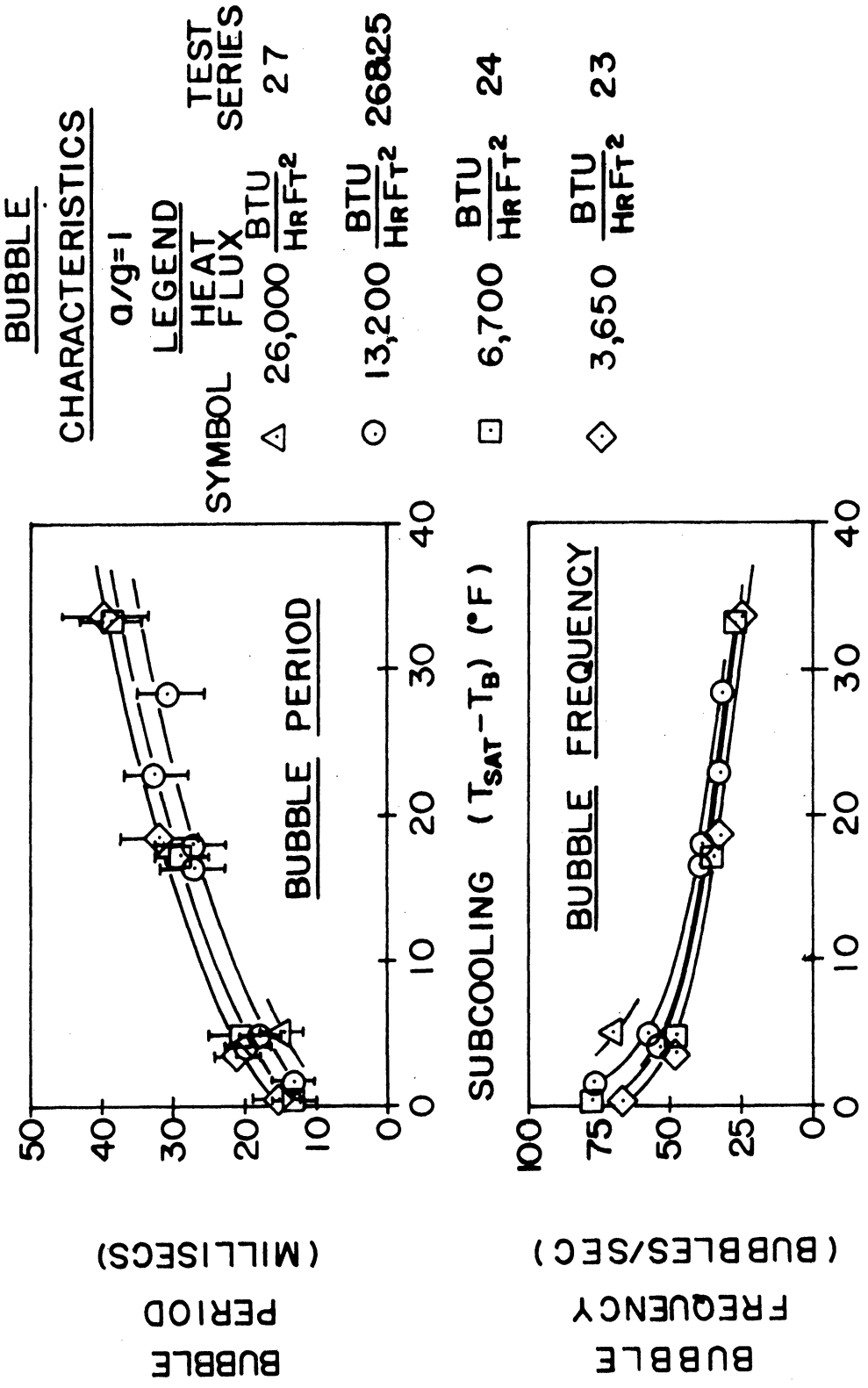

Figure 44. Composite Period And Frequency Results At a/g = 1.

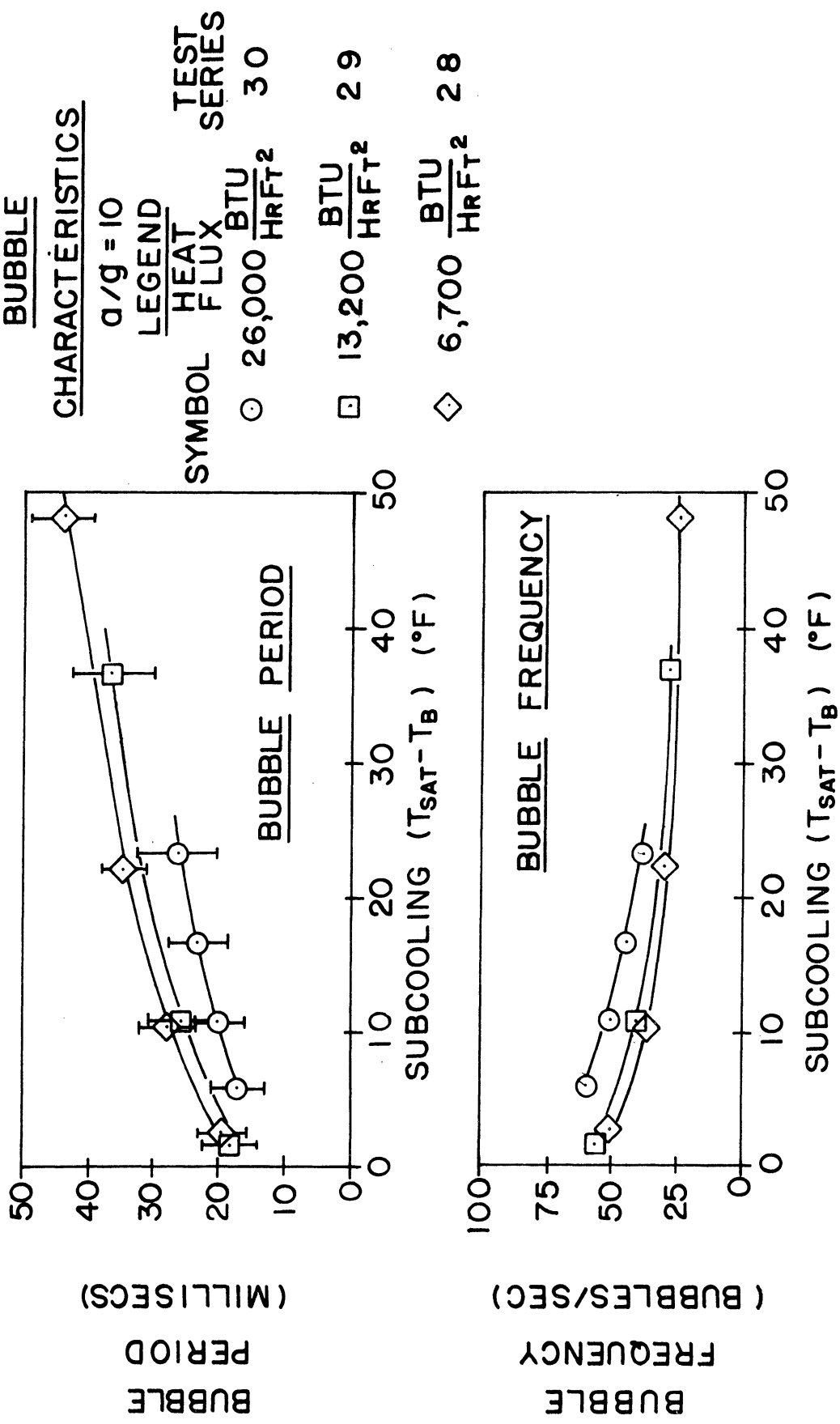

Figure 45. Composite Period And Frequency Results At a/g = 10.

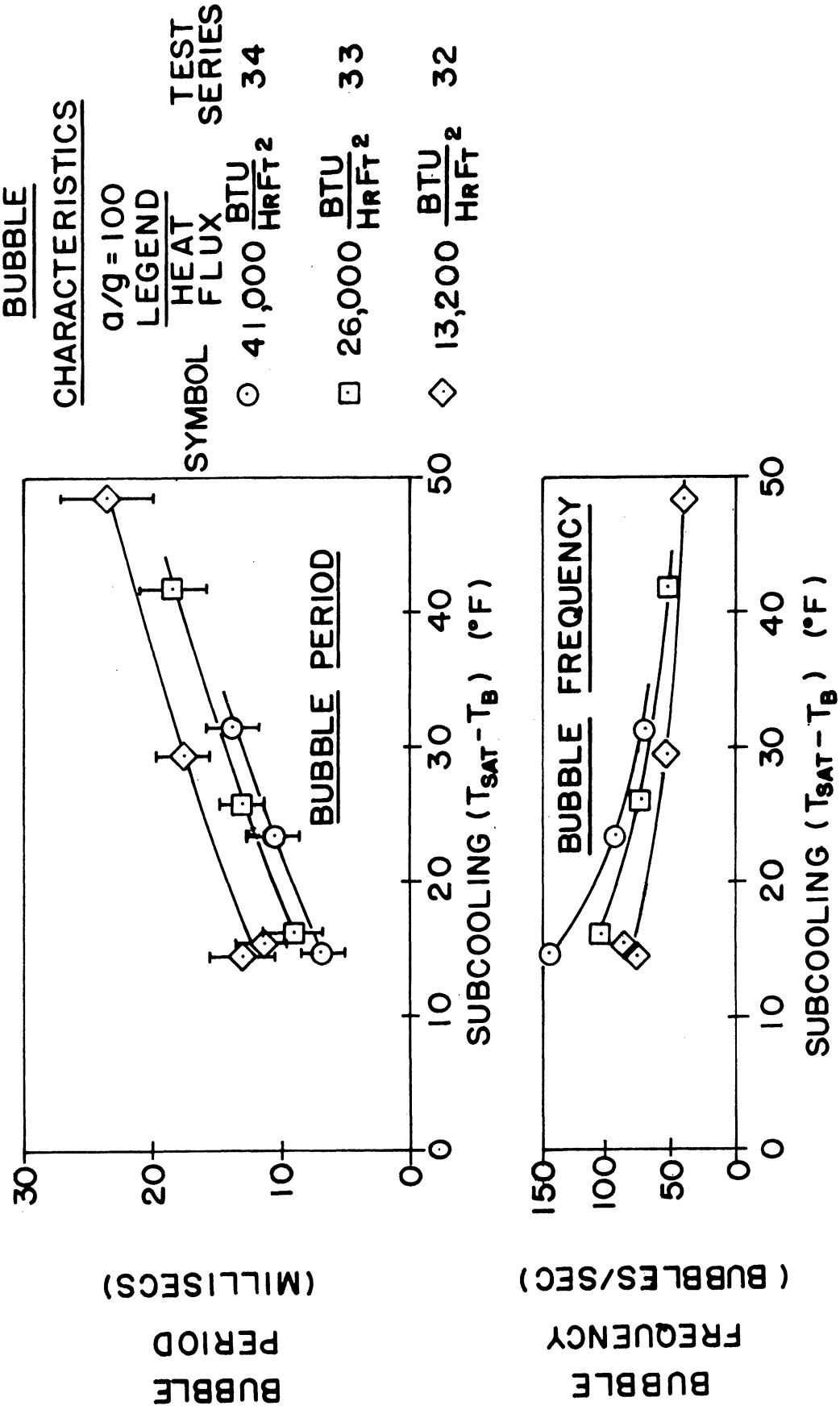

Figure 46. Composite Period And Frequency Results At a/g = 100.

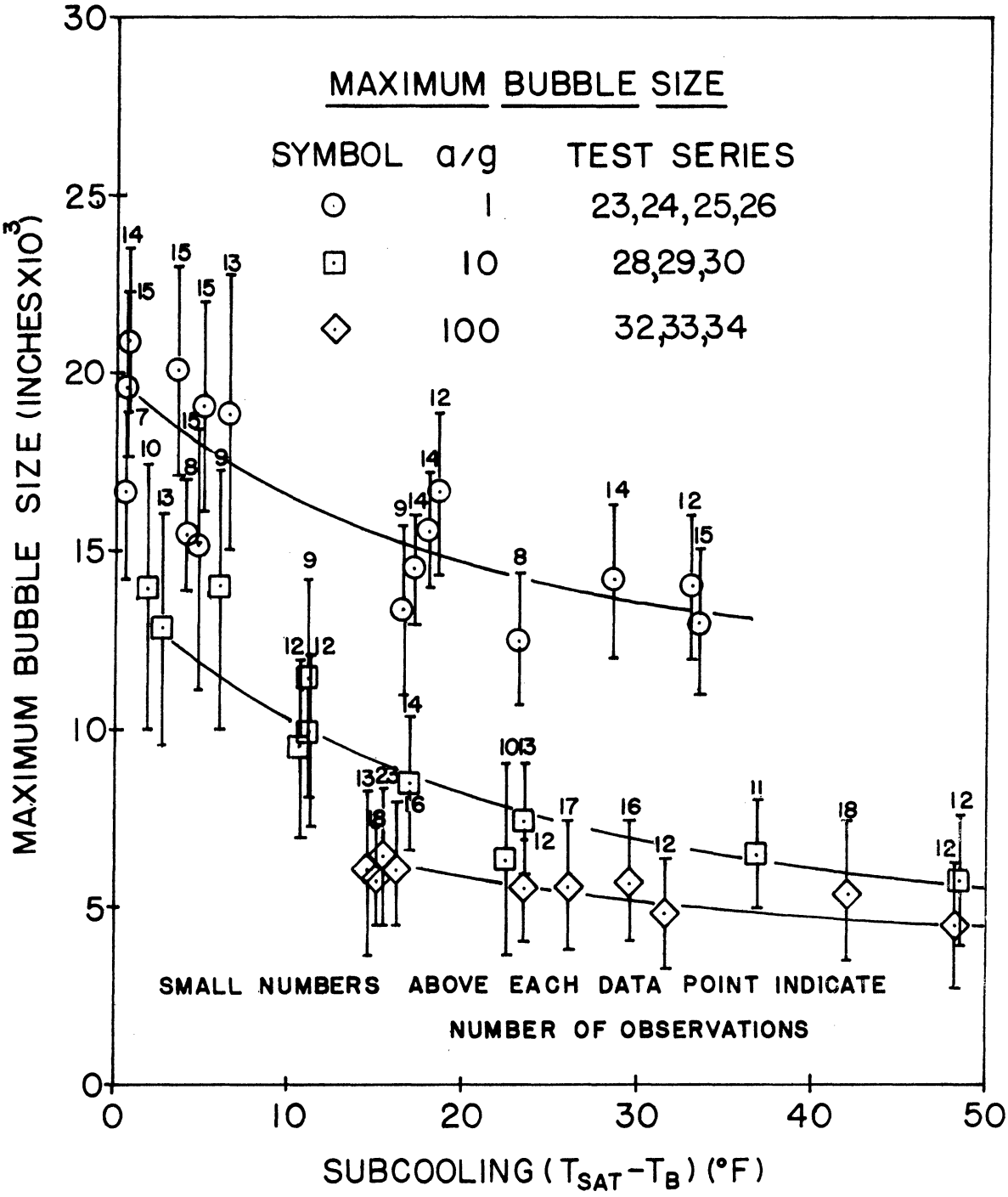

Figure 47. Maximum Bubble Size Results.

in the measurements. This uncertainty is in part due to the variation in the maximum bubble size and in part due to the insensitivity of the measuring technique. The magnitude of the uncertainty, corresponding to the extreme variations in the measurements of maximum bubble size, is indicated by the vertical bar on each of the data points. The small number above each bar indicates the number of observations from which the value plotted was calculated.

CHAPTER VII

DISCUSSION

A. Reproducibility Of The Boiling Curve

The varying behaviour of the characteristic boiling curve exhibited in Figures 23 to 25 introduced an undesireable element in the present investigation, in that great care was required in determining the effect of changes in acceleration and subcooling. The fact that some agreement was observed within each set of data suggests the existence of an unknown and hence uncontrolled variable. The cause of the varying behaviour of the characteristic curve is not certain; obviously something acts to change the ability of the heat transfer surface to dissipate heat by nucleate boiling under conditions which are ostensibly identical.

The sequence of events associated with two typical test series is shown in Figure 48. The two cases represented are identical with the exception of the manner in which the vapour space within the test package was pressurized during the period of time between consecutive test series. In Case #1 the vapour space was vented to atmosphere after the temperature of the Freon had decreased below the saturation temperature, whereas in Case #2, the vapour space atmosphere was maintained, although leakage caused the pressure level to decrease to atmospheric over a period of many hours. The pressurization procedure described above was observed to have a pronounced effect upon the resulting nucleate boiling phenomenon; the subsequent reference test results were found to agree with Characteristic Curve #1 in the former case and Characteristic Curve #2 in the latter case. This observation suggests that different amounts of dissolved gas were responsible for the uncontrolled shift in the reference test results.

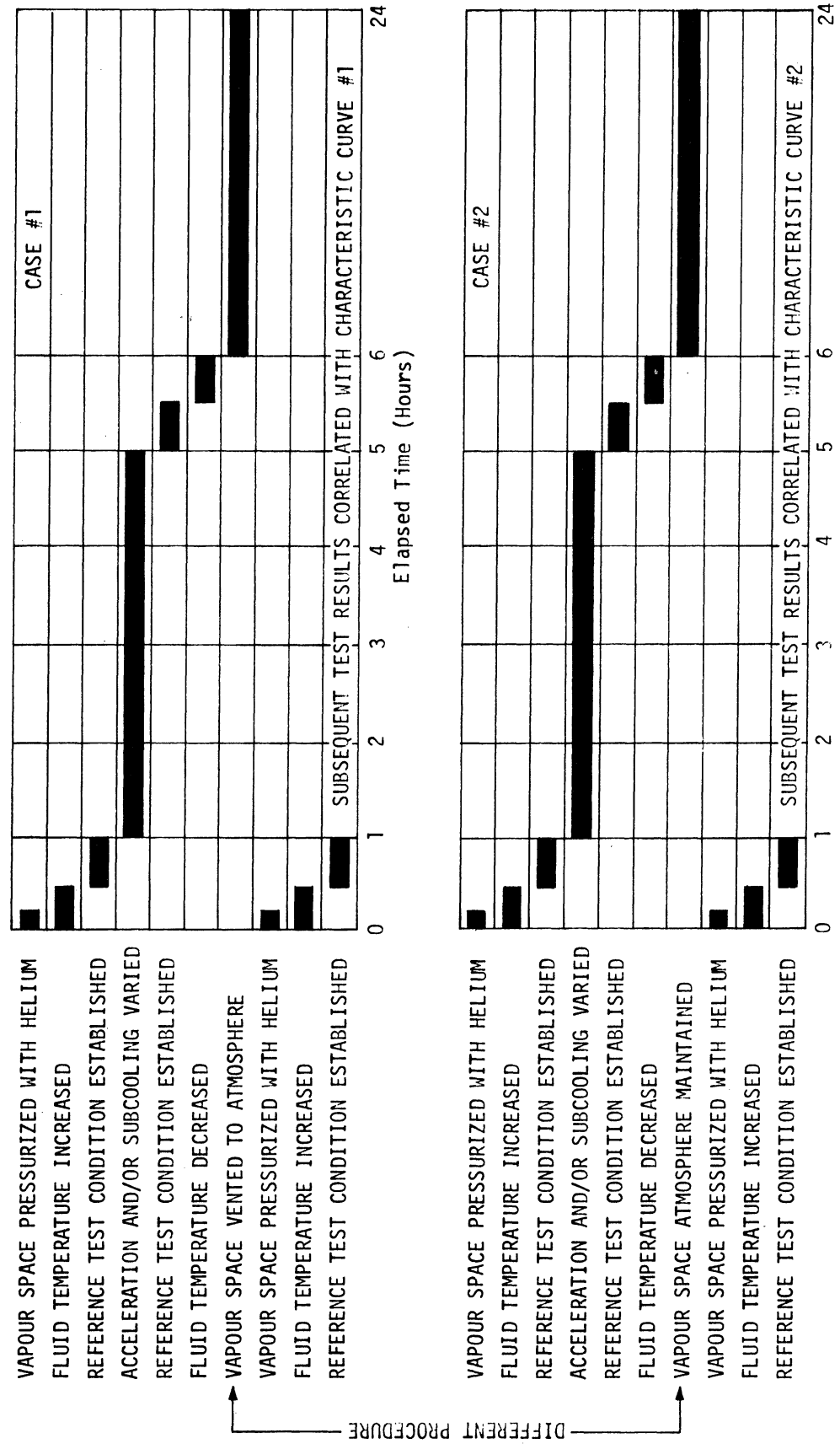

Figure 48. Sequence Of Events Associated With Two Typical Test Series.

The maximum amount of helium which could be dissolved in the Freon was small, calculated to be 2.5% by volume. Were all of the helium dissolved to come out of solution, the effect upon the pressure of the gas-vapour mixture occupying the vapour space would be negligible since the volume of the vapour space is seven times the volume of the liquid and the volume of the gas coming out of solution before expanding to fill the vapour space is a small portion of the liquid volume. Consequently, changes in saturation temperature resulting from the release of dissolved helium cannot explain the differences in the characteristic boiling curves. However, McAdams[44] and Pike, Miller and Beatty[45] have reported that small concentrations of dissolved gas caused the characteristic boiling curve to shift to lower values of superheat under steady boiling conditions. Accordingly, it is suggested that Characteristic Curve #1 and Characteristic Curve #2 correspond to two different concentrations of dissolved gas and that Characteristic Curve #1 corresponds to a lower gas concentration than Characteristic Curve #2. This hypothesis is reinforced by the following observations.

(1) Reducing the vapour space pressure at an elevated temperature somewhat less than the saturation temperature would result in the diffusion of helium from the Freon in response to the reduction of the helium partial pressure in the vapour space. As noted previously, the reference test results obtained subsequent to such a pressure reduction correlated with Characteristic Curve #1.

(2) Reabsorption of helium would cause the reference test results to shift toward Characteristic Curve #2. The data presented in Figure 25 indicates that the agreement of the first five data points with

Characteristic Curve #2 became progressively better, presumeably resulting from the absorption of helium gas with elapsed time.

Although the foregoing discussion advances an explanation of the behaviour of the characteristic boiling curve which is consistent with observation, it is emphasized that the explanation is only a hypothesis. It is not essential that the exact cause be known, since the varying behaviour can be compensated as will be described in Section B, Chapter VII.

B. Heat Transfer

The test procedure involving the establishment of reference test conditions before and after each test series was explained previously. The purpose of this procedure was to obtain test results for the particular level of heat flux investigated under saturated boiling conditions at $a/g = 1$ before and after changing subcooling and/or acceleration. Figures 24 and 25 are comprised of the reference test results obtained. The following paragraph explains how the reference test results were used to separate the effect of changes in subcooling and/or acceleration from the effect of uncontrolled variations in the characteristic boiling curve.

It is significant that each of the curves presented in Figures 27 to 29 correlating the heat transfer results for a particular combination of heat flux and acceleration are essentially parallel to one another at all levels of subcooling and that the amount by which the supposedly duplicate curves are offset is the same amount by which the corresponding reference test results are offset. The implication of these observation is that the apparent lack of reproducibility in the

heat transfer results was caused by uncontrolled variations in the nucleate boiling phenomenon, independent of subcooling and acceleration. Accordingly, the heat transfer results were "normalized" by shifting all of the heat transfer results by the amount which the corresponding reference test results were offset from Characteristic Curve #2. In this manner, the effect of uncontrolled variations in the nucleate boiling phenomenon was eliminated, and the effect of variation in subcooling and/or acceleration was emphasized. The normalized heat transfer results are presented in Figures 49 to 51 for $a/g = 1$, 10 and 100 respectively. For the sake of comparison, Figure 49 includes the results of Rallis, Kok and Greenland[12] for water boiling on a horizontal nickel wire 0.020 inches diameter and Figures 49 and 50 include the results of Merte and Clark[20] for water boiling on a horizontal chromium plated copper surface 3 inches diameter.

Subcooling has a marked effect upon the superheat at constant heat flux as illustrated in Figures 49 to 51. Increasing subcooling first causes the superheat to increase slightly and then causes the superheat to decrease markedly. This effect is observed at all levels of acceleration for heat flux levels sufficiently high enough ($Q/A \geq 4{,}000$ BTU/hr ft^2 at $a/g = 1$; $Q/A \geq 7{,}000$ BTU/hr ft^2 at $a/g = 10$; $Q/A \geq 25{,}000$ BTU/hr ft^2 at $a/g = 100$). The value of subcooling corresponding to the maximum value of superheat increases with increasing heat flux. This type of behaviour is in qualitative agreement with the observation of Rallis, Kok and Greenland[12] and Merte and Clark[20] although the magnitude of the effect is different, possibly because of differences in the characteristics of the systems investigaged.

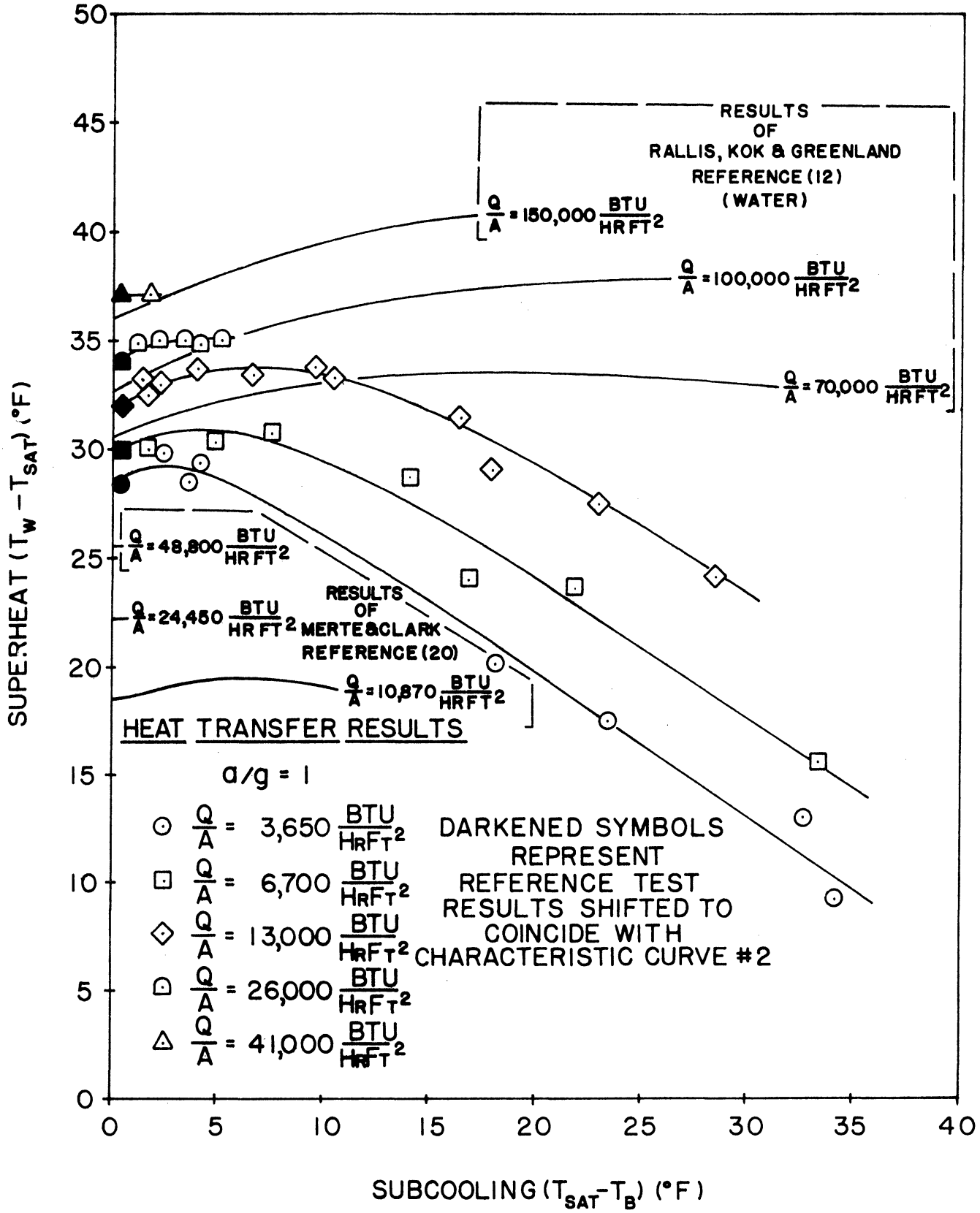

Figure 49. Normalized Heat Transfer Results At a/g = 1.

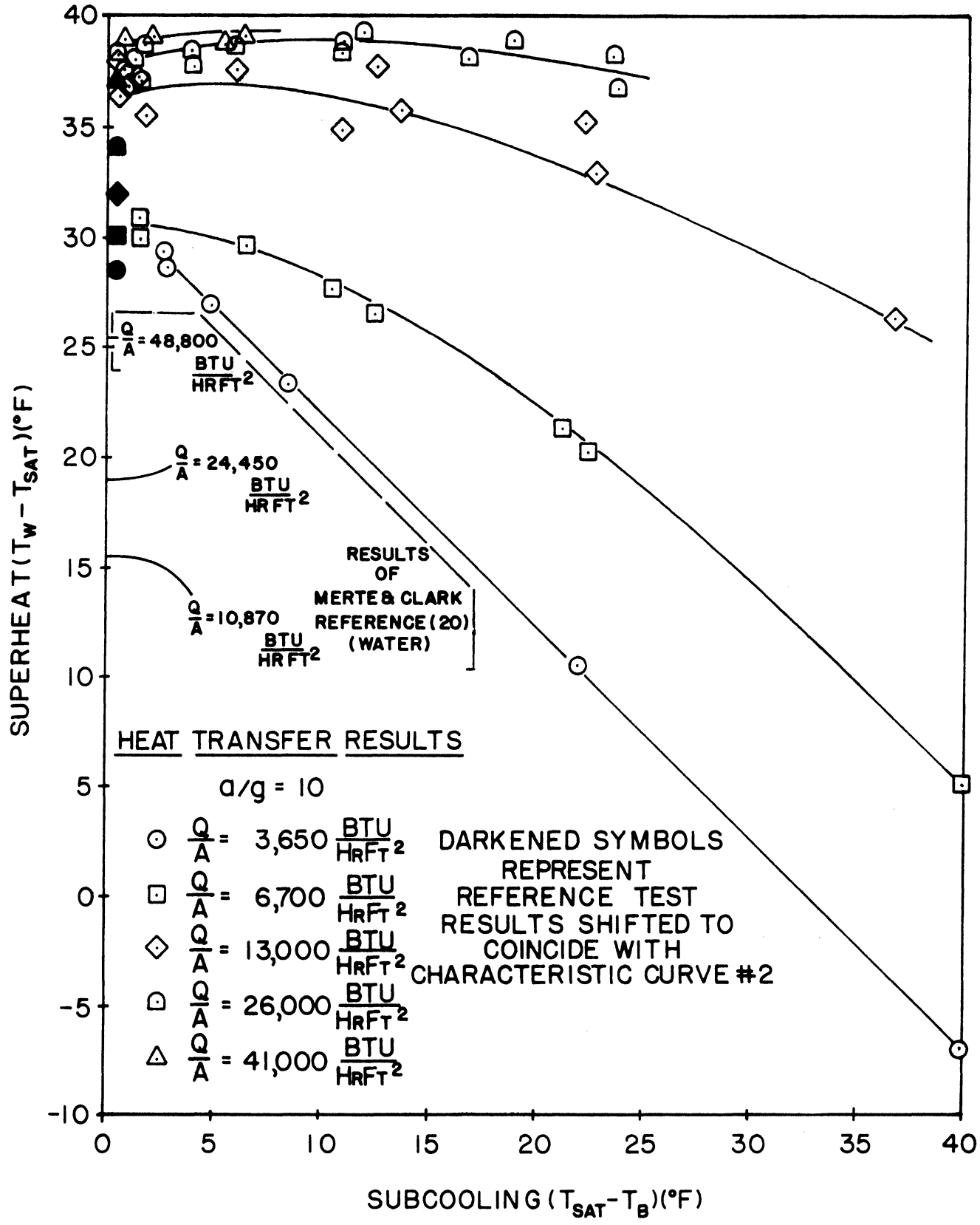

Figure 50. Normalized Heat Transfer Results At a/g = 10.

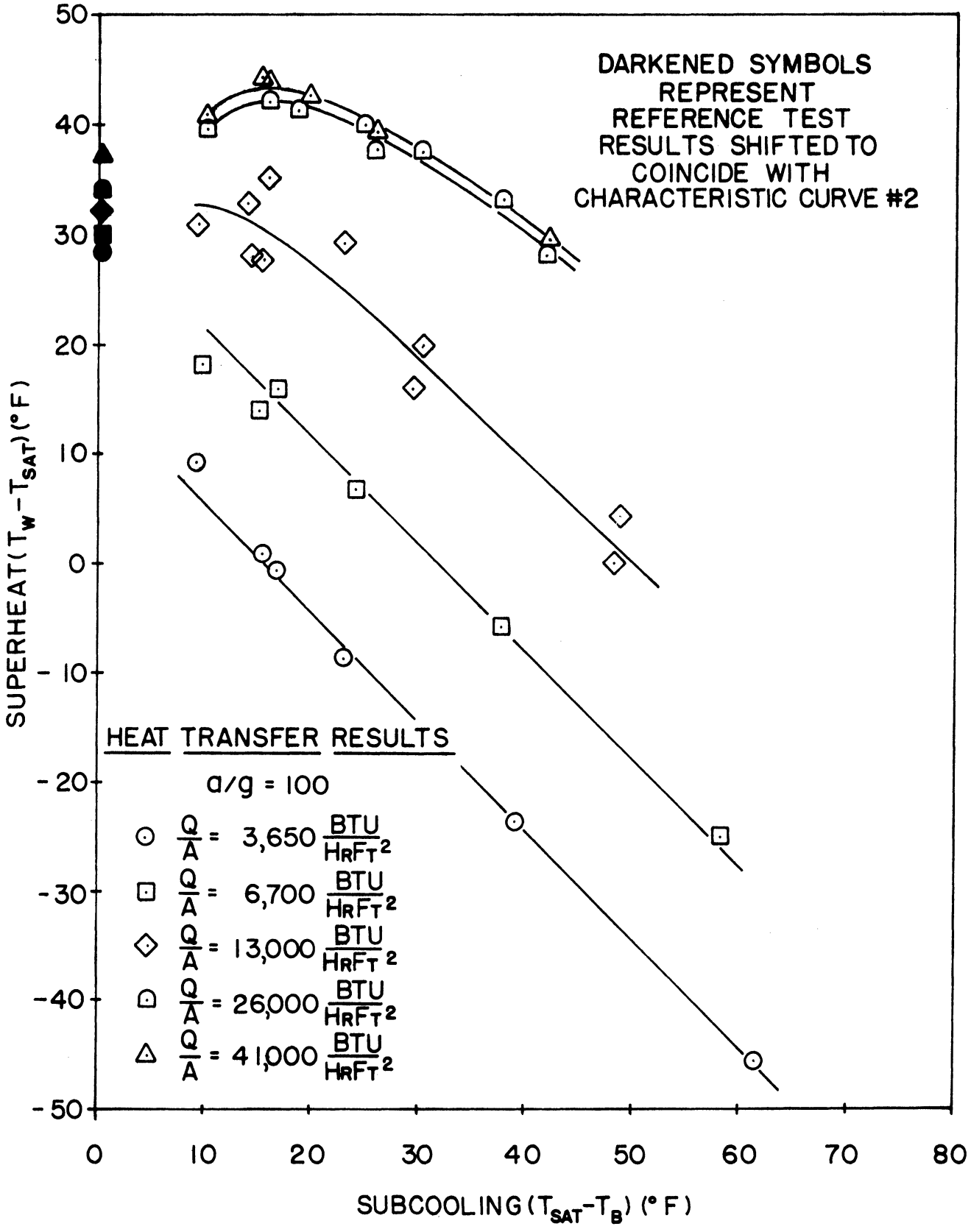

Figure 51. Normalized Heat Transfer Results At a/g = 100.

Figure 52 is a crossplot of the normalized heat transfer results presented in Figures 49 to 51. The transition between boiling heat transfer and non boiling heat transfer can be seen to shift to higher values of heat flux as subcooling and/or acceleration increases. As acceleration increases within the limits $1 \leq a/g \leq 100$, the superheat level required to transfer heat at $Q/A = 25{,}000$ BTU/hr ft^2 increases approximately 4°F whereas the superheat level required to transfer heat at $Q/A = 7{,}000$ BTU/hr ft^2 decreases approximately 9°F for small values of subcooling in the range $0°F \leq (T_{SAT}-T_B) \leq 10°F$. The difference in behaviour is the result of the difference in response of natural convection and nucleate boiling to the increase in acceleration. Subcooling has a pronounced effect upon the superheat at all levels of acceleration in the non boiling regime where natural convection is predominant but the effect is smaller in the boiling regime, in agreement with the observations of Rohsenow and Clark[5] and McAdams.[44]

Figure 53 presents a comparison of the oxide coated heater surface test results and the metal foil heater surface test results obtained at $Q/A = 26{,}000$ BTU/hr ft^2 and $a/g = 1$, 10 and 100. Both sets of results have been normalized with respect to the corresponding characteristic boiling curves (Characteristic Curve #2 and Characteristic Curve #3 in Figure 26 respectively). The excellent agreement observed in Figure 26 and Figure 53 for fully established nucleate boiling at $a/g = 1$ is not observed at $a/g = 10$ and $a/g = 100$, although the variation of superheat with subcooling is similar. As a result, it may be concluded that the nucleate boiling heat transfer phenomenon is a function of surface condition and that despite the similarity in roughness measurements indicated in Table I, the oxide coated heater surface and metal foil heater

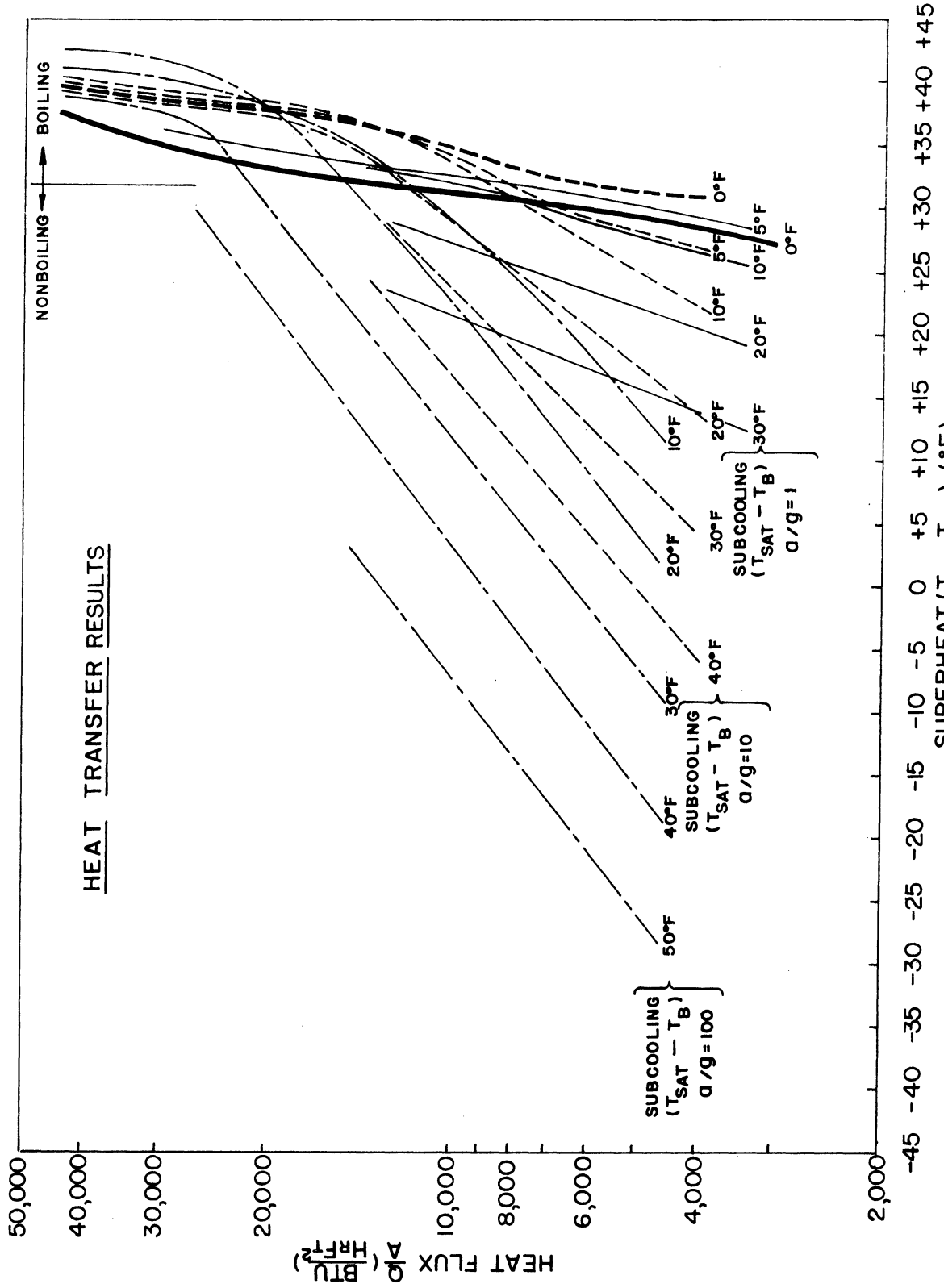

Figure 52. Crossplot Of Heat Transfer Results.

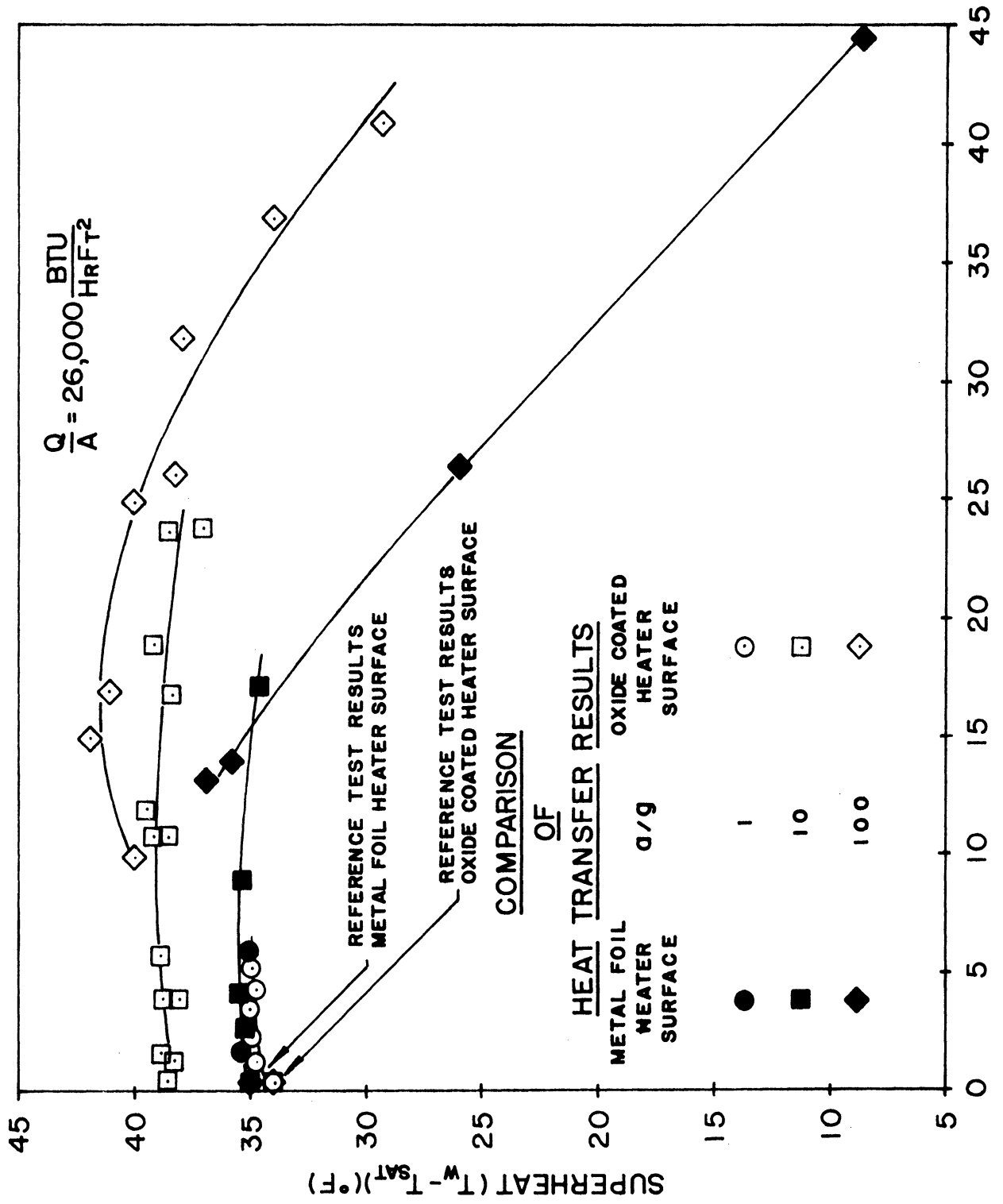

Figure 53. Comparison Of Heat Transfer Results For Different Heater Surfaces.

surface differ in some significant manner. One surface condition was maintained throughout the present study by the use of a single heater surface, and therefore the conclusions of the present investigation concerning the influence of heat flux, subcooling and acceleration upon the nucleate boiling heat transfer phenomenon may be peculiar to the particular fluid-surface combination.

C. Temperature Profiles

The influence of heat flux, subcooling and acceleration upon the thickness of the "thermal boundary layer" adjacent to the heat transfer surface is considered in this section. The boundary layer thickness is defined as that displacement from the heat transfer surface at which the temperature gradient in the liquid approaches an approximately constant value. It is recognized that this criterion is arbitrary and includes a degree of subjectiveness, but it is also felt that relative values will not be changed significantly by any criterion. Using the criterion outlined above, sufficient information was extracted from the temperature profiles presented in Figures 31 to 37 to plot Figure 54, which correlates the boundary layer thickness with heat flux, subcooling and acceleration.

Increasing heat flux causes boundary layer thickness to decrease, in qualitative agreement with the results of Marcus and Dropkin[34] for saturated nucleate boiling of water on a nickel plated copper heater surface under standard gravity conditions. On the other hand, increasing subcooling causes the boundary layer thickness to increase. The rate of increase appears to be somewhat dependent on heat flux. Furthermore, the boundary layer thickness decreases as the acceleration increases from

$a/g = 1$ to $a/g = 10$ and although it was not possible to measure the boundary layer thickness at $a/g = 100$, it is thought that boundary layer thickness decreases further as acceleration increases from $a/g = 10$ to $a/g = 100$.

Recently, Lippert and Dougall[46] measured temperature profiles for saturated boiling Freon with a microthermocouple made from wire five times the diameter of the wire from which the microthermocouple of the present investigation was made. The temperature profiles reported are in excellent agreement with the temperature profiles of the present investigation for displacements greater than ten thousandths of an inch and accordingly the boundary layer thickness is nearly identical to that plotted in Figure 54 for saturated boiling at $a/g = 1$. However, as might be expected, the temperature profiles differ somewhat for displacements less than ten thousandths of an inch; those reported in the present investigation are thought to be more reliable because the temperature measurements upon which they are based were more precise owing to the smaller size of wire used.

D. Site Density

The results presented in Figures 38 to 40 pertaining to the active site density are crossplotted in Figure 55 to demonstrate the influence of heat flux, subcooling and acceleration upon this parameter. The results pertaining to the average population density vary similary and consequently the relative effects indicated in Figure 55 for active site density pertain to average population density as well. The average population density and active site density are correlated in Section G, Chapter VII.

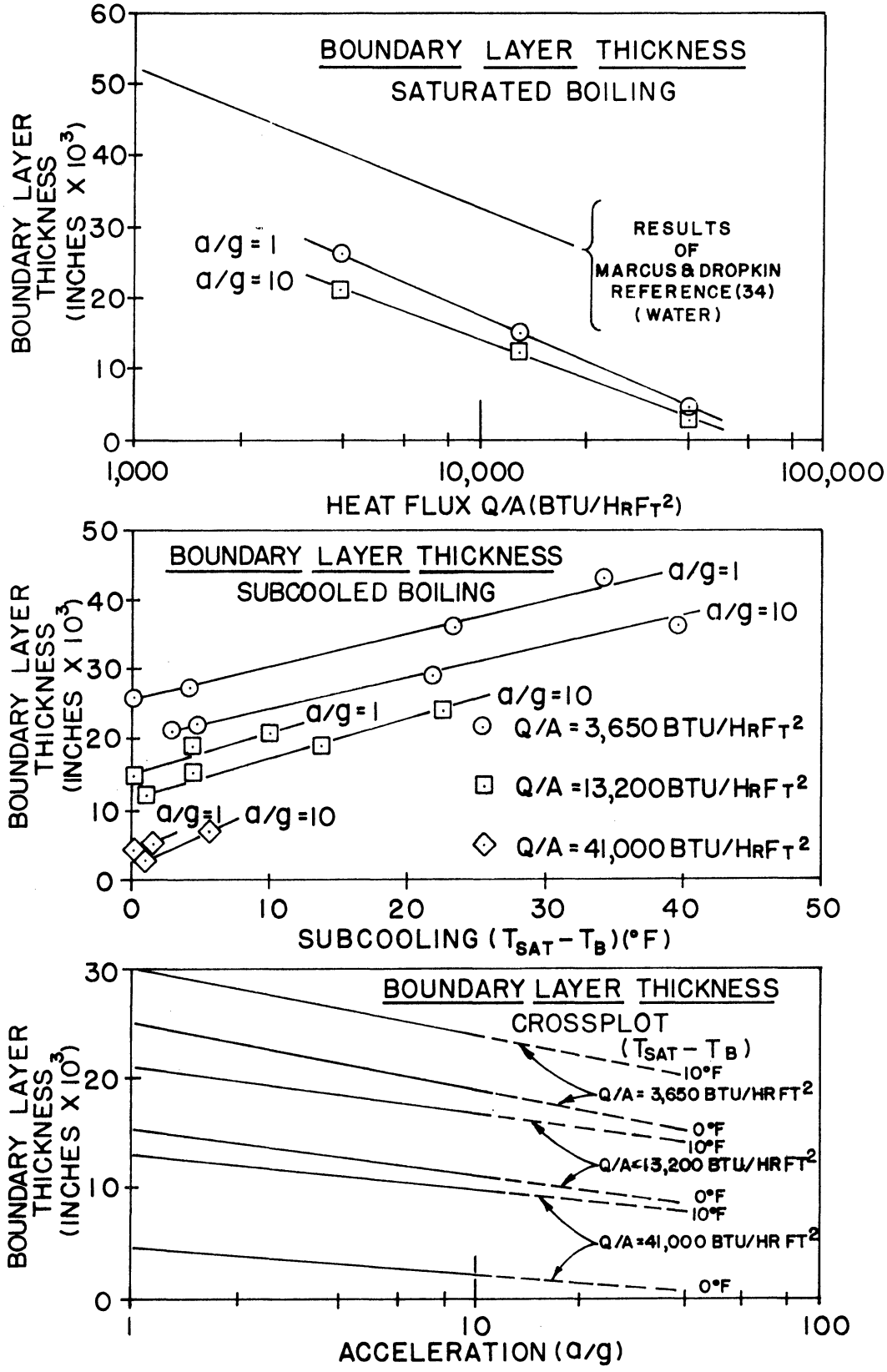

Figure 54. Boundary Layer Thickness Results.

In accordance with the results of numerous investigators, including Westwater and Kirby[31] and Gaertner and Westwater,[47] increasing heat flux can be seen to cause additional nucleation sites to become active to facilitate the transfer of the additional heat. The results of Westwater and Kirby[31] for carbon tetrachloride boiling on an artificially roughened oxide coated glass surface and the results of Gaertner and Westwater[47] for a water-nickel salt solution boiling on a copper surface are included on Figure 55 for the sake of comparison. It is apparent that differences in surface-fluid characteristics greatly influence active site density, since a comparison of the standard gravity results at a common heat flux level indicates that the site densities observed in the present investigation are approximately one order of magnitude greater than those observed by Westwater and Kirby[31] and approximately three orders of magnitude greater than those observed by Gaertner and Westwater.[47] However, these results are consistent according to the Gaertner site activation theory which is discussed below.

Gaertner[48] advanced a site activation theory in which the active site density was related to the fluid properties, system pressure and surface temperature by the relationship

$$\left(\frac{N}{A}\right) = N_o \exp\left\{ -\left[\frac{16\pi\sigma^3 M^2 N^*}{3\,\rho_\ell^2\, R\, [\ln(\frac{P_\infty}{P_v})]^2} \right] \phi \left(\frac{1}{T_W}\right)^3 \right\} \qquad (15)$$

in which N_o and ϕ are arbitrary constants which were included to correct the bulk fluid nucleation model upon which the theory was based for the effect of nucleation at a surface. Only a single set of data

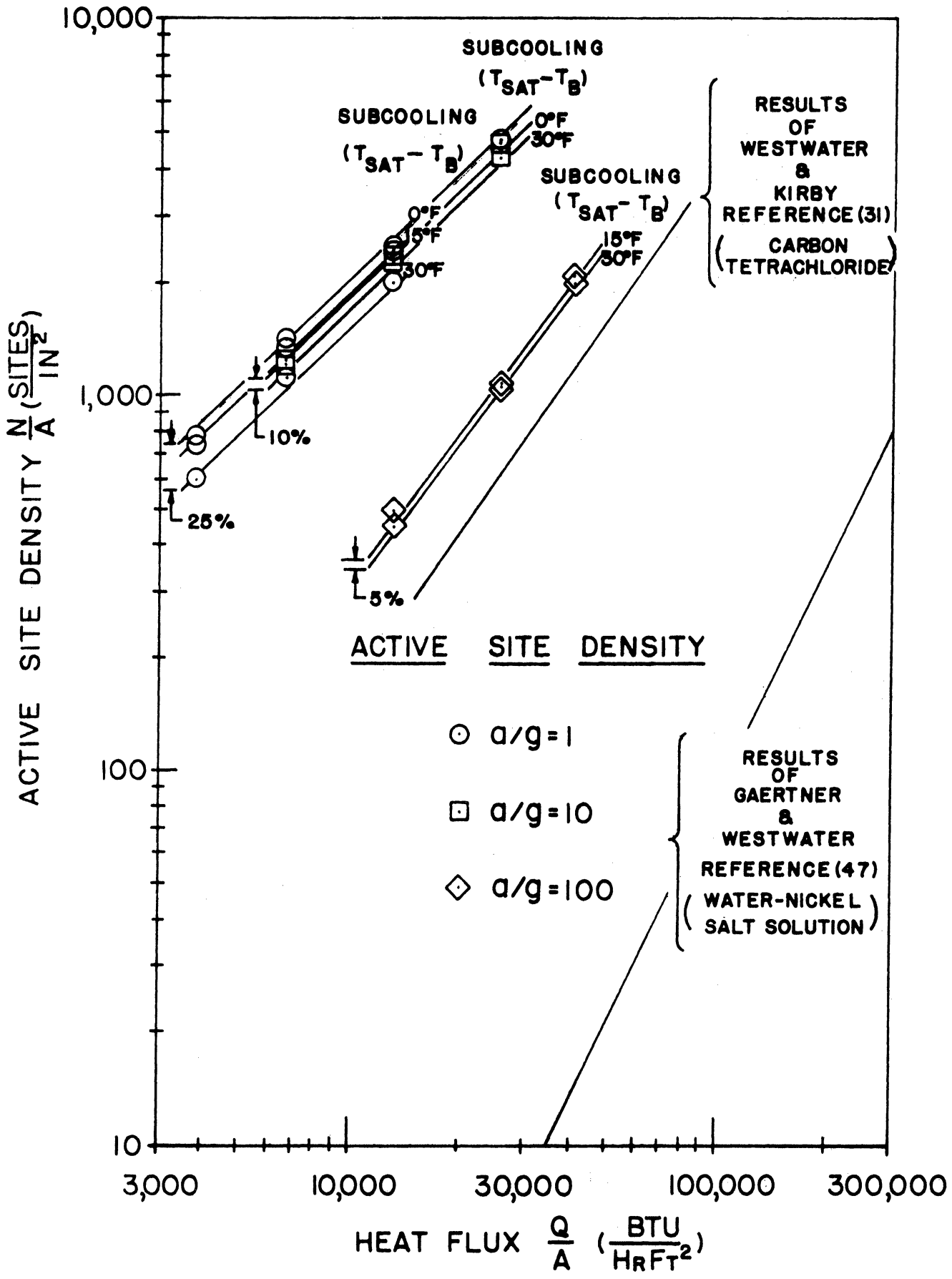

Figure 55. Active Site Density Results.

drawn from Reference (46) was available to test this theory, and although it was possible to demonstrate that active site density varied with surface temperature in the manner predicted, it was not possible to investigate the influence of fluid property variations. The three sets of data presented in Figure 55 enable this effect to be evaluated.

Figure 56 depicts the variation of the logarithm of active site density with inverse surface temperature cubed. The results of the present investigation for saturated boiling Freon at standard gravity have been correlated by a straight line, indicating that active site density varies with the exponential of inverse temperature cubed as predicted by the Gaertner site activation theory. Two additional straight lines have been plotted, corresponding to the carbon tetrachloride results of Reference 31 evaluated by the present author and the water-nickel salt solution results of Reference 47 evaluated in Reference 48. The correlation of the three sets of data plotted in the manner outlined above enables the surface-fluid characteristic constants N_o and ϕ to be evaluated for each surface-fluid combination represented; the numerical values obtained have been indicated on Figure 56 and listed in Table IX. The straight lines correlating active site density with inverse temperature cubed for Freon, carbon tetrachloride and water-nickel salt solution are observed to be nearly parallel in Figure 56 as a result of the fact that the product

$$\left[\frac{16\pi\sigma^3 M^2 N^*}{3\rho_\ell^2 R^3 \left[\ln\left(\frac{P_\infty}{P_v}\right)\right]^2} \right] \phi$$

is almost invariant for the three fluids as indicated in the right hand column of Table IX.

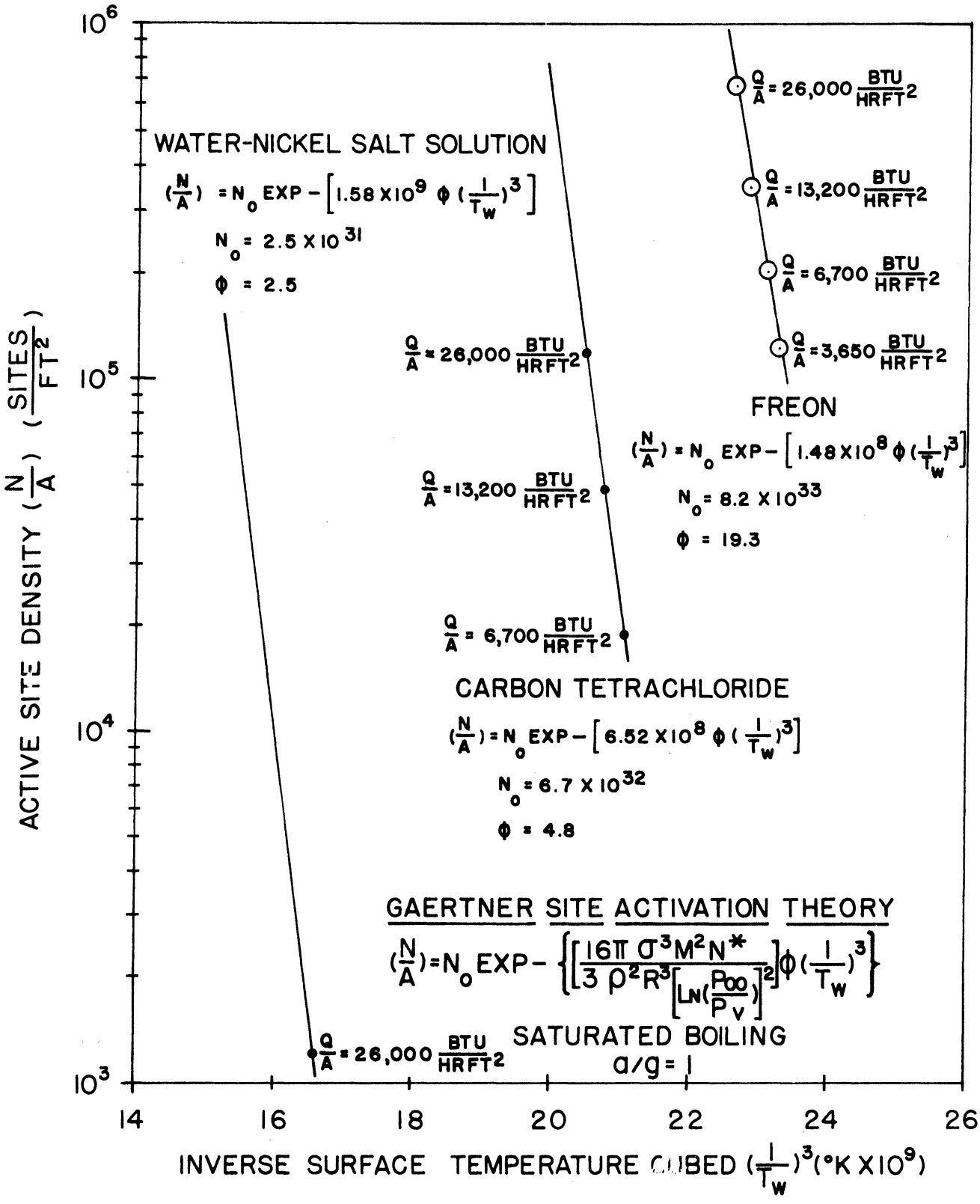

Figure 56. Evaluation Of Gaertner Site Activation Theory.

TABLE IX

TABULATION OF PARAMETERS IN GAERTNER
SITE ACTIVATION THEORY

Fluid	$\left[\frac{16\pi\sigma^3 M^2 N^*}{3\rho_\ell^2 R^3 [\ln(\frac{P_\infty}{P_v})]^2}\right]$	N_o	ϕ	$\left[\frac{16\pi\sigma^3 M^2 N^*}{3\rho_\ell^2 R^3 [\ln(\frac{P_\infty}{P_v})]^2}\right] \phi(\frac{1}{T_W})^3$
Freon	1.48×10^8 °K^3	8.2×10^{33}	19.3	$2.85\times10^9/T_W^3$
Carbon Tetrachloride	6.52×10^8 °K^3	6.7×10^{32}	4.8	$3.12\times10^9/T_W^3$
Water-Nickel Salt Solution	1.58×10^9 °K^3	2.5×10^{31}	2.5	$3.95\times10^9/T_W^3$

The influence of surface-fluid characteristics upon the active site density can be explained by the Gaertner site activation theory. The exponential term (describing the fraction of the potentially active sites activated by a particular combination of system pressure and surface temperature) and the coefficient (describing the number of potentially active sites per unit area for a particular fluid-surface combination) determine the active site density. The fluid properties and surface-fluid characteristic constants affect the exponential term and coefficient in such a way that the active site density for Freon is predicted to be approximately one order of magnitude greater than that for carbon tetrachloride and approximately three orders of magnitude greater than that for water-nickel salt solution when the surface temperatures corresponding to a common heat flux level are substituted.

Despite the apparent success in correlating the active site density measurements, the Gaertner site activation theory cannot be used to predict heat flux-superheat relationships at the present time since it is not possible to predict the amount of heat transferred by each nucleation site a priori.

The results of the present investigation in Figure 55 indicate that subcooling has much less influence on the active site density than heat flux and that the effect of a change in subcooling becomes progressively less significant as the acceleration level increases. The lack of influence of subcooling is rather surprising in as much as it was expected that increasing subcooling would cause the total suppression of vapour bubble nucleation when subcooling became large enough to make natural convection the dominate heat transfer mechanism. Despite the fact that according to the analysis performed in Section G, Chapter VII, subcooling was increased sufficiently for natural convection to dominate in several of the test series which were photographed, the corresponding decrease in active site density was not nearly as great as expected. Unfortunately, no comparable results are known which would enable the observed variation in active site density to be corroborated.

In addition to the effect described above, Figure 55 indicates that an increase in acceleration level from $a/g = 1$ to $a/g = 10$ results in a 10% reduction in the active site density and that further increase in acceleration level from $a/g = 10$ to $a/g = 100$ results in an 80% reduction in the active site density. Both Graham and Hendricks[24] and Beckman, Merte and Clark[28] commented upon similar acceleration

induced changes in active site density observed in conjunction with their experimental investigations of water boiling on the surface of narrow Chromel ribbons. Graham and Hendricks[24] reported data which indicate a large reduction in active site density resulting from an increase in acceleration level from $a/g = 1$ to $a/g = 10$ but the geometry of the heat transfer surface is so different from that of the present investigation that a comparison of the magnitudes of the acceleration effect would not be meaningful.

E. Bubble Frequency

The influence of heat flux, subcooling and acceleration upon the frequency of vapour bubble emission is illustrated in Figure 57 in which the results of Figures 44 to 46 are replotted on a single graph. The curves presented show that the frequency of vapour bubble emission varies directly with heat flux and indirectly with subcooling. Furthermore, bubble frequency is unaffected by a change in acceleration level from $a/g = 1$ to $a/g = 10$ but is increased twofold by a change in acceleration level from $a/g = 10$ to $a/g = 100$. These effects are discussed more completely below.

Figure 58, in which the bubble period results of Figure 41 are replotted, demonstrates that both the total period and active period decrease with increasing heat flux. The heat flux effect is explained by the fact that both the surface temperature and the temperature of the fluid adjacent to the heat transfer surface increase with increasing heat flux. As a consequence, vapour bubbles grow more rapidly because of the enhancement of heat transfer in the boundary

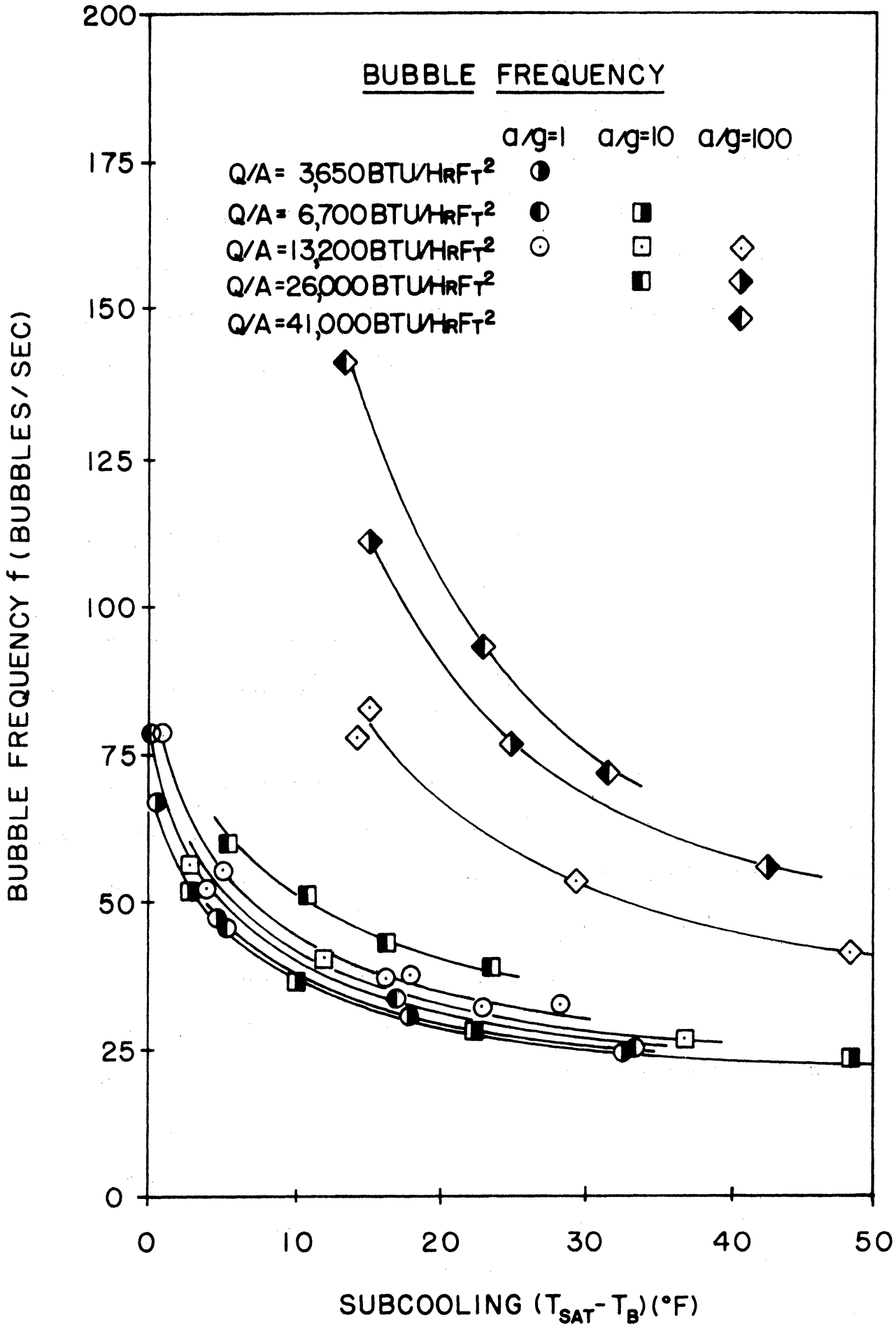

Figure 57. Composite Bubble Frequency Results.

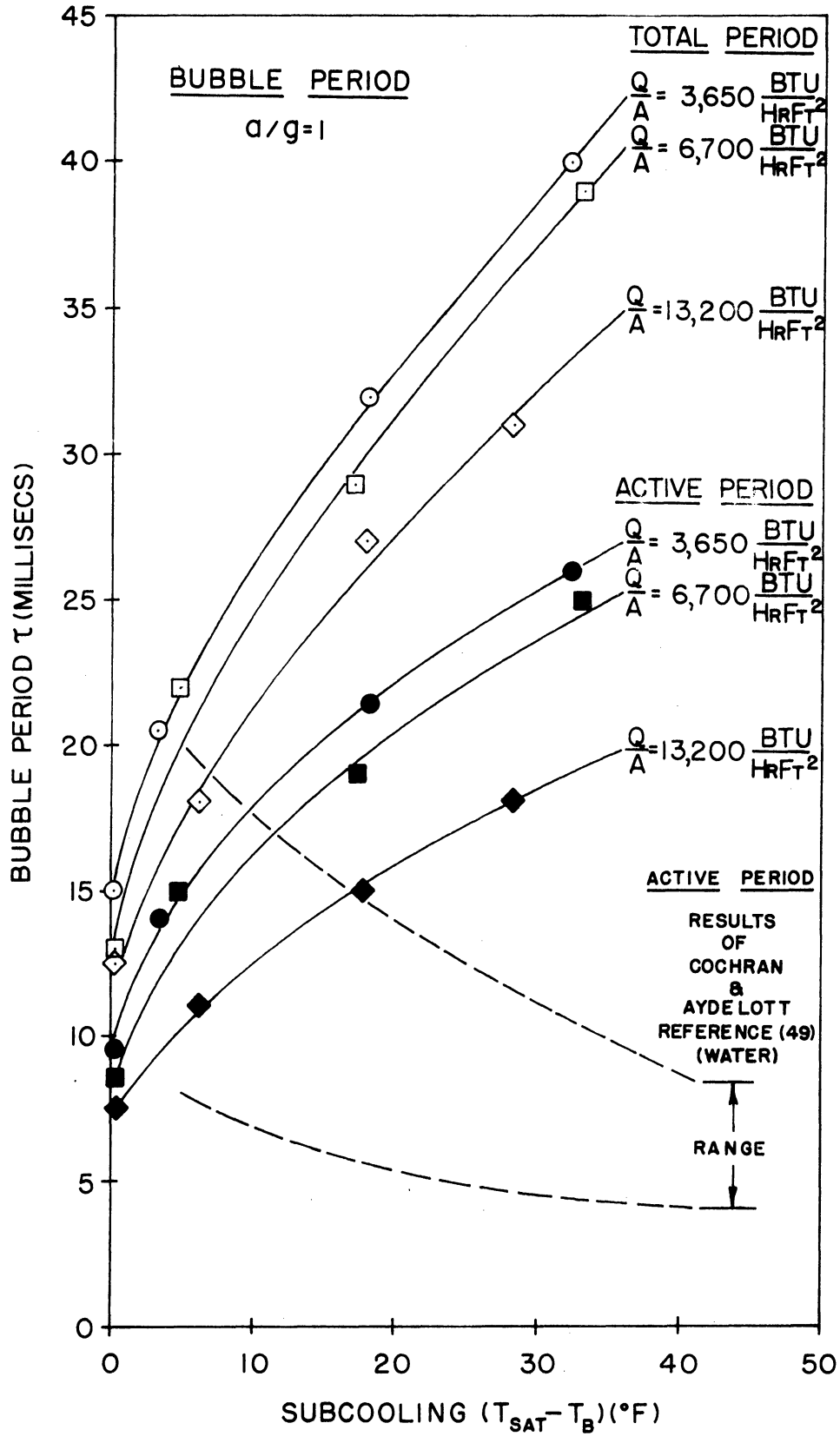

Figure 58. Comparison Of Bubble Period Results.

layer and at the heat transfer surface. The process of vapour bubble departure or collapse commences sooner since the vapour bubbles attain maximum size in a shorter interval of time. The effect of heat flux upon the frequency of vapour bubble emission depicted in the upper portion of Figure 59, in which the results of Figure 57 are crossplotted to show the heat flux effect, is consistent with the explanation advanced above.

As indicated in Figure 57, the influence of subcooling upon the frequency of vapour bubble emission is quite pronounced. Unfortunately, no comparable results are known which would enable the subcooling effect to be evaluated. However, the effect of subcooling upon bubble lifetime (active period) was studied in an investigation of water boiling at the surface of a thin Chromel ribbon at $Q/A = 28{,}900$ BTU/hr ft^2 by Cochran and Aydelott[49] who reported that increasing subcooling decreased the active period. This result is opposite to the results of the present investigation as indicated in Figure 58. The reason for the difference is thought to be differences in bubble dynamics associated with the different fluids; such differences are suggested by the fact that Cochran and Aydelott[49] reported that all of the vapour bubbles observed detached from the heat transfer surface even at high subcooling, whereas the results of the present investigation presented in Table XIV, Appendix D, suggest that the percentage of collapsing bubbles progressively increased with increasing subcooling. However, the bubble samples observed were small in both cases so that these observations are somewhat tenuous. With regard to the present investigation, it would appear that the

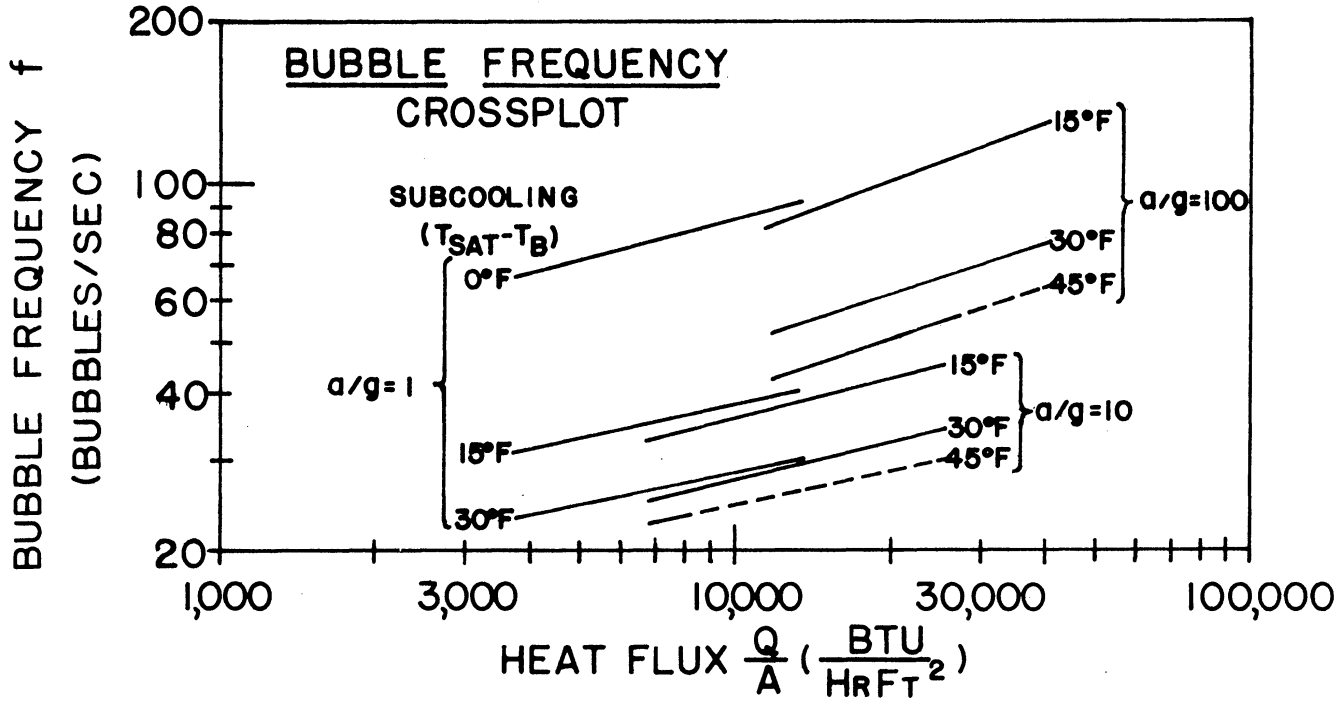

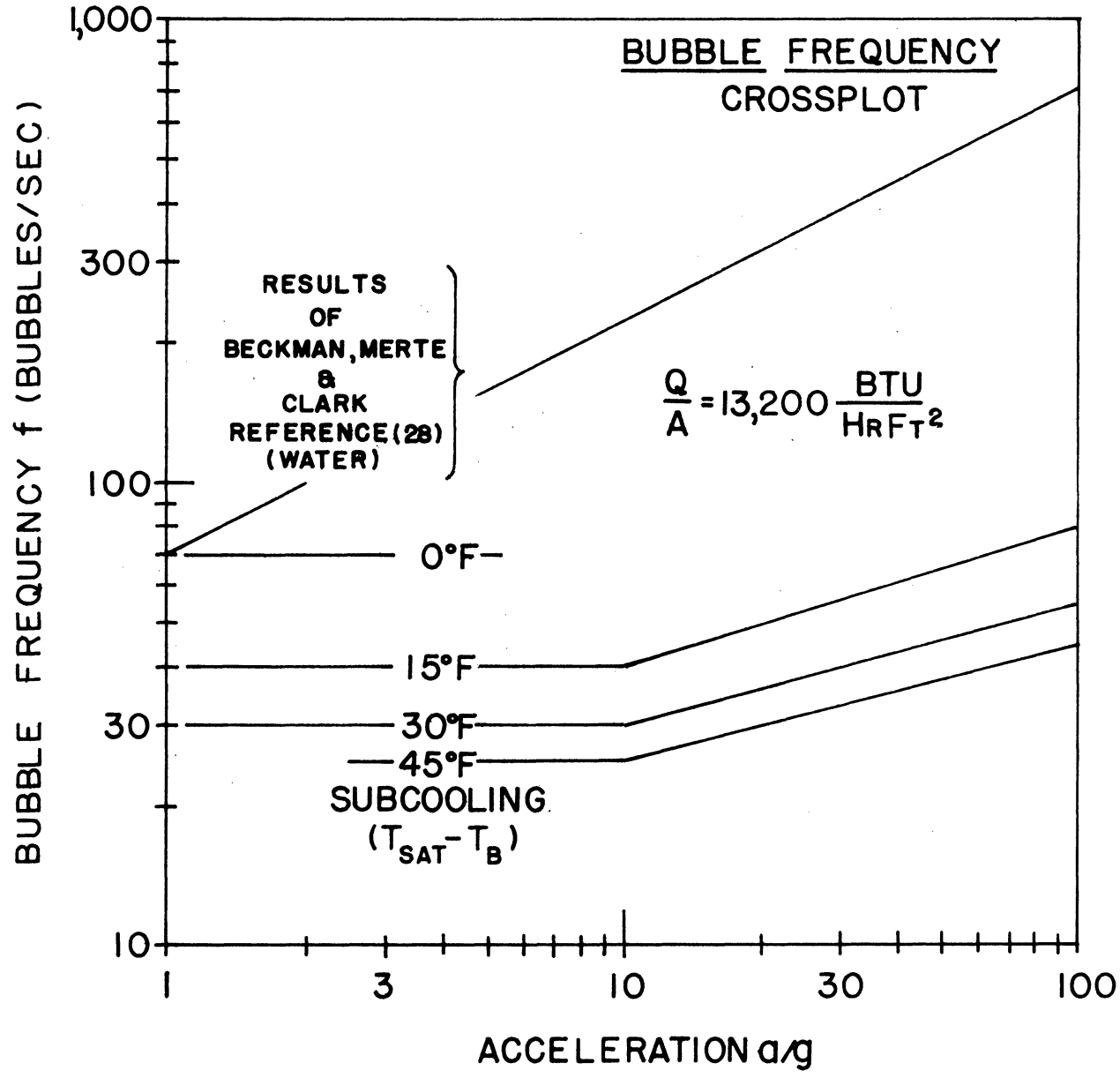

Figure 59. Crossplot Of Bubble Frequency Results.

growth rate was reduced with increasing subcooling, resulting in an increase in the period of time during which the bubble developed before departure or collapse commenced as indicated in Figure 58. Increasing subcooling also increased the inactive period, the difference of the total period and active period plotted in Figure 58, in accordance with the fact that a greater period of time was required to heat the liquid which contacted the surface after the departure or collapse of a vapour bubble to a temperature level at which nucleation could occur.

The influence of acceleration upon the frequency of vapour bubble emission indicated in Figure 57 is emphasized in the lower portion of Figure 59 in which the results of Figure 57 for $Q/A = 13,200$ BTU/hr ft^2 are crossplotted to show the acceleration effect. This heat flux level is the only one for which bubble frequency results are available at all three levels of acceleration. However, it can be seen by referring to the partial results for $Q/A = 6,700$ BTU/hr ft^2 and $Q/A = 26,000$ BTU/hr ft^2 presented in Figure 57 that the acceleration effect observed at $Q/A = 13,200$ BTU/hr ft^2 is not peculiar to this particular heat flux level. The results of Beckman, Merte and Clark[28] for water boiling at the surface of a thin Chromel ribbon which indicate a tenfold increase in frequency of vapour bubble emission corresponding to an increase in acceleration level from $a/g = 1$ to $a/g = 100$ are included in Figure 59 for the sake of comparison.

F. Maximum Bubble Size

The results presented in Figure 47 pertaining to maximum bubble size have been reproduced in Figure 60 for comparison with the experimental results of Van Stralen[50] and Beckman, Merte and Clark.[28] From the

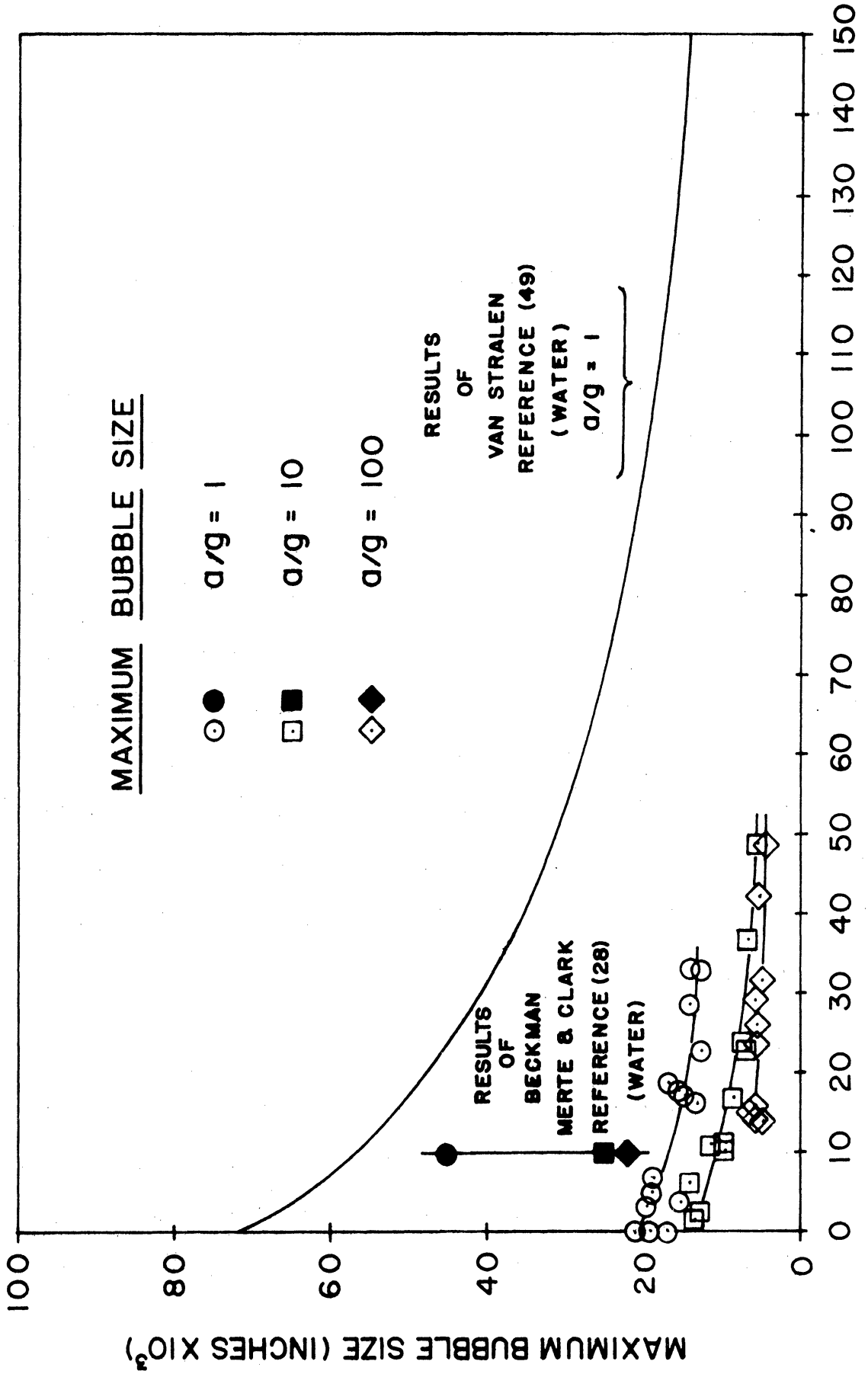

Figure 60. Comparison Of Maximum Bubble Size Results.

graph, it is immediately apparent that the maximum bubble size observed in boiling Freon was much smaller than that observed in boiling water. As explained previously, no attempt was made to indicate the influence which heat flux may have had upon the maximum bubble size results since any heat flux effect was such that it could not be distinguished from the uncertainty in the measurements. Beckman, Merte and Clark[28] and Gaertner[51] have found that maximum bubble size is independent of heat flux and consequently it might be concluded that the heat flux effect is actually non existent. The results of the present investigation for Freon boiling on an oxide coated heater surface show the same dependence upon subcooling as those of Van Stralen[50] for water boiling on a platinum wire at $a/g = 1$ and approximately the same dependence upon acceleration as those of Beckman, Merte and Clark[28] for water boiling on a chromel ribbon at ΔT_{SUB}=10°F; the maximum bubble size for Freon at $a/g = 1$ is approximately one third of the maximum bubble size for water at all levels of subcooling and the influence of acceleration is such that at $\Delta T_{SUB} = 10°F$, a change in acceleration level from $a/g = 1$ to $a/g = 10$ causes an approximate 50% reduction in the maximum bubble size whereas a change in acceleration level from $a/g = 10$ to $a/g = 100$ causes a further 10% reduction in the maximum bubble size for both Freon and water.

G. Interpretation

The discussion to this point has been concerned with the presentation of physical effects which have been deduced from the results of the present investigation. In the section which follows, the discussion is directed towards the interpretation of the heat transfer results in

terms of the various parameters which have been measured including boundary layer thickness, average population density, active site density, frequency of vapour bubble emission and maximum bubble size. The ultimate purpose of this discussion is the clarification of certain aspects of the problem concerning the influence of heat flux, subcooling and acceleration upon nucleate boiling heat transfer which is permitted by the measurements obtained.

The random nature of vapour bubble nucleation, growth and departure or collapse has long been recognized. Bubble characteristics such as average population density, active site density and frequency of vapour bubble emission are best described by statistical distributions provided that sufficient independent measurements are available to make statistical analysis meaningful. Despite the fact that it was not possible to treat the measurements of the present investigation in this fashion because of the relatively small samples available for examination, the average values obtained are thought to be representative. The discussion which follows supports this view by demonstrating the consistency of the measurements of average population density, active site density, active bubble period and inactive bubble period presented in Figures 38 to 43 inclusive.

In terms of average values, average population density and active site density are related through the relationship

$$\begin{bmatrix}\text{Average}\\ \text{Population}\\ \text{Density}\end{bmatrix} \left(\frac{n}{A}\right) = \begin{bmatrix}\text{Probability}\\ \text{Of A Site}\\ \text{Being Active}\end{bmatrix} p \times \begin{bmatrix}\text{Active}\\ \text{Site}\\ \text{Density}\end{bmatrix} \left(\frac{N}{A}\right) \qquad (16)$$

The probability that a particular site is active at a particular instant of time is given by

$$\left[\begin{array}{c}\text{Probability}\\ \text{Of A Site}\\ \text{Being Active}\end{array}\right] \quad p = \left[\frac{\text{Active Bubble Period}}{\text{Total Bubble Period}}\right] \quad \frac{\tau_a}{\tau_a+\tau_i} \tag{17}$$

Combining Equation (16) and Equation (17) leads to the following relationship

$$\left[\frac{(n/A)}{(N/A)}\right] = \frac{\tau_a}{\tau_a+\tau_i} = \frac{\tau_a}{\tau_t} \tag{18}$$

All the bubble characteristics were measured independently from the same source. Hence, the consistency of the values measured under various combinations of heat flux, subcooling and acceleration would be demonstrated by a positive correlation of $\left[\frac{(n/A)}{(N/A)}\right]$ with $(\frac{\tau_a}{\tau_t})$ in the manner indicated by Equation (18). Figure 61 presents such a plot of $\left[\frac{(n/A)}{(N/A)}\right]$ versus $(\frac{\tau_a}{\tau_t})$ which includes a straight line representing Equation (18) and demonstrates favourable overall agreement of the experimentally determined values with the theoretical relationship.

The consistency of the measurements of average population density, active site density, active bubble period and inactive bubble period is thereby demonstrated. However, despite the favourable overall agreement demonstrated in Figure 61, trends are observed which indicate that variations in heat flux, subcooling and acceleration also influenced the correlation of the bubble characteristics. The effects of the variation of these parameters are emphasized in Figure 62 in which $\left[\frac{(n/A)}{(N/A)}\right]$ from Figure 61 has been crossplotted against heat flux, subcooling and acceleration respectively after being divided by $\left[\frac{(n/A)}{N/A}\right]^*$,

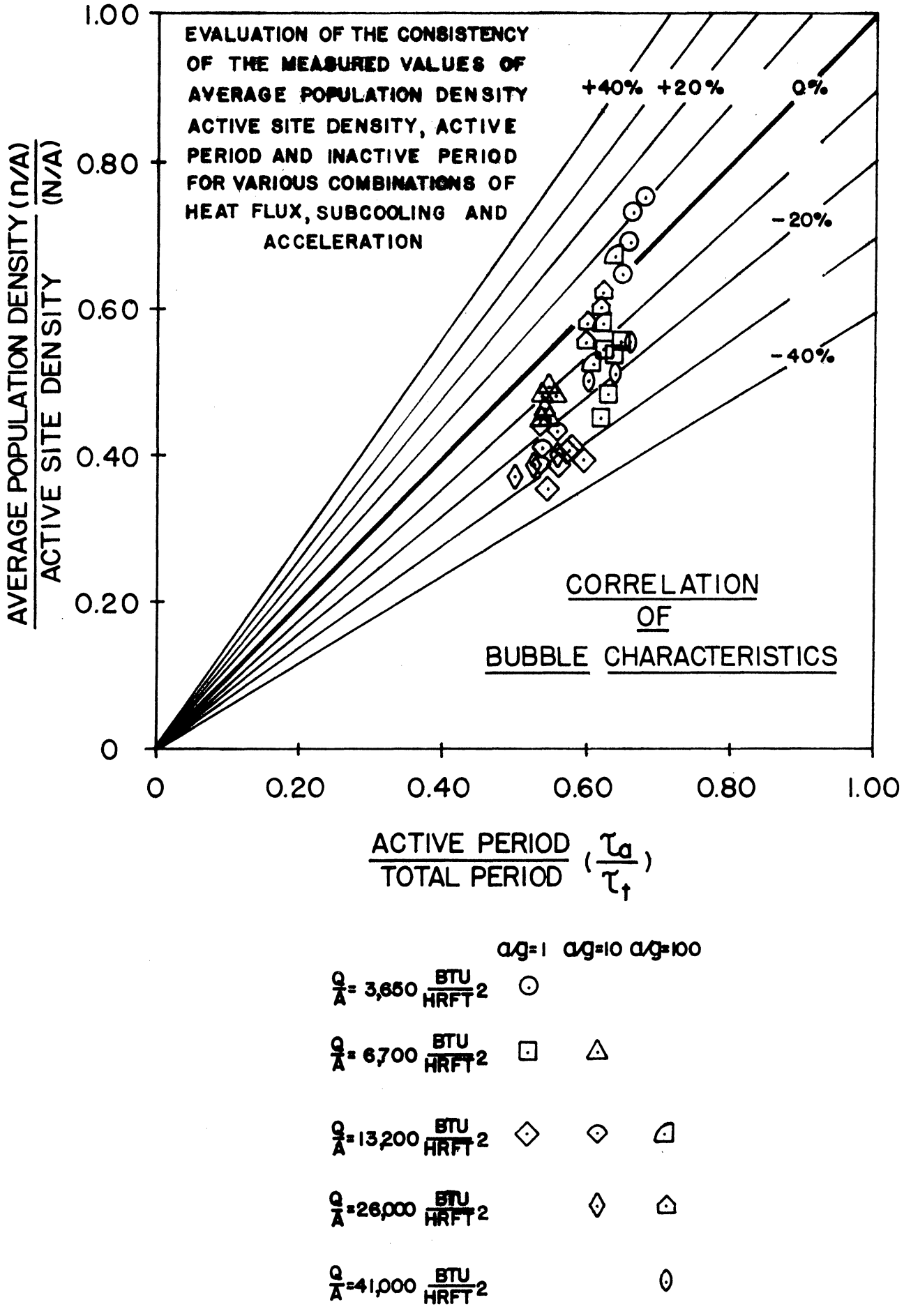

Figure 61. Correlation Of Bubble Characteristics.

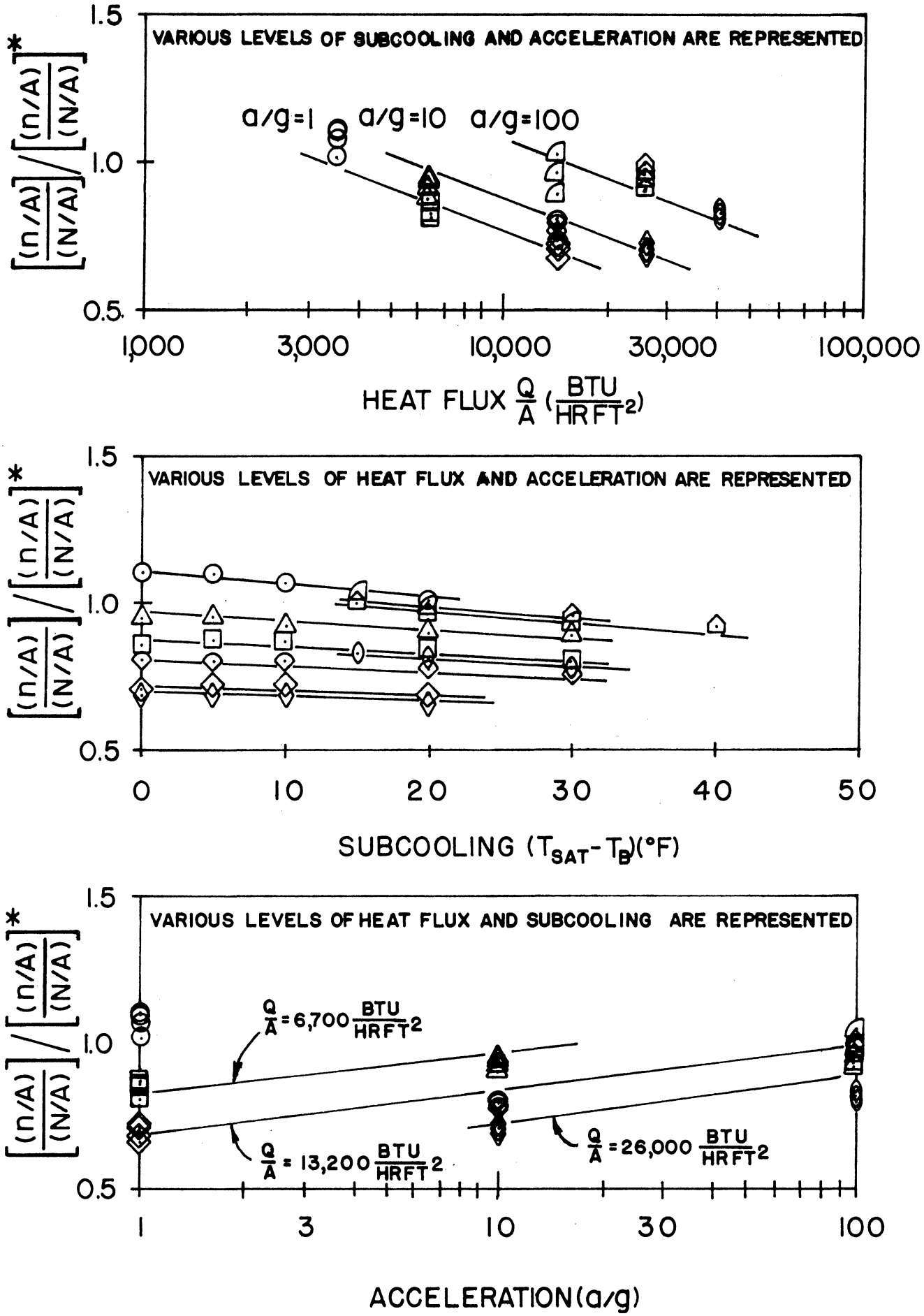

Figure 62. Influence Of Heat Flux, Subcooling And Acceleration Upon Correlation Of Bubble Characteristics.

the value of $\left[\frac{(n/A)}{(N/A)}\right]$ predicted by Equation (18), in order to remove the influence of variations in $(\frac{\tau_a}{\tau_t})$. It is observed that $\left[\frac{(n/A)}{(N/A)}\right] \Big/ \left[\frac{(n/A)}{(N/A)}\right]^*$, which represents the fraction of the active sites occupied at a particular instant of time, decreases with increasing heat flux and subcooling but increases with increasing acceleration. The reason for this dependence is not known but apparently variations in heat flux, subcooling and acceleration affect the mechanics of vapour bubble nucleation, growth and departure or collapse in such a way as to cause the effects observed.

Turning next to the heat transfer results, a relationship expressing natural convection heat transfer was sought in order that the natural convection heat transfer component might be separated from the nucleate boiling heat transfer component in the subsequent analysis. The data required to derive such an expression was selected from the heat transfer results presented in Figures 49 to 51 by making use of the fact that in natural convection heat transfer, the surface-fluid temperature difference remains constant when heat flux and acceleration are maintained constant and subcooling is varied. The consequence of this fact, which is expressed mathematically by the relationship

$$(T_W - T_B) = (T_W - T_{SAT}) + (T_{SAT} - T_B) = \text{Constant} \qquad (19)$$

is that when superheat $(T_W - T_{SAT})$ is differentiated by subcooling $(T_{SAT} - T_B)$, the relationship

$$\frac{d(T_W - T_{SAT})}{d(T_{SAT} - T_B)} = -1 \qquad (20)$$

is obtained, implying that the curve relating superheat to subcooling at constant heat flux and acceleration assumes a negative 45° slope. Figures 49 to 51 indicate that this condition was satisfied for a number of combinations of heat flux, subcooling and acceleration among which five distinctively different natural convection heat transfer conditions were identified and used to plot Nusselt number versus Prandtl-Grashof number in Figure 63. The straight line correlating these data points is expressed by the relationship

$$Nu = 0.160\ (PrGr)^{1/3} \tag{21}$$

which can be seen to be in excellent agreement with the correlations of Fishenden and Saunders[41] and Kutateladze and Borishanskii.[52]

In accordance with Merte and Clark,[20] it was assumed that natural convection and nucleate boiling act independently of each other. Further, it was assumed that the heat transferred by nucleate boiling Q_{NB} and the heat transferred by natural convection Q_{NC} were confined to the area fractions A_{NB}/A_T and A_{NC}/A_T respectively which varied with heat flux, subcooling and acceleration as a result of the influence of these parameters upon maximum bubble size and average population density. As a consequence of these assumptions, the total heat transferred Q_T could be written

$$Q_T = Q_{NB} + Q_{NC} \tag{22}$$

and the total heat flux Q_T/A_T could be written

$$\frac{Q_T}{A_T} = \left(\frac{Q_{NB}}{Q_T}\right)\left(\frac{Q_T}{A_T}\right) + \left(\frac{Q_{NC}}{A_{NC}}\right)\left(\frac{A_{NC}}{A_T}\right) \tag{23}$$

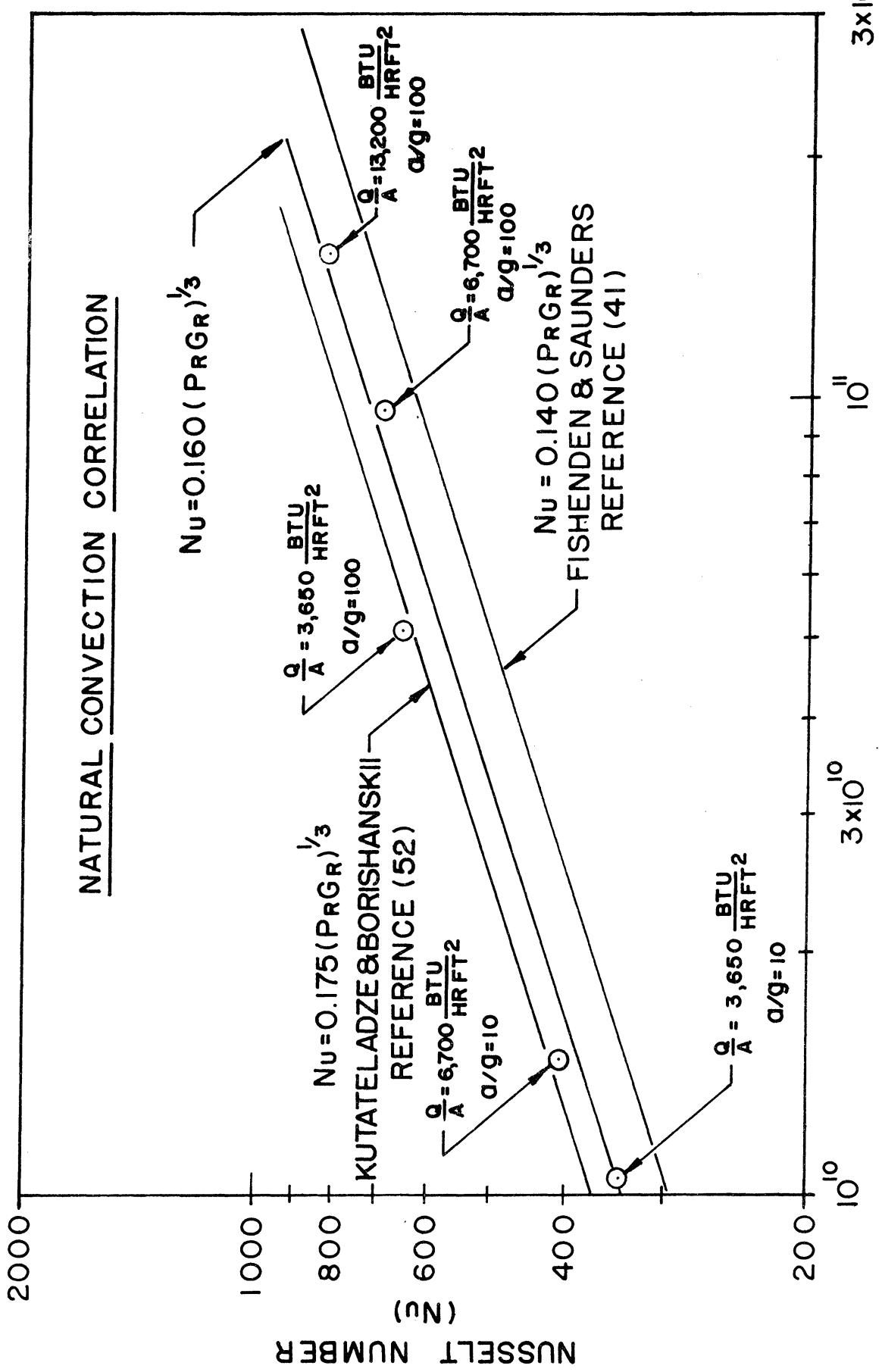

Figure 63. Natural Convection Correlation.

Equation (23) was then arranged to read

$$\frac{Q_{NB}}{Q_T} = 1 - \left[\frac{(Q_{NC}/A_{NC})}{(Q_T/A_T)} \right] \left(\frac{A_{NC}}{A_T} \right) \tag{24}$$

where the natural convection heat flux fraction $\frac{(Q_{NC}/A_{NC})}{(Q_T/A_T)}$ is given by

$$\frac{(Q_{NC}/A_{NC})}{(Q_T/A_T)} \simeq \frac{16.0(a/g)^{1/3} (T_W - T_B)^{4/3}}{(Q_T/A_T)} \tag{25}$$

and the natural convection area fraction (A_{NC}/A_T) is given by

$$\left(\frac{A_{NC}}{A_T} \right) = \left(1 - \frac{A_{NB}}{A_T} \right) = \left[1 - K \times \frac{\pi}{4} D_{MAX}^2 \left(\frac{n}{A} \right) \right] \tag{26}$$

The numerator of the natural convection heat flux fraction Q_{NC}/A_{NC} given by Equation (25) was derived by regrouping Equation (21) and substituting the fluid property values for Freon which remained nearly constant over the range of temperatures concerned; the denominator Q_T/A_T is simply the total heat flux generated at the heat transfer surface. The natural convection heat flux fraction, obtained by substituting the particular surface-fluid temperature difference corresponding to each combination of heat flux, subcooling and acceleration represented in Figures 49 to 51, is plotted in Figure 64.

The natural convection area fraction A_{NC}/A_T given by Equation (26) was obtained by subtracting the portion of the total heat transfer surface occupied by vapour bubbles at a given instant of time from unity. The occupied portion of the total heat transfer surface is

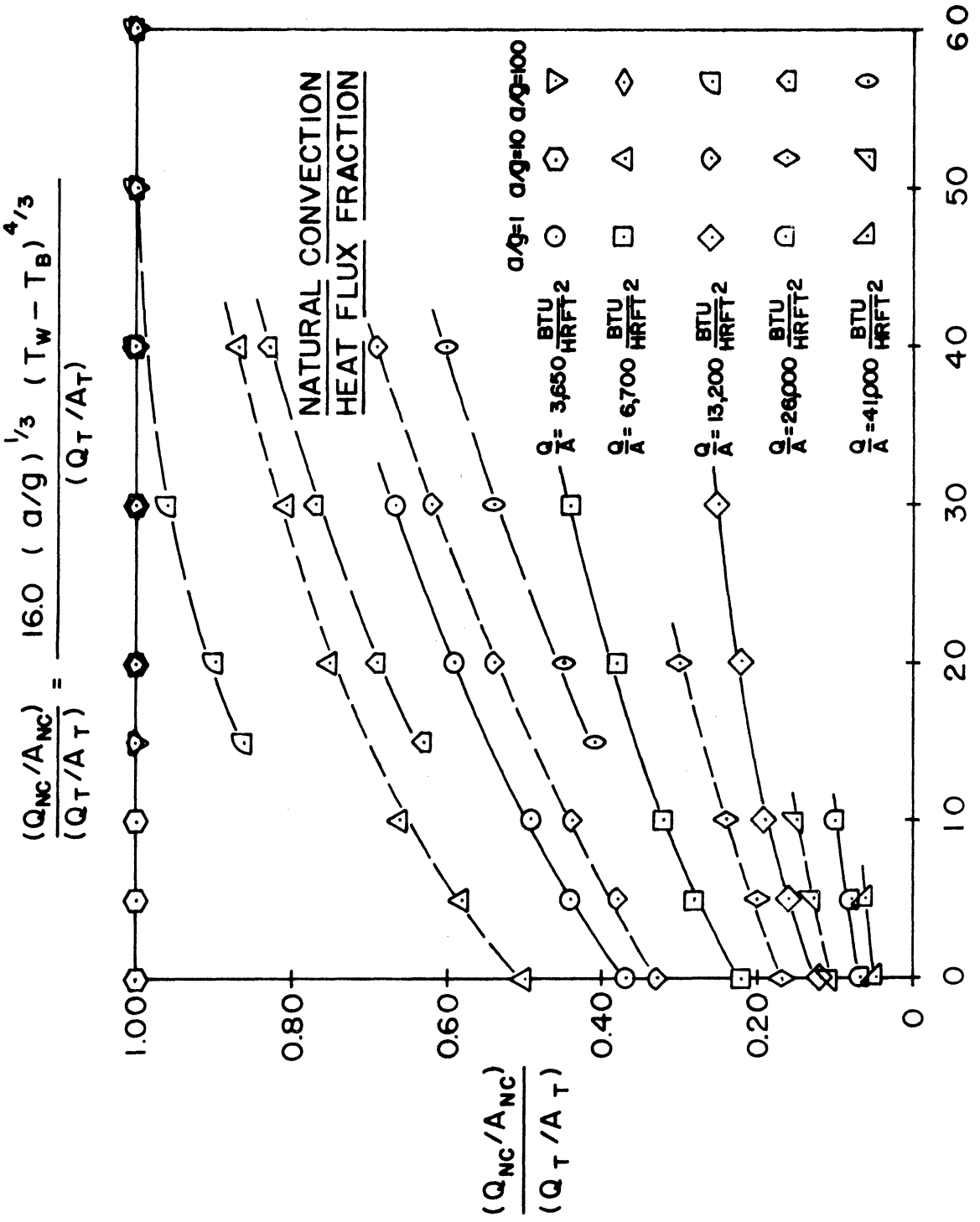

Figure 64. Natural Convection Heat Flux Fraction.

expressed by the product of the measured projected area of the vapour bubbles $\frac{\pi}{4} D^2_{MAX}$, the measured average population density $(\frac{n}{A})$ and a coefficient K which was introduced to relate the area influenced by a bubble to the projected area of the bubble. Obviously, $K = 1$ is the lower limit of the coefficient whereas the upper limit is not known. Han and Griffith,[15] who investigated the area influenced by a departing bubble by means of a simple experiment in which a sphere was pulled from the bottom of a tank of water which had been covered with chalk dust, reported that the area influenced had approximately twice the diameter of the sphere. Assuming that the area influenced bears the same relationship to the bubble diameter, then $K = 4$ is the upper limit of the coefficient. In the analysis which follows, $K = 3$ was used since the use of $K = 4$ leads to the unreasonable conclusion that A_{NB}/A_T is greater than unity for some combinations of heat flux, subcooling and acceleration. Figure 65 depicts the natural convection area fraction corresponding to each combination of heat flux, subcooling and acceleration for which measurements of maximum bubble size and average population density were obtained.

Figure 66 depicts the natural convection heat transfer fraction given by the relationship

$$\frac{Q_{NC}}{Q_T} = \left[\frac{(Q_{NC}/A_{NC})}{(Q_T/A_T)} \right] \left(\frac{A_{NC}}{A_T} \right) \qquad (27)$$

as a function of heat flux, subcooling and acceleration. All of the curves plotted increase with increasing subcooling and it is observed that the natural convection heat flux fraction decreases with increasing

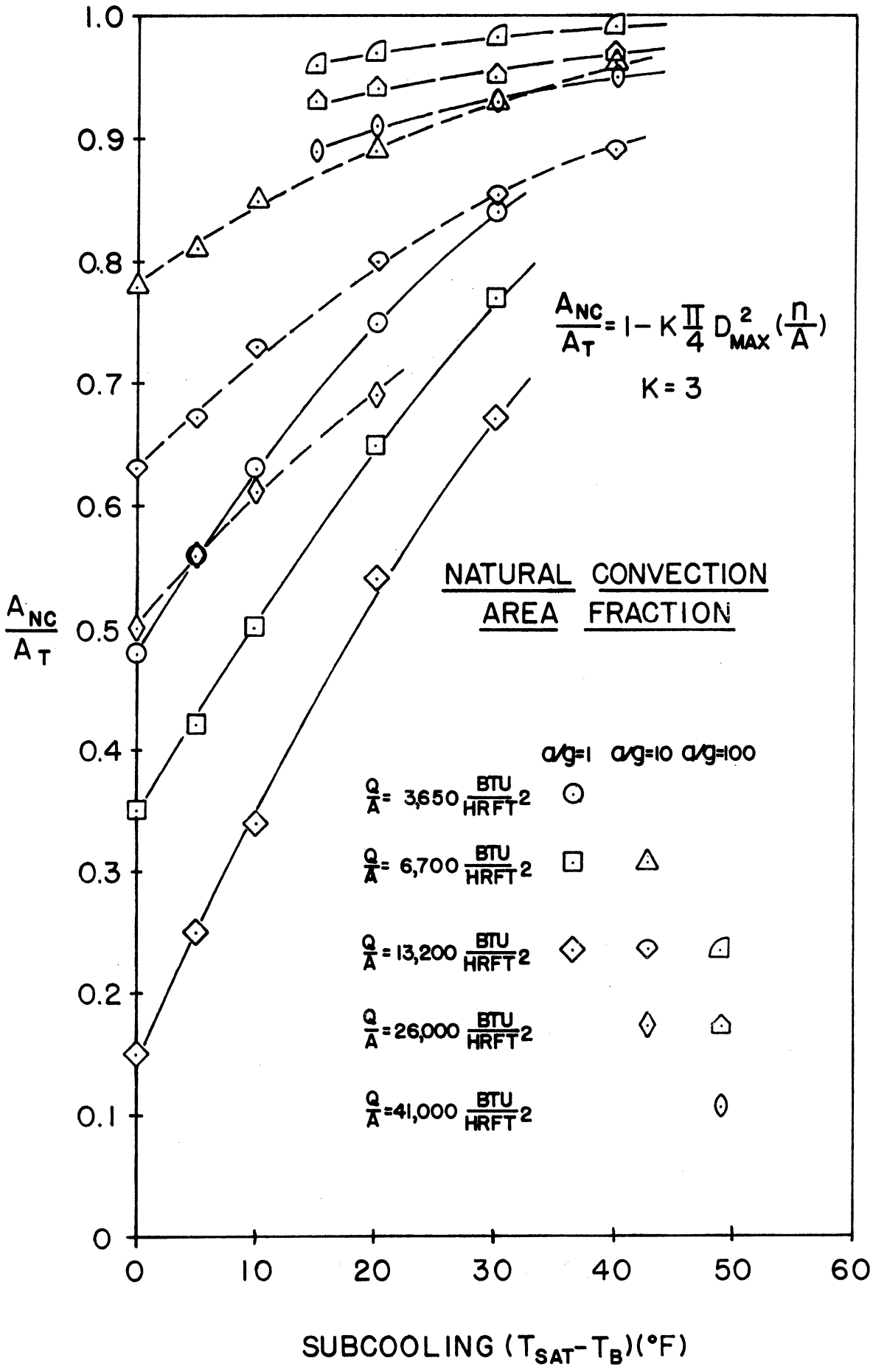

Figure 65. Natural Convection Area Fraction.

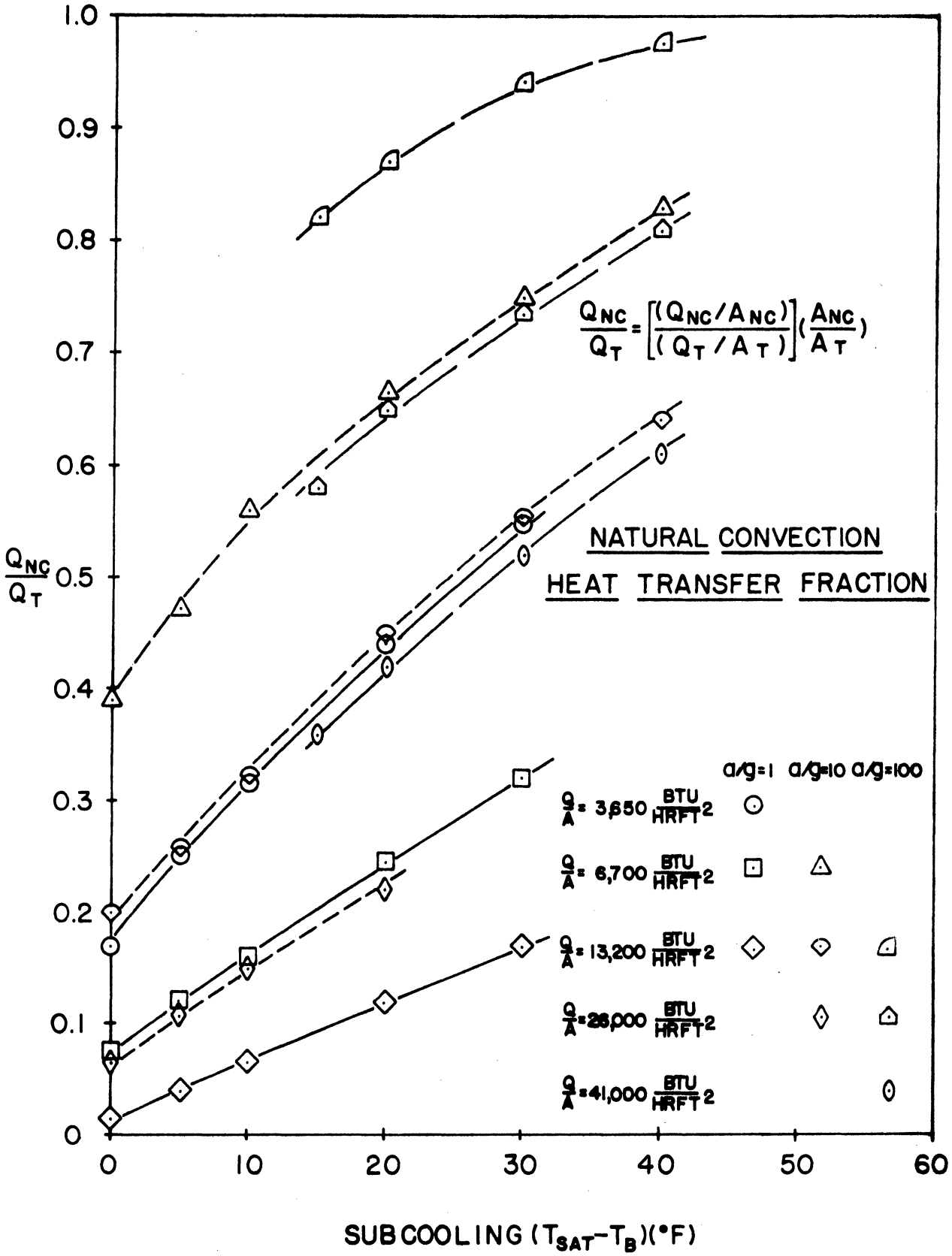

Figure 66. Natural Convection Heat Transfer Fraction.

heat flux at constant acceleration and increases with increasing acceleration at constant heat flux. The functional relationship between natural convection heat transfer fraction and heat flux, subcooling and acceleration is expressed by the empirical correlation

$$\frac{Q_{NC}}{Q_T} = 1 - \exp - \left[63.0 \frac{(a/g)^{0.57}(\Delta T_{SUB}+10.0)}{(Q_T/A_T)} \right] \qquad (28)$$

Figure 67 demonstrates the excellent agreement of the data points representing various levels of heat flux, subcooling and acceleration with the relationship expressed by Equation (28). Since Equation (28) predicts that the natural convection heat transfer fraction approaches unity asymptotically, then the conditions under which natural convection dominates the heat transfer phenomenon can be computed by the relationship

$$- \frac{(a/g)^{0.57}(\Delta T_{SUB}+10.0)}{(Q_T/A_T)} > (\ln 0.01) \times (\frac{1}{63.0}) > -0.075 \qquad (29)$$

which has been derived by assuming that 0.99 is equivalent to unity for the purposes of this numerical analysis. Whenever any two of the independent variables heat flux, subcooling and acceleration are specified, then Equation (29) may be used to determine the value of the third independent variable for the conditions under which natural convection dominates the heat transfer phenomenon.

The remainder of this section concerns the determination of the total bubble heat transfer, that quantity of heat transferred by the growth and subsequent departure or collapse of a single vapour bubble.

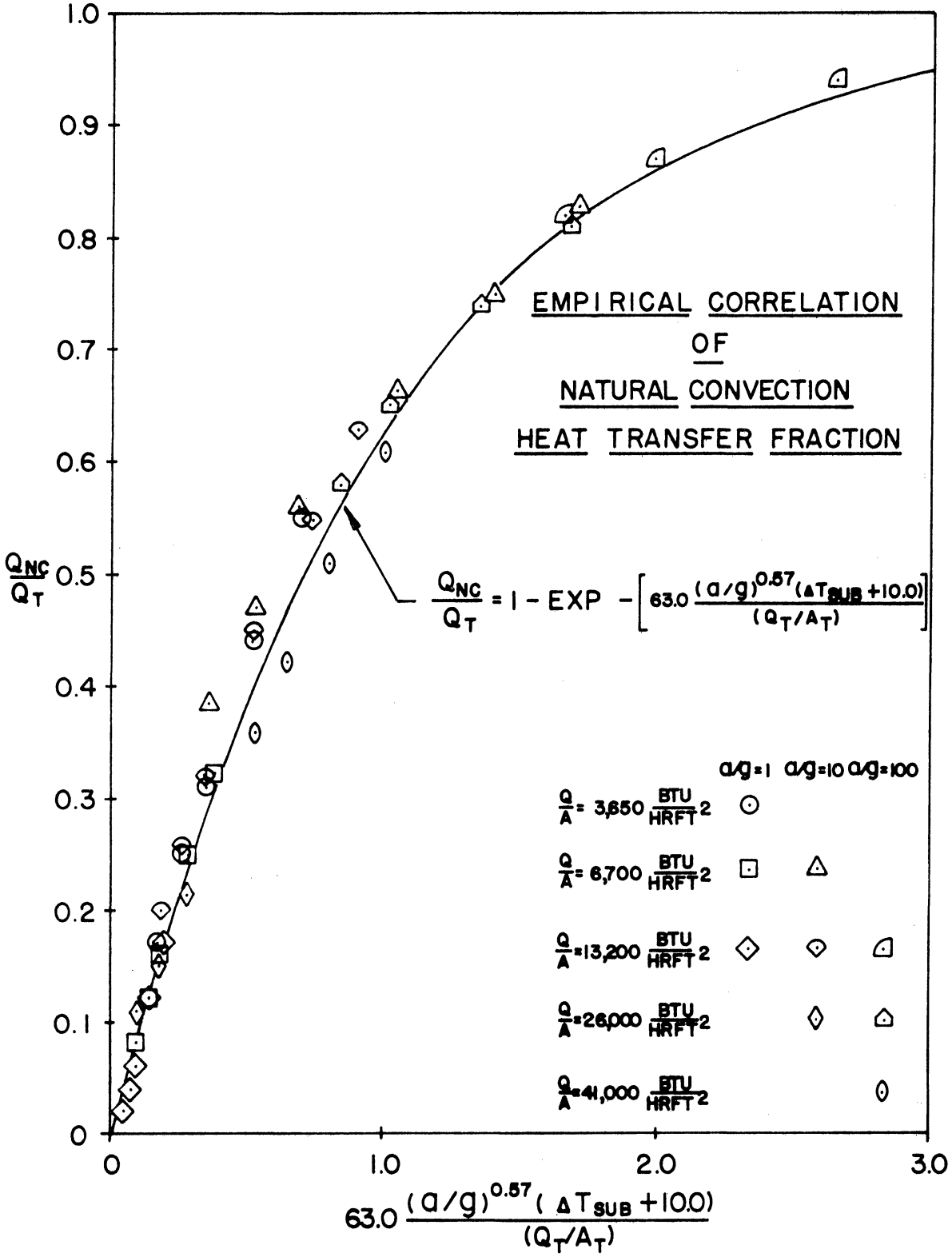

Figure 67. Empirical Correlation Of Natural Convection Heat Transfer Fraction.

When Equation (27) is substituted into Equation (24), the identity

$$\frac{Q_{NB}}{Q_T} = 1 - \left[\frac{(Q_{NC}/A_{NC})}{(Q_T/A_T)} \right] \left(\frac{A_{NC}}{A_T}\right) = \left[1 - \frac{Q_{NC}}{Q_T}\right] \tag{30}$$

is obtained, relating the nucleate boiling heat transfer fraction Q_{NB}/Q_T to the natural convection heat transfer fraction Q_{NC}/Q_T plotted in Figure 66. The nucleate boiling heat transfer fraction is required to compute the overall nucleate boiling heat flux Q_{NB}/A_T in accordance with the relationship

$$\frac{Q_{NB}}{A_T} = \left(\frac{Q_{NB}}{Q_T}\right) \times \left(\frac{Q_T}{A_T}\right) \tag{31}$$

Division of the overall nucleate boiling heat flux by the active site density yields the heat transfer per active nucleation site and division of the heat transfer per active nucleation site by the frequency of vapour bubble emission yields the heat transfer associated with a single bubble. This quantity, which has been defined as the total bubble heat transfer $Q_{\substack{TOTAL \\ BUBBLE}}$ is calculated by the relationship

$$Q_{\substack{TOTAL \\ BUBBLE}} = \frac{(Q_{NB}/A_T)}{(N/A_T) \times f} \tag{32}$$

in accordance with the procedure outlined above. Figure 68 depicts the variation of the total bubble heat transfer with heat flux, subcooling and acceleration.

The most striking feature of Figure 68 is the apparent independence of total bubble heat transfer and heat flux for saturated boiling

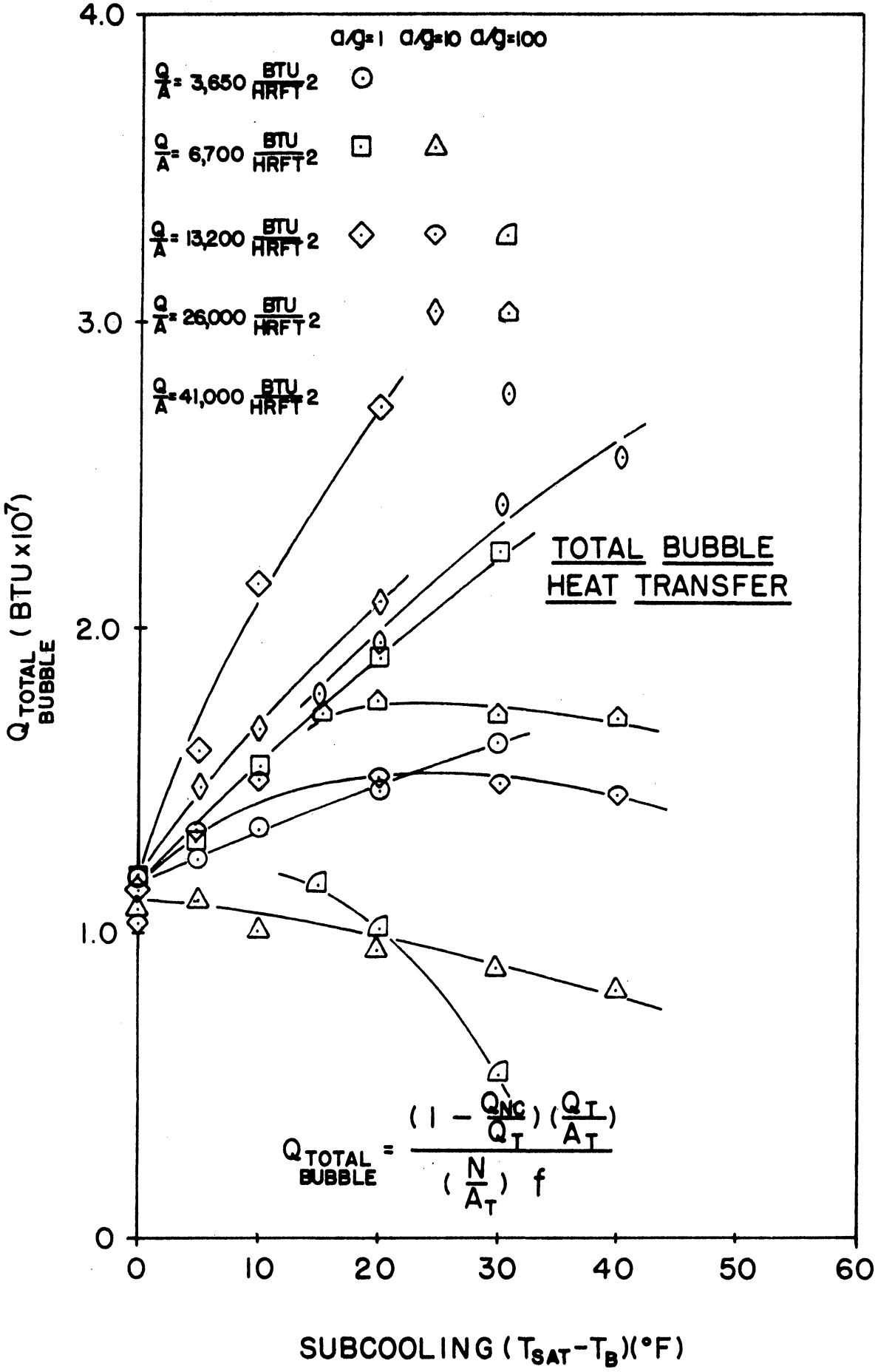

Figure 68. Total Bubble Heat Transfer.

conditions at $a/g = 1$ and $a/g = 10$. Figure 68 clearly shows that

$$Q_{\substack{TOTAL \\ BUBBLE}} = 1.2 \times 10^{-7} \text{ BTU} \tag{33}$$

under the conditions stated above. Furthermore, it would appear that the relationship expressed by Equation (33) is valid at $a/g = 100$ also, although this observation is somewhat tenuous since the particular curves involved have to be extrapolated to zero subcooling in order to determine the total bubble heat transfer. It would appear then that total bubble heat transfer is independent of both heat flux and acceleration for saturated boiling conditions. The implication of this observation is that the overall nucleate boiling heat flux is simply a linear function of the number of bubbles emitted per unit area per unit time.

The total bubble heat transfer may be considered as being comprised of three components

$$Q_{\substack{TOTAL \\ BUBBLE}} = Q_{\substack{LATENT \\ HEAT}} + Q_{\substack{BUBBLE \\ CONVECTION}} + Q_{\substack{MICROLAYER \\ EVAPORATION}} \tag{34}$$

but it is not within the scope of this investigation to evaluate these components numerically. Obviously, for saturated boiling conditions, the three components interact in such a way as to render $Q_{\substack{TOTAL \\ BUBBLE}}$ constant irrespective of heat flux and acceleration as noted above. Furthermore, Figure 68 indicates that subcooling affects $Q_{\substack{LATENT \\ HEAT}}$, $Q_{\substack{BUBBLE \\ CONVECTION}}$ and $Q_{\substack{MICROLAYER \\ EVAPORATION}}$ in such a way that $Q_{\substack{TOTAL \\ BUBBLE}}$ increases with increasing heat flux at constant acceleration and decreases with increasing acceleration at constant heat flux. The explanation of these effects is not

possible until the mechanisms governing total bubble heat transfer are fully understood. However, it is possible to obtain insight into the nature of these mechanisms by noting that heat transfer by latent heat transport is predicted by the relationship

$$Q_{\substack{\text{LATENT}\\\text{HEAT}}} = \rho_v h_{fg} V_{BUBBLE} \tag{35}$$

and that the ratio $Q_{\substack{\text{TOTAL}\\\text{BUBBLE}}} / Q_{\substack{\text{LATENT}\\\text{HEAT}}}$, obtained from experimentally determined values of $Q_{\substack{\text{TOTAL}\\\text{BUBBLE}}}$ and V_{BUBBLE} and plotted in Figure 69 as a function of heat flux, subcooling and acceleration, serves to indicate the significance of the other two components. It is evident from Figure 69 that bubble convection and microlayer evaporation become increasingly important relative to latent heat transport as heat flux, subcooling and acceleration increase. Figure 69 also shows that $Q_{\substack{\text{TOTAL}\\\text{BUBBLE}}} / Q_{\substack{\text{LATENT}\\\text{HEAT}}}$ is a linear function of subcooling, implying that bubble convection and microlayer evaporation are proportional to bubble volume and subcooling since

$$\frac{Q_{\substack{\text{TOTAL}\\\text{BUBBLE}}}}{Q_{\substack{\text{LATENT}\\\text{HEAT}}}} = \left[1 + \frac{Q_{\substack{\text{BUBBLE}\\\text{CONVECTION}}} + Q_{\substack{\text{MICROLAYER}\\\text{EVAPORATION}}}}{\rho_v h_{fg} V_{BUBBLE}}\right] \alpha \, \Delta T_{SUB} \tag{36}$$

and thus to a first order approximation

$$\left[Q_{\substack{\text{BUBBLE}\\\text{CONVECTION}}} + Q_{\substack{\text{MICROLAYER}\\\text{EVAPORATION}}}\right] \alpha \left[\rho_v h_{fg} V_{BUBBLE} \Delta T_{SUB}\right] \tag{37}$$

The symbol α signifies proportionality in the foregoing relationships.

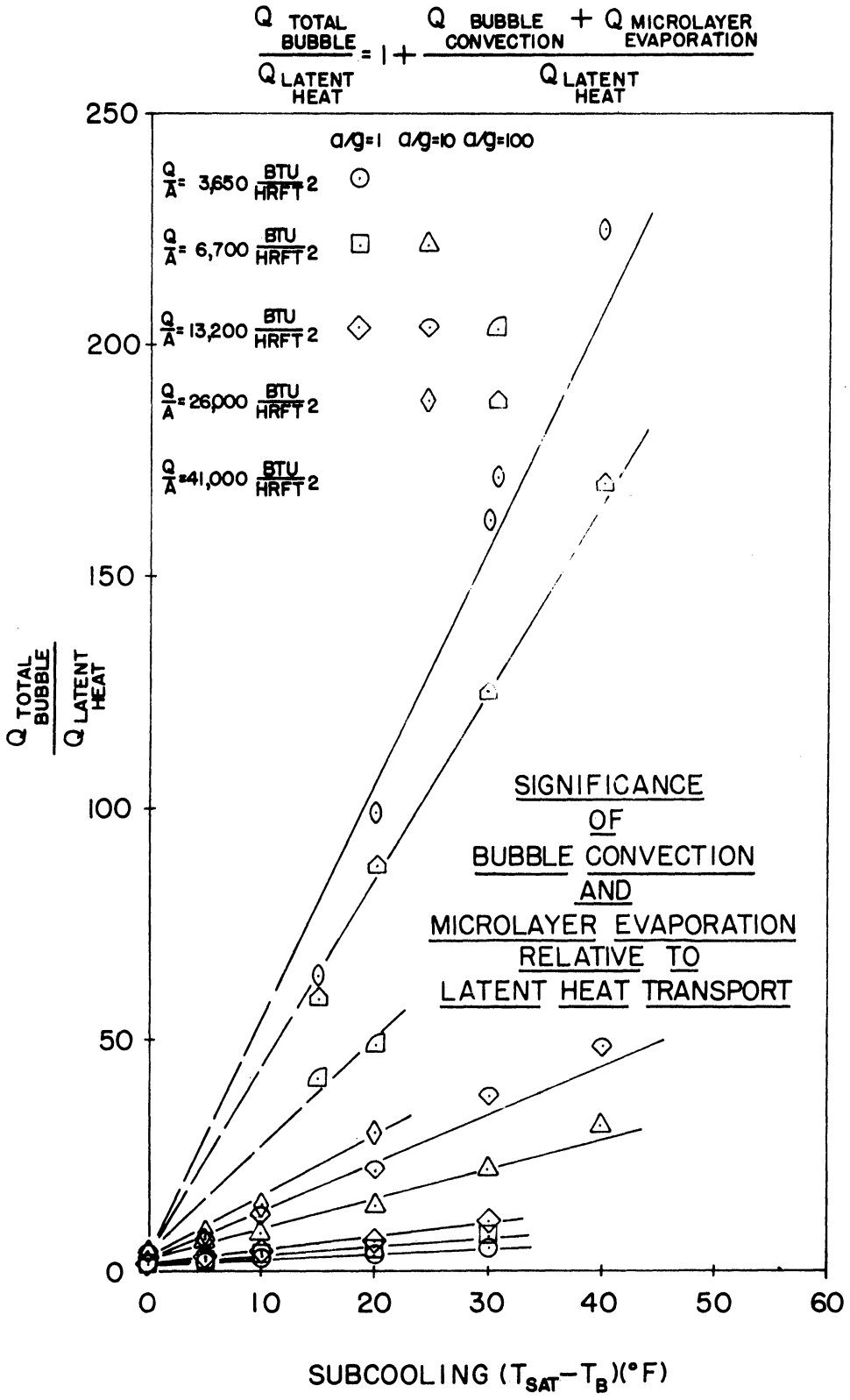

Figure 69. Significance Of Bubble Convection And Microlayer Evaporation Relative To Latent Heat Transport.

H. Evaluation of Nucleate Boiling Models

The set of independent measurements of surface temperature, boundary layer thickness, average population density, active site density, frequency of vapour bubble emission and maximum bubble size obtained in the present investigation for one particular fluid-surface combination affords a unique opportunity to evaluate the various models which have been advanced to explain nucleate boiling heat transfer. Accordingly, in the section which follows, the validity of six different models has been assessed by the comparison of the predictions of these models with the measurements of the present investigation. The results of this analysis indicate that none of these models is capable of explaining the influence of subcooling and acceleration upon the nucleate boiling heat transfer phenomenon.

1. Latent Heat Transport Model

Jakob[4] was one of the first to suggest that the rate of heat transfer by nucleate boiling was determined by the mechanism of latent heat transport in which each vapour bubble growing and departing from the heater surface removed a bubble volume of latent heat. This explanation of the nucleate boiling heat transfer mechanism later fell into disregard but the relatively recent results of Rallis and Jawurek[53] for saturated boiling of water on a horizontal wire lend credence to it, in as much as the total heat flux was satisfactorily correlated by the relationship

$$(Q/A)_{\substack{\text{LATENT}\\\text{HEAT}}} = \rho_v h_{fg} \sum^{N} fV/A \qquad (38)$$

which requires a knowledge of the frequency of emission and bubble departure size at each nucleation site. In terms of the averaged

measurements of the present investigation, the latent heat transport model may be expressed by the relationships

$$\frac{Q_{NB}}{A_T} = \rho_v h_{fg} V_{BUBBLE} \left(\frac{N}{A_T}\right) f \tag{39}$$

$$Q_{\substack{TOTAL \\ BUBBLE}} = \frac{Q_{NB}/A_T}{(N/A_T)xf} = \rho_v h_{fg} V_{BUBBLE} \tag{40}$$

Figure 70, in which the experimentally determined values of $Q_{\substack{TOTAL \\ BUBBLE}}$ are plotted against the corresponding values of V_{BUBBLE} determined from the measurements of maximum bubble size, illustrates the lack of agreement between the results of the present investigation and the relationship expressed by Equation (40). The results plotted indicate that each bubble transfers considerably more heat than predicted for all combinations of heat flux, subcooling and acceleration with the possible exception of saturated boiling at $a/g = 1$, as noted previously in connection with the discussion of Figure 69.

2. Vapour Liquid Exchange Model

The vapour liquid exchange model postulated by Forster and Grief,[10] in which the heat transfer by nucleate boiling was explained by the exchange of a volume of liquid at the bulk temperature for a volume of liquid at the wall temperature each time that a bubble departed or collapsed is expressed by the relationships

$$\frac{Q_{NB}}{A_T} = \rho_\ell C_\ell V_{BUBBLE} (T_W - T_B)\left(\frac{N}{A_T}\right) f \tag{41}$$

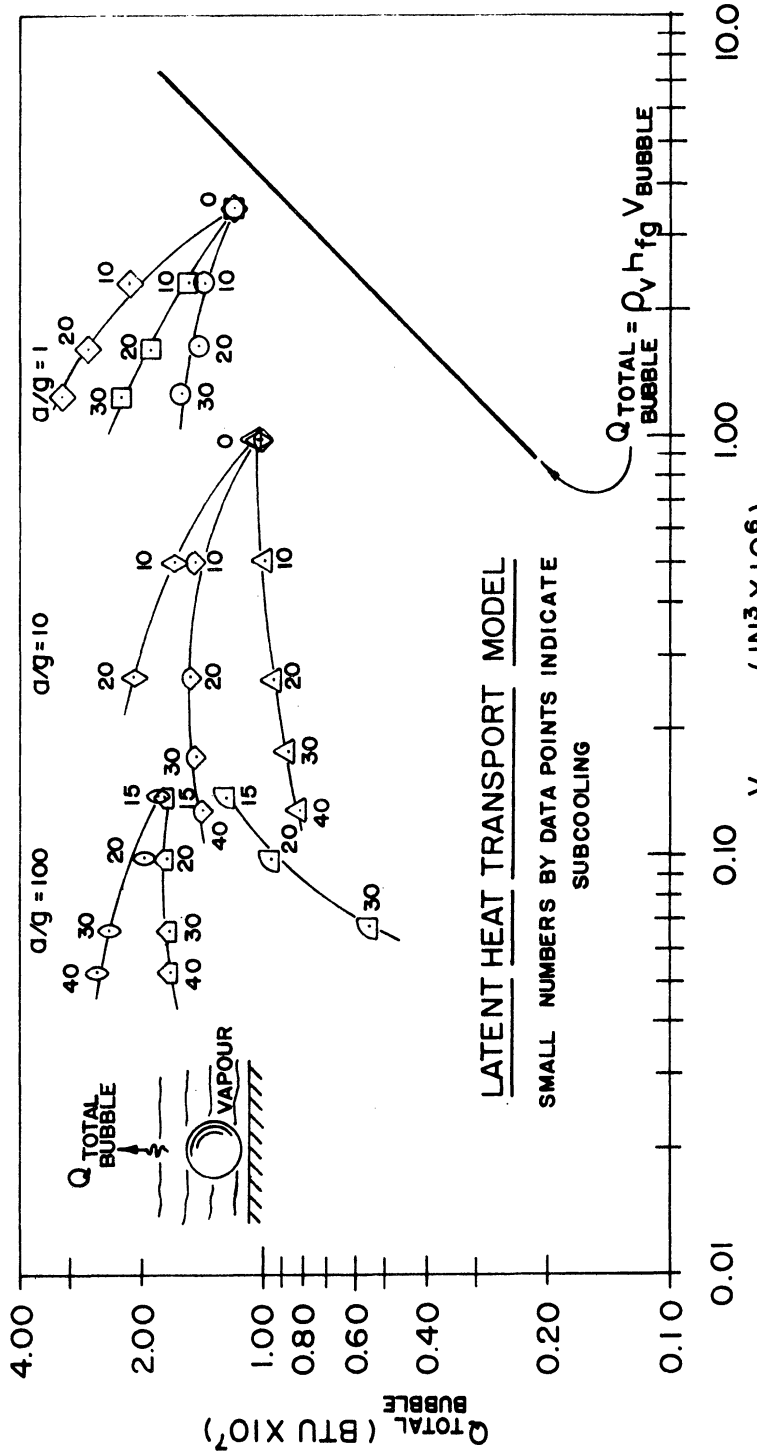

Figure 70. Evaluation Of Latent Heat Transport Model.

$$Q_{\substack{TOTAL \\ BUBBLE}} = \frac{Q_{NB}/A_T}{(N/A_T)xf} = \rho_\ell C_\ell V_{BUBBLE}(T_W-T_B) \qquad (42)$$

Figure 71 illustrates the correlation of $Q_{\substack{TOTAL \\ BUBBLE}}/V_{BUBBLE}$ computed from the experimentally determined values of $Q_{\substack{TOTAL \\ BUBBLE}}$ and V_{BUBBLE} with the temperature difference (T_W-T_B) and compares the results of the present investigation with the relationship expressed by Equation (42). It is apparent that this particular treatment of the results of the present investigation eliminates the dependence upon heat flux, although acceleration dependence remains. Figure 71 indicates that each bubble transfers less heat than predicted at $a/g = 1$ and $a/g = 10$ but more heat than predicted $a/g = 100$. Moreover, subcooling appears to have a more marked influence upon the correlation of the results than that predicted by the model.

3. Enthalpy Transport Model

Han and Griffith[15] formulated a model in which the enthalpy transported by a single bubble was equated to the superheat enthalpy associated with an approximately cylindrical volume of twice the bubble departure diameter and height equivalent to the thermal layer thickness at the instant of departure. The model accounted for heat transfer from the portion of the surface unaffected by nucleate boiling by incorporating a natural convection heat transfer term. Accordingly, the total heat transfer associated with nucleate boiling from a heated surface was given by the relationship

$$\frac{Q_T}{A_T} = \left[(1-\pi \sum^{N} R_i^2)Nu\alpha/D+2 \sum^{N} \{f[R_i^2\delta_d-(R_d^2/3)(\delta_d-\delta)]\}\right] \rho_\ell C_\ell (T_W-T_B) \qquad (43)$$

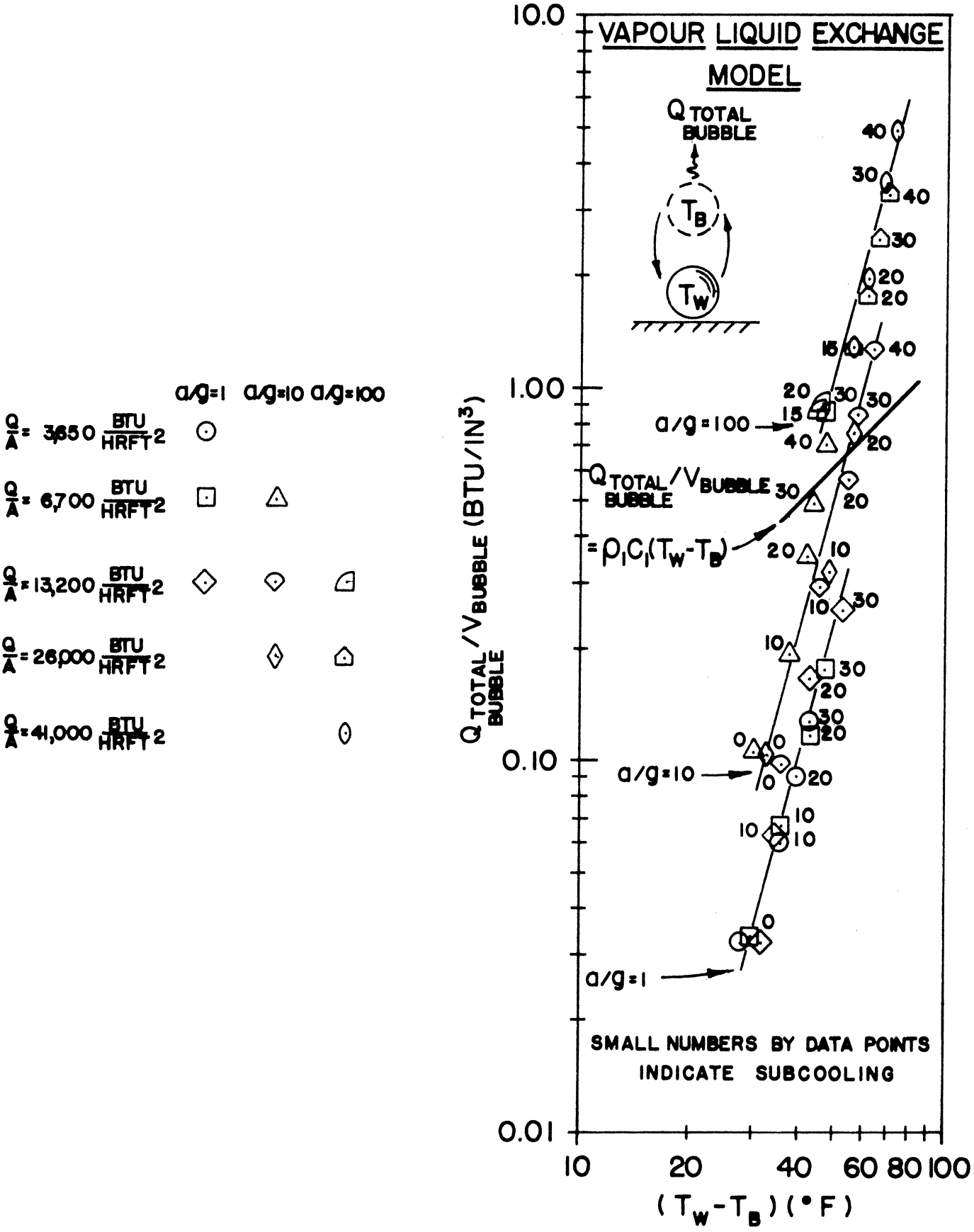

Figure 71. Evaluation Of Vapour Liquid Exchange Model.

which requires a knowledge of the frequency of emission and bubble departure size at each nucleation site. In terms of the averaged measurements of the present investigation, the enthalpy transport model may be expressed by the relationship

$$\frac{Q_T}{A_T} = \left[[1-\pi R_i^2(\frac{N}{A_T})]Nu\alpha/D+2 \quad \{f[R_i^2\delta_d-(R_d^2/3)(\delta_d-\delta)](\frac{N}{A_I})\} \right] \rho_\ell C_\ell (T_W-T_B) \quad (44)$$

This relationship may be simplified by noting that

$$\rho_\ell C_\ell \left[1 - \pi R_i^2(\frac{N}{A_T})\right] Nu \frac{\alpha}{D} (T_W-T_B) = \frac{Q_{NC}}{A_T} \quad (45)$$

Thus

$$\frac{Q_{NB}}{A_T} = \left[\frac{Q_T}{A_T} - \frac{Q_{NC}}{A_T} \right] = 2\rho_\ell C_\ell \quad \{f[R_i^2\delta_d-(R_d^3/3)(\delta_d-\delta)] (\frac{N}{A_T})\} (T_W-T_B) \quad (46)$$

and

$$Q_{\substack{TOTAL \\ BUBBLE}} = \frac{Q_{NB}/A_T}{(N/A_T)xf} = 2\rho_\ell C_\ell [R_i^2\delta_d-(R_d^2/3)(\delta_d-\delta)](T_W-T_B) \quad (47)$$

Han and Griffith[15] postulated that $R_i = 2R_d$ and hence

$$Q_{\substack{TOTAL \\ BUBBLE}} = 2\rho_\ell C_\ell R_d^2\delta_d[4 - \frac{1}{3}(1 - \frac{\delta}{\delta_d})](T_W-T_B)$$

$$\simeq \frac{1}{2} \rho_\ell C_\ell D_{MAX}^2\delta_d[4 - \frac{1}{3}(1 - \frac{\delta}{\delta_d})](T_W-T_B) \quad (48)$$

where $\delta = \sqrt{\pi\alpha_\ell\tau_i}$ and $\delta_d = \sqrt{\pi\alpha_\ell(\tau_i+\tau_a)}$.

Figure 72 illustrates the correlation of $Q_{\substack{TOTAL \\ BUBBLE}}/D_{MAX}^2\delta_d$ computed from

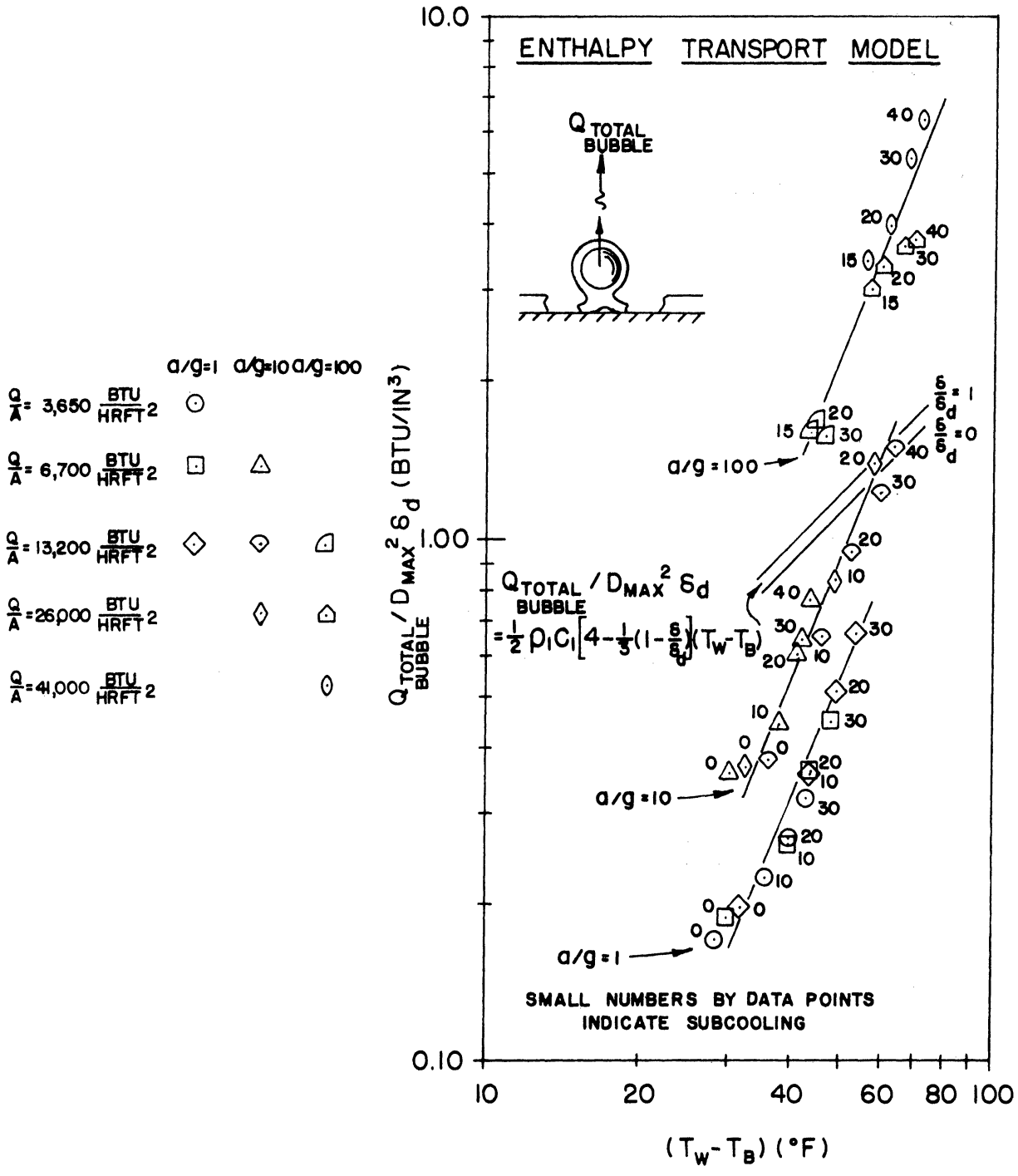

Figure 72. Evaluation Of Enthalpy Transport Model.

the experimentally determined values of Q_{TOTAL}, D_{MAX} and δ_d with the temperature difference (T_W-T_B). Figure 72 demonstrates the lack of agreement between the results of the present investigation and the relationship expressed by Equation (48). Each bubble transfers less heat than predicted at $a/g = 1$ and $a/g = 10$ but more heat than predicted at $a/g = 100$. Figure 72 shows that the influence of subcooling is not properly accounted for in as much as the deviation of the experimental results from the relationship expressed by Equation (48) is dependent upon subcooling.

4. Turbulent Natural Convection Model

Zuber[54] observed the similarity between nucleate boiling and turbulent natural convection resulting from the existence of an "up draught" induced circulation which determines the heat transfer in both cases. This similarity was employed to devise a model in which the equation predicting turbulent natural convection heat transfer was modified to predict nucleate boiling heat transfer by incorporating the void fraction associated with the vapour bubbles in the evaluation of the effective density of the fluid. Accordingly, the total heat transfer associated with nucleate boiling from a heated surface was given by the relationship

$$\frac{Q_T}{A_T} = 0.16 \left[\left(\frac{a}{g}\right) \frac{g\rho_\ell^2 C_\ell k_\ell}{\mu_\ell} \left(\beta\Delta T + \alpha_W \frac{\Delta\rho}{\rho_\ell}\right) \right]^{1/3} \Delta T + \rho_v h_{fg} V_{BUBBLE} \left(\frac{N}{A_T}\right) f \qquad (49)$$

where $\alpha_W = V_{BUBBLE} \left(\frac{N}{A_T}\right) f/U$, $U = 1.18 \left[\frac{\sigma g g_c (\rho_\ell - \rho_v)}{\rho_\ell^2}\right]^{1/4}$

$\Delta T = T_W - T_B$ and $\Delta\rho = \rho_W - \rho_\ell$

In Equation (49), the coefficient 0.16 was substituted in place of the coefficient 0.32 which appeared in Reference 54 and the latent heat transport term was added. The justification for the change in coefficient is that Equation (49) reduces to Equation (21) identically when the product $V_{BUBBLE} \left(\frac{N}{A_T}\right) f$ approaches zero and hence Equation (49) automatically correlates approximately one third of the results of the present investigation for which natural convection was the predominant heat transfer mechanism. Zuber[54] himself suggested the inclusion of a term to account for latent heat transport but failed to do so in his formulation. Figure 73 illustrates the comparison of the results of the present investigation with the relationship expressed by Equation (49) and indicates excellent agreement with the saturated boiling results at $a/g = 1$. However, the influence of subcooling and acceleration are not properly accounted for; the discrepancy arises because the product $V_{BUBBLE}\left(\frac{N}{A_T}\right) f$ tends to zero before the corresponding value of ΔT increases sufficiently to offset the decreased nucleate boiling contribution with an increased natural convection contribution.

5. Wake Flow Model

Tien[55] devised a model based upon the hypothesis that each rising column of bubbles induced a rising flow of liquid in its wake which approximated inverted stagnation flow. The formulation which involved the use of a heat transfer relationship for stagnation flow,

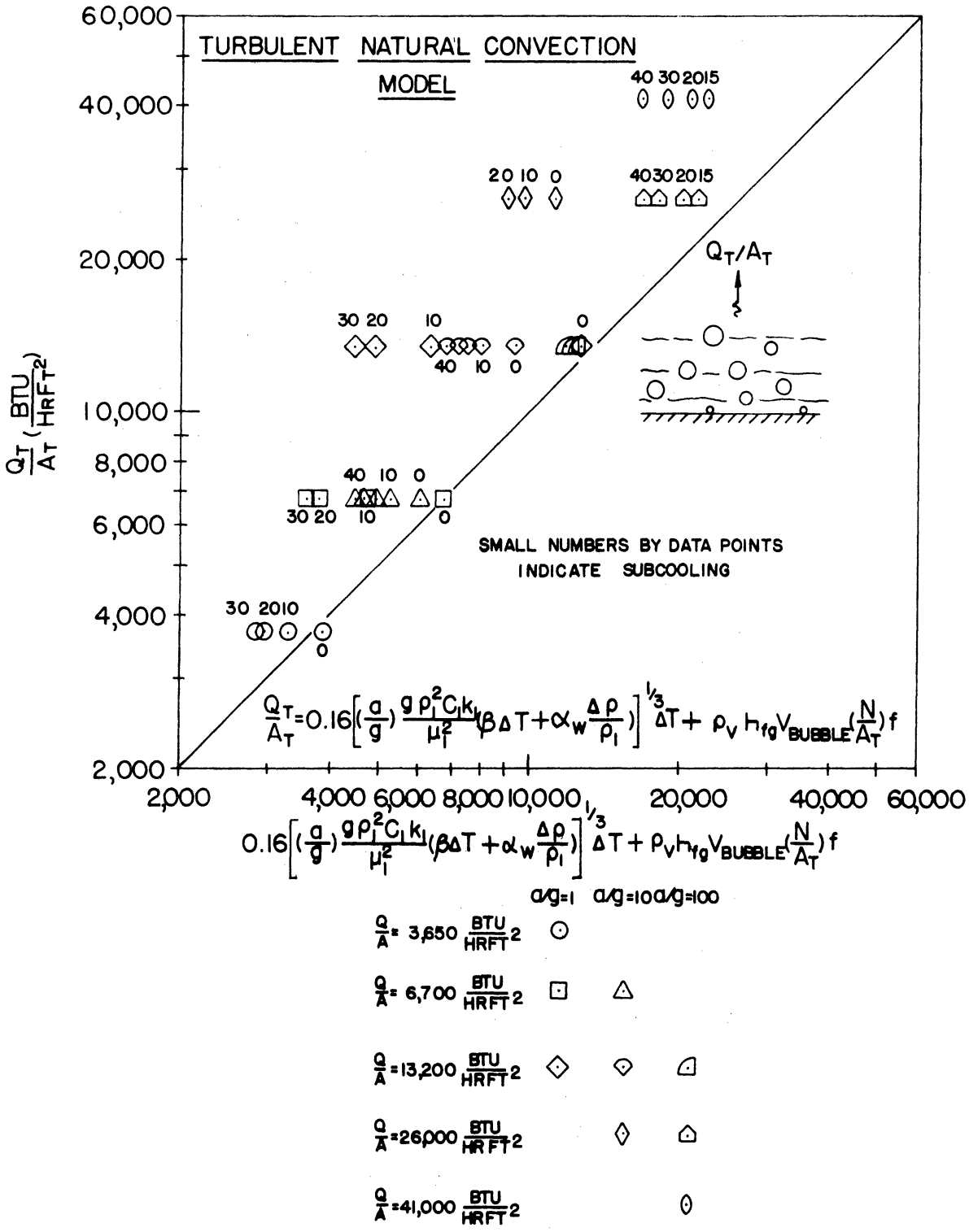

Figure 73. Evaluation Of Turbulent Natural Convection Model.

required the evaluation of a coefficient and consequently, the relationship derived

$$\frac{Q_T}{A_T} = 61.2(Pr)^{1/3}k(T_W-T_{SAT})(\frac{N}{A_T})^{1/2} \qquad (50)$$

is valid for nucleate boiling water only. Figure 74 depicts the correlation of Q_T/A_T with the product $(T_W-T_{SAT})(\frac{N}{A_T})^{1/2}$ and compares the results plotted with the relationship expressed by Equation (50). The fact that no agreement is observed might be expected because of differences in fluid properties. The results corresponding to saturated boiling at $a/g = 1$ and $a/g = 10$ can be correlated by a single straight line of the form

$$\frac{Q_T}{A_T} \alpha \left[(T_W-T_{SAT})(\frac{N}{A_T})^{1/2}\right]^{3/2} \qquad (50)$$

when the results are plotted in this fashion but unfortunately no saturated boiling results are available at $a/g = 100$ to indicate whether this correlation is entirely independent of acceleration level. It is apparent, however, that this particular model cannot satisfactorily explain the influence of subcooling, which appears in Equation (50) only indirectly through its influence upon (N/A_T).

6. Similarity Model

Novakovic and Stefanovic[56] formulated a model which postulated that the actual rate of vapour formation computed from measurements of active site density, bubble size and departure velocity was related to the hypothetical rate of vapour formation resulting from the complete

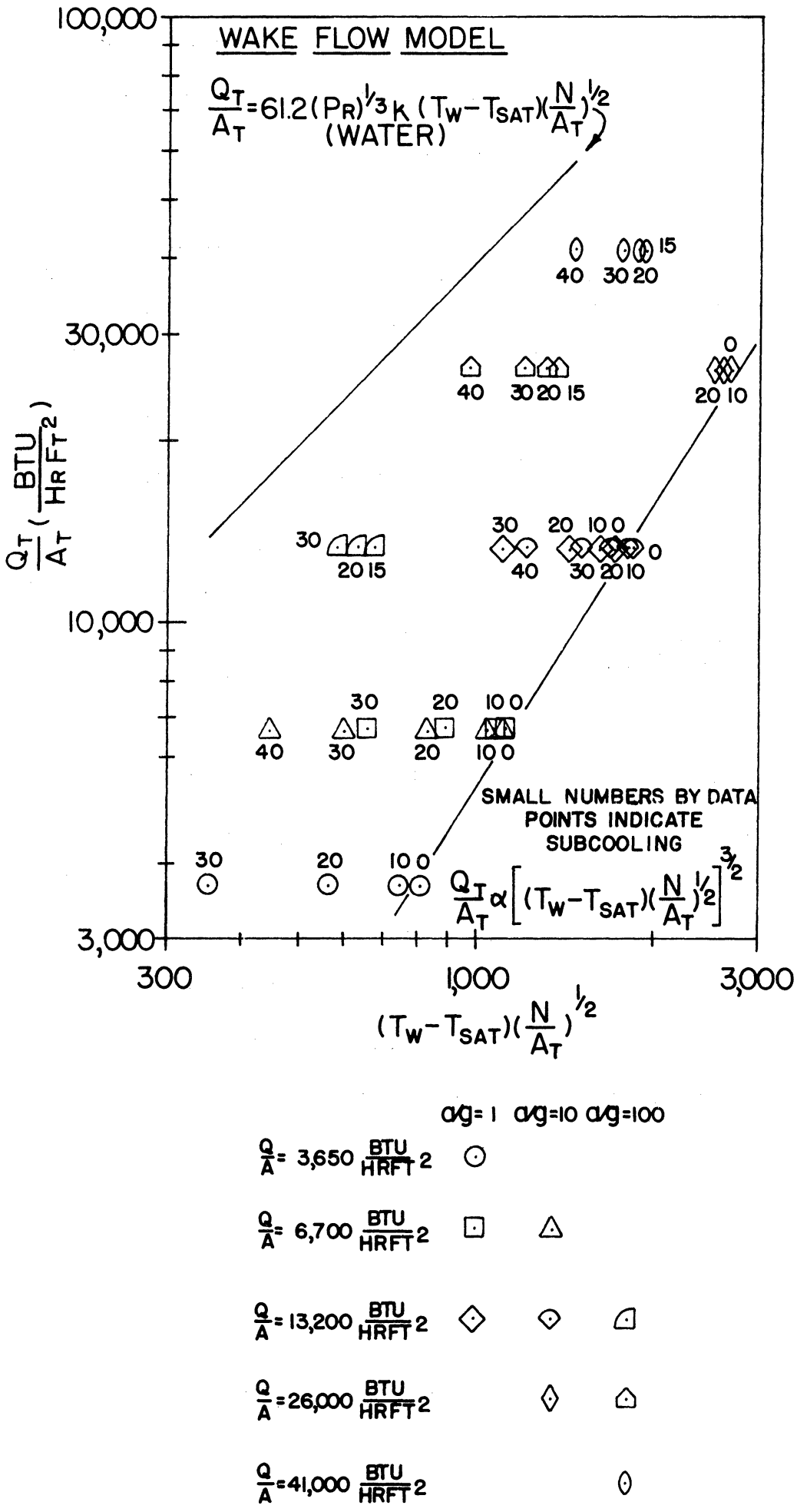

Figure 74. Evaluation Of Wake Flow Model.

evaporation of the thermal layer as the heat transmission by enthalpy flow was related to the heat transmission by thermal diffusion. This hypothesis led to the dimensionless relationship

$$\frac{(N/A_T)A_T D_{MAX}/\tau_a}{k_\ell(T_W-T_{SAT})/\sqrt{\pi\alpha_\ell \tau_a}\rho_v h_{fg}} \alpha \frac{(Q_T/A_T)}{\rho_v h_{fg}\alpha_\ell}\sqrt{\frac{(g_c/g)}{(a/g)}\frac{\sigma}{(\rho_\ell-\rho_v)}} \equiv \begin{matrix}\text{BUBBLE}\\ \text{PECLET}\\ \text{NUMBER}\end{matrix} \quad (51)$$

which was observed to satisfactorily correlate data for saturated water and alcohol boiling on the surface of a pool of liquid mercury. Figure 75 depicts

$$\frac{(N/A_T)A_T D_{MAX}/\tau_a}{k_\ell(T_W-T_{SAT})/\sqrt{\pi\alpha_\ell \tau_a}\rho_v h_{fg}} \text{ plotted against } \frac{(Q_T/A_T)}{\rho_v h_{fg}\alpha_\ell}\sqrt{\frac{(g_c/g)}{(a/g)}\frac{\sigma}{(\rho_\ell-\rho_v)}}$$

and compares the results of the present investigation with the correlations corresponding to saturated nucleate boiling water and alcohol. No agreement is observed as might be expected because of differences in fluid properties and this particular treatment of the data is not capable of explaining the influence of subcooling and acceleration as evidenced by the observation that subcooling and acceleration dependence has not been eliminated in the results plotted in Figure 75.

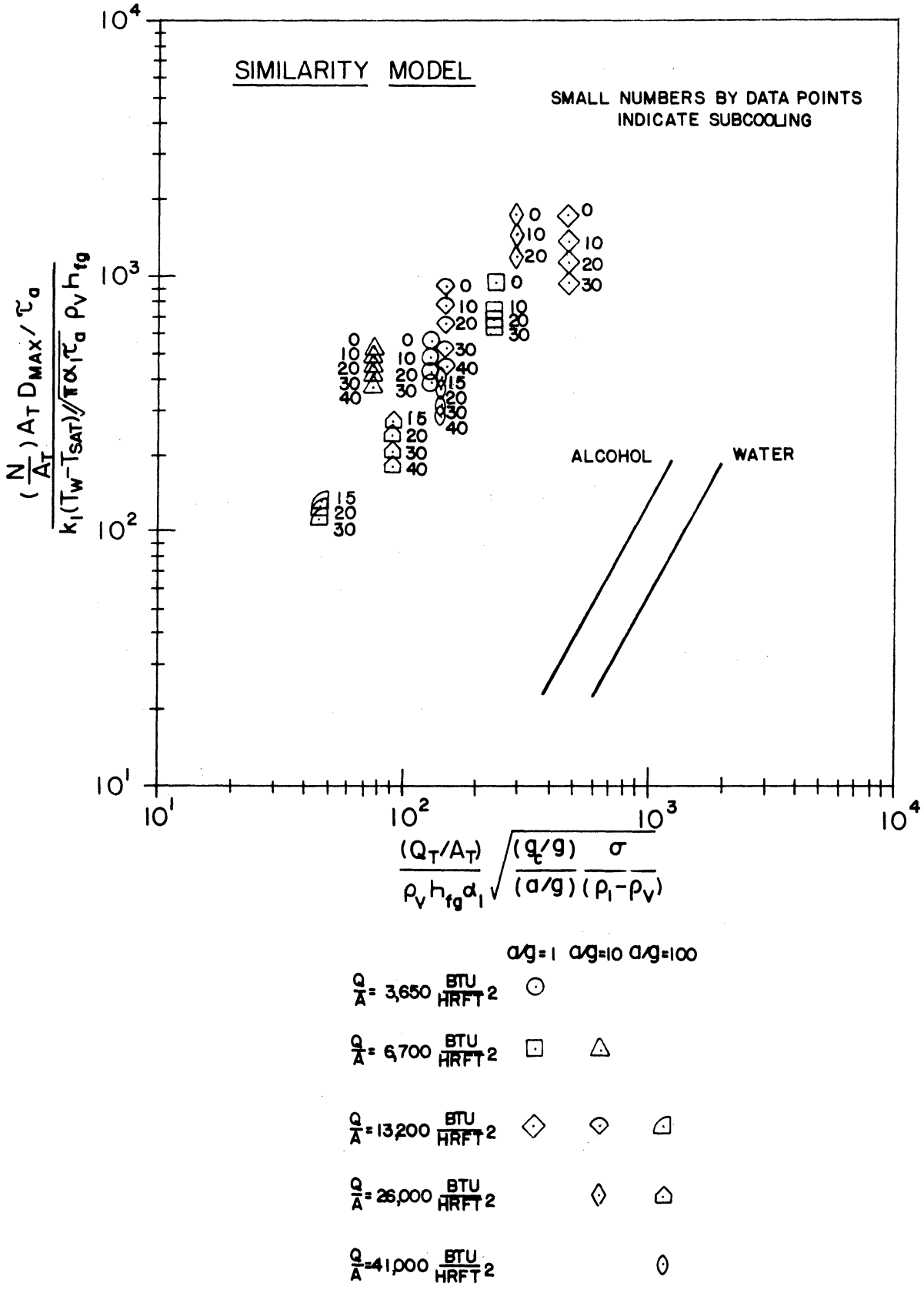

Figure 75. Evaluation Of Similarity Model.

CHAPTER VIII

CONCLUSION

1. The results of the present investigation comprise a consistent set of measurements of surface temperature, boundary layer thickness, active site density, average population density, frequency of vapour bubble emission and maximum bubble size pertaining to Freon boiling on an oxide coated glass heating surface for various combinations of heat flux ranging from 4,000 BTU/hr ft^2 to 40,000 BTU/hr ft^2, subcooling ranging from 0°F to 50°F and acceleration ranging from 1 to 100 times standard gravitational acceleration.

2. Two different heat transfer mechanisms were observed to interact; increasing subcooling and/or acceleration at constant heat flux simultaneously enhanced the natural convection heat transfer mechanism and diminished the nucleate boiling heat transfer mechanism.

3. Boundary layer thickness varied inversely with acceleration and varied directly with subcooling.

4. Active site density and average population density were little affected by a change in acceleration level from 1 to 10 times standard gravitational acceleration but decreased five fold when acceleration level changed from 10 to 100 times standard gravitational acceleration. Subcooling was observed to have little affect upon active site density and average population density within the range of subcooling investigated.

5. Bubble frequency was not significantly affected by a change in acceleration level from 1 to 10 times standard gravitational acceleration but increased by a factor of two when acceleration level

changed from 10 to 100 times standard gravitational acceleration. Bubble frequency varied inversely with subcooling.

6. Maximum bubble size varied inversely with subcooling and acceleration.

7. Natural convection heat transfer was correlated by the relationship

$$Nu = 0.160(PrGr)^{1/3}$$

and it was found the conditions under which natural convection dominated the heat transfer phenomenon were predicted by the relationship

$$\frac{(a/g)^{0.57}\ (\Delta T_{SUB} + 10.0)}{(Q_T/A_T)} > 0.075$$

8. Nucleate boiling heat transfer and natural convection heat transfer were separated by the assumption of an additive model. This approach enabled $Q_{\substack{TOTAL \\ BUBBLE}}$, the quantity of heat transferred by the growth and departure or collapse of a single vapour bubble to be calculated. It was found that

$$Q_{\substack{TOTAL \\ BUBBLE}} = 1.2 \times 10^{-7} \text{ BTU}$$

irrespective of heat flux and acceleration for saturated boiling conditions. On the assumption that

$$Q_{\substack{TOTAL \\ BUBBLE}} = Q_{\substack{LATENT \\ HEAT}} + Q_{\substack{BUBBLE \\ CONVECTION}} + Q_{\substack{MICROLAYER \\ EVAPORATION}}$$

it was demonstrated that

$$Q_{\substack{\text{BUBBLE}\\\text{CONVECTION}}} + Q_{\substack{\text{MICROLAYER}\\\text{EVAPORATION}}} \alpha \rho_v h_{fg} V_{\text{BUBBLE}} \Delta T_{\text{SUB}}$$

9. The predictions of six different models advanced to explain the mechanics of nucleate boiling heat transfer, entitled respectively

Latent Heat Transfer Model

Vapour Liquid Exchange Model

Enthalpy Transport Model

Turbulent Natural Convection Model

Wake Flow Model

Similarity Model

were evaluated using the set of independent measurements obtained in the present investigation. The results of this analysis indicated that none of the models was capable of explaining the influence of subcooling and acceleration upon the nucleate boiling phenomenon. The relationship derived for the Turbulent Natural Convection Model satisfactorily correlated the saturated boiling results at $a/g = 1$ and the natural convection results at $a/g = 10$ and $a/g = 100$. However, this model could not account for the influence of subcooling and acceleration upon the nucleate boiling results.

APPENDICES

APPENDIX A

INVESTIGATION OF UNIFORMITY OF DEPOSITED OXIDE COATING

The distribution of electrical potential in the oxide coating on the surface of a test specimen is indicative of the degree of uniformity of the oxide coating. A simple experiment was performed in which the variation in electrical potential resulting from a potential difference impressed at the silver contact bands was measured across the width of the test specimen at five different locations along the length. The results of this experiment and the deviation of the experimental results from the values predicted by one dimensional flow through a uniform resistance are presented in Figure 76. Excellent agreement is observed with no significant trend in the deviation of experimental results from predicted values; discrepancies observed are well within experimental uncertainty.

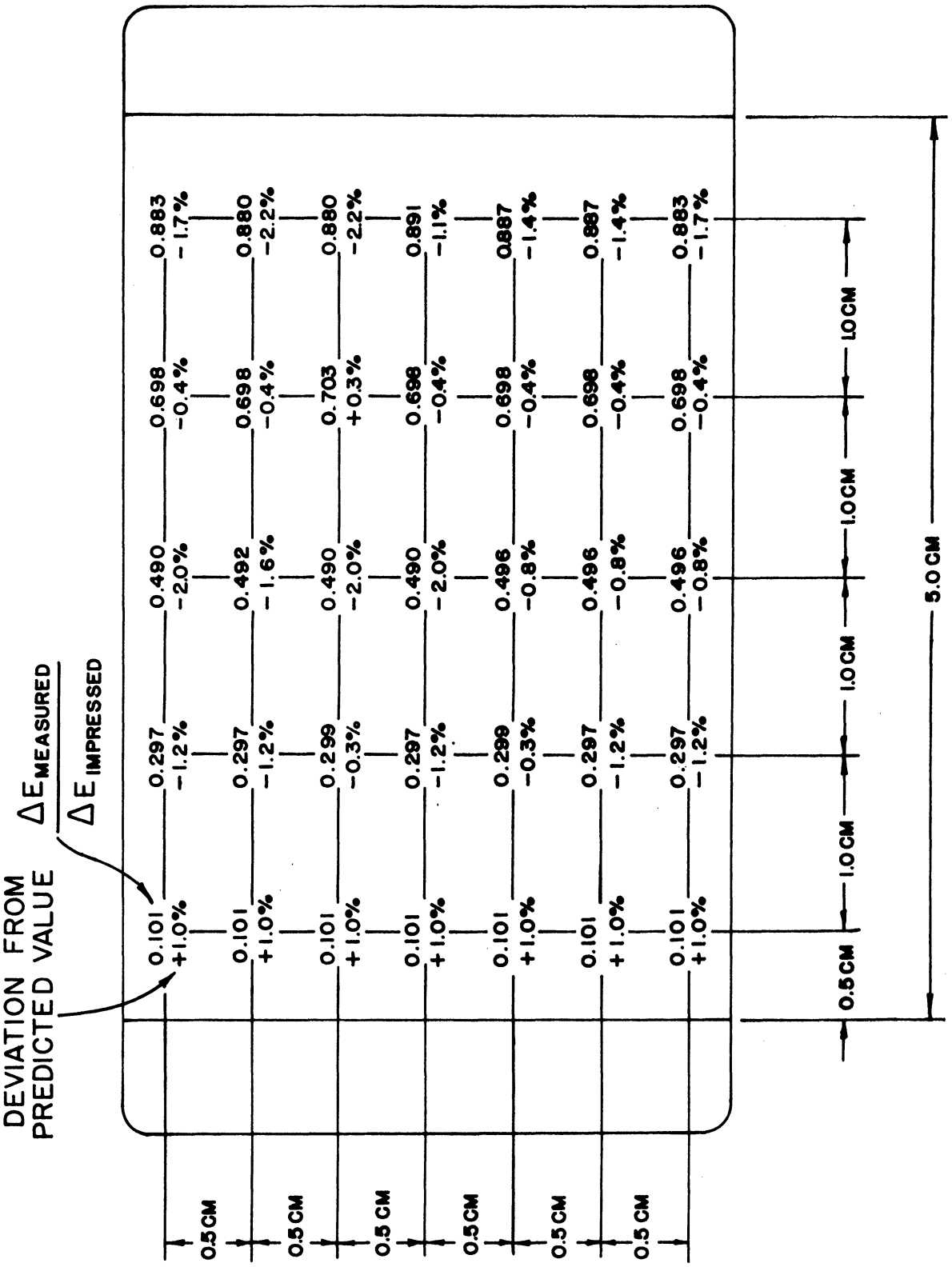

Figure 76. Distribution Of Electrical Potential In Oxide Coating.

APPENDIX B

DERIVATION OF EQUATION DESCRIBING TEMPERATURE DISTRIBUTION IN TEST SPECIMEN

The derivation of an approximate two dimensional temperature distribution used to evaluate the temperature variation within the field of view of the optical system is presented below. Figure 77 is a schematic representation of the test specimen. For the purpose of the derivation, a conservative result is obtained by considering the oxide film and/or metal foil as a two dimensional plane source of heat which subjects the upper surface of the glass plate to a uniform heat flux. The magnitude of the heat flux q'' is proportional to the rate at which heat is transferred by conduction to the edges, which are assumed to be at a uniform temperature T_o and by the rate at which heat is transferred by convection to the air beneath at temperature T_∞ in the presence of a finite heat transfer coefficient h. The difference in temperature between the upper and lower surfaces of the glass plate was assumed to be negligible in the formulation of the problem since the glass plate is thin, the thermal conductivity of glass is moderate and the flow of heat through the glass plate is small.

The differential equation governing the two dimensional temperature distribution assuming the temperature variation to be lumped in the Z direction is

$$\frac{\partial^2\theta}{\partial x^2} + \frac{\partial^2\theta}{\partial y^2} - m^2(\theta-\theta_\infty) = -n \qquad (52)$$

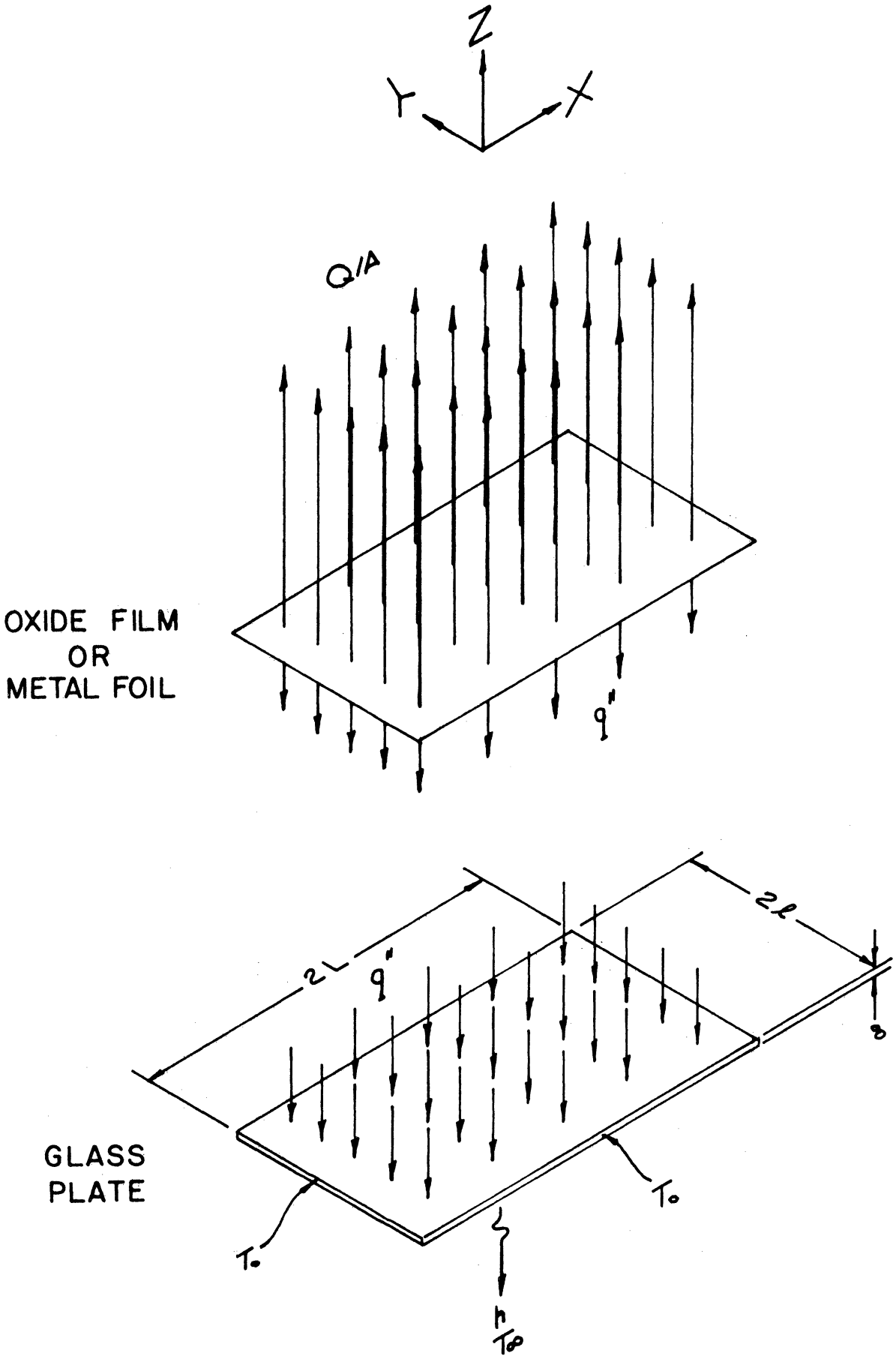

Figure 77. Schematic Representation Of Test Specimen.

in which $\theta = T-T_o$, $\theta_\infty = T_\infty - T_o$, $m^2 = h/k\delta$ and $n = q''/k\delta$, subject to the boundary conditions

$$\theta(L,y) = 0 \qquad \theta(x,\ell) = 0$$

$$\frac{\partial\theta(0,y)}{\partial x} = 0 \qquad \frac{\partial\theta(x,0)}{\partial y} = 0$$

The substitution of a solution of the form

$$\theta(x,y) = \theta_1(x,y) + \theta_2(x)$$

into Equation (52) results in two differential equations

$$\frac{\partial^2\theta_1}{\partial x^2} + \frac{\partial^2\theta_1}{\partial y^2} - m^2\theta_1 = 0$$

$$\frac{d^2\theta_2}{dx^2} - m^2(\theta_2-\theta_\infty) = -n \qquad (53)$$

subject to the boundary conditions

$$\theta_1(L,y) = 0 \qquad \theta_1(x,\ell) = -\theta_2(x)$$

$$\frac{\partial\theta_1(0,y)}{\partial x} = 0 \qquad \frac{\partial\theta_1(x,0)}{\partial y} = 0$$

and

$$\frac{d\theta_2(0)}{dx} = 0 \qquad \theta_2(L) = 0$$

respectively. The solutions of these equations are

$$\theta_1(x,y) = \sum_{n=0}^{\infty} a_n \cosh \mu_n y \cos \lambda_n x$$

where $\lambda_n L = (2n+1)\pi/2$ and $\mu_n = \sqrt{\lambda_n^2 + m^2}$

$$\theta_2(x) = m^2\left(\frac{n}{m^2} + \theta_\infty\right)\left[1 - \frac{\cosh mx}{\cosh mL}\right]$$

which combine through the boundary condition $\theta_1(x,\ell) = -\theta_2(x)$ to give

$$\theta(x,y) = m^2\left(\frac{n}{m^2} + \theta_\infty\right)\left[1 - \frac{\cosh mx}{\cosh mL} - 2 \sum_{n=0}^{\infty} \frac{m^2}{\mu_n^2} \frac{(-1)^n}{\lambda_n L} \frac{\cosh \mu_n y}{\cosh \mu_n \ell} \cos \lambda_n x\right] \quad (54)$$

Figure 78 illustrates the variation of temperature with distance from the geometric center of the test specimen. The values plotted were obtained from Equation (54), normalized with respect to the value predicted at the geometric center. Three profiles are shown, corresponding to the variation along the axis $X = 0$, the axis $Y = 0$ and the diagonal $X = 1.45Y$ respectively. The numerical results indicate that the temperature varies less than 2 per cent within the field of view of the optical system and hence it is reasonable to assume that the temperature at the heat transfer surface is uniform in the vicinity of the geometric center of the test specimen.

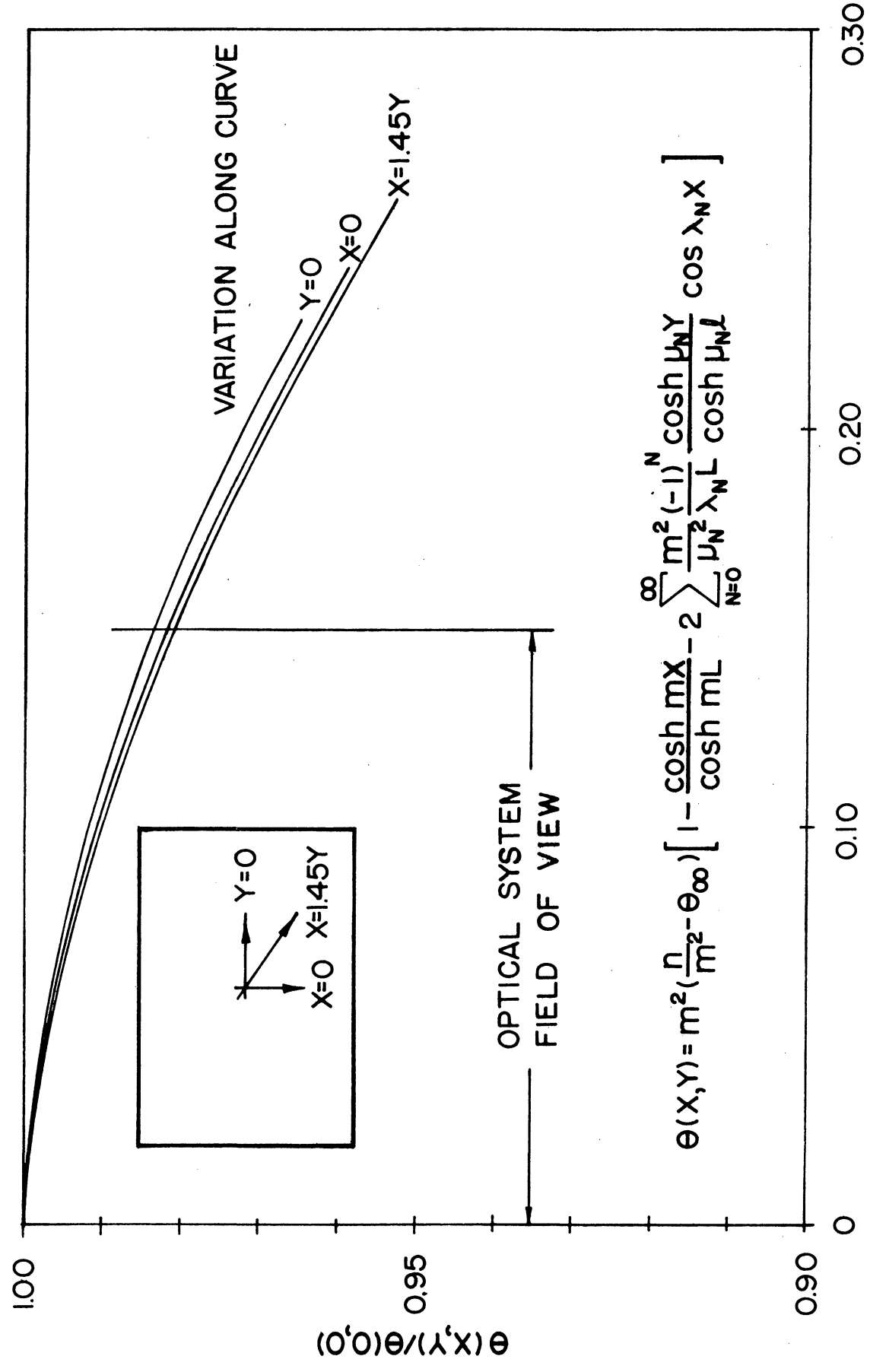

Figure 78. Variation In Temperature With Distance From Geometric Center.

APPENDIX C

REPRESENTATIVENESS OF PHOTOGRAPHIC DATA SAMPLES

The representativeness of the photographic data samples analysed in the determination of active site density, average population density and bubble frequency was evaluated by comparing the results obtained from samples selected in the manner indicated in Chapter V with the results obtained from larger samples. The particular test conditions investigated were selected for analysis because of the availability of sufficient active nucleation sites undergoing complete cycles of bubble emission for a larger sample to be drawn. The results obtained are presented in Table X.

Each of the forty photographs comprising Figure 79 and 87 in Appendix E was analysed to determine the total number of active sites in the area between the wires. Both the cumulative total and instantaneous total were computed; the former value corresponds to the total number of active sites observed in all the photographs up to and including the photograph associated with the value tabulated, whereas the latter value corresponds to the total number of active sites observed in each of the individual photographs. The results associated with the five photographs comprising the standard sample have been boxed in Table X for identification purposes.

The results obtained indicated that the active site density based upon the standard sample is approximately 20% smaller than the active site density based upon the larger sample. However, the additional sites were observed to emit only a single vapour bubble during a period of time in which each of the other sites emitted four or five vapour bubbles.

Consequently, it was concluded that these sites contributed little to the boiling process and that the effective site density was not significantly affected by their omission.

The film strips from which the photographs were printed were analysed in detail to determine the period of time between cycles of bubble emission for forty different bubbles at various nucleation sites. Both active period and inactive period were measured. The mean value of both periods was calculated for the standard sample comprised of ten bubbles and the larger sample comprised of forty bubbles.

The results obtained can be seen to differ slightly. A statistical "t" test performed upon the mean values of the two samples indicated that there was insufficient evidence to indicate that the samples were drawn from different populations. Although the larger sample was finite in size, it is believed that further increasing the size would not have appreciably altered the results. Consequently it is reasonable to conclude that the results based upon the standard sample are representative of the phenomenon under investigation.

TABLE X

ANALYSIS OF PHOTOGRAPHIC DATA

$Q/A=3,850$ BTU/hr ft^2 $\Delta T_{SUB}=0.2°F$ $a/g=1$

Total Active Sites	Cumulative Instant.	Total Active Sites	Cumulative Instant.	Total Active Sites	Cumulative Instant.	Total Active Sites	Cumulative Instant.
18	18	26	19	28	22	30	20
19	19	26	20	28	24	30	21
20	20	26	20	29	20	30	21
21	21	26	19	29	23	30	22
22	20	27	18	29	23	31	22
22	19	27	18	29	22	31	20
23	21	27	20	29	23	31	23
24	19	28	19	30	20	31	24
24	22	28	22	30	22	31	22
25	19	28	24	30	20	31	23

Standard Sample

N = 26 Sites
n = 20.0 Sites $\sigma = \pm 1.3$ Sites

Larger Sample

N = 31 Sites
n = 21.0 Sites $\sigma = \pm 1.9$ Sites

Bubble Period (Millisecs)		Bubble Period (Millisecs)		Bubble Period (Millisecs)		Bubble Period (Millisecs)	
Active	Inactive	Active	Inactive	Active	Inactive	Active	Inactive
9	5	8	4	11	6	12	6
11	6	10	3	6	6	11	7
9	4	7	4	11	5	12	5
10	7	8	5	13	8	12	5
7	6	8	5	12	6	13	8
10	4	10	5	9	6	8	5
10	7	9	6	10	3	11	6
10	3	10	3	9	5	8	6
9	7	13	5	9	5	6	6
11	5	7	6	10	5	8	5

Standard Sample

τ_a = 9.6 Millisecs $\sigma = \pm 1.2$ Millisecs
τ_i = 5.4 Millisecs $\sigma = \pm 1.4$ Millisecs

Larger Sample

τ_a = 9.7 Millisecs $\sigma = \pm 1.9$ Millisecs
τ_i = 5.3 Millisecs $\sigma = \pm 1.3$ Millisecs

TABLE X (CONT'D)

$Q/A = 42,300$ BTU/hr ft^2 $\Delta T_{SUB} = 14.9°F$ a/g = 100

Total Active Sites Cumulative	Instant.	Total Active Sites Cumulative	Instant.	Total Active Sites Cumulative	Instant.	Total Active Sites Cumulative	Instant.
25	25	39	27	43	24	45	21
28	22	39	22	43	23	45	22
31	27	40	21	43	23	45	23
33	24	41	22	44	24	45	22
34	26	41	26	44	22	45	25
36	23	41	23	44	20	45	23
36	22	42	24	44	20	46	25
37	24	42	25	44	21	46	26
37	26	42	21	44	19	46	24
38	21	43	22	44	20	46	23

Standard Sample

N = 40 Sites
n = 23.0 Sites $\sigma = \pm 1.9$ Sites

Larger Sample

N = 46 Sites
n = 23.0 Sites $\sigma = \pm 2.1$ Sites

Bubble Period (Millisecs) Active	Inactive	Bubble Period (Millisecs) Active	Inactive	Bubble Period (Millisecs) Active	Inactive	Bubble Period (Millisecs) Active	Inactive
7	3	7	3	5	3	5	2
4	4	5	2	5	2	5	2
5	1	6	2	5	3	6	4
5	1	5	2	5	5	5	3
4	4	5	3	4	2	5	4
5	5	6	4	4	2	4	2
4	2	5	3	6	4	4	2
5	1	4	4	4	3	5	2
4	3	4	2	5	4	4	3
4	2	6	3	5	3	4	3

Standard Sample

$\tau_a = 4.7$ Millisecs $\sigma = \pm 1.0$ Millisecs
$\tau_i = 2.6$ Millisecs $\sigma = \pm 1.4$ Millisecs

Larger Sample

$\tau_a = 4.9$ Millisecs $\sigma = \pm 0.9$ Millisecs
$\tau_i = 2.8$ Millisecs $\sigma = \pm 1.0$ Millisecs

APPENDIX D

DATA TABULATION

TABLE XI

HEAT TRANSFER DATA

TEST SERIES	a/g	Q/A	P_T	T_{SAT}	T_W	T_B	ΔT_{SUP}	ΔT_{SUB}
		$\frac{BTU}{hrft^2}$	$\frac{pounds}{in^2}$	°F	°F	°F	°F	°F
0	1	3,750	22.03	140.2	169.0	139.7	28.8	0.5
	1	6,800	21.67	139.3	170.1	139.4	30.7	-0.1
	1	13,500	21.83	139.7	172.5	139.8	32.8	-0.1
	1	26,400	21.63	139.2	175.8	139.0	36.6	0.2
	1	41,700	21.55	139.0	178.8	138.8	39.8	0.2
1	1	26,200	21.56	139.0	175.4	138.8	36.4	0.2
	1	13,400	21.90	139.9	175.3	140.1	35.4	-0.2
	1	6,600	21.77	139.5	173.4	139.3	33.9	-0.2
	1	3,650	21.67	139.3	172.4	139.1	33.1	0.2
	1	1,950	21.76	139.5	166.0	139.3	26.5	0.2
2	1	3,850	21.46	138.8	174.7	138.9	35.9	-0.1
	1	13,500	21.68	139.3	176.0	139.5	36.7	-0.2
	1	42,200	22.04	140.2	181.5	140.3	41.3	-0.1
3	1	13,300	21.87	139.8	177.4	140.0	37.6	-0.2
	1	3,700	21.78	139.6	174.9	139.8	35.3	-0.2
	1	1,900	21.95	140.0	165.1	140.1	25.1	-0.1
4	1	3,650	22.43	141.2	176.3	141.4	35.1	-0.2
	1	13,300	22.07	140.3	178.1	140.4	37.8	-0.1
	1	41,900	21.98	140.1	182.2	140.0	42.1	0.1
5	1	13,400	22.31	140.9	179.0	141.1	38.1	-0.2
	1	3,700	22.10	140.4	175.8	140.5	35.4	-0.1
	1	1,900	21.99	140.1	165.0	140.2	24.9	-0.1
6	1	3,700	21.62	139.2	171.7	138.9	32.5	0.3
	1	3,650	21.74	139.5	173.4	137.1	33.9	2.4
	1	3,650	21.99	140.1	153.3	105.8	13.2	34.3
	1	3,650	22.06	140.3	161.8	116.8	21.5	23.5
	1	3,600	21.35	138.5	171.9	134.2	33.4	4.3
	1	3,600	21.75	139.5	171.9	139.3	32.4	0.2

TABLE XI (CONT'D)

TEST SERIES	a/g	Q/A $\frac{BTU}{hrft^2}$	P_T $\frac{pounds}{in^2}$	T_{SAT} °F	T_W °F	T_B °F	ΔT_{SUP} °F	ΔT_{SUB} °F
7	1	6,600	21.87	139.8	177.2	140.2	37.4	-0.5
	1	6,650	21.98	140.1	181.6	138.2	41.5	1.9
	1	6,750	21.70	139.4	174.2	117.5	34.8	21.9
	1	6,800	21.79	139.6	179.3	125.4	39.7	14.2
	1	6,800	21.63	139.2	181.0	131.5	41.8	7.7
	1	6,750	21.79	139.6	180.2	140.0	40.6	-0.4
8	1	13,300	21.78	139.6	177.7	139.7	38.1	-0.1
	1	13,200	21.55	139.0	178.7	136.8	39.7	2.2
	1	13,300	21.46	138.8	178.7	128.3	39.9	10.5
	1	12,900	21.70	139.4	179.9	130.0	40.5	9.4
	1	13,300	21.54	139.0	179.7	134.4	40.7	4.6
	1	13,500	21.66	139.3	179.4	138.9	40.1	0.4
9	1	26,200	21.42	138.7	176.5	138.4	37.8	0.3
	1	26,100	21.38	138.6	177.3	136.6	38.7	2.0
	1	26,100	21.80	139.6	178.5	136.1	38.9	3.5
	1	26,100	21.64	139.2	177.9	138.2	38.7	1.0
	1	26,100	21.75	139.5	178.2	139.3	38.7	0.2
10	1	42,600	21.56	139.0	177.3	138.8	38.3	0.2
	1	42,200	21.70	139.4	177.1	137.7	37.7	1.7
11	1	3,600	21.83	139.7	167.9	137.7	28.2	2.0
	10	3,650	22.39	141.1	169.2	137.9	28.1	3.2
	10	3,650	22.32	140.7	133.7	100.9	-7.0	39.8
	10	3,650	22.10	140.4	150.8	118.3	10.4	22.1
	10	3,650	21.94	140.0	163.3	131.6	23.3	8.4
	10	3,650	22.06	140.3	167.2	135.4	26.9	4.9
	10	3,600	22.05	140.3	170.7	137.3	30.4	3.0
	1	3,600	21.71	139.4	169.0	136.4	29.6	3.0
12	1	6,750	22.26	140.8	169.8	140.6	29.8	0.2
	10	6,100	22.83	142.2	172.0	140.9	29.8	1.3
	10	6,650	22.75	142.0	147.1	102.2	5.1	39.8

TABLE XI (CONT'D)

TEST SERIES	a/g	Q/A $\frac{BTU}{hrft^2}$	P_T $\frac{pounds}{in^2}$	T_{SAT} °F	T_W °F	T_B °F	ΔT_{SUP} °F	ΔT_{SUB} °F
	10	6,650	22.70	141.9	163.2	120.7	21.3	21.2
	10	6,600	22.59	141.6	168.1	129.0	26.5	12.6
	10	6,550	22.59	141.6	171.2	135.1	29.6	6.5
	10	6,700	22.71	141.9	172.9	140.7	31.0	1.2
	1	6,650	22.23	139.7	167.5	138.5	27.8	1.2
13	1	13,400	22.46	141.3	173.4	141.0	32.1	0.3
	10	13,400	23.03	142.7	179.9	141.4	37.2	1.3
	10	12,600	22.83	142.2	177.9	128.4	35.7	13.8
	10	13,500	22.78	142.1	175.0	119.4	32.9	22.7
	10	13,400	22.79	142.1	179.7	136.1	37.6	6.0
	10	13,400	23.25	143.4	180.0	142.3	36.6	1.1
	1	13,400	21.87	139.8	170.7	138.6	30.9	1.2
14	1	13,200	21.56	139.0	172.6	139.1	33.6	-0.1
	10	13,200	22.00	140.1	178.0	139.5	37.9	0.6
	10	13,200	21.34	138.5	176.0	116.8	37.5	22.2
	10	13,200	21.47	138.8	178.6	126.2	39.8	12.6
	10	13,200	21.80	139.6	179.1	139.1	39.5	0.5
	1	13,200	20.66	136.3	169.8	135.2	33.5	1.1
15	1	25,900	21.75	139.5	171.1	138.8	31.6	0.7
	10	25,900	22.36	141.0	173.9	139.7	32.9	1.3
	10	26,200	22.15	140.5	172.3	116.7	31.8	23.8
	10	25,900	22.08	140.3	173.8	129.4	33.5	10.9
	10	25,900	21.95	140.0	172.7	136.1	32.7	3.9
	10	25,800	21.90	139.9	171.8	138.1	31.9	1.8
	1	25,800	21.17	137.9	164.3	135.9	26.4	2.0
16	1	25,900	22.03	140.2	171.7	140.1	31.5	0.1
	10	26,200	22.44	141.2	175.7	140.4	34.5	0.8
	10	25,900	22.22	140.7	175.1	121.7	34.4	19.0

TABLE XI (CONT'D)

TEST SERIES	a/g	Q/A $\frac{BTU}{hrft^2}$	P_T $\frac{pounds}{in^2}$	T_{SAT} °F	T_W °F	T_B °F	ΔT_{SUP} °F	ΔT_{SUB} °F
	10	26,200	22.07	140.3	175.2	128.4	34.9	11.9
	10	26,100	21.95	140.0	173.8	136.0	33.8	4.0
	10	25,800	22.11	140.4	173.1	139.6	32.7	0.8
	1	25,800	22.08	140.3	167.9	139.3	27.6	1.0
17	1	41,400	21.15	140.5	174.4	140.4	33.9	0.1
	10	41,900	22.67	141.8	176.6	141.0	34.8	0.8
	10	41,700	22.58	141.6	175.8	135.9	34.2	5.7
	10	41,700	22.50	141.4	174.0	140.5	32.6	0.9
	1	41,000	21.34	138.5	170.1	137.7	31.6	0.8
18	1	3,700	22.06	140.3	168.7	138.1	28.4	2.2
	100	3,700	22.36	141.0	142.1	125.5	1.1	15.5
	100	3,650	22.36	141.0	95.5	79.3	-45.5	61.7
	100	3,650	22.36	141.0	117.5	101.7	-23.5	39.3
	100	3,650	22.36	141.0	132.4	116.7	-8.6	23.3
	100	3,650	22.36	141.0	140.2	124.0	-0.8	17.0
	1	3,700	22.26	140.8	171.2	136.8	30.4	4.0
19	1	6,400	22.48	141.3	170.8	139.5	29.5	1.8
	100	6,850	22.39	141.1	153.0	125.7	11.9	15.4
	100	6,800	22.39	141.1	113.5	82.7	-25.6	58.4
	100	6,800	22.39	141.1	133.3	103.2	-7.8	37.9
	100	6,750	22.39	141.0	146.1	116.5	5.0	24.5
	100	6,700	22.39	141.0	155.0	124.3	13.9	16.7
	1	6,700	21.87	139.8	166.8	137.8	27.0	2.0
20	1	13,200	22.36	141.0	169.2	140.8	28.2	0.2
	100	13,200	22.27	140.8	170.1	126.8	29.3	14.0
	100	13,200	22.27	140.8	141.0	91.2	0.2	49.6
	100	13,100	22.27	140.8	158.7	109.8	17.9	31.0
	100	13,200	22.27	140.8	167.2	117.8	26.4	23.0

TABLE XI (CONT'D)

TEST SERIES	a/g	Q/A $\frac{BTU}{hrft^2}$	P_T $\frac{pounds}{in^2}$	T_{SAT} °F	T_W °F	T_B °F	ΔT_{SUP} °F	ΔT_{SUB} °F
	100	13,300	22.27	140.8	175.0	124.5	34.2	16.3
	1	13,400	22.10	140.4	166.6	138.5	26.2	1.9
21	1	25,900	22.15	140.5	174.1	139.9	33.6	0.6
	100	26,300	22.39	141.1	179.0	121.8	37.9	19.3
	100	26,100	22.39	141.1	171.0	103.1	29.9	38.0
	100	25,800	22.39	141.1	175.3	110.7	34.2	30.4
	100	25,700	22.39	141.1	177.7	116.0	36.6	25.1
	100	25,900	22.39	141.1	179.1	123.2	38.0	18.9
	1	25,500	22.38	141.1	168.9	138.4	27.8	2.7
22	1	41,700	21.87	139.8	174.7	139.3	34.9	0.5
	100	41,900	22.43	141.2	181.3	125.9	40.1	15.3
	100	40,000	22.43	141.2	177.3	117.6	36.1	23.6
	100	41,200	22.43	141.2	179.6	121.4	38.4	19.8
	100	41,900	22.43	141.2	180.8	125.4	39.6	15.8
	1	41,700	22.55	141.5	172.7	139.1	31.2	2.4
23	1	3,850	22.08	140.3	169.2	140.1	28.9	0.2
	1	3,900	22.30	140.9	154.2	108.1	13.4	32.8
	1	3,850	22.36	141.0	161.5	122.3	20.5	18.7
	1	3,800	22.27	140.8	169.6	137.1	28.8	3.7
24	1	6,750	22.26	140.8	173.6	140.4	32.8	0.4
	1	6,800	22.35	141.0	159.8	107.6	18.8	33.4
	1	6,800	22.39	141.1	167.9	123.7	26.9	17.4
	1	6,900	22.54	141.5	174.9	135.5	33.4	5.0
25	1	13,600	22.31	140.9	179.6	140.3	38.7	0.6
	1	13,300	21.68	139.3	173.9	116.4	34.6	22.9
	1	13,300	21.82	139.7	178.6	123.2	38.9	16.5
	1	13,100	21.75	139.5	180.4	135.4	40.9	4.1
	1	13,200	21.75	139.5	180.0	138.1	40.5	1.4

TABLE XI (CONT'D)

TEST SERIES	a/g	Q/A $\frac{BTU}{hrft^2}$	P_T $\frac{pounds}{in^2}$	T_{SAT} °F	T_W °F	T_B °F	ΔT_{SUP} °F	ΔT_{SUB} °F
26	1	13,400	22.39	141.1	178.7	140.6	37.6	0.5
	1	13,600	22.23	140.7	171.0	112.1	30.3	28.6
	1	13,300	21.98	140.1	175.1	122.2	35.0	17.9
	1	13,400	22.46	141.3	180.8	134.6	39.5	6.7
	1	13,300	22.31	140.9	179.6	138.8	38.7	1.9
27	1	26,000	22.48	141.3	182.9	140.9	41.7	0.4
	1	26,100	22.41	141.2	183.4	135.9	42.2	5.3
	1	26,500	22.39	141.1	183.0	137.2	41.9	3.9
28	1	6,900	21.51	138.9	167.7	138.3	28.8	0.6
	10	6,750	23.00	142.6	169.1	139.8	27.1	2.8
	10	6,750	22.67	141.8	142.5	93.4	0.7	48.4
	10	6,750	22.42	141.2	159.9	118.8	18.7	22.4
	10	6,750	22.31	140.9	167.0	130.3	26.1	10.6
	1	6,650	21.94	140.0	168.0	137.6	28.0	2.4
29	1	13,300	22.02	140.2	173.1	140.1	32.9	0.1
	10	13,300	22.67	141.8	177.3	140.0	35.5	1.8
	10	13,400	22.19	140.6	167.0	103.8	26.4	36.8
	10	13,200	21.43	138.7	173.4	127.7	34.7	11.0
	1	13,200	22.55	141.5	174.2	140.1	32.7	1.4
30	1	26,300	22.36	141.0	175.1	140.5	34.1	0.5
	10	26,200	23.65	144.4	183.0	142.7	38.6	1.7
	10	26,100	23.52	144.1	182.3	120.5	38.2	23.6
	10	26,200	23.40	143.7	182.4	132.7	38.7	11.0
	10	26,000	23.19	143.3	181.6	137.3	38.3	6.0
	10	25,900	23.00	142.6	180.7	125.7	38.1	16.9
	1	26,200	22.23	140.7	174.8	139.2	34.1	1.5
31	1	42,500	22.40	141.1	177.3	140.6	36.2	0.5
	10	42,300	23.09	142.9	180.4	140.4	37.5	2.5

TABLE XI (CONT'D)

TEST SERIES	a/g	Q/A	P_T	T_{SAT}	T_W	T_B	ΔT_{SUP}	ΔT_{SUB}
		$\frac{BTU}{hrft^2}$	$\frac{pounds}{in^2}$	°F	°F	°F	°F	°F
	10	42,100	22.07	142.8	180.3	136.4	37.5	6.4
	1	42,100	22.56	141.5	176.5	140.1	35.0	1.4
32	1	13,500	22.43	141.2	174.7	141.1	33.5	0.1
	100	13,500	22.39	141.1	169.4	126.5	28.3	14.6
	100	13,500	22.39	141.1	141.6	92.5	0.5	48.6
	100	13,400	22.39	141.1	157.8	111.5	16.7	29.6
	100	13,300	22.39	141.1	168.5	125.8	27.4	15.3
33	1	26,200	22.03	140.2	176.2	140.0	36.0	0.2
	100	26,300	22.43	141.2	183.8	125.0	42.6	16.2
	100	26,200	22.43	141.2	169.7	99.0	28.5	42.2
	100	26,500	22.43	141.2	179.2	115.1	38.0	26.1
	1	26,300	22.59	141.6	174.7	139.2	33.1	2.4
34	1	42,000	22.19	140.6	177.5	139.9	36.9	0.7
	100	42,300	22.38	141.1	184.9	126.2	43.8	14.9
	100	41,900	22.38	141.1	180.7	109.4	39.6	31.7
	100	42,400	22.38	141.1	183.6	117.6	42.5	23.5
	1	41,700	21.75	139.5	174.7	137.6	35.2	2.2
35	1	3,650	21.76	139.5	165.1	139.3	25.6	0.2
	1	13,400	22.35	141.0	171.4	140.7	30.4	0.3
	1	42,200	22.35	141.0	176.2	140.8	35.3	0.1
36	1	13,200	22.39	141.1	171.5	141.0	30.4	0.1
	1	3,700	21.67	139.3	165.2	139.5	25.9	-0.2
	-	-	-	-	-	-	-	-
37	1	4,000	22.11	140.4	173.8	138.8	33.4	1.6
	1	6,750	22.46	141.3	178.8	140.6	37.5	0.7
	1	13,400	22.45	141.3	175.9	141.1	34.6	0.2
	1	24,000	22.43	141.2	176.2	141.0	35.0	0.2
38	1	12,800	22.43	141.2	173.4	141.0	32.2	0.2

TABLE XI (CONT'D)

TEST SERIES	a/g	Q/A $\frac{BTU}{hrft^2}$	P_T $\frac{pounds}{in^2}$	T_{SAT} °F	T_W °F	T_B °F	ΔT_{SUP} °F	ΔT_{SUB} °F
	1	6,500	22.43	141.2	171.5	140.4	30.2	0.8
	1	3,600	22.47	141.3	165.2	139.7	23.9	1.6
39	1	24,500	22.39	141.1	170.8	140.8	29.7	0.3
	1	24,800	22.23	140.7	169.7	134.5	29.0	6.2
	1	24,400	22.22	140.7	169.9	138.9	29.2	1.8
	1	25,100	22.27	140.8	170.4	140.5	29.6	0.3
40	1	24,800	22.39	141.1	170.7	140.8	29.6	0.3
	10	24,800	23.03	142.7	171.6	139.9	28.9	2.8
	10	24,500	22.87	142.3	170.5	125.1	28.2	17.2
	10	24,300	22.86	142.3	171.3	133.2	29.0	9.1
	10	24,500	22.75	142.0	170.9	137.7	28.9	4.3
	1	25,000	22.47	141.3	169.2	140.2	27.9	1.1
41	1	24,800	22.27	140.8	170.0	139.9	30.2	0.9
	100	24,600	22.27	140.8	170.4	127.6	30.6	13.2
	100	24,200	22.27	140.8	143.2	96.2	2.4	44.6
	100	24,200	22.27	140.8	160.6	114.2	19.8	26.6
	100	24,500	22.27	140.8	170.3	126.9	29.5	13.9
	1	24,400	22.35	141.0	168.4	138.3	27.4	2.7
	-	-	-	-	-	-	-	-
42	1	3,750	21.91	139.9	171.1	139.6	31.2	0.3
	100	3,700	21.63	139.2	151.3	129.6	12.1	9.6
43	1	6,900	22.11	140.4	172.3	140.4	32.9	0.0
	100	6,650	21.90	139.9	160.5	130.0	20.6	9.9
44	1	12,800	21.87	139.8	177.1	139.0	37.3	0.8
	100	13,300	21.95	140.0	174.1	130.5	34.1	9.5
45	1	26,300	21.35	138.5	171.9	137.8	33.4	0.7
	100	26,000	22.03	140.2	179.2	129.9	38.7	10.3
46	1	41,400	21.95	140.0	178.6	140.2	38.6	-0.2
	100	41,200	21.59	139.1	181.0	128.6	41.9	10.5

TABLE XII

TEMPERATURE SCAN DATA

TEST SERIES I

$Q/A = 3{,}650 BTU/HrFt^2$
$a/g = 1$ $T_{SAT}=139.3^oF$
$T_B=139.1^oF$ $T_W=172.4^oF$

Z Inches	T ^oF
$3.73x10^{-3}$	154.1
6.05 "	142.4
10.68 "	139.1
15.46 "	138.8
19.74 "	138.5
24.42 "	137.9
28.88 "	137.9
32.98 "	137.6
37.49 "	137.6
42.17 "	137.9
46.63 "	137.6

$Q/A = 13{,}400 BTU/HrFt^2$
$a/g = 1$ $T_{SAT}=139.9^oF$
$T_B=140.1^oF$ $T_W=175.3^oF$

Z Inches	T ^oF
$1.50x10^{-3}$	148.3
4.89 "	140.7
8.90 "	139.2
13.58 "	138.8
17.69 "	138.8
22.19 "	138.8
26.96 "	138.8
31.47 "	138.8
36.02 "	138.8
40.39 "	138.8
45.16 "	138.8

$Q/A = 41{,}700 BTU/HrFt^2$
$a/g = 1$ $T_{SAT}=139.0°F$
$T_B=138.8°F$ $T_W=178.8°F$

Z Inches	T ^oF
$1.50x10^{-3}$	140.2
2.43 "	137.7
7.16 "	137.7
11.89 "	137.7
16.53 "	137.7
20.94 "	137.7
25.31 "	137.7
30.08 "	137.7
34.59 "	137.7
38.83 "	137.7

TABLE XII (CONT'D)

TEST SERIES 6

$Q/A = 3,700 BTU/HrFt^2$
$a/g = 1$ $T_{SAT}=139.2^oF$
$T_B=138.9^oF$ $T_W=171.7^oF$

Z Inches	T ^oF
$1.50x10^{-3}$	156.9
6.49 "	140.7
11.09 "	138.5
15.72 "	137.9
20.38 "	138.2
24.82 "	137.4
29.28 "	137.4
34.01 "	137.4
38.42 "	137.1
43.02 "	136.8
47.39 "	137.1

$Q/A = 3,650 BTU/HrFt^2$
$a/g = 1$ $T_{SAT}=140.1^oF$
$T_B=105.8^oF$ $T_W=153.3^oF$

Z Inches	T ^oF
$1.50x10^{-3}$	145.5
5.69 "	131.7
10.24 "	107.6
14.56 "	104.7
19.34 "	105.3
23.66 "	104.1
28.30 "	103.6
32.63 "	106.5
37.04 "	103.0
41.64 "	103.0
46.32 "	103.0

$Q/A = 3,650 BTU/HrFt^2$
$a/g = 1$ $T_{SAT}=140.3^oF$
$T_B=116.8^oF$ $T_W=161.8^oF$

Z Inches	T ^oF
$1.50x10^{-3}$	147.2
6.09 "	125.0
10.82 "	116.9
15.50 "	116.9
19.60 "	116.9
24.38 "	113.5
28.88 "	113.5
33.16 "	116.9
37.62 "	116.9
42.08 "	113.5
46.27 "	112.9

$Q/A = 3,600 BTU/HrFt^2$
$a/g = 1$ $T_{SAT}=138.5^oF$
$T_B=134.2^oF$ $T_W=171.9^oF$

Z Inches	T ^oF
$1.50x10^{-3}$	157.1
7.20 "	137.6
12.11 "	133.1
16.79 "	132.0
21.21 "	131.5
25.67 "	132.0
29.95 "	131.5
34.23 "	131.5
38.65 "	132.0
43.06 "	132.0
47.88 "	132.0

$Q/A = 3,600 BTU/HrFt^2$
$a/g = 1$ $T_{SAT}=139.5^oF$
$T_B=139.3^oF$ $T_W=171.9^oF$

Z Inches	T ^oF
$1.50x10^{-3}$	153.3
9.75 "	138.2
10.06 "	137.6
14.47 "	137.6
18.93 "	137.4
23.31 "	137.4
27.81 "	137.6
32.31 "	137.6
36.69 "	137.1
41.19 "	137.6
45.65 "	137.1

$Q/A = 3,650 BTU/HrFt^2$
$a/g = 1$ $T_{SAT}=139.3^oF$
$T_B=139.1^oF$ $T_W=172.4^oF$

Z Inches	T ^oF
$3.73x10^{-3}$	154.1
6.05 "	142.4
10.68 "	139.1
15.46 "	138.8
19.74 "	138.5
24.42 "	137.9
28.88 "	137.9
32.98 "	137.6
37.49 "	137.6
42.17 "	137.9
46.63 "	137.6

TABLE XII (CONT'D)

TEST SERIES 8

$Q/A = 13{,}300 BTU/HrFt^2$
$a/g = 1$ $T_{SAT}=139.6^oF$
$T_B=139.7^oF$ $T_W=177.7^oF$

Z Inches	T ^oF
$1.50x10^{-3}$	154.2
6.27 "	139.6
11.00 "	138.8
15.63 "	137.4
20.09 "	137.9
24.69 "	137.9
29.28 "	137.9
33.61 "	137.9
38.25 "	137.9
42.66 "	137.9
47.12 "	137.9

$Q/A = 13{,}300 BTU/HrFt^2$
$a/g = 1$ $T_{SAT}=138.8^oF$
$T_B=128.3^oF$ $T_W=178.7^oF$

Z Inches	T ^oF
$1.50x10^{-3}$	150.8
6.71 "	132.6
11.58 "	131.6
15.95 "	131.2
20.01 "	131.6
24.96 "	131.2
29.24 "	128.3
33.83 "	128.9
38.16 "	129.2
42.80 "	128.3
47.17 "	128.3

$Q/A = 13{,}300 BTU/HrFt^2$
$a/g = 1$ $T_{SAT}=139.0^oF$
$T_B=134.4^oF$ $T_W=179.7^oF$

Z Inches	T ^oF
$1.50x10^{-3}$	156.6
7.03 "	136.0
10.51 "	135.4
14.88 "	135.4
19.60 "	135.1
23.93 "	134.0
28.52 "	134.8
33.07 "	134.8
37.53 "	134.5
41.81 "	134.3
46.19 "	134.3

$Q/A = 13{,}400 BTU/HrFt^2$
$a/g = 1$ $T_{SAT}=139.9^oF$
$T_B=140.1^oF$ $T_W=175.3^oF$

Z Inches	T ^oF
$1.50x10^{-3}$	148.3
4.89 "	140.7
8.90 "	139.2
13.58 "	138.8
17.69 "	138.8
22.19 "	138.8
26.96 "	138.8
31.47 "	138.8
36.02 "	138.8
40.39 "	138.8
45.16 "	138.8

TABLE XII (CONT'D)

TEST SERIES 10

$Q/A = 42{,}600 BTU/HrFt^2$
$a/g = 1$ $T_{SAT}=139.0^oF$
$T_B=138.8^oF$ $T_W=177.3^oF$

Z Inches	T ^oF
$1.50x10^{-3}$	-
4.26 "	138.2
8.90 "	138.2
13.32 "	137.9
18.13 "	137.9
22.59 "	137.9
27.05 "	137.9
31.56 "	137.9
36.28 "	137.9
40.21 "	137.9
45.03 "	137.9

$Q/A = 42{,}200 BTU/HrFt^2$
$a/g = 1$ $T_{SAT}=139.4^oF$
$T_B=137.7^oF$ $T_W=177.1^oF$

Z Inches	T ^oF
$1.50x10^{-3}$	-
3.99 "	137.4
8.10 "	137.4
12.42 "	137.4
16.84 "	137.4
21.48 "	137.4
26.29 "	137.4
30.80 "	137.4
35.21 "	137.4
39.32 "	137.4
43.87 "	137.4

$Q/A = 41{,}700 BTU/HrFt^2$
$a/g = 1$ $T_{SAT}=139.0^oF$
$T_B=138.8^oF$ $T_W=178.8^oF$

Z Inches	T ^oF
$1.50x10^{-3}$	140.2
2.43 "	137.7
7.16 "	137.7
11.89 "	137.7
16.53 "	137.7
20.94 "	137.7
25.31 "	137.7
30.08 "	137.7
34.59 "	137.7
38.83 "	137.7

TABLE XII (CONT'D)

TEST SERIES II

$Q/A = 3,650 BTU/HrFt^2$ $a/g = 10$ $T_{SAT}=141.1^oF$ $T_B=137.9^oF$ $T_W=169.2^oF$

Z Inches	T ^oF
$1.50x10^{-3}$	158.1
6.51 "	152.5
10.96 "	140.2
15.60 "	138.5
19.94 "	138.0
24.58 "	138.0
29.00 "	138.0
33.51 "	138.0
37.98 "	138.0
42.27 "	138.0
46.81 "	137.4

$Q/A = 3,650 BTU/HrFt^2$ $a/g = 10$ $T_{SAT}=140.7^oF$ $T_B=100.9^oF$ $T_W=133.7^oF$

Z Inches	T ^oF
$1.50x10^{-3}$	123.9
6.18 "	116.5
11.14 "	99.8
15.78 "	98.6
20.10 "	97.4
24.63 "	98.0
29.33 "	98.0
33.85 "	97.4
38.34 "	97.4
42.56 "	97.4
47.27 "	97.4

$Q/A = 3,650 BTU/HrFt^2$ $a/g = 10$ $T_{SAT}=140.4^oF$ $T_B=118.3^oF$ $T_W=150.8^oF$

Z Inches	T ^oF
$1.50x10^{-3}$	140.3
5.17 "	132.4
9.97 "	121.0
14.34 "	119.9
18.71 "	117.6
23.27 "	118.7
27.68 "	117.6
32.17 "	117.6
36.53 "	117.6
41.01 "	117.6
45.43 "	117.6

$Q/A = 3,650 BTU/HrFt^2$ $a/g = 10$ $T_{SAT}=140.0^oF$ $T_B=131.6^oF$ $T_W=163.3^oF$

Z Inches	T ^oF
$1.50x10^{-3}$	152.5
5.55 "	145.8
10.18 "	134.6
14.37 "	132.3
19.46 "	131.2
23.80 "	131.2
28.44 "	131.2
32.77 "	131.2
37.18 "	131.2
42.06 "	131.2
46.63 "	131.2

$Q/A = 3,650 BTU/HrFt^2$ $a/g = 10$ $T_{SAT}=140.3^oF$ $T_B=135.4^oF$ $T_W=167.2^oF$

Z Inches	T ^oF
$1.50x10^{-3}$	158.1
5.42 "	153.6
9.84 "	138.0
14.70 "	135.7
18.85 "	134.6
23.44 "	135.7
27.99 "	134.6
32.49 "	134.6
36.77 "	134.6
41.23 "	134.6
45.86 "	134.6

$Q/A = 3,600 BTU/HrFt^2$ $a/g = 10$ $T_{SAT}=140.3^oF$ $T_B=137.3^oF$ $T_W=170.7^oF$

Z Inches	T ^oF
$1.50x10^{-3}$	160.3
6.09 "	149.2
10.55 "	142.4
15.37 "	139.1
20.41 "	138.0
25.58 "	138.0
29.77 "	138.0
34.05 "	138.0
38.51 "	138.5
43.11 "	138.0
47.52 "	138.5

TABLE XII (CONT'D)

TEST SERIES 13

Q/A = 13,400BTU/HrFt^2 a/g = 10 T_{SAT}=142.7^{o}F T_B=141.4^{o}F T_W=179.9^{o}F

Z Inches	T ^{o}F
1.50x10^{-3}	148.9
6.27 "	141.9
11.13 "	141.3
15.32 "	141.3
20.01 "	141.3
24.42 "	141.3
28.84 "	141.3
33.47 "	141.3
37.89 "	141.3
42.44 "	141.3
46.85 "	141.3

Q/A = 12,600BTU/HrFt^2 a/g = 10 T_{SAT}=142.2^{o}F T_B=128.4^{o}F T_W=177.9^{o}F

Z Inches	T ^{o}F
1.50x10^{-3}	144.5
6.22 "	134.0
10.86 "	132.9
15.72 "	132.9
19.87 "	132.9
24.73 "	132.9
29.19 "	133.5
33.43 "	132.3
38.29 "	132.3
42.48 "	131.8
46.94 "	132.9

Q/A = 13,500BTU/HrFt^2 a/g = 10 T_{SAT}=142.1^{o}F T_B=119.4^{o}F T_W=175.0^{o}F

Z Inches	T ^{o}F
1.50x10^{-3}	135.9
7.33 "	121.6
12.03 "	121.0
16.23 "	119.9
20.52 "	120.4
25.01 "	119.9
29.47 "	120.4
33.96	119.9
38.37 "	120.4
42.89 "	121.0
47.30 "	120.4

Q/A = 13,400BTU/HrFt^2 a/g = 10 T_{SAT}=142.1^{o}F T_B=136.1^{o}F T_W=179.7^{o}F

Z Inches	T ^{o}F
1.50x10^{-3}	142.5
7.20 "	137.1
11.49 "	137.1
16.66 "	136.8
20.99 "	136.8
25.49 "	137.4
29.73 "	136.5
34.10 "	136.5
38.87 "	136.3
43.33 "	136.5
48.06 "	136.3

Q/A = 13,400BTU/HrFt^2 a/g = 10 T_{SAT}=143.4^{o}F T_B=142.3^{o}F T_W=180.0^{o}F

Z Inches	T ^{o}F
1.50x10^{-3}	146.9
6.63 "	142.7
11.35 "	142.4
15.86 "	142.2
20.09 "	141.9
24.64 "	141.9
28.97 "	141.9
33.43 "	141.9
38.07 "	141.9
42.44 "	141.9
46.76 "	141.9

TABLE XII (CONT'D)

TEST SERIES 17

$Q/A = 41,900 BTU/HrFt^2$
$a/g = 10$ $T_{SAT}=141.8^oF$
$T_B=141.0^oF$ $T_W=176.6^oF$

Z Inches	T ^oF
$1.50x10^{-3}$	142.8
5.78 "	142.2
10.42 "	141.3
14.93 "	141.3
19.51 "	141.3
24.22 "	141.3
28.37 "	141.3
32.78 "	141.3
36.93 "	141.3
41.73 "	141.3
46.15 "	141.3

$Q/A = 41,700 BTU/HrFt^2$
$a/g = 10$ $T_{SAT}=141.6^oF$
$T_B=135.9^oF$ $T_W=175.8^oF$

Z Inches	T ^oF
$1.50x10^{-3}$	141.4
5.51 "	140.2
9.88 "	140.2
14.39 "	139.7
19.02 "	139.1
23.35 "	139.1
28.17 "	139.1
32.58 "	138.5
36.91 "	138.5
41.55 "	137.9
45.20 "	137.9

$Q/A = 41,700 BTU/HrFt^2$
$a/g = 10$ $T_{SAT}=141.4^oF$
$T_B=140.5^oF$ $T_W=174.0^oF$

Z Inches	T ^oF
$1.50x10^{-3}$	142.5
5.24 "	141.3
9.88 "	141.3
14.30 "	141.3
18.35 "	141.3
22.81 "	141.3
27.63 "	141.3
31.73 "	141.3
36.56 "	141.3
40.92 "	141.3
45.25 "	141.3

TABLE XIII

ACTIVE SITE DENSITY AND BUBBLE FREQUENCY DATA

TEST SERIES	a/g	Q/A	ΔT_{SUB}	ACTIVE SITE DENSITY	ACTIVE PERIOD	INACTIVE PERIOD	BUBBLE FREQUENCY
—	—	$\frac{BTU}{hrft^2}$	^oF	$\frac{Sites}{in^2}$	Millisec	Millisec	$\frac{Bubbles}{Sec}$
23	1	3,850	0.2	785	9.5	5.5	66.7
		3,900	32.8	575	26.0	14.0	25.0
		3,850	18.7	735	21.5	10.5	31.3
		3,800	3.7	895	14.0	6.5	48.8
24	1	6,750	0.4	1,380	8.5	4.5	77.0
		6,800	33.4	1,205	25.0	14.0	25.7
		6,800	17.4	1,410	19.0	10.0	34.4
		6,900	5.0	1,425	15.0	7.0	45.4
25	1	13,600	0.6	2,495	7.5	5.5	76.9
		13,300	22.9	2,020	22.0	11.0	30.3
		13,300	16.5	2,170	18.5	8.0	37.7
		13,100	4.1	2,230	11.5	7.5	52.7
26	1	13,600	28.6	2,080	18.0	13.0	32.3
		13,300	17.9	2,380	15.0	12.0	37.1
		13,400	6.7	2,490	11.0	7.0	55.6
27	1	26,100	5.3	4,680	8.0	6.5	68.8
28	10	6,750	2.8	1,220	11.5	8.0	51.3
		6,750	48.4	935	24.0	19.5	23.0
		6,750	22.4	1,335	18.5	16.0	28.9
		6,750	10.6	1,250	16.5	11.5	35.7
29	10	13,300	1.8	2,550	11.0	7.0	55.6
		13,400	36.8	2,365	20.0	16.0	27.8
		13,200	11.0	2,650	13.5	12.0	39.3
30	10	26,100	23.6	4,560	13.5	12.5	38.5
		26,200	11.0	4,650	11.0	9.0	50.0
		26,000	6.0	4,650	10.0	7.0	58.8
		25,900	16.9	4,620	12.0	11.0	43.5
31	10	42,100	6.4	*	*	*	*

TABLE XIII (CONT'D)

TEST SERIES	a/g	Q/A	ΔT_{SUB}	ACTIVE SITE DENSITY	ACTIVE PERIOD	INACTIVE PERIOD	BUBBLE FREQUENCY
—	—	$\frac{BTU}{hrft^2}$	^oF	$\frac{Sites}{in^2}$	Millisec	Millisec	$\frac{Bubbles}{Sec}$
32	100	13,500	14.6	460	7.0	6.0	76.9
		13,500	48.6	515	13.0	10.5	42.5
		13,400	29.6	580	11.5	6.0	57.3
		13,300	15.3	510	7.5	4.0	87.0
33	100	26,300	16.2	1,020	6.5	2.5	111.0
		26,200	42.2	975	11.0	7.0	55.6
		26,500	26.1	1,070	8.0	5.0	76.9
34	100	42,300	14.9	2,060	4.5	2.5	143.0
		41,900	31.7	2,000	7.5	6.5	71.4
		42,400	23.5	2,100	6.5	4.0	95.3

* The active site density and bubble period could not be determined from the film strips obtained for this test condition.

TABLE XIV

AVERAGE POPULATION DENSITY, MAXIMUM BUBBLE SIZE

AND

PROPORTION OF COLLAPSING BUBBLES IN TEN BUBBLE SAMPLE

TEST SERIES	a/g	Q/A	ΔT_{SUB}	AVERAGE POPULATION DENSITY	MAXIMUM BUBBLE SIZE	COLLAPSING BUBBLES / COLLAPSING + DEPARTING BUBBLES
—	—	$\frac{BTU}{hrft^2}$	^oF	$\frac{Bubbles}{in^2}$	Inches	—
23	1	3,850	0.2	610	19.6×10^{-3}	0.1
		3,900	32.8	360	14.0 x "	0.6
		3,850	18.7	465	16.7 "	0.5
		3,800	3.7	590	20.0 "	0.2
24	1	6,750	0.4	910	20.8 "	0.0
		6,800	33.4	510	12.9 "	0.4
		6,800	17.4	645	14.6 "	0.3
		6,900	5.0	790	19.0 "	0.2
25	1	13,600	0.6	1,010	16.6 "	0.0
		13,300	22.9	885	12.5 "	0.5
		13,300	16.5	920	13.3 "	0.3
		13,100	4.1	970	15.4 "	0.0
26	1	13,600	28.6	850	14.2 "	0.3
		13,300	17.9	930	15.6 "	0.1
		13,400	6.7	1,000	18.8 "	0.0
27	1	26,100	5.3	1,900	15.2 "	0.1
28	10	6,750	2.8	610	12.8 "	0.0
		6,750	48.4	480	5.7 "	0.9
		6,750	22.4	650	6.3 "	0.7
		6,750	10.6	640	9.5 "	0.6
29	10	13,300	1.8	1,130	13.9 "	0.2
		13,400	36.8	930	6.5 "	1.0
		13,200	11.0	1,150	9.9 "	0.6
30	10	26,100	23.6	1,610	7.4 "	0.6
		26,200	11.0	1,780	11.5 "	0.1
		26,000	6.0	1,810	14.0 "	0.0
		25,900	16.9	1,740	8.4 "	0.5
31	10	42,100	6.4	*	*	*

TABLE XIV (CONT'D)

TEST SERIES	a/g	Q/A	ΔT_{SUB}	AVERAGE POPULATION DENSITY	MAXIMUM BUBBLE SIZE	COLLAPSING BUBBLES: COLLAPSING / (COLLAPSING + DEPARTING BUBBLES)
—	—	$\frac{BTU}{hrft^2}$	^oF	$\frac{Bubbles}{in^2}$	Inches	—
32	100	13,500	14.6	370	5.9×10^{-3}	0.6
		13,500	48.6	270	4.4 "	0.9
		13,400	29.6	335	5.7 "	0.7
		13,300	15.3	390	6.5 "	0.6
33	100	26,300	16.2	630	6.0 "	0.6
		26,200	42.2	475	5.4 "	1.0
		26,500	26.1	570	5.6 "	0.8
34	100	42,300	14.9	1,140	5.8 "	0.5
		41,900	31.7	1,060	4.9 "	0.7
		42,400	23.5	1,070	5.5 "	0.8

* The average population density, the maximum bubble size and the proportion of collapsing bubbles in the sample examined could not be determined from the film strips obtained for this test condition.

APPENDIX E

TYPICAL BUBBLE PHOTOGRAPHS

COMMENTS PERTINENT TO TYPICAL BUBBLE PHOTOGRAPHS

A. Bubbles Attached To Surface

B. Bubbles Detached From Surface

C. Attached Bubble: Well Defined Outline And High Image Density

D. Detached Bubble: Poorly Defined Outline And Low Image Density

E. Most Severe Condition Photographed: Most Powerful Light Source Run 20% Beyond Rated Output

F. Phenomena Can Be Photographed Only When The Bubbles Above The Surface Clear Away: Photographs Tend To Be Overexposed

G. Vapour Masses Resulting From The Coallescence Of Bubbles Above The Heat Transfer Surface

H. Only The Photographs In Which The Vapour Masses Clear Away Could Be Analysed

I. Dark Spots Are Vapour Bubbles Forming Despite The Fact That The Surface Temperature Is Equivalent To The Saturation Temperature: Analysis Indicates That All The Heat Dissipated Could Be Transferred By Natural Convection

J. Dark Streaks Are Thought To Indicate Density Gradients In The Fluid: The Fact That Bubbles Are Observed To Form Along Streaks Suggests That Sites Are Activated By The Passage Of A Stream Of Hot Fluid

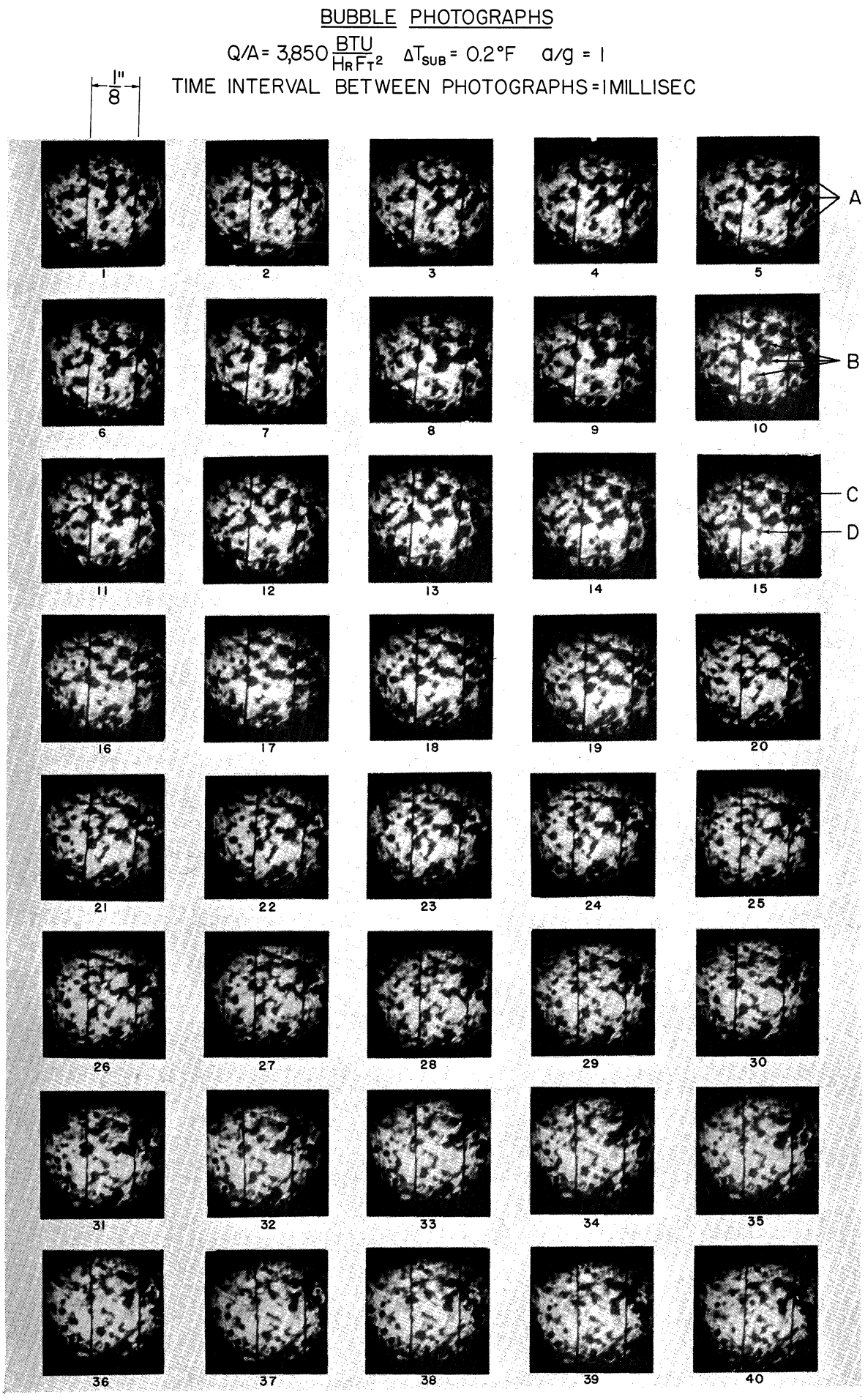

Figure 79. Bubble Photographs, Low Heat Flux, Low Subcooling, a/g = 1.

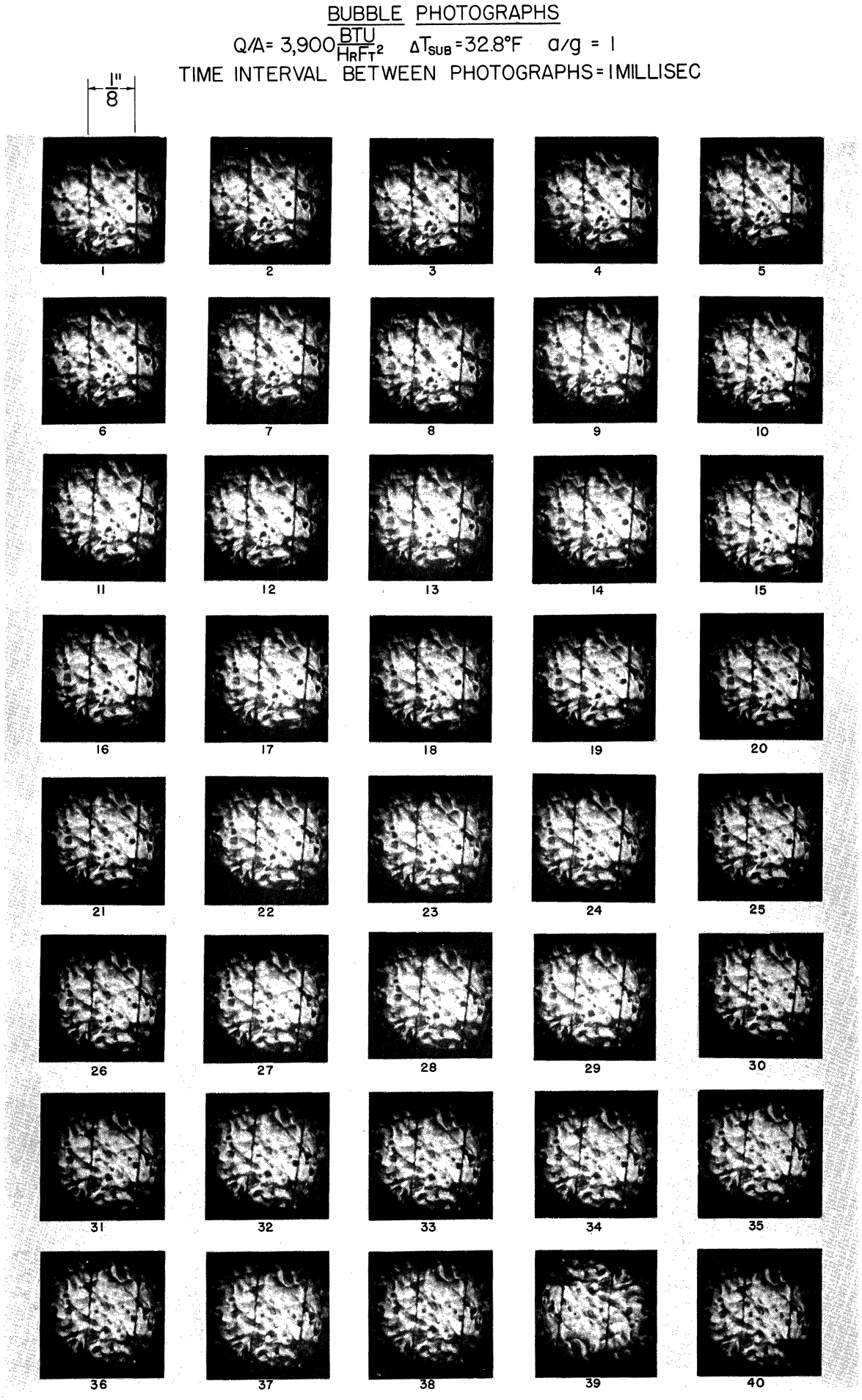

Figure 80. Bubble Photographs, Low Heat Flux, High Subcooling, a/g = 1.

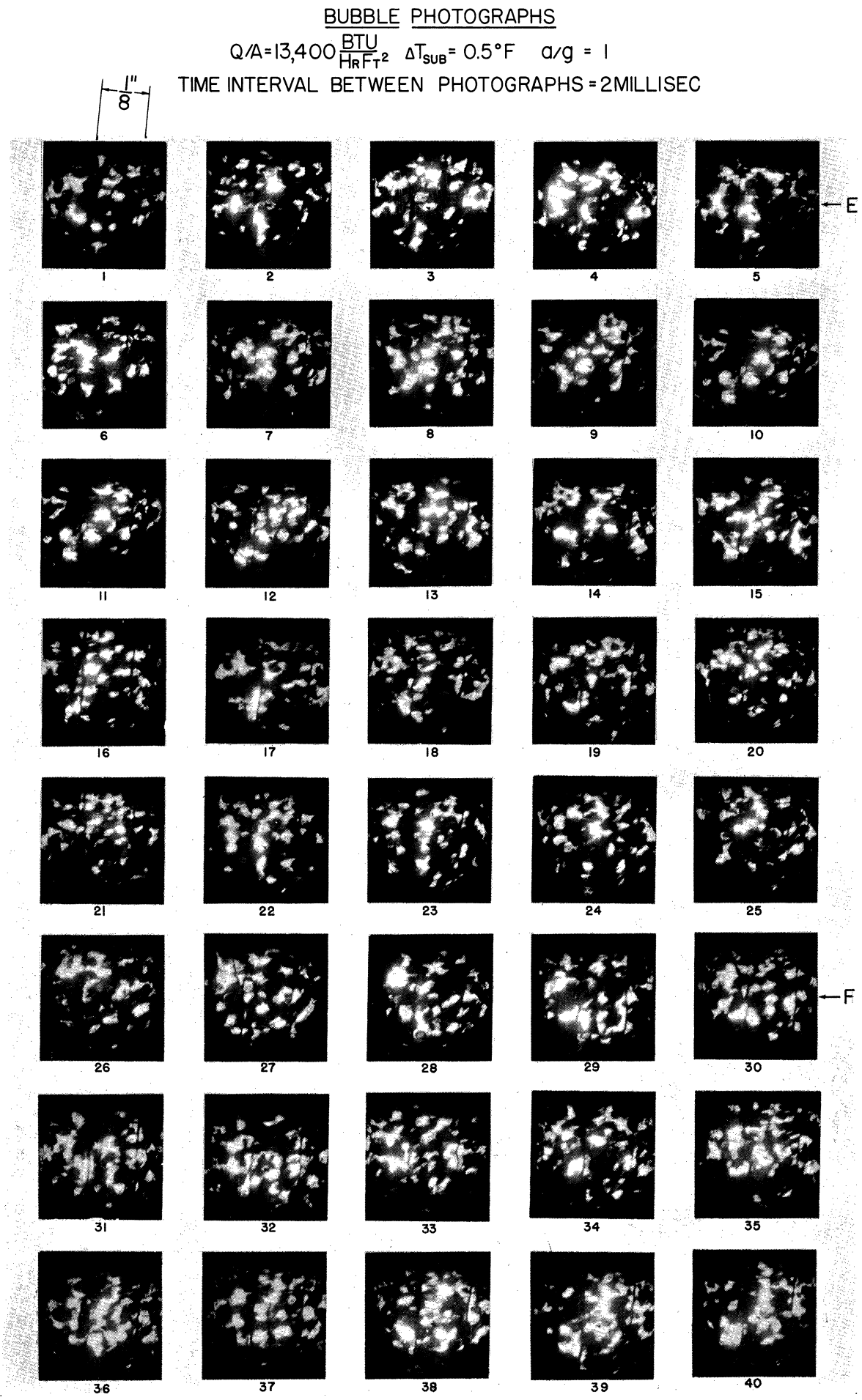

Figure 81. Bubble Photographs, Medium Heat Flux, Low Subcooling, a/g = 1.

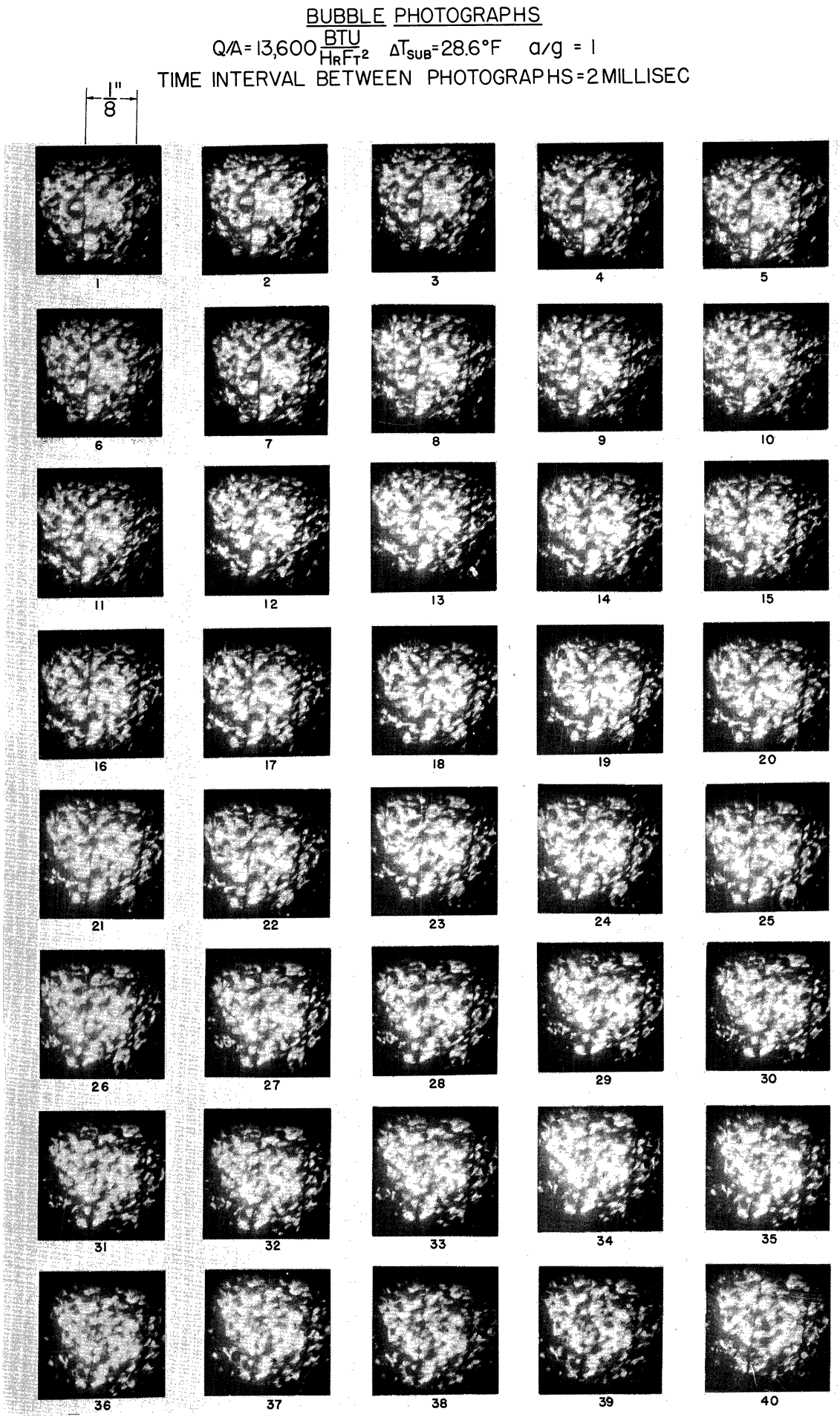

Figure 82. Bubble Photographs, Medium Heat Flux, High Subcooling, a/g = 1.

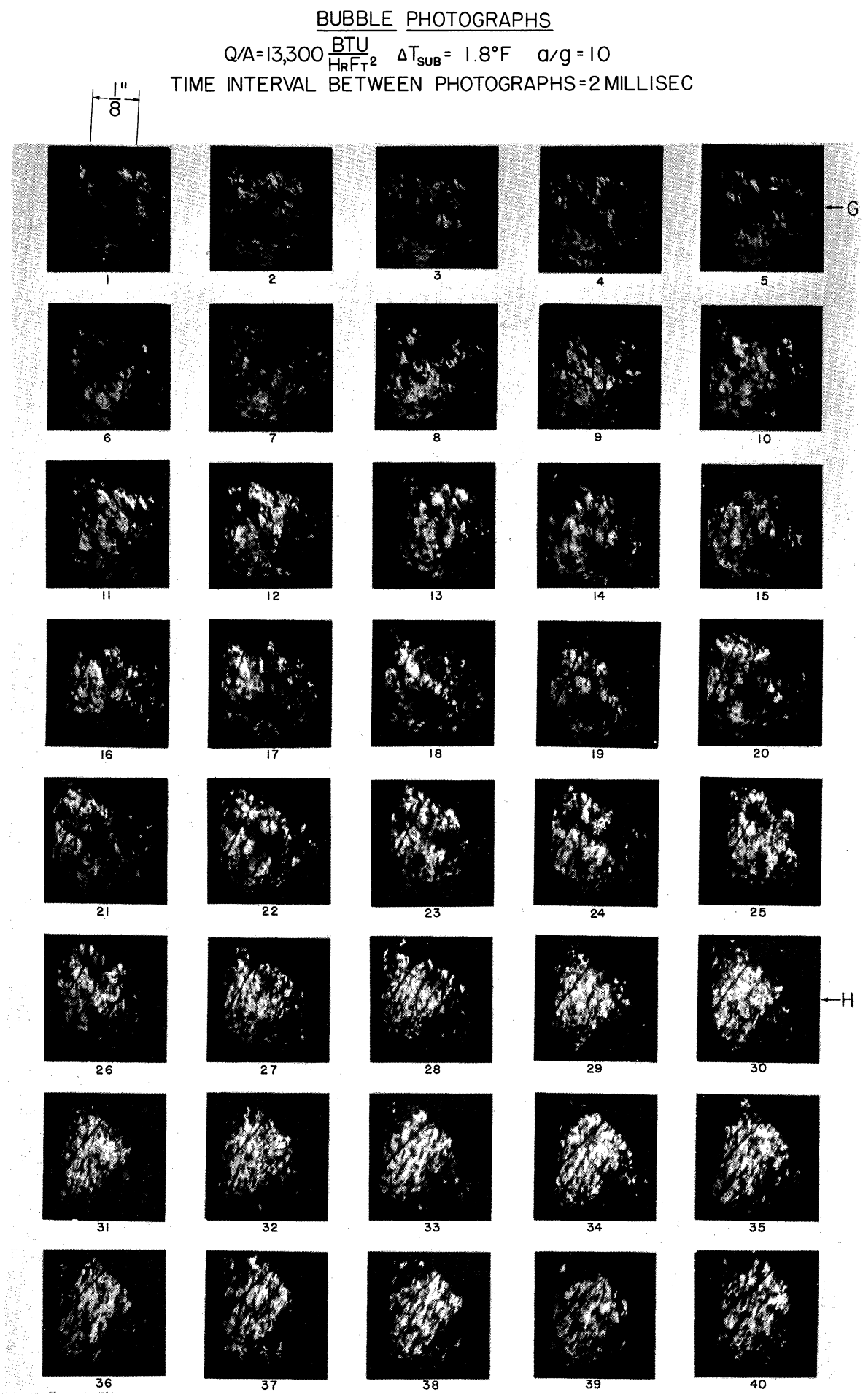

Figure 83. Bubble Photographs, Medium Heat Flux, Low Subcooling, a/g = 10.

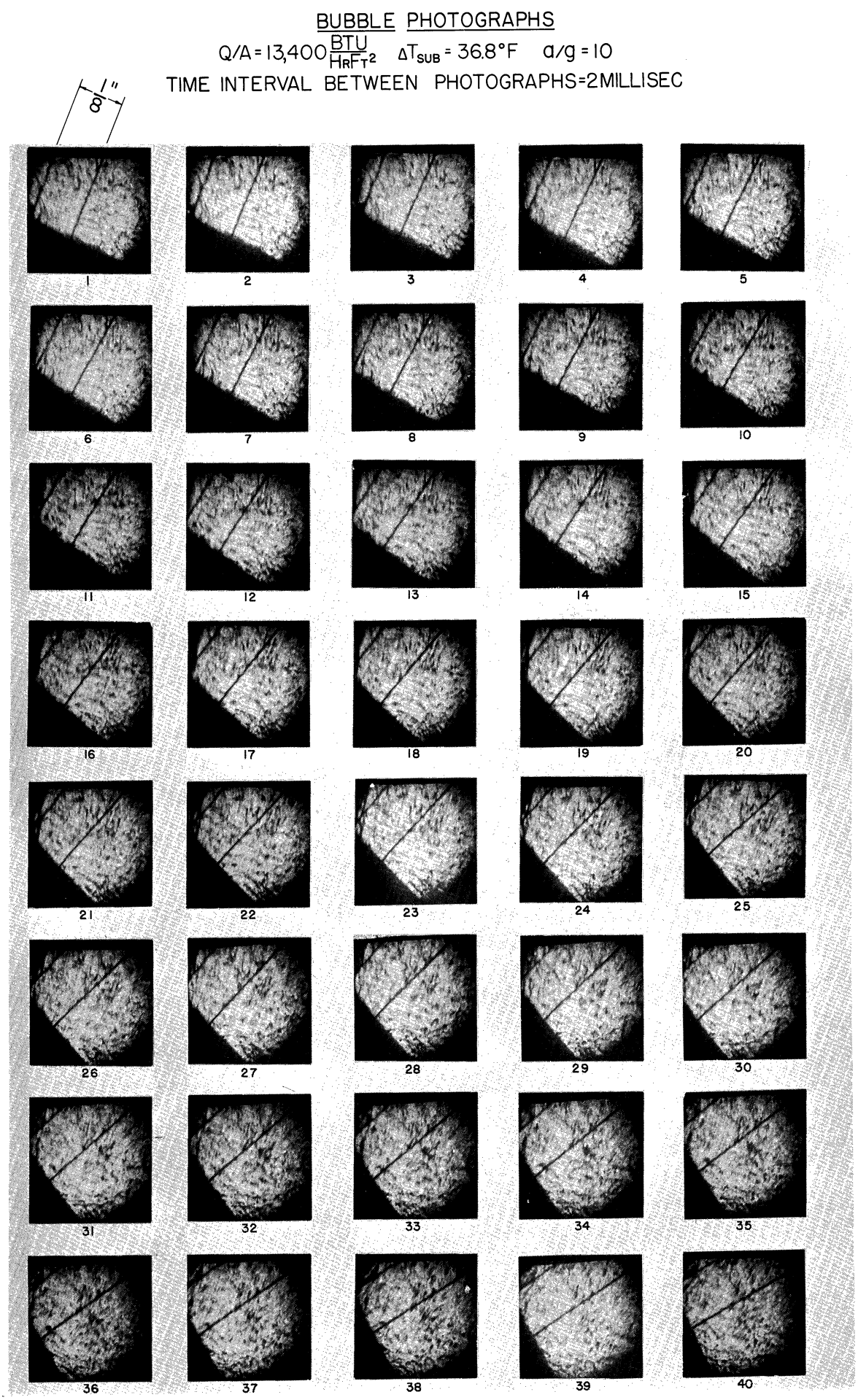

Figure 84. Bubble Photographs, Medium Heat Flux, High Subcooling, a/g = 10.

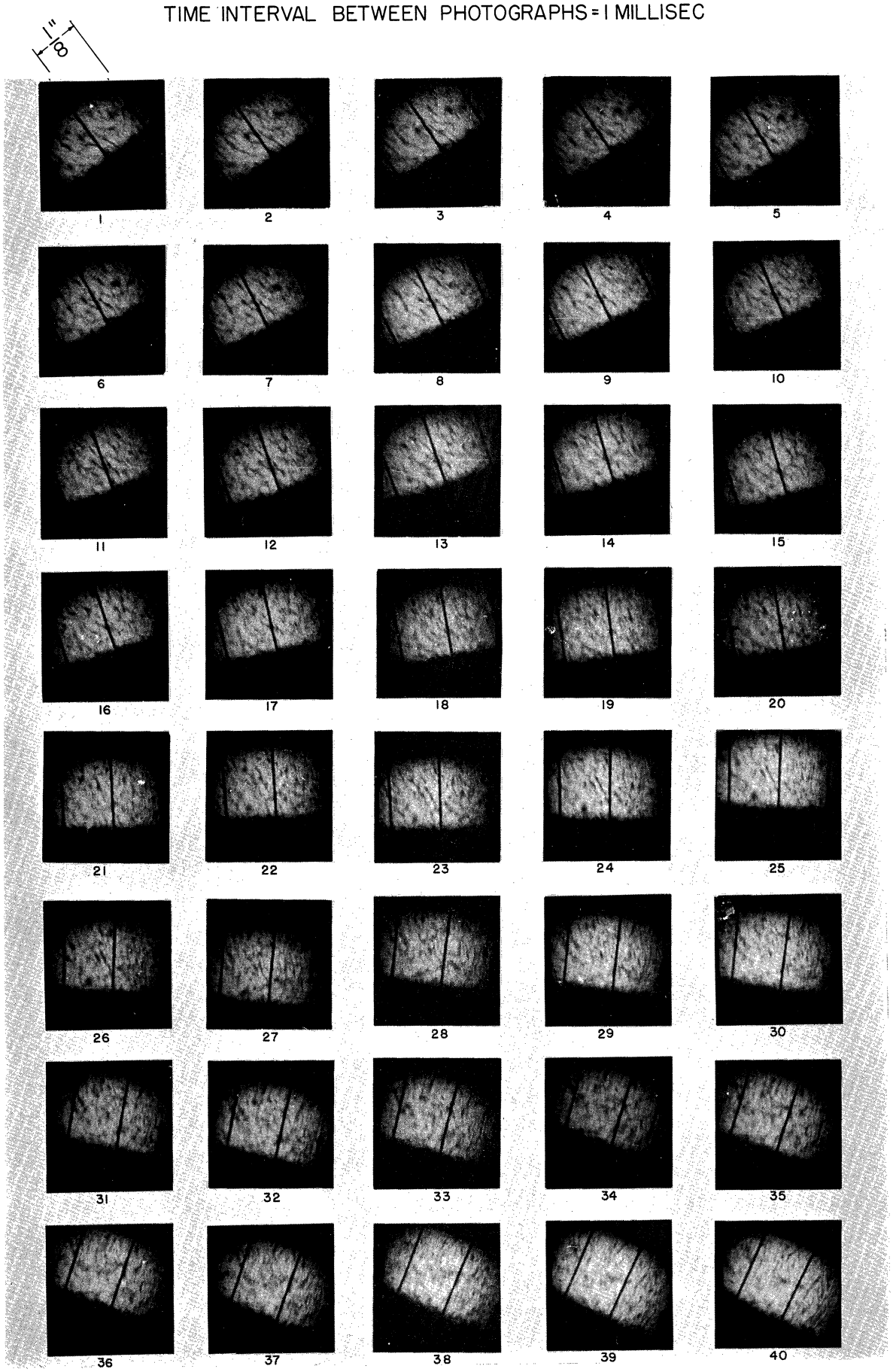

Figure 85. Bubble Photographs, Medium Heat Flux, Low Subcooling, a/g = 100.

BUBBLE PHOTOGRAPHS

$Q/A = 13{,}500 \frac{BTU}{HR FT^2}$ $\Delta T_{SUB} = 48.6°F$ $a/g = 100$

TIME INTERVAL BETWEEN PHOTOGRAPHS = 1 MILLISEC

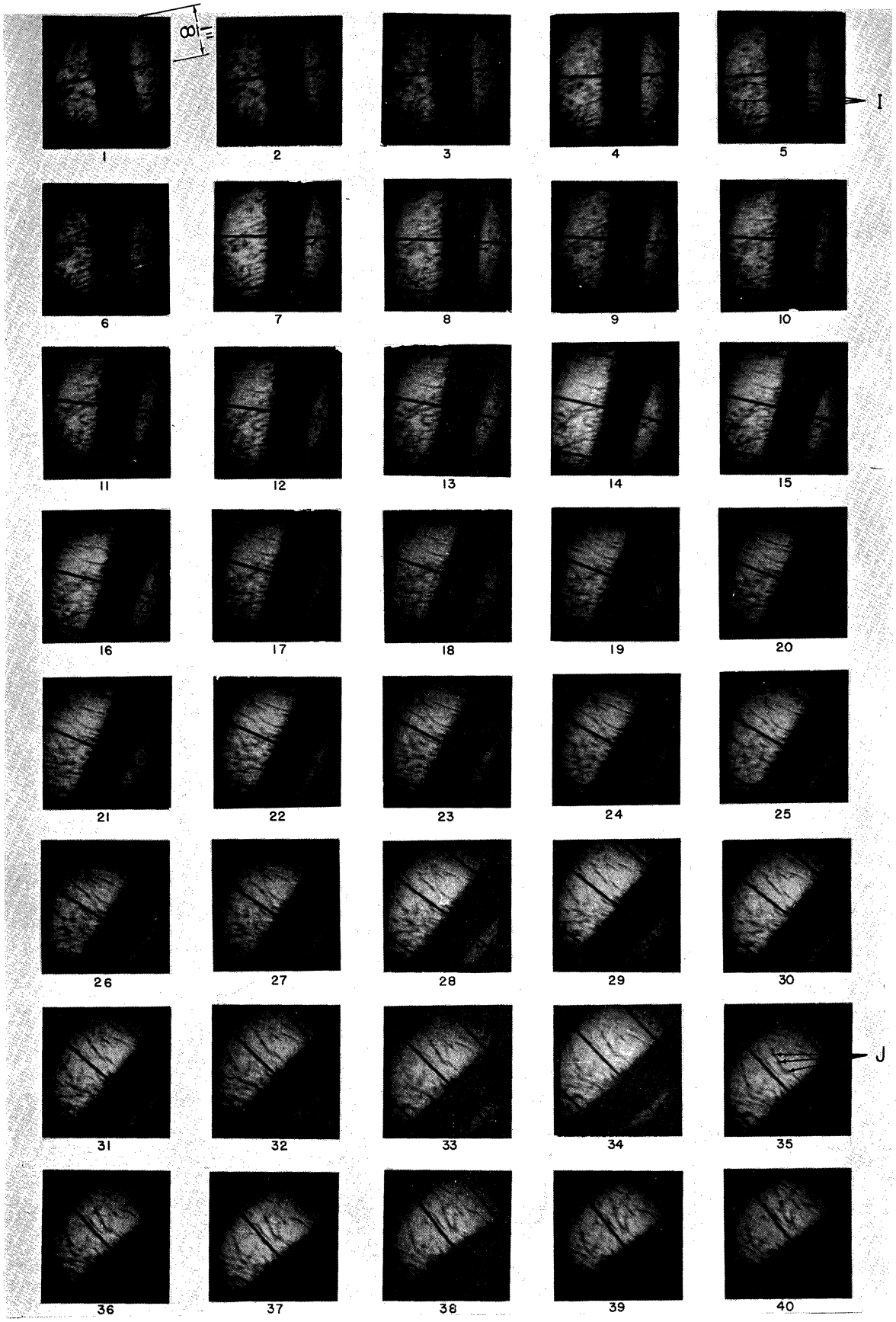

Figure 86. Bubble Photographs, Medium Heat Flux, High Subcooling, a/g = 100.

BUBBLE PHOTOGRAPHS

$Q/A = 42{,}300 \frac{BTU}{Hr\,Ft^2}$ $\Delta T_{SUB} = 14.9°F$ $a/g = 100$

TIME INTERVAL BETWEEN PHOTOGRAPHS = 1 MILLISEC

Figure 87. Bubble Photographs, High Heat Flux, Low Subcooling, a/g = 100.

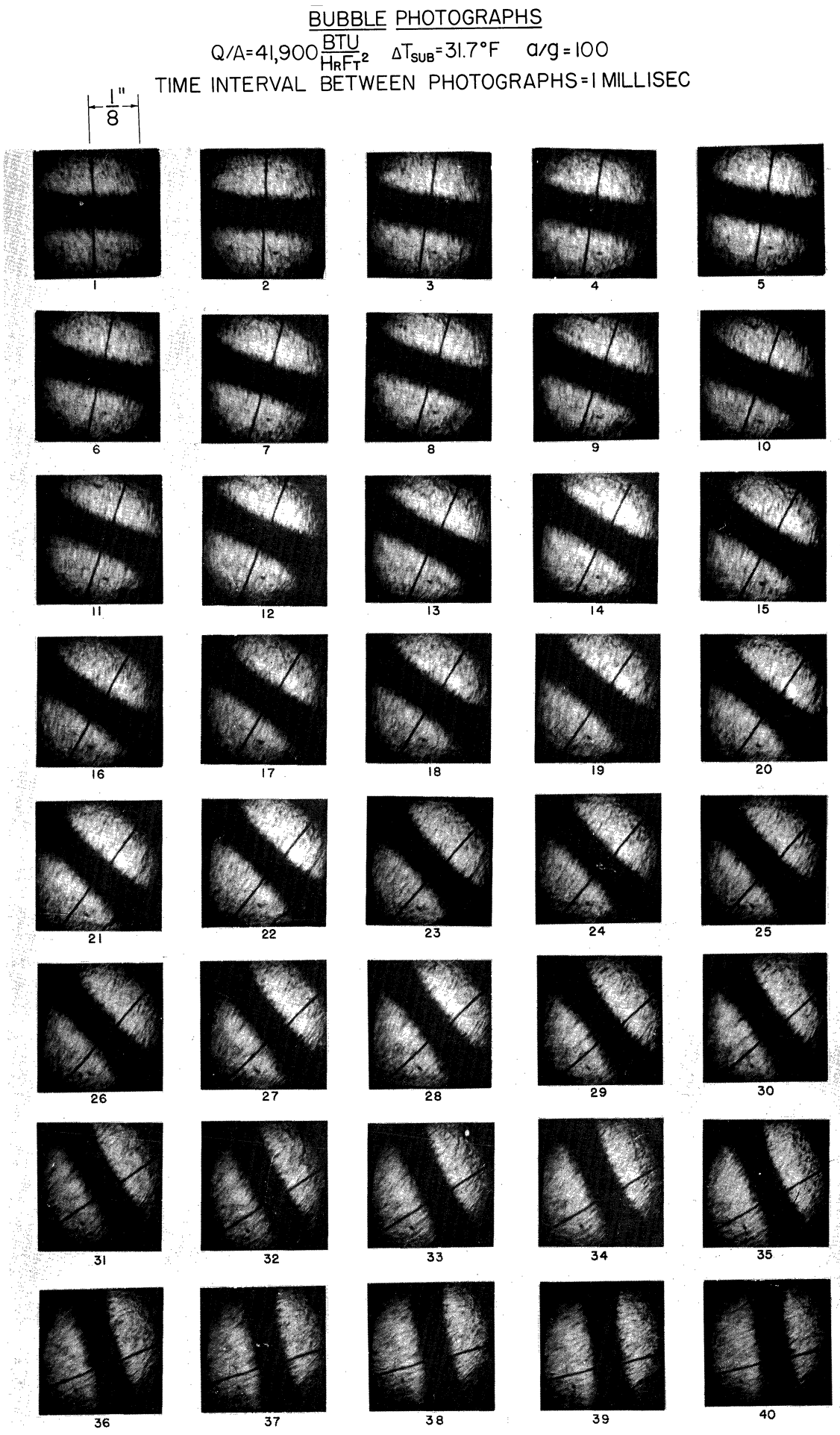

Figure 88. Bubble Photographs, High Heat Flux, High Subcooling, a/g = 100.

BIBLIOGRAPHY

1. Zuber, N., "Recent Trends in Boiling Heat Transfer Research," Applied Mechanics Reviews, Volume 17, Number 9, 1964.

2. Rohsenow, W. H., "Heat Transfer with Boiling," ASHRE Semi Annual Meeting, January 1966.

3. Westwater, J. W., "Boiling Heat Transfer," American Scientist, Volume 47, Number 9, 1959.

4. Jakob, M., Heat Transfer, John Wiley & Sons, 1949.

5. Rohsenow, W. H., and J. A. Clark, "A Study of the Mechanism of Boiling Heat Transfer," Transactions ASME, Volume 73, Number 5, 1951.

6. Gunther, F. C., and F. Kreith, "Photographic Study of Bubble Formation in Heat Transfer to Subcooled Water," Proceedings of the Heat Transfer and Fluid Mechanics Institute, 1949.

7. Rohsenow, W. M., "A Method of Correlating Heat Transfer Data from Surface Boiling Liquids," Transactions ASME, Volume 74, Number 7, 1952.

8. Levy, S., "Generalized Correlation of Boiling Heat Transfer," Transactions ASME Journal of Heat Transfer, Series C, Volume 81, Number 1, 1959.

9. Mixon, F. O., W. Y. Chon and K. O. Beatty, "The Effect of Electrolytic Gas Evolution on Heat Transfer," Chemical Engineering Progress Symposium Series, Volume 56, Number 30, 1960.

10. Forster, H. K., and R. Grief, "Heat Transfer to a Boiling Liquid-Mechanisms and Correlations," Transactions ASME Journal of Heat Transfer, Series C, Volume 81, Number 1, 1959.

11. Bergles, A. E., and W. M. Rohsenow, "The Determination of Forced Convection Surface Boiling Heat Transfer," Transactions ASME Journal of Heat Transfer, Series C, Volume 86, Number 3, 1964.

12. Rallis, C. J., R. V. Greenland and A. Kok, "Stagnant Pool Nucleate Boiling from Horizontal Wires Under Saturated and Subcooled Conditions," South African Mechanical Engineer, Volume 10, Number 1, 1961.

13. Hara, T., "The Mechanism of Nucleate Boiling Heat Transfer," International Journal Heat Mass Transfer, Volume 6, 1963.

14. Nishikawa, K., and K. Yamagata, "On the Correlation of Nucleate Boiling Heat Transfer," International Journal Heat Mass Transfer, Volume 1, 1960.

15. Han, C. Y., and P. Griffith, "The Mechanism of Heat Transfer in Nucleate Pool Boiling," International Journal Heat Mass Transfer, Volume 8, 1965.

16. Moore, F. D., and R. B. Mesler, "The Measurement of Rapid Surface Temperature Fluctuations During the Nucleate Boiling of Water," AIChE Journal, Volume 7, Number 4, 1961.

17. Hendricks, R. C., and R. R. Sharp, "Initiation of Cooling Due to Bubble Growth on a Heating Surface," NASA Technical Note D2290, 1964.

18. Siegel, R., and C. Usiskin, "A Photographic Study of Boiling in the Absence of Gravity," Transactions ASME Journal of Heat Transfer, Series C, Volume 81, Number 3, 1959.

19. Usiskin, C., and R. Siegel, "An Experimental Study of Boiling in Reduced and Zero Gravity Fields," Transactions ASME Journal of Heat Transfer, Series C, Volume 83, Number 3, 1961.

20. Merte, H., and J. A. Clark, "Pool Boiling in an Accelerating System," Transactions ASME Journal of Heat Transfer, Series C, Volume 83, Number 3, 1961.

21. Costello, C. P., and M. E. Tuthill, "Effects of Acceleration on Nucleate Pool Boiling," Chemical Engineering Progress Symposium Series, Volume 57, Number 32, 1961.

22. Slember, R. J., An Investigation of Pool Boiling Under Increased Body Force Conditions, Ph.D. Thesis, University of Pittsburg, 1961.

23. Adelberg, M., "Gravitational Effect Upon Nucleate Boiling Heat Transfer," Advances in the Astronautical Sciences, Volume 14, 1963.

24. Graham, R. W., and R. C. Hendricks, "The Study of the Effect of Multi-G Accelerations on Nucleate Boiling Ebullition," NASA Technical Note D-1196, 1963.

25. Merte, H., and J. A. Clark, "Boiling Heat Transfer with Cryogenic Fluids at Standard, Fractional and Near-Zero Gravity," Transactions ASME Journal of Heat Transfer, Series C, Volume 86, Number 3, 1964.

26. Siegel, R., and E. G. Keshock, "Effects of Reduced Gravity on Nucleate Boiling Bubble Dynamics in Water," AIChE Journal, Volume 10, Number 4, 1964.

27. Rehm, T. R., "Gravity as a Removal Force in Nucleate Boiling," AIChE Symposium on Effects of Zero Gravity on Fluid Dynamics and Heat Transfer, February 1965.

28. Beckman, W. A., H. Merte and J. A. Clark, "A Photographic Study of Boiling in an Accelerating System," Transactions ASME Journal of Heat Transfer, Series C, Volume 87, Number 3, 1965.

29. Schwartz, S. H., Saturated Pool Boiling of Water in a Reduced Gravity Environment, Ph.D. Thesis, University of Southern California, 1966.

30. Adelberg, M., and S. H. Schwartz, "Nucleate Pool Boiling at High G Levels," Proceedings of the Ninth National Heat Transfer Conference, 1967.

31. Westwater, J. W., and D. B. Kirby, "Bubble and Vapour Behaviour on a Heated Horizontal Plate During Pool Boiling Near Burnout," Chemical Engineering Progress Symposium Series, Volume 61, Number 57, 1965.

32. Hsu, Y. Y., "Gradual Transition of Nucleate Boiling from Discrete Bubble Regime to Multibubble Regime," NASA Technical Note D-2564, 1964.

33. National Bureau of Standards, "Reference Tables for Thermocouples," NBS Publication Number 561, 1955.

34. Marcus, B. D., and D. Dropkin, "Measured Temperature Profiles within the Superheated Boundary Layer Above a Horizontal Surface in Saturated Nucleate Pool Boiling of Water," Transactions ASME Journal of Heat Transfer, Series C, Volume 87, Number 3, 1965.

35. Gelb, G. H., B. D. Marcus and D. Dropkin, "On the Manufacture of Fine Wire Thermocouple Probes," Review of Scientific Instruments, Volume 35, Number 1, 1964.

36. E. I. Du Pont de Nemours & Company, "Thermodynamic Properties of Freon 113," Freon Products Division Publication Number T-113A, 1964.

37. E. I. Du Pont de Nemours & Company, "Liquid and Vapour Thermal Conductivity of Freon Refrigerants," Freon Products Division Publication Number B-9A, 1965.

38. E. I. Du Pont de Nemours & Company, "Surface Tension of Freon Compounds," Freon Products Division Publication Number D-27, 1965.

39. Kline, S. J., and F. A. McClintock, "Describing Uncertainties in Single Sample Experiments," Mechanical Engineering, Volume 75, 1953.

40. Tong, L. S., L. E. Efferding and A. A. Bishop, "A Photographic Study of Subcooled Boiling Flow and DNB of Freon 113 in a Vertical Channel," ASME Paper 66-WA/HT-39.

41. Fishenden, M., and O. A. Saunders, An Introduction to Heat Transfer, Oxford, 1960.

42. Corty, C., and A. S. Foust, "Surface Variables in Nucleate Boiling," Chemical Progress Symposium Series, Volume 51, Number 17, 1955.

43. Lady, E. R., Low Heat Flux Boiling, Ph.D. Thesis, University of Michigan, 1963.

44. McAdams, W. H., W. E. Kennel, D. S. Minden, R. Carl, P. M. Picornell and J. Dew, "Heat Transfer at High Rates to Water with Surface Boiling," Industrial and Engineering Chemistry, Volume 41, 1949.

45. Pike, F. R., P. D. Miller and K. O. Beatty, "Effect of Gas Evoluion on Surface Boiling at Wire Coils," Chemical Engineering Progress Symposium Series, Volume 51, Number 17, 1955.

46. Lippert, T. E., and R. S. Dougall, "A Study of the Temperature Profiles Measured in the Thermal Sublayer of Water, Freon 113 and Methyl Alcohol During Pool Boiling," Proceedings of the Tenth National Heat Transfer Conference, 1968.

47. Gaertner, R. F., and J. W. Westwater, "Population of Active Sites in Nucleate Boiling Heat Transfer," Chemical Engineering Progress Symposium Series, Volume 46, Number 30, 1960.

48. Gaertner, R. F., "Distribution of Active Sites in the Nucleate Boiling of Liquids," Chemical Engineering Progress Symposium Series, Volume 59, Number 41, 1963.

49. Cochran, T. H., and J. C. Aydelott, "Effects of Subcooling and Gravity Level on Boiling in the Discrete Bubble Regime," NASA Technical Note D3449, 1966.

50. Van Stralen, S. J. D., "The Mechanism of Nucleate Boiling in Pure Liquids and Binary Mixtures," International Journal Heat Mass Transfer, Volume 10, Number 11, 1967.

51. Gaertner, R. F., "Photographic Study of Nucleate Pool Boiling on a Horizontal Surface," Transactions ASME Journal of Heat Transfer, Series C, Volume 87, Number 1, 1965.

52. Kutateladze, S. S., and V. M. Borishanskii, A Concise Encyclopedia of Heat Transfer, Pergamon Press, 1966.

53. Rallis, C. J., and H. H. Jawurek, "Latent Heat Transport in Saturated Nucleate Boiling," International Journal Heat Mass Transfer, Volume 7, 1964.

54. Zuber, N., "Nucleate Boiling. The Region of Isolated Bubbles and the Similarity with Natural Convection," International Journal Heat Mass Transfer, Volume 6, 1963.

55. Tien, C. L., "A Hydrodynamic Model for Nucleate Pool Boiling," International Journal Heat Mass Transfer, Volume 5, 1962.

56. Novakovic, M. M., and M. S. Stefanovic, "Nucleation from a Mercury Surface," Proceedings of the Third International Heat Transfer Conference, 1966.